

Stochastic Transport in Complex Environments: Applications in Cell Biology

Dissertation

zur Erlangung des Grades
des Doktors der Naturwissenschaften

der Naturwissenschaftlich-Technischen Fakultät
der Universität des Saarlandes

von
Robin Jose

Saarbrücken
2020

Tag des Kolloquiums: 04.03.2021

Dekan: Prof. Dr. Jörn Walter

Berichterstatter: Prof. Dr. Ludger Santen
Prof. Dr. Dr. h.c. Heiko Rieger
Prof. Dr. Stefan Klumpp

Vorsitz: Prof. Dr. Albrecht Ott

Akd. Mitarbeiter: Dr. Christian Spengler

Abstract

Living organisms would not be functional without active processes. This general statement is valid down to the cellular level. Transport processes are necessary to create, maintain and support cellular structures. In this thesis, intracellular transport processes, driven by concentration gradients and active matter, as well as the dynamics of migrating cells are studied.

Many studies deal with diffusive intracellular transport in the complex environment of neuronal dendrites, however, focusing on a few spines. In this thesis, a model was developed for diffusive transport in a full dendritic tree. A link was established between complex structural changes by diseases and transport characteristics.

Furthermore, recent experimental studies of search processes in migration of dendritic cells show a link between speed and persistence. In this thesis, a correlation between them was included in a stochastic model, which lead to increased search efficiency.

Finally, this thesis deals with the question of how active, bidirectional transport by molecular motors in axons can be efficient. Generically, traffic jams are expected in confined environments. Limitations of bypassing mechanisms are discussed with a bidirectional non-Markovian exclusion process, developed in this thesis. Experimental findings of cooperative effects and microtubule modifications have been incorporated in a stochastic model, leading to self-organized lane-formation and thus, efficient bidirectional transport.

Kurzzusammenfassung

Ohne aktive Prozesse wären lebendige Organismen nicht funktionsfähig. Dies gilt bis herab zur Zellebene. Transportprozesse sind notwendig um zelluläre Strukturen aufzubauen und zu erhalten. In dieser Arbeit werden intrazelluläre Transportprozesse, getrieben von Konzentrationsgradienten und aktiver Materie, sowie die Dynamik in Zellmigration untersucht.

Viele Studien beschäftigen sich mit passivem Transport in der komplexen Umgebung von neuronalen Dendriten, vorwiegend jedoch mit einzelnen Dornvorsätzen (*spines*). In dieser Arbeit wurde ein Modell zu Diffusion in einer vollständigen Dendritenstruktur entwickelt und eine Relation zwischen Krankheitsverläufen und neuronalen Funktionen gefunden.

Die Migration von dendritischen Zellen zeigen einen Zusammenhang zwischen ihrer Geschwindigkeit und Persistenz. Dieser wurde in ein stochastisches Modell übernommen welches zeigte, dass die Sucheeffizienz der Zellen damit gesteigert werden kann.

Außerdem geht es um die Frage wie aktiver, bidirektionaler Transport durch molekulare Motoren in Axonen effizient sein kann. In einem so begrenzten Raum sind Verkehrsstaus zu erwarten. In dieser Arbeit wurden lokale Austauschmechanismen anhand des entwickelten Nicht-Markovschen, bidirektionalen Exklusionsprozess diskutiert. Experimentell entdeckte kooperative Effekte und Mikrotubulimodifikationen wurde in ein stochastisches Modell übernommen, was zu selbstorganisierter Spurbildung und damit zu effizientem bidirektionalem Transport führte.

Contents

Nomenclature	ix
1 Introduction	13
2 Biological background	17
2.1 The cytoskeleton	18
2.1.1 Microtubules	19
2.2 Molecular motors and other MAPs	20
2.2.1 Kinesin	20
2.2.2 Dynein	22
2.2.3 Interaction of MAPs and the MT	23
2.3 Bidirectional transport by molecular motors	26
2.4 Intracellular transport in neurons	27
2.4.1 Axons	27
2.4.2 Dendrites	28
2.4.3 Organization of the MT network influences motor driven transport	30
2.4.4 Neurodegenerative diseases	31
2.5 Migration of dendritic cells	31
2.6 Chapter summary	33
3 Theoretical Background	35
3.1 Stochastic processes	36
3.1.1 Markov processes	36
3.1.2 Sampling methods for Markov processes	37
3.2 The random walker	38
3.2.1 The ordinary random walker	38
3.2.2 Mean square displacement	39
3.2.3 First-passage time	39
3.3 Non-Markovian processes	41
3.3.1 Examples of non-Markovian random walks	41
3.3.2 Sampling methods for non-Markovian processes	42
3.4 Renewal processes and residual waiting times	42
3.5 Chapter summary	44

4	Random walk models for passive transport and cell migration	45
4.1	Diffusion in neuronal dendrites	46
4.1.1	Diffusion in branched channels	46
4.1.2	Diffusion in spiny dendrites	47
4.2	Discrete treelike networks	49
4.3	Mapping a random walk on treelike networks to a one-dimensional random walk	51
4.4	Reconstructing network structure by transport properties	51
4.5	Persistent random walks in cell migration	52
4.6	Chapter summary	54
5	Lattice gas models for active transport	55
5.1	Unidirectional exclusion processes	55
5.1.1	The totally asymmetric simple exclusion process	56
5.1.2	TASEP with Langmuir kinetics	58
5.1.3	Local irregularities	59
5.1.4	Conservation of particles in the reservoir	60
5.1.5	Unidirectional multi-lane models	62
5.1.6	Non-Markovian exclusion processes	62
5.2	Bidirectional exclusion processes	64
5.2.1	Site-exchange models	65
5.2.2	Bidirectional multi-lane models	67
5.3	Chapter summary	71
6	Own work	73
6.1	Passive transport in treelike structures	74
6.1.1	Trapping in and escape from branched structures of neuronal dendrites	74
6.1.2	Unraveling the structure of treelike networks from first-passage times of lazy random walkers	76
6.2	Search processes in cell migration	78
6.2.1	Persistence-speed coupling enhances the search efficiency of migrating cells	78
6.3	Active bidirectional intracellular transport	79
6.3.1	Bidirectional non-Markovian exclusion processes	80
6.3.2	Self-organized lane formation in bidirectional transport of molecular motors	83
7	Conclusion & Outlook	87
	Bibliography	91
	Publications and manuscripts	113

Addendum I	Trapping in and Escape from Branched Structures of Neuronal Dendrites	115
Addendum II	Unraveling the structure of treelike networks from first-passage times of lazy random walkers	129
Addendum III	Persistence-Speed Coupling Enhances the Search Efficiency of Migrating Cells	139
Addendum IV	Bidirectional non-Markovian exclusion processes	145
Addendum V	Self-organized lane-formation in bidirectional transport of molecular motors	171

Nomenclature

+TIP	Microtubule plus-end tracking proteins
ADP	Adenosine diphosphate
ASEP	Asymmetric simple exclusion process
ATP	Adenosine triphosphate
CDF	Cumulative distribution function
DC	Dendritic cell
EB	End-binding proteins
GDP	Guanosine diphosphate
GTP	Guanosine triphosphate
MAP	Microtubule associated protein
MC	Monte Carlo
MFPT	Mean first-passage time
MSD	Mean square displacement
MTOC	Microtubule organizing center
MT	Microtubule
OBC	Open boundary conditions
PBC	Periodic boundary conditions
PDF	Probability density function
PTM	Posttranslational modifications
RW	Random walker
TASEP	Totally asymmetric simple exclusion process

List of Figures

2.1	Image of the cytoskeleton of a hippocampal neuron	18
2.2	Microtubule structure and dynamics	19
2.3	Kinesin and dynein	21
2.4	Interaction between microtubules and MAPs	23
2.5	Posttranslational modifications on the MT	24
2.6	Microtubule lattice compaction	25
2.7	Bidirectional transport	26
2.8	Axons and dendrites in the neuron	28
2.9	Cross-section of the MT network	29
2.10	Spiny dendritic channel in diseases	29
2.11	Spiny dendrites in diseases	30
2.12	Dendritic cell migration types	32
3.1	Age and residual life	43
4.1	Anomalous diffusion in spiny dendrites	47
4.2	Mapping three-dimensional structure to a topological graph	49
4.3	Cayley tree	50
5.1	TASEP	56
5.2	TASEP phase space	58
5.3	TASEP with Langmuir kinetics	59
5.4	Confined diffusion	61
5.5	Non-Markovian TASEP fundamental diagram	63
5.6	TASEP site-exchange	65
5.7	TASEP with explicit diffusive lane	68
5.8	TASEP with particle attraction	69
6.1	Dendritic tree model	74
6.2	Unraveling the network structure	77
6.3	Schematic drawing of motor driven transport in the axon	80
6.4	Bidirectional non-Markovian site-exchange	82

Chapter 1

Introduction

Transport processes are an important part of non-equilibrium and biological physics. For maintaining transport processes, energy has to be provided. This is possible either by establishing and maintaining concentration gradients that drive passive transport or by directly providing energy to active particles. In cell biology, this flow of energy eventually is required to generate and maintain the functional cellular structures which represent, from a physical point of view, states far from equilibrium [1].

Applications for non-equilibrium transport in cell biology range over large length scales, from the diffusion of microscopic chemical signals inside cells up to the migration of a whole cell. Also, one can divide intracellular transport in passive gradient-driven and active transport such as by molecular motors along the cytoskeleton of the cell [2]. Besides its variety, many transport processes share similar characteristics. For this thesis, an important characteristic is the impact of the environment in which transport takes place. In neuronal axons, for example, active transport is heavily affected by the organization of the cytoskeleton on which it relies on [3,4]. This connection is in particular interesting because disturbed transport has been found in relation to diseases such as Alzheimer's, Parkinson's and Huntington's disease [5,6]. It has been found that neurodegenerative diseases can highly affect the structure of dendrites and spines [7,8]. It is, therefore, crucial to better understand the requirements and processes of biological transport.

Many achievements have been made by experiments but also theoretical descriptions are useful in order to reduce complexity and conceptualize. Theoretical modeling has been widely applied to describe transport processes in cell biology [9–12]. In this thesis, the focus is on stochastic modeling and Monte Carlo simulations. The models developed are based on two extensively studied model classes: Diffusion by random walks [9,13] and driven lattice gases [9,10].

The objective of this thesis is to investigate applications of stochastic modeling transport processes in cell biology with a special focus on environmental influences. The work is structured in three parts, i.e. passive transport in branched, treelike channels of neuronal dendrites, active transport of migrating dendritic cells and active bidirectional transport by molecular motor proteins in crowded environments of neuronal axons.

The first project deals with the diffusive transport of chemical signals in treelike

geometries such as neuronal dendrites. Although diffusion has been widely studied, passive transport is still an active field in intracellular transport since it strongly depends on the environment [9, 13]. The diverse scenarios in biological systems lead to a variety of different effects such as non-Markovian characteristics emerging from interactions with the environment [14, 15] or anomalous diffusion and localization in small protrusions found along dendrites, called spines [16–19]. In the **publication of Jose *et al.* in Biophysical J. 2018 (Addendum I)**, structural influences on transport properties are investigated with a random walk model for chemical signals in neuronal dendrites. Essential key structural parameters are identified and calibrated to healthy and dendrites under disease progression. The goal is to link structural key parameters to transport characteristics by determining search (escape) times into the cell soma.

The opposite scenario is considered in the **publication of Shaebani *et al.* in Physical Review E 2018 (Addendum II)**. Here, the random walk model on treelike structures is used to predict key parameters of a hidden tree. By measuring escape times of random walkers moving along the tree, a method is developed to predict the structure.

In the second project, a random walker approach is applied to the search problem in cell migration. Dendritic cells (DCs) actively migrate in the body to search for pathogens [20]. Studies did investigate search problems such as in the migration of dendritic cells in two dimensions [11, 21]. It has been shown that the search can be optimized by tuning relevant parameters such as the persistence [21]. However, these parameters are not always independent of each other. For DCs, it has been found that cell speed and cell persistence are correlated [22–24]. Instead of tuning a single parameter, a new class of search optimizations is investigated in this thesis, which combines a coupling of the relevant parameters. The objective of the **manuscript of Shaebani *et al.* (Addendum III)** is to investigate how a correlation between speed and persistence is affecting the search efficiency.

The third project addressed in this thesis is bidirectional, intracellular transport actively carried out by molecular motors along the cytoskeleton of neurons. Whereas the first and second projects deal with single or independent objects, bidirectional transport by molecular motors requires a many body treatment. The large spatial extension of cargoes in the crowded environment of the axon is expected to cause interactions and traffic jams. Cluster formation is generically observed for bidirectional transport with volume exclusion in extended one-dimensional systems [25–27]. Traffic jams are, however, usually not observed in healthy neurons. Thus, it is necessary to investigate the mechanism that leads to stable transport.

A common lattice gas model for collective transport in one dimension is the totally asymmetric exclusion process (TASEP). Bidirectional transport has, for example, been addressed in two-species exclusion processes with Markovian site-exchange [27]. However, this description leads to transport that is fully determined by the local exchange rate in a cluster region of a traffic jam. For collective effects that lead

to complex blockage situations, constant ability to switch positions and reorganize in a cluster is highly questionable. Hence, assuming particle movements without memory effects might not be a valid description of the interaction in a crowded environment [14]. In the **publication of Jose *et al.* in JSTAT 2020 (Addendum IV)**, a non-Markovian variation of the two-species TASEP with algebraic exchange-time distributions is investigated with respect to the transport efficiency.

An alternative approach to efficient bidirectional transport is the organization of transport in quasi-unidirectional sub-systems as known for engineered systems such as in vehicle traffic [28]. The question arises of how such an organization could be implemented inside the cell. Recent studies emphasize the impact of posttranslational modifications (PTMs) on the cytoskeleton [29, 30]. They have been observed to lead to lane-formation in motor-driven transport in dendrites [31] and cilia [32]. However, such a mechanism is not known for transport in axons where the cytoskeleton structurally differs from the one in cilia or dendrites [31–33]. Recent findings give clues to a promising candidate for such a mechanism. Shima *et al.* reported that molecular motors can modify the structure of filaments while walking on them. This lead to a higher binding affinity of motors on that modified filament [34]. This essentially initiates a feedback loop. In the **manuscript of Jose *et al.* (Addendum V)**, this mechanism is implemented in a bidirectional two-species exclusion process with the goal to investigate if the feedback can lead to self-organized lane-formation of transport along the cytoskeleton in axons.

This thesis is organized as follows: The biological background for the different applications in cell biology is given in chapter 2. The theoretical framework for the stochastic description of transport processes by random walkers and exclusion processes is presented in chapter 3. I review previous literature on the field of random walks and search problems in chapter 4. Thereby, the first part focuses on diffusive transport in dendritic structures and on networks, the second part on persistent walks and cell migration. In chapter 5, I review literature on modeling active uni- and bidirectional transport with respect to TASEP variations and intracellular transport. In chapter 6, I introduce my own work which was developed in the context of this thesis. The presentation is based on the original publications and manuscripts. A summary of the results and outlook to future applications is given in chapter 7. The publications and manuscripts presented in chapter 6 are attached in Addendum I-V.

Chapter 2

Biological background

Contents

2.1	The cytoskeleton	18
2.1.1	Microtubules	19
2.2	Molecular motors and other MAPs	20
2.2.1	Kinesin	20
2.2.2	Dynein	22
2.2.3	Interaction of MAPs and the MT	23
2.3	Bidirectional transport by molecular motors	26
2.4	Intracellular transport in neurons	27
2.4.1	Axons	27
2.4.2	Dendrites	28
2.4.3	Organization of the MT network influences motor driven transport	30
2.4.4	Neurodegenerative diseases	31
2.5	Migration of dendritic cells	31
2.6	Chapter summary	33

From a physicist's point of view, the cell is an exciting example of a complex system, consisting of many components that interact in various combinations [20]. Transport processes are essential, in order to organize internally and provide functionality. In neurons, for example, mitochondria, which serve as power plants and Ca^{2+} buffers, need to be distributed to distal regions such as synapses and axonal branches [35]. Intracellular transport can be carried out passively by diffusion, which is driven by concentration gradients, or actively such as the movement by molecular motor proteins along filaments [2, 12, 20, 36–39]. In addition, transport is not only important inside cells. Some cells also need to migrate as a whole. Dendritic cells, for instance, migrate from tissues to lymph nodes, where they can activate T cells to coordinate the immune response [20, 40, 41].

In this chapter, I provide basic information about the biological systems in which transport processes are studied in this thesis. I introduce components of the cell which are important for active intracellular transport as well as for cell migration such as the cytoskeleton and molecular motor proteins. Thereby, I will discuss the

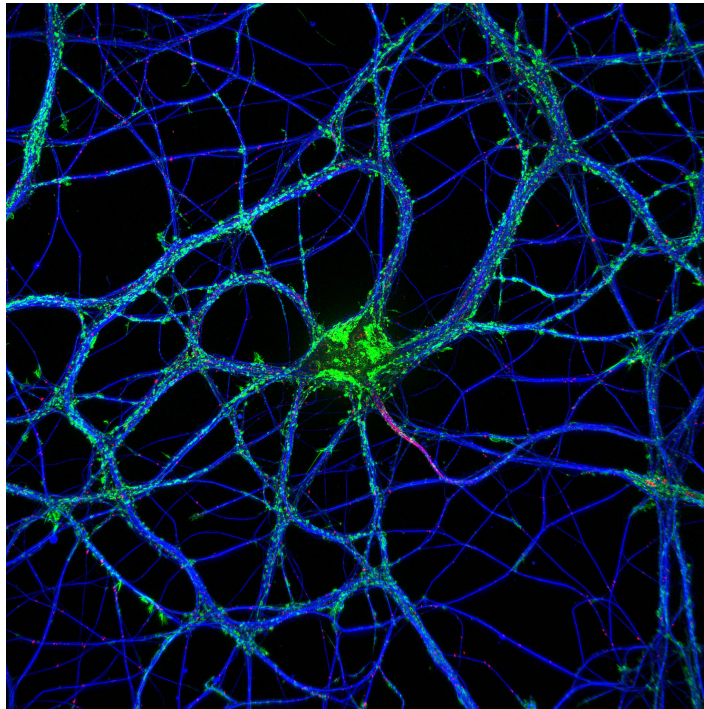


Figure 2.1: Image of the cytoskeleton of a hippocampal neuron labeled for actin (green), microtubules (blue) and neurofascin (red). Reprinted with permission from Christophe Leterrier, <http://www.neurocytolab.org>, Copyright (2020), accessed https://inp.univ-amu.fr/sites/inp.univ-amu.fr/files/galerie/neurocyto_pic3.jpg on 25. February 2020.

nerve cell as an environment for active and passive intracellular transport. Cell migration such as found for a dendritic cell (DC) is reviewed afterward. A large fraction of the content of this chapter is based on the book *Molecular Biology of the Cell* by Alberts *et al.* [20]. Other resources used are stated in the text.

2.1 The cytoskeleton

The first section of this chapter deals with the cytoskeleton. It is build from protein filaments that can be divided in three groups: *actin filaments*, *microtubules* (MTs) and *intermediate filaments* [20]. Filaments of these groups differ in their composition, properties, and appearance in the cytoskeleton [20]. The helical structure of actin filaments is produced by polymerizing sub-units. In this way, filaments form long and rather flexible structures. Many of these actin filaments are combined and connected by accessory proteins in order to form the actin cortex of the cytoskeleton. MTs are tube-like filaments build from tubulin dimers. Actin filaments and microtubules are the most common and most studied filament groups. Intermediate filaments denote a filament class of huge variety. Figure 2.1 shows a fluorescence spectroscopy image of

a hippocampal neuron cell. Microtubules have been labeled in blue, actin filaments in green. Since the cytoskeleton is present over the cell, a good impression of the overall shape can be gained from the location of filaments. In this thesis, the focus is on microtubules which are discussed in detail in the following section.

2.1.1 Microtubules

A microtubule is a tube-like structure that develops by successively polymerizing tubulin dimers (see figure 2.2). A tubulin sub-unit consists of α -tubulin and β -tubulin monomers forming a dimer of 8 nm length. From these polar dimers, protofilaments can be built by adding up head to tail (see figure 2.2 (a)). The complete microtubule consists of 13 of these protofilaments arranged in a tube structure. Protofilaments

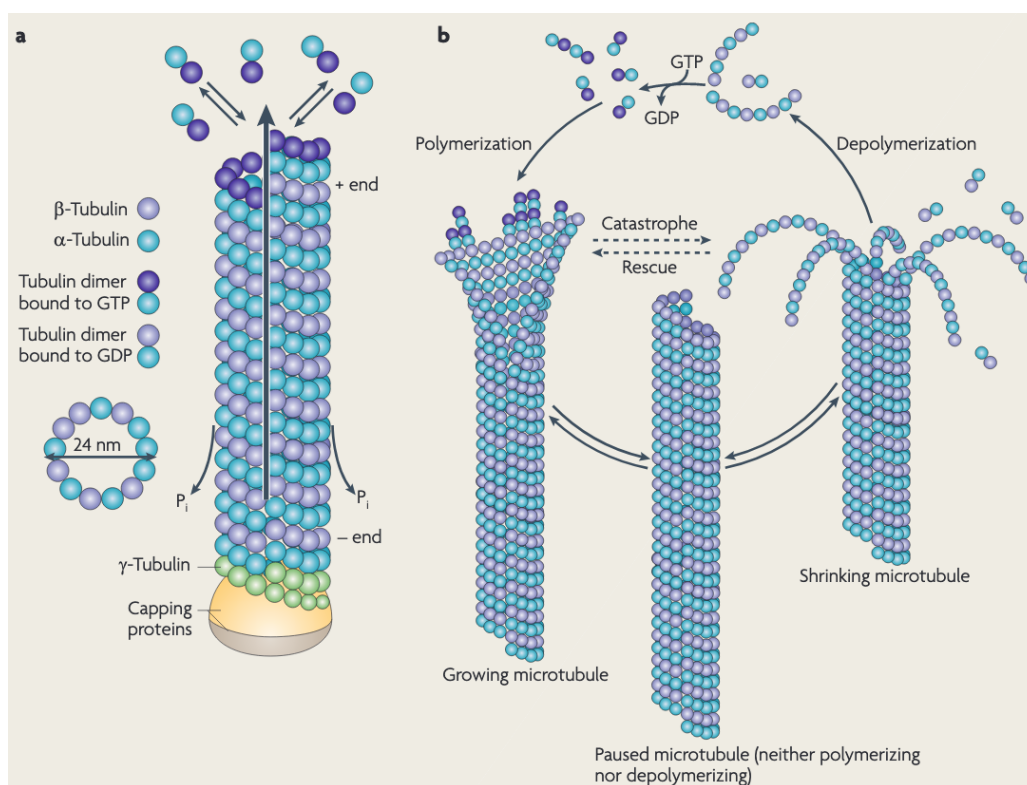


Figure 2.2: Microtubules are polar filaments built from tubulin dimers. The minus-end is typically capped by proteins and thus stabilized, the plus-end exhibits dynamic instability. GTP bound dimers polymerize to the tip and transition in the GDP state. By catastrophe events, the MT switches into the depolymerization state. This shrinking is stopped by a rescue event leading to a metastable MT which can either start to polymerize or depolymerize again. Reprinted from Nature Reviews Neuroscience, 10, Conde *et al.*, Microtubule assembly, organization and dynamics in axons and dendrites Cecilia, 319-332, Copyright (2009), with permission from Springer Nature.

are aligned parallel and slightly shifted along the tube axis (see figure 2.2 (b)). The resulting MT has an outer diameter of approximately 25 nm and the composition structure formed by the sub-units is named MT *lattice*. The largest shift between monomers in the MT lattice is called *seam*. The dimer polarity is eventually reflected in the whole MT, resulting in a plus-end and a minus-end.

The stability of the MT lattice depends on the conformational state of tubulin molecules [29,42]. Furthermore, tubulin dimers have tails of amino acid sequences that do point out of the microtubule structure [43]. The β -tubulin of a sub-unit can be found in a GTP-state (Guanosine triphosphate) or a GDP-state (Guanosine diphosphate). The transition between the two states is facilitated by adding and removing guanine nucleotides [44]. Note that the MT lattice is more stable in the GTP state than in the GDP state.

Switching between the two GTP and GDP states can lead to *growing* and a *shrinking* states in the so called process of *dynamic instability* [42,44]. GTP-dimers are added to the MT during polymerization. This GTP state will eventually transition to a GDP-state over time. The full MT is therefore stabilized by adding GTP-dimers (GTP cap) to the tip and destabilized by losing the GTP cap over time. The GDP filament can then switch to depolymerization which is called *catastrophe*. The switch back to the polymerizing state is called *rescue* [42,44] (see figure 2.2 (c)).

The dynamic instability is usually restricted to the plus-end of the MT because the minus-end is stabilized. This is provided by proteins such as CAMSAP2 in axons [45] or by the microtubule organizing center (MTOC) which is close to the cell nucleus in eukaryotic cells [20].

2.2 Molecular motors and other MAPs

In section 2.1, the structure of microtubules has been introduced. In this section, the focus is on microtubule associated proteins (MAPs) that interact with the MT. Important representatives of MAPs are the classes of motor proteins. They are further divided into *myosin*, *kinesin* and *dynein*. The names are thereby referring to large superfamilies with many members. Myosins are associated with actin filaments [2]. Kinesins and dyneins bind to the MT. Bound motors walk along the filament with a given run-length until they detach from the filament again. The stepwise propagation consumes energy provided by ATP hydrolysis (Adenosine triphosphate).

Besides the motor proteins, many other MAPs interact with microtubules such as CAMSAP2 for stabilizing minus-ends [45] which will be further discussed at the end of this section.

2.2.1 Kinesin

The first superfamily of motor proteins introduced in this thesis is kinesin. In the family, at least 90 different members are known [46,47]. Despite a structural variety between members of this family, an important part called the motor domain is very similar for members of the superfamily kinesin. The motor domain connects to the

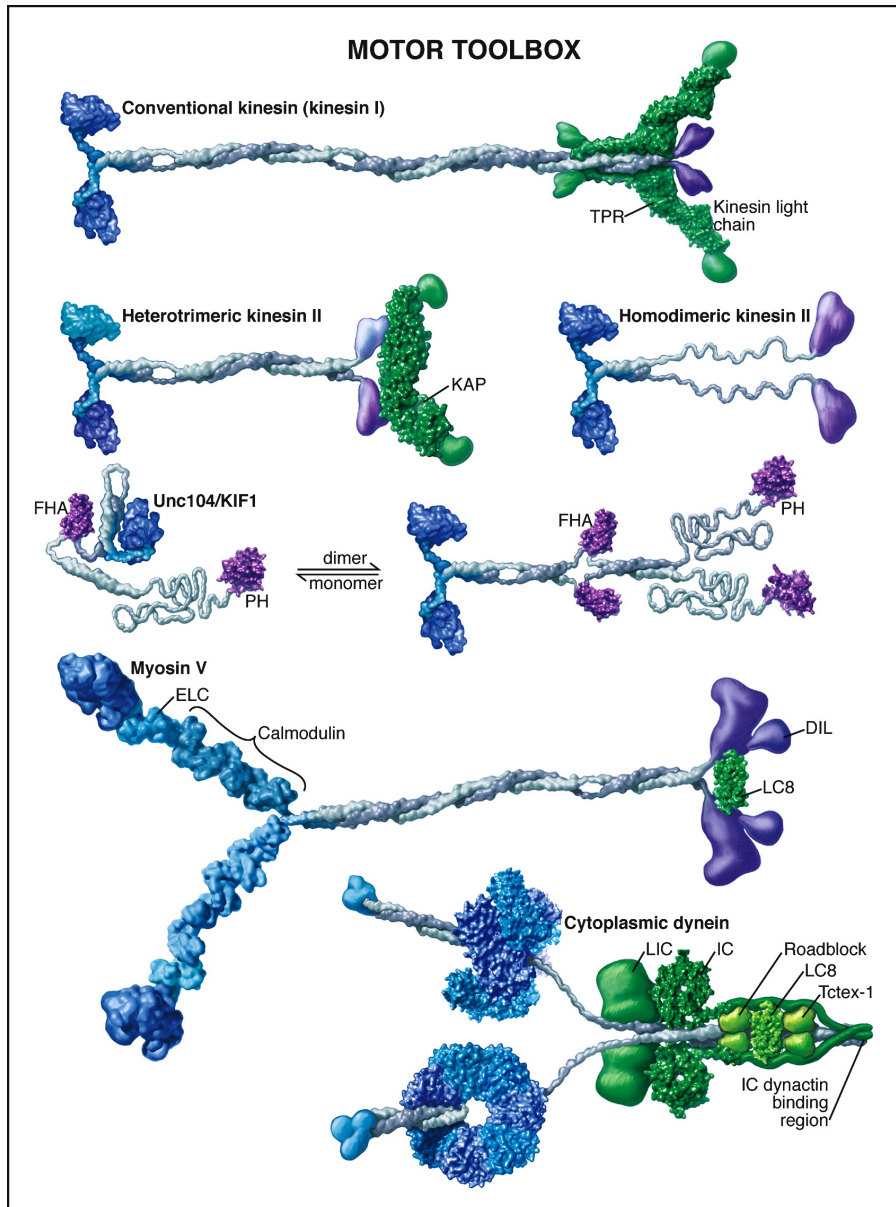


Figure 2.3: Kinesin, myosin, and dynein are molecular motor proteins consisting of a motor domain and a tail which is connected to a load or a cargo. The myosin motor domain moves along actin filaments, kinesin and dynein walk along microtubules. Kinesin moves in the plus-end direction and dynein towards the minus-end of the MT. Besides the direction, both MT associated motor proteins heavily differ in their structure. Reprinted from *Cell*, 112 / 4, Ronald D. Vale, *The Molecular Motor Toolbox for Intracellular Transport*, 467-480, Copyright (2003), with permission from Elsevier.

MT, whereas the subsequent tail can strongly differ in order to serve as a binding component to various types of cargoes [2, 48] (see figure 2.3). Kinesin 1, also called *conventional kinesin*, is often considered to be a standard example of the superfamily [48] (see figure 2.3).

Displacement is generated by the two heads stepping in a hand over hand motion [49] with a step size of one tubulin dimer, i.e., 8 nm [50]. The energy for this mechanism is provided by the ATP-hydrolysis cycle in which the binding of motor-heads to the MT and unbinding from the filament is repeated. For heads bound to ATP (adenosine triphosphate), stronger binding to the filament is generated than for ADP (adenosine diphosphate) bound heads. Hence, a ATP bound head sticks to the MT until it hydrolyzes the ATP to ADP and phosphate in a conformational change of the head and finally detaches from the MT. The head now is displaced along the MT and can change to the ATP state again and eventually rebind to the MT. In this process, the second head changes to the weak binding state and detaches so that the cycle can start again [51]. Repetition of the cycle leads to a hand over hand pattern of motorheads and eventually displacement along the MT [2].

Some kinesin motor proteins, such as conventional kinesin, perform a processive motion along the MT [52] whereas others such as *ncd* detach immediately after one step [48, 53]. The run length is approximately 1 μm [34, 54] where a migration speed between 0.3 $\mu\text{m/s}$ and 1 $\mu\text{m/s}$ has been observed [34, 55]. The speed is depending on the load applied to the kinesin motor protein. The rate of detachment events is determined by the run length. Together with the attachment rate, binding and unbinding rates of a motor are often given in the form of dissociation rates [34].

Despite the similar motor domain, not all kinesin walk in the same direction on the microtubule in the hydrolysis cycle [56]. Conventional kinesin is usually directed toward the plus-end of the MT [20] but kinesin motors such as *ncd* walk toward the minus-end [57].

2.2.2 Dynein

In contrast to the usually plus-end directed kinesin, the class of dynein motor proteins is considered to be minus directed [2, 20]. The dynein superfamily is divided into the two families of *cytoplasmic dynein* and *axonemal dynein* which is responsible for retrograde transport in axons [58]. The high complexity of dynein is reflected in its heavy molecular weight [59]. Different adaptors such as dynactin or BICD cargo adaptors regulate dynein's function and localization in the cell [60] (see figure 2.3). Dynein can be in a diffusing state and needs to be activated for processive walking. This can be achieved by mechanical interaction applying forces on the motor protein [12, 61].

Similar to kinesin, dynein motors also walk by consuming ATP in a processive motion along the MT and can take run lengths in the micrometer scale [62, 63]. By alternating steps of the dynein heads, a movement is generated [64]. Dynein steps length has been observed between one tubulin sub-unit (8 nm) such as for kinesin, and up to 32 nm [63, 64]. In addition, dyneins show side steps to neighbor protofilaments on

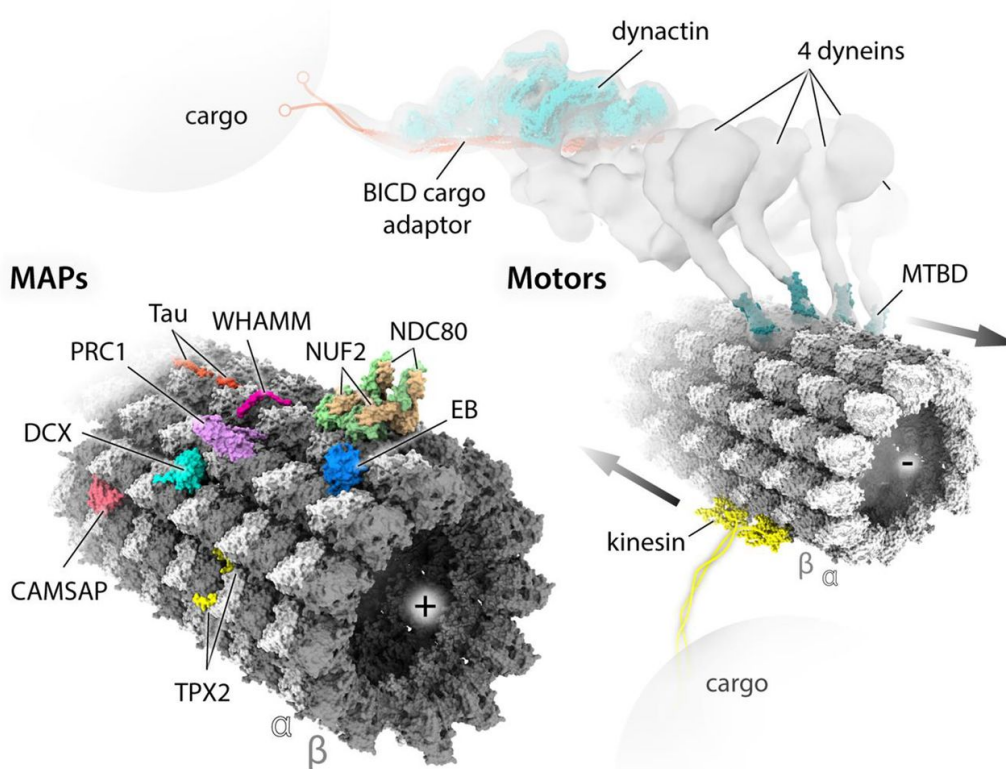


Figure 2.4: Bottom left: Atomic model of the MT lattice build from tubulin dimers and MAPs on the relevant locations on the MT lattice. **Top right:** Cargo transport by molecular motors along the MT lattice. Kinesin is directly bound to the cargo, dynein via dynactin and a BICD adaptor protein. Reprinted with permission from Portland Press, *Essays in Biochemistry*, 62, 6, 737-751 (2018), open access under a CC BY license.

the MT, a phenomenon which is not common for kinesin [60,64–66].

2.2.3 Interaction of MAPs and the MT

In this section, I give several examples of MAPs that interact with the MT. In the context of active intracellular transport by molecular motors, it is worth to look closer at the complex interactions which might help to coordinated transport. Beside molecular motors, the MT interacts with other MAPs. This further increase complexity of the MT structure and intracellular transport. So called *posttranslational modifications* (PTMs) on the MTs lead to tubulin heterogeneity, different functionalities of MTs [29,43] (see figure 2.5). Recent studies bring knowledge on many PTMs together to a *tubulin code* which might regulates the functionality of MTs in cells [29,30,43,67].

Several examples of MAPs are shown schematically in figure 2.4 and MAP-MT interactions are presented in this section. CAMSAP proteins for instance stabilize

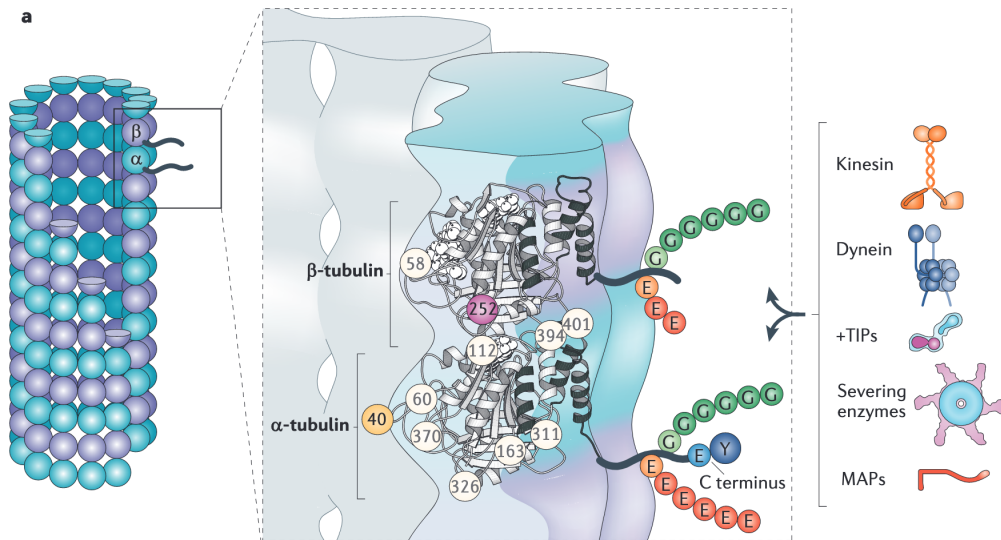


Figure 2.5: Schematics of the tubulin structure embedded in a microtubule. PTMs take place on the tubulin tails that reach out of the MT and therefore can interact with enzymes, +TIPs, motor proteins and other MAPs. Reprinted from *Nature Reviews Molecular Cell Biology*, 12, C. Janke and J. Bulinski, Post-translational regulation of the microtubule cytoskeleton: Mechanisms and functions, 773-786, Copyright (2011), with permission from Springer Nature.

the MT minus-ends [45, 68], DCX stabilizes the 13 protofilament architecture of MTs [68–70] and WHAMM links the MT to the actin network [68, 71, 72]. Tau proteins act stabilizing on the MT lattice [68] but in addition, interacts with motor proteins. *In vitro* experiments showed that kinesin binding affinity was lowered in presence of tau [73] and also the detachment from the MT was enhanced in an other experiment [74], however, the speed was not affected by tau [75]. Kinesin dependent traffic was observed to be inhibited when tau was overexpressed [76]. The protein MAP7 and tau have been found to compete for binding to microtubules [77], which can regulate motor movements due to MAP7 strongly recruiting kinesin to the MT *in vitro* and not affecting dynein [77].

Furthermore, the protein family of end-binding proteins (EB proteins +TIPs) recognize growing plus-ends of microtubules and can modify MT-dynamics [68, 78] (see figure 2.6). EB induces hydrolysis of GTP and leads to a compaction of MT lattice in the cap [79]. This is consistent with other studies showing that the MT lattice is compacted when going from the GTP cap towards the GDP bulk of the MT [80–82].

Kinesin modifies the MT lattice

In the study by Shima *et al.* [34], it has been reported that even kinesins cooperatively can modify the MT lattice. By binding and migrating along MTs, a slight conformational change between the α - and β -tubulin monomers has been induced. As a result,

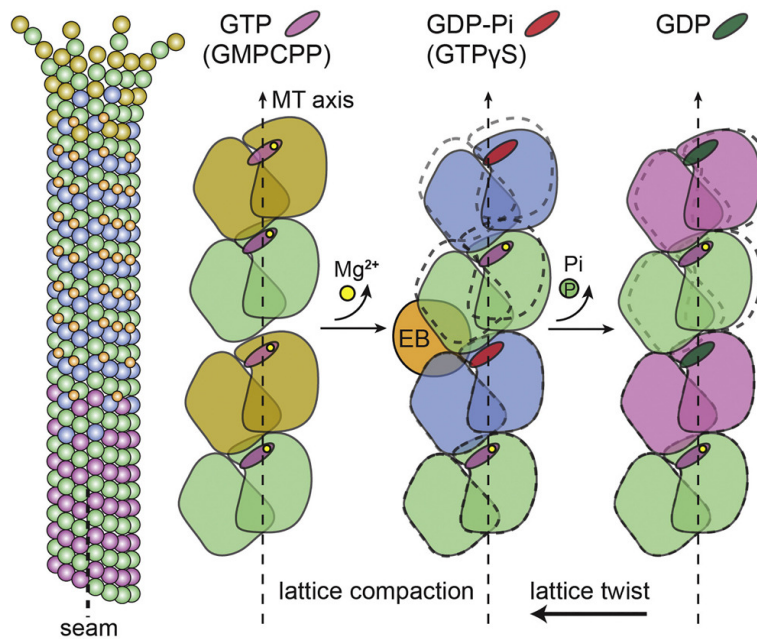


Figure 2.6: Lattice compaction of a microtubule in the process of transitioning between the GTP cap towards the GDP configuration of tubulin. Reprinted from Cell, 162, Zhang *et al.*, Mechanistic Origin of Microtubule Dynamic Instability and Its Modulation by EB Proteins Graphical, 849-859, Copyright (2015) with permission from Elsevier.

the MT lattice is elongating along the axial pitch by approximately 2 % [34, 83]. This lattice elongation was associated with changing the GDP structure towards the more stable GTP-like form, similar to the contrary lattice compaction seen in the presence of EB proteins (see figure 2.6).

It is remarkable that kinesin motors also have been found to show a higher binding affinity for MTs that have been elongated by former kinesin trajectories. In the experiment by Shima *et al.*, kinesins showed a higher binding rate but a constant run length, i.e. unbinding rate. The effect of higher binding has been decaying over time in the order of minutes. This is a rather slow process compared to the speed of kinesin stepping which is approximately 60 steps in a second [34].

The concentration of kinesins per tubulin dimers is relevant for the pitch elongation. A minimum value of approximately 10 % saturation has to be fulfilled to observe the cooperative conformational change in the MT lattice [34]. Kinesins have been found to distribute heterogeneously among the MTs in the *in vitro* experiment if the concentration of motors in the solution is not too high. The cooperative effect of kinesins is in accordance with cooperative accumulation in *in vitro* decoration ex-

periments of kinesins [84] and myosin motors [85]. Also in the experiment by Muto *et al.* [86], the binding of kinesins on a microtubule showed a long-range cooperative interaction. Binding of kinesin enhanced the binding of other kinesin motors in a region near the first kinesin that has a length of micrometers

These cooperative effects essentially provide a mechanism of a feedback loop between kinesin motors and the MT filament that could influence the transport by molecular motors. A similar effect for dynein motors has not yet been found to my knowledge.

2.3 Bidirectional transport by molecular motors

In addition to single motor proteins, cargoes such as organelles or vesicles are required to be transported. While walking on MTs, both motor types may also be bound to a cargo, such as vesicles or organelles [2,87,88]. The combination of a cargo and one or more molecular motors is called *motor-cargo complex* in the following (see figure 2.4). Active intracellular transport can be generated by motors pulling the connected cargo. Since there are the minus-directed and plus-directed molecular motors,

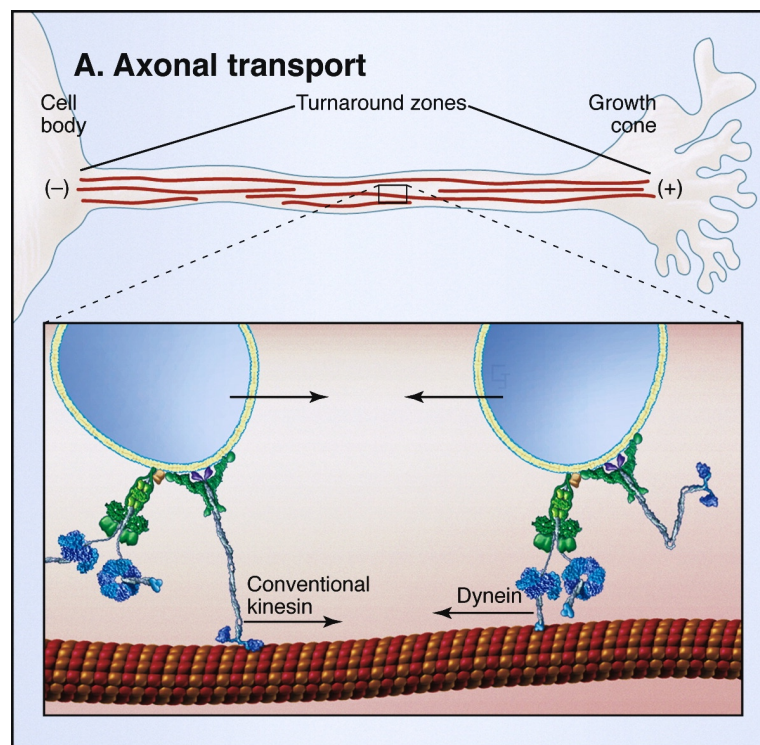


Figure 2.7: In intracellular transport, cargoes can be transported by molecular motors in both directions along the MT. Reprinted from Cell, 112 / 4, Ronald D. Vale, The Molecular Motor Toolbox for Intracellular Transport, 467-480 figure 2 a, Copyright (2003), with permission from Elsevier.

transport is possible in both directions of the MT (see figure 2.7). In other words, transport is *bidirectional*.

Various interactions between the motor proteins, the cargo, and the environment might influence the transport. Both kinesin and dynein share the same binding site on MTs [89,90], hence both motor types might even compete about the binding sites. If more than one motor is bound to a cargo and the filament, motor proteins are not independent but instead apply forces on each other which leads to many cooperative effects in cargo transport such as *Tug of War* [12]. In addition, the motor-cargo complexes can interact with each other via volume exclusion and may also be influenced by their environment. Thereby one has to distinguish between *in vitro* experiments where transport usually takes place in a solution [34] and *in vivo* transport that has to perform in the living environment of a cell. I will present the environment in further detail in section 2.4.

2.4 Intracellular transport in neurons

After introducing the components involved in intracellular transport along microtubules and the basic framework for active bidirectional transport, this section covers the neuron as an environment for intracellular transport. In figure 2.1, an image of the cytoskeleton of a neuron has been shown. Many extended protrusions are visible in this image. The main components of a neuron are the cell body (*soma*) which includes the nucleus, a long tube-like extension named *axon* and treelike structures called *dendrites*. Axons and dendrites connect different neurons with each other via synapses [20]. In figure 2.8, a scheme of a neuronal cell is drawn. I will discuss aspects of the outer neuronal morphology and structure as well as the MT network inside neurons in the following. These aspects will clarify key points that are crucial for intracellular transport inside neurons *in vivo*.

2.4.1 Axons

The axon is a very long, thin channel (up to 1 m in length, several μm diameter [20]) which grows from the soma to the neuron's environment. On the end of a growing axon (distal region), a so-called *growth cone* can be found. This area is developed by the dynamics of the actin and microtubule network [91]. The nerve cell can transmit signals to other neurons with the axon. In order to do so, the axon builds synaptic connections with dendrites from other cells. The axon is of special interest because of its enormous extension while at the same time having a small diameter. The question is how active, bidirectional transport in such a long and confined system can be efficient.

Active, MT based, intracellular transport which has been discussed so far, is now regarded in the environment of the axons. Inside the axon, microtubules are aligned in parallel, pointing with the plus-end towards the distal region of the axon [92]. MTs in this network has a length of approximately 10 μm [3,93] but can be found as long as 100 μm [94]. The distance between the parallel MTs has been measured as less

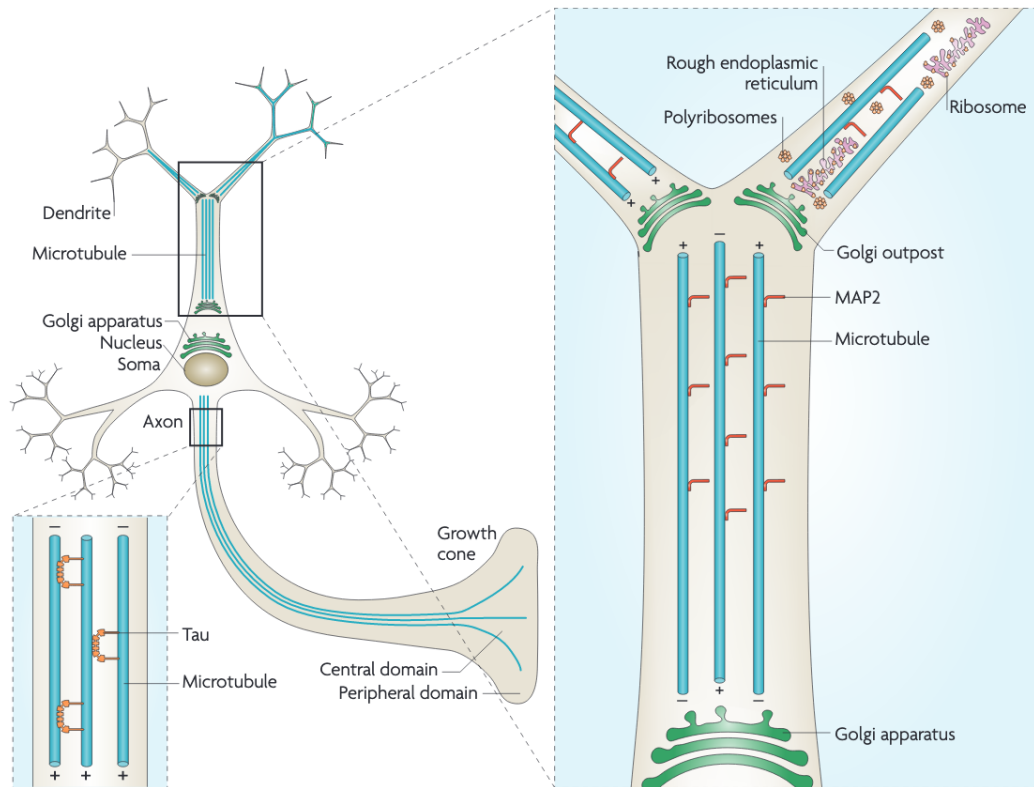


Figure 2.8: Scheme of a neuron including dendrites and the axon as well as the inner MT network. The nucleus is located inside the soma from which the axon grows out into a long, tube-like protrusion where the growth cone is located at the end. Inside, a parallel and identically polarized MT network is situated and stabilized by tau proteins. Moreover, many dendritic trees point out of the soma, which also includes an MT network, but not in an identically polarized orientation. Furthermore many components can be found inside neurons such as mitochondria, vesicles, Golgi apparatus or ribosomes. Reprinted from Nature Reviews Neuroscience, 10, Conde *et al.*, Microtubule assembly, organization and dynamics in axons and dendrites Cecilia, 319-332, Copyright (2009), with permission from Springer Nature.

than 50 nm [3,95] which means they are tightly packed considering their diameter of 25 nm (see figure 2.9). Tau proteins further regulate bundling of MTs and thereby form the MT network [96]. The inner part of the axon is, therefore, a crowded environment for intracellular transport.

2.4.2 Dendrites

In addition to the axon, the second type of protrusions from the soma is called dendrites (see figure 2.8). Dendrites form branched treelike structures and receive the neurotransmission that is generated by axons. Although dendrite morphology dif-

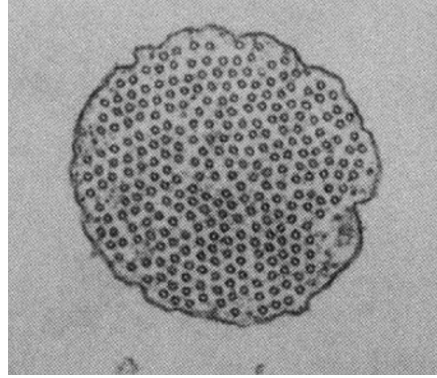


Figure 2.9: Cross-section of the MT network in an axon in electron micrographs. Reprinted from *Nature*, 360, R. J. Chen *et al.*, Projection domains of MAP2 and tau determine spacings between microtubules in dendrites and axons, 674-677, Copyright (1992), with permission from Springer Nature.

fers for different types of neurons and regions in the body [97], there are general features such as branching at acute angles [98, 99] and decreased diameter of branches far from the soma [100].

Complex protrusions called spines are distributed along the dendritic channels [101, 102] (see figures 2.10 and 2.11). Spines receive and compartmentalize excitatory synaptic input [102]. During different states of dendrite development and activity, spines may dynamically change their structure [103–105]. The shape and structure are often categorized in several schematic groups such as thin, stubby or mushroom-like [106]. However, the shape can show high diversity [107]. Also, the density of spines has been found to vary between different segments of the dendrite up to 40 % around the mean value [108, 109]. Mushroom-like spines play a role in retaining receptors in the spine and therefore localize them in the dendritic channel [16].

Similar to axons, the growing end of dendrite branches is called growth cone. Thereby, microtubules point from the tree structure into the growth cone area. In contrast to axons, MTs are not identically polarized in dendrites [42, 92, 110].

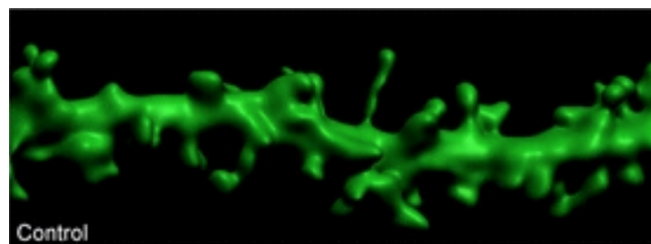


Figure 2.10: Example of a dendrite segment from a pyramidal neuron. Reprinted from *J Neuroinflammation* 12, 34 Chang *et al.*, Docosahexaenoic acid (DHA): a modulator of microglia activity and dendritic spine morphology, 1-15, Copyright (2015), under open access license.

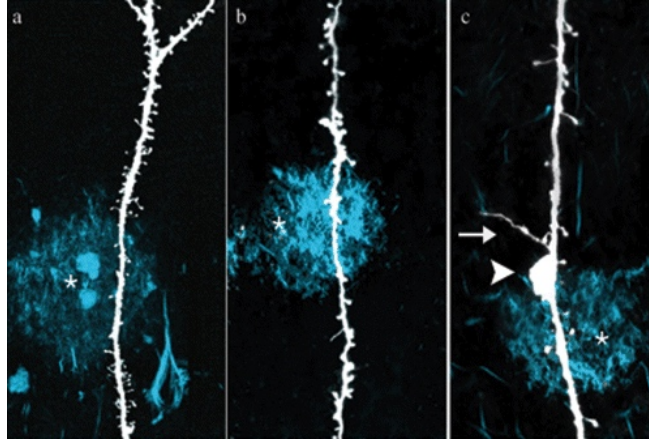


Figure 2.11: Abnormalities in geometry and spine density in dendritic branches near to fibrillar amyloid deposits in Alzheimer’s disease. **a)** and **b)** Decreased spine density in deposits, **c)** Varicosity and sprouting on a branch. Reprinted from *Annals of the New York Academy of Sciences*, 1097, Grutzendler *et al.*, Various Dendritic Abnormalities Are Associated with Fibrillar Amyloid Deposits in Alzheimer’s Disease, 674-677, Copyright (2007), with permission from John Wiley and Sons.

I discussed previously that intracellular transport is often carried out actively by molecular motors. However, small chemical signals such as ions also diffuse inside the cytoplasm. In neuronal dendrites, synaptic input of chemical signals diffuses through spines and eventually through dendritic channels. Thereby the spines can act as traps for the chemical signals [17]. The structural features of dendrites are crucial for describing passive intracellular transport of chemical signals in dendrites. In this thesis, I will study how the dendritic environment affects the diffusion of the signals inside the dendrites.

2.4.3 Organization of the MT network influences motor driven transport

If cargo transport is carried out by molecular motors walking on microtubules, transport is affected by the MT network structure. First, the small distance between neighboring MTs may act as obstacles. Whereas the distance between MTs is typically less than 50 nm [3,95], cargo size is often found in the same magnitude for vesicles [111] or even a magnitude above for example for mitochondria [20]. Second, in the small space, motor-cargo complexes carried along different filaments are likely to interact with each other. Third, it has been reported by Yogeve *et al.* that transport is interrupted at the end tips of MT until it continues along the next MT [3]. This organization of the MT network, therefore, influences intracellular transport in axons.

It is even more intriguing how bidirectional transport is organized among different microtubules as in the following example. The primary cilium is an antenna-like protrusion found for most vertebrate cells which include a network of uniformly polarized microtubule doublets [20]. In the study by Stepanek and Pigo [32] it has

been found that transport is carried out in lanes, i.e. anterograde and retrograde transport are distributed among the two MTs in the doublets.

A difference between the MT network structure of axons and dendrites is that MTs are equally polarized in axons but not in dendrites (see sections 2.4.1 and 2.4.2). In the study by Tas *et al.* [31], it has been shown that the MT network in dendrites is not randomly but organized in bundles of the same orientation. In addition, the entrance of motor proteins into the initial segment of dendrites [31, 112], and axons [113] can be highly regulated by for example by PTMs. Cargo transport that is carried out by a single type of motor is then also able to perform in both, retrograde and anterograde direction of the cell. Inside a bundle, however, plus-directed transport is unidirectional [31]. The organization in bundles could, therefore, be an advantage for the spatial cargo interactions because cargo-cargo interactions could be reduced compared to bidirectional transport in a bundle. For axons, however, using only motors of one direction in the transport cannot perform retrograde and anterograde since the MT network is unipolar.

2.4.4 Neurodegenerative diseases

After introducing important components and environments of intracellular transport, I give further motivation to investigate transport in neurons. Neurodegenerative diseases such as Alzheimer's disease, amyotrophic lateral sclerosis (ALS), Huntington's disease, and Parkinson's disease might occur in the context of disturbed intracellular transport [5]. In axonal pathologies, swellings with abnormal accumulations of proteins, vesicles and organelles can be linked to dysfunctional intracellular transport [5, 114, 115]. Also, the MT network structure has been found to be affected in diseases such as Alzheimer's disease where a reduction of MT density has been observed [116].

Structural changes can be beyond the internal components and also affect the outer morphology of neurons. In dendrites, the length, diameter, and curvature [7, 108, 117] as well as the number and extent of branches [7, 118] can be modified in progress of neurodegenerative diseases. Moreover, spine morphology is affected in density and shape [7, 8, 108, 117–120]. In Alzheimer's disease, typically an accumulation of amyloid plaques can be found [8] which can lead to irregularities in the dendrite morphology and spine distribution localized near the amyloid plaque [121] (see figure 2.11).

2.5 Migration of dendritic cells

After discussing components of intracellular transport with a focus on neurons, I introduce the migration of dendritic cells (DCs) as an additional example of transport in biological systems. DCs denote the comprehensive class of sub-types which differ in function and localization for instance [11]. The so-called *migratory* DCs will be the representative of dendritic cells in this work.

The ability to migrate is important for the protective pro-inflammatory as well as immune responses [41]. In tissues, DCs are able to recognize pathogens and antigens, and bring them to lymph nodes. In this process, DCs can activate T cells which then respond to the pathogens [20] in the tissue. Remarkably, DCs are heavily influenced by the environment they are migrating in. For example, migration relies on proteins such as CDC42 *in vivo* but not in an two-dimensional setting [122, 123].

DCs have shown complex modes of migration such as *amoeboid-like migration* resulting from contractions of the cell rear and *cell crawling* in which the cell pulls forward by adhesion on a substrate [11]. In crawling types, the cytoskeleton pushes against the membrane and forms protrusions, called *lamellipodia*, in the front of the cell. On these protrusions, the cell forms new adhesion points (focal adhesion) in order to make contact with the substrate (see figure 2.12). Stress fibers of actin connect different adhesion points [124]. The adhesion is released in the rear of the cell so that the cell body is pulled towards the front and the cell eventually migrates [125]. Both in the formation of lamellipodia and in the pulling process of the cell body, the actin cortex and MT network play a crucial role [124, 126]. It has been shown that lamellipodia can be formed by actin polymerization independently of microtubules, however, cell migration and tail retraction rely on microtubules [127].

An alternative mechanism for the cell to migrate in three dimensions is to push in several directions against its environment in order to generate friction rather than adhesion [11] (see figure 2.12). Thereby, the cell has to make directional choices in the complex three-dimensional environment of tissues. The ability to form directions is determined by the ability to polarize [11]. The polarization of the cell and thereby

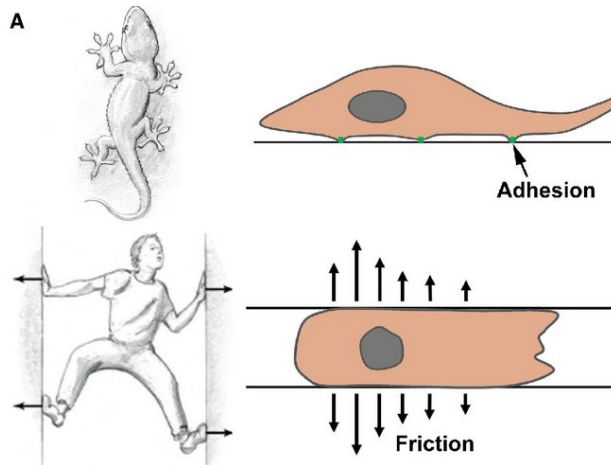


Figure 2.12: Schematic drawing about the different types of migration of dendritic cells. **Top:** Without confinement, DCs can form focal adhesion points. **Bottom:** In a confinement, DCs can migrate by using friction against the confining walls. Cropped and reprinted from *Immunological Reviews*, 1, Heuzé *et al.* Migration of dendritic cells: Physical principles, molecular mechanisms, and functional implications, 240-254, Copyright (2013) with permission from John Wiley and Sons.

directed motion has been observed to be strongly correlated to actin polymerization waves [22]. This might result in the positive coupling which has been observed between cell speed and persistence [23,24].

In order to search for antigens, DCs are expected to cover wide areas in the body. It is not clear how the search is efficiently organized, in particular, because many complex interactions with the environment influence the cell. In addition to the physical environment discussed above, it has been found that migration patterns [128], speed and persistence [11] are affected by chemokines. During search, when *sampling* the environment for antigens, DC migration exhibits periods of fast and slow motility [129–131]. DCs might not efficiently collect antigens during fast migration states [11,132] which opens questions on how the cell can organize an efficient search.

2.6 Chapter summary

In this chapter, the essential components of intracellular transport in neurons and cell migration have been presented. For this thesis, I differ between active transport and passive transport. Neurodegenerative diseases have been related to disordered intracellular transport and structural changes of its environment.

Passive transport is governed by diffusion, mostly of small chemical signals. The diffusion is performed in the environment of the cell. This environment can be very confining in axons and dendrites of neurons because of their long extend, small diameter and comb-like structures of spines. However, little is known about the exact influence of these structural characteristics on passive transport.

Active transport is carried out by molecular motor proteins along filaments. In this thesis, the focus is on microtubule-based motors, kinesins and dyneins. Together with other MAPs, they show complex interactions with the MTs which influences and might lead to organization and coordination of transport. Furthermore, motors are connected to cargoes such as vesicles and transport them along the MT. Transport can be unidirectional or bidirectional. In the confined environment of the axon, cargoes interact with other cargoes and the environment. The question is how active intracellular transport can be efficient.

Many of these components are also involved in the migration process of the whole cell. Actin filaments and microtubules form new protrusions in the membrane and stress fibers in the cell. Together with adhesion, the cell can pull forward which results in migration. During their complex migration patterns, dendritic cells have to search for antigens. It is not clear how complex migration influences the search for these antigens.

Chapter 3

Theoretical Background

Contents

3.1	Stochastic processes	36
3.1.1	Markov processes	36
3.1.2	Sampling methods for Markov processes	37
3.2	The random walker	38
3.2.1	The ordinary random walker	38
3.2.2	Mean square displacement	39
3.2.3	First-passage time	39
3.3	Non-Markovian processes	41
3.3.1	Examples of non-Markovian random walks	41
3.3.2	Sampling methods for non-Markovian processes	42
3.4	Renewal processes and residual waiting times	42
3.5	Chapter summary	44

In the previous chapter, important components of intracellular transport and cell migration have been introduced. The many components of the cell interact with each other and their environment, which can change the properties of the components. This makes the cell an example of a complex system. To effectively describe transport in such a system or transport of the system itself, where not all degrees of freedom are known, a stochastic modeling approach is often reasonable. The motion is seen as a combination of a regular movement and a noisy component. Statistical evaluation of stochastic models can then be used to describe the system [133]. In this way, general statements can be concluded from an ensemble of stochastic realizations.

In this chapter, theoretical methods are introduced that are important for modeling and evaluating results in this thesis. Stochastic processes and ways to deduce properties out of them are reviewed in section 3.1. The special example of the *random walker* as a stochastic process, and is presented in section 3.2. The stochastic processes are categorized in *Markovian* and *non-Markovian* processes. Non-Markovian versions of random walkers and their description in stochastic processes are discussed in section 3.3. In section 3.4, another class of stochastic processes is presented, the renewal process.

3.1 Stochastic processes

A detailed description of stochastic processes can be found in Van Kampen [134] and Gardiner [135]. A selection of important concepts such as Markov chains, master equations and computational methods for this thesis is summarized from these books and presented in this section.

A *stochastic process* is described by a random variable $\mathbf{X} = (X_1, X_2, \dots, X_r)$ that depends on time ($\mathbf{X}(t)$). Measuring possible values \mathbf{x} for \mathbf{X} at different times t_i generates a set of values for the random variable. A set of joint probability densities determines the stochastic process [135]. Important information such as averages and higher moments can be deduced from the probability density function (PDF) $P_{\mathbf{X}}(\mathbf{x})$ of \mathbf{X} .

3.1.1 Markov processes

One kind of stochastic process has proven to be very useful for physical models, the *Markov process*. It is defined by the *Markov property* which says the following: The conditional probability density function is exclusively determined by the current state, hence the memory of older states has no influence on the future dynamics. The age of the process, meaning the time since the last transition did occur, is therefore also not relevant for the transition probability between states. For a discrete sequence \mathbf{x}_n with $n \in \mathbb{N}$ and times $t_1 \leq t_2 \leq t_3 \leq \dots \leq t_n$, the Markov property is given by

$$P(\mathbf{x}_n, t_n | \mathbf{x}_{n-1}, t_{n-1}; \dots; \mathbf{x}_1, t_1) = P(\mathbf{x}_n, t_n | \mathbf{x}_{n-1}, t_{n-1}), \quad (3.1)$$

where $P(\mathbf{x}_n, t_n | \mathbf{x}_{n-1}, t_{n-1})$ is the conditional PDF for finding the system in state \mathbf{x}_n at time t_n given the system was in state \mathbf{x}_{n-1} at time t_{n-1} . A discrete Markov process is called *Markov chain*. In this chain, the time-evolution is determined by the conditional PDF at time t and the initial condition due to successively going through the chain. By neglecting the past and concentrating on the momentary state of the system, the description of the stochastic process is fully determined.

Now consider the probability of finding the system in one of the states \mathbf{x} at time t . The time-evolution of this probability can be calculated and described by the *master equation* which is given by [134]

$$\frac{\partial P(\mathbf{x}, t)}{\partial t} = \sum_{\mathbf{x}' \neq \mathbf{x}} [\omega(\mathbf{x}' \rightarrow \mathbf{x}, t)P(\mathbf{x}', t) - \omega(\mathbf{x} \rightarrow \mathbf{x}', t)P(\mathbf{x}, t)] \quad (3.2)$$

in continuous time and by

$$P(\mathbf{x}, t + \Delta t) - P(\mathbf{x}, t) = \sum_{\mathbf{x}' \neq \mathbf{x}} [\omega(\mathbf{x}' \rightarrow \mathbf{x}, \Delta t)P(\mathbf{x}', t) - \omega(\mathbf{x} \rightarrow \mathbf{x}', \Delta t)P(\mathbf{x}, t)] \quad (3.3)$$

for discrete time intervals Δt . The form of the master equation shows gain terms (from \mathbf{x}' to \mathbf{x}) and loss terms (from \mathbf{x} to \mathbf{x}') for the probabilities of finding the system in state \mathbf{x} [134]. The factors $\omega(\mathbf{x}' \rightarrow \mathbf{x})$ and $\omega(\mathbf{x} \rightarrow \mathbf{x}')$ are called transition rates between

states \mathbf{x}' and \mathbf{x} in case of continuous time and transition probabilities in discrete time. For finite time intervals Δt , there is a probability for transitions between two states, in first order given by

$$p(\mathbf{x} \rightarrow \mathbf{x}') = \omega(\mathbf{x} \rightarrow \mathbf{x}')\Delta t. \quad (3.4)$$

Alternatively in continuous time, the time between two transitions (waiting time until the next event happens) can be calculated directly. For age independent transition probabilities, waiting times are required to be exponentially distributed (*Poisson assumption*)

$$p(t_w) = \omega \exp(-\omega t_w). \quad (3.5)$$

The stationary state of the system is often used to describe the properties of the stochastic process. The left-hand side of eq. 3.3 can be set to zero which simplifies the equation.

3.1.2 Sampling methods for Markov processes

By calculating solutions of the master equation, the time-evolution of a stochastic process is fully determined. However, often the master equation is analytically not solvable. Besides the rare cases where it is possible, numerical methods to solve the equations, approximations as well as numerical simulations help to describe the stochastic process.

In order to generate realizations of a stochastic process by sampling the underlying probability densities, one needs to draw random numbers from given distributions. A standard method to do so is *inverse sampling* [136,137] that transforms independent identically distributed (*i.i.d.*) random numbers in random numbers drawn from the demanded distribution. Correlated *i.i.d.* random numbers can be drawn by the *sum-of-uniforms* method [138,139].

Sampling the stochastic process means that several realizations from initial conditions give an ensemble of paths in the system's phase space. This ensemble approximates the PDF of the stochastic process. Sampling methods have to fulfill rules in order to generate physically meaningful realizations.

The first method I briefly present is *Gillespie's algorithm* [136] which generates realizations of the stochastic process in continuous time. The algorithm calculates waiting times for all possible events by using the transition rates ω_n and *inverse sampling* [136,137]. For constant rates ω , waiting times are drawn from

$$\Delta t = -\frac{\ln(u)}{\omega}, \quad (3.6)$$

where u is a uniform random number.

Two different versions of Gillespie's algorithm have been introduced which are called *direct method* and *first-reaction method* [136]. In the direct method, a transition is chosen, based on the statistical weight of its transition rate among all possible transitions. In the second step, the matching waiting time is calculated by inverse transform sampling. In the first reaction method, waiting times for all reactions are calculated and the event with the smallest waiting time is chosen to be the next transition.

The other waiting times will be forgotten, and after the transition, the procedure is repeated. However, many waiting times will be calculated and deleted for a large state space in every event step which decreases the efficiency of the algorithm.

An alternative to the first reaction algorithm is the *next reaction method* [140]. Here, switching from relative time intervals to absolute times for events and storage of these times allows reusing reaction times for other events than the first reaction. The drawback is that a list of all waiting times and reactions has to be organized and updated. Gibson *et al.* [140] showed that the reuse of random numbers is valid in their algorithm and thus found an equivalent method to the Gillespie versions for Markov processes.

Often it is not necessary to use the exact update structure of Gillespie's algorithm. Going to discrete time steps again allows building algorithms that are based on accepting and rejecting events. In the *random-sequential update*, the next reaction is chosen based on its statistical weight (*tower sampling*) similar to the direct method by Gillespie. Afterward, a decision is made if the chosen event is executed or not within the time interval Δt by evaluating the probability for the transition in the given time interval. In case the stochastic process has an internal running order, other rejection based updates might better suit such as the *sequential* or *parallel update* [141].

3.2 The random walker

A famous example of a stochastic process in statistical physics is the *random walker*. It is traditionally a way to model Brownian motion [142] and, hence, diffusion. This model class is the basic concept for the models developed in the projects about passive intracellular transport and cell migration in this thesis.

3.2.1 The ordinary random walker

A well-studied example of stochastic processes is the *ordinary random walker*. Essentially, a random walker (RW) is a sum of random variables. Each of these variables corresponds to a displacement X so that the sum denotes the total displacement of the random walker.

Similar to the section before, a random walker can be described in discrete or continuous time, as well as in continuous space or discrete space, i.e. steps on a d -dimensional lattice [143]. I will focus on the discrete case in this thesis. In the simplest case of a one-dimensional lattice of step length 1, the random walker moves one step to the right or to the left at each time step with probabilities p and $q = 1 - p$, respectively [143]. This characteristic identifies the ordinary random walker as a Markov chain because the probabilities stay constant over time so that the next state (position) of the RW is only depending on the current state and not on the past. The total displacement after n steps is then given by $X_n = X_0 + \sum_{t=0}^n Z_t$ with $Z_t = \pm 1$, the initial condition $X(t = 0) = X_0$ and mean value $(2p - 1)t$. This shows that the random walker has a drift for asymmetric probabilities $p \neq 1/2$ and the total displacement will diverge in the limit of large times. However, the RW is recurrent in

the symmetric case which means that the number of visits diverges for an infinite time. Note that the recurrence time still is expected to be infinite [143].

The time-evolution of the discrete random walker is described by a master equation (see equation 3.3):

$$P(X_{n+1} = x, n + 1) = pP(X_n = x - 1, n) + qP(X_n = x + 1, n) \quad (3.7)$$

with initial condition $P(x) = \delta_{x,0}$. By the *central limit theorem*, the RW's master equation is solved by a Gaussian distribution in continuous time and space

$$P(x, n) = \frac{1}{\sqrt{2\pi\sigma^2}} e^{-(x-\mu)^2/(2\sigma^2)} \quad (3.8)$$

with mean value $\mu = (2p - 1)n$ and variance $\sigma^2 = 4np(1 - p)$. The solution of the master equation is also called occupation probability since the RW occupies a position or state at time t .

3.2.2 Mean square displacement

A common statistical measure to describe the dynamics of random walks is the mean square displacement $\langle x^2 \rangle$ (MSD). It measures the average quadratic displacement over time and is related to the time by a power law $\langle x^2 \rangle \propto t^\alpha$ [144]. The MSD is especially useful to express the diffusivity of a random walker. For Brownian particles the exponent α is equal to one [145], for $0 < \alpha < 1$ the random walk is *sub diffusive* and for $1 < \alpha < 2$ *super diffusive*, where $\alpha = 2$ is considered to refer to ballistic motion [143, 144, 146, 147].

From the central limit theorem, it is expected that the long term behavior asymptotic of the MSD is diffusive for ordinary random walks [9]. However, several modifications to the RW also lead to super and subdiffusive behavior for transient time regimes as well as asymptotic times [148–150]. At the so-called percolation threshold, no crossover between anomalous diffusion and diffusion is observed anymore [151].

Examples for modifications are intermittent and run-and-tumble walks [150, 152–154] or *Lévy flights* and *Lévy walks* [144, 146, 147, 150, 155] where diverging second moments of the displacement can lead to not following the central limit theorem anymore. Also, interactions with the environment of the walker can result in anomalous diffusion [9, 14, 17, 147, 156].

3.2.3 First-passage time

Besides the MSD, a second tool to measure a random walker's motion is the time at that the random walker visits a particular site of the lattice space for the first time (first-passage time). The first-passage time is, therefore, a meaningful tool to describe search processes, i.e. it gives the time a searcher finds the target for the first time. The calculation of first-passage times from the master equation is briefly summarized from [157] in the following.

From solving the master equation, the occupation probability $P(x, t)$ of the walker is found on site x at time t is related to the probability $F(x, t)$ of passing x for the first time at time t . The occupation probability is expected to decay slower over time since the random walker can contribute to the occupation several times, whereas the first-passage probability is only depending on the first visit.

Let's consider a one-dimensional random walker that initially starts at site $x = 0$ at time $t = 0$. The probability of visiting site x at time t is related to the process of passing x at time $t' \leq t$ for the first time and then coming back at time $t - t'$ by the convolution theorem [134, 157]

$$P(x, t) = \delta_{x,0}\delta_{t,0} + \sum_{t' \leq t} F(x, t')P(0, t - t'). \quad (3.9)$$

If x is an absorbing state such that there is zero probability to leave the state x again after visiting it, this equation simplifies, i.e.

$$P(x, t) = \delta_{x,0}\delta_{t,0} + \sum_{t' \leq t} F(x, t'). \quad (3.10)$$

Generating functions are introduced [157] in order to solve calculate the first-passage time

$$P(x, z) = \sum_{t=0}^{\infty} P(x, t)z^t, \quad F(x, z) = \sum_{t=0}^{\infty} F(x, t)z^t. \quad (3.11)$$

For a symmetrical one-dimensional random walker with initial condition $\delta_{x,0}\delta_{t,0}$, a reflecting boundary at site 0 and an absorbing state $x > 0$, the following system of master equations is given

$$\begin{aligned} P(0, t + 1) &= \frac{1}{2}P(1, t) + \delta_{x,0}\delta_{t,0} \\ P(1, t + 1) &= P(0, t) + \frac{1}{2}P(2, t) \\ &\vdots \\ P(x - 2, t + 1) &= \frac{1}{2}P(x - 3, t) + \frac{1}{2}P(x - 1, t) \\ P(x - 1, t + 1) &= \frac{1}{2}P(x - 2, t) \\ P(x, t + 1) &= P(x, t) + \frac{1}{2}P(x - 1, t). \end{aligned} \quad (3.12)$$

An alternative relation between P and F is found to be $P(x, t) = P(x, t - 1) + F(x, t)$. Making use of the generating function leads to the equations

$$\begin{aligned} P(0, z) &= \frac{z}{2}P(1, z) + 1 \\ P(1, z) &= zP(0) + \frac{z}{2}P(2, z) \\ &\vdots \\ P(x - 2, z) &= \frac{z}{2}P(x - 3, z) + \frac{z}{2}P(x - 1, z) \\ P(x - 1, z) &= \frac{z}{2}P(x - 2, z) \\ P(x, z) &= \frac{z}{2}P(x - 1, z)/(1 - z) \end{aligned} \quad (3.13)$$

and a simple equation for the first-passage probability $F(z) = \frac{z}{2}P(x-1, z)$. This form has the advantage that the time difference has vanished and equation 3.13 is therefore algebraically solvable. The drawback is that the solution has to be transformed back to real time t afterwards.

In many cases it is difficult to find the full solution for all occupation probabilities. However, often it is sufficient to calculate the mean first-passage time (MFPT). It can be deduced from $F(z)$ as follows [157]

$$\begin{aligned}\langle t \rangle &= \sum_{t=1}^{\infty} tF(t) \\ &= \sum_{t=1}^{\infty} tF(t)z^t \Big|_{z \rightarrow 1} \\ &= z \frac{d}{dz} F(z) \Big|_{z \rightarrow 1}.\end{aligned}\tag{3.14}$$

3.3 Non-Markovian processes

Markovian processes such as ordinary random walks assume that the past has no influence on the future of the process. The Markov property in equation 3.1 has to be fulfilled. In section 3.1.1, it has been concluded, that for the Markov process in continuous time, waiting times between events have to be exponentially distributed (Poissonian assumption). That means that as soon as the distribution of waiting times is not exponential anymore, the stochastic process is not Markovian. In this thesis, stochastic processes with algebraically distributed waiting times are considered. Therefore, a non-Markovian description of them is required.

For physical processes, interacting with their environment, is not always reasonable to assume that the Markov property applies [14]. Examples for non-Markovian processes and how to sample realizations for non-Markovian processes are discussed in the following.

3.3.1 Examples of non-Markovian random walks

So far, the ordinary random walker has been discussed as an example for Markov processes. There are, however, many modifications to random walkers that increase the complexity but also adapt the basic model to various situations such as intermittent walkers, two-state run-and-tumble motion [150, 152–154] or Lévy walks [144, 146, 147, 150, 155].

Despite the increased complexity, most of the examples fulfill the Markov property. The stochastic process can be even more complicated if the past has an influence on the future dynamics of such a random walker, making it a non-Markovian random walker with memory.

An example of a RW is given in [158], where the next step depends on a former step which is chosen randomly from any time in the past of the walk. Depending on a memory parameter, the diffusivity of the walker varies from localized towards superdiffusive regimes.

If the influence of the memory is weaker, Markovian and non-Markovian formulations of random walks may even lead to the same results for occupation probabilities [159]. Also, short term memory can sometimes still be modeled in a Markovian model such as for persistent random walks where the next step depends on the additional variable of the direction between the last two steps instead of the explicit positions of the present and past [160].

In contrast, there are non-Markovian random walker models that cannot easily be transferred into Markovian versions. An example is a walker that, in between stepping periods, falls in traps that it escapes with a non-exponential waiting time distribution [144,147,150].

An important observation for this thesis is that interactions with the environment can lead to an effective non-Markovian behavior of a random walk [14]. For example, diffusion which is strongly confined in spines has been modeled as a non-Markovian random walker [15].

3.3.2 Sampling methods for non-Markovian processes

Heavy tailed power-law distributions for waiting times are not compatible with the Markov assumption because the age of the stochastic process influences the probability of performing an event in a given time interval. Thus, the update mechanism discussed in section 3.1.2 has to be adjusted in order to perform physically meaningful realizations of the stochastic process.

One option is to use time-dependent rates instead of constant rates as used in the former method by Gillespie [136,161] (see section 3.1.2). A second option is an adaptation of the first reaction method by Gillespie, named *next reaction method* [140]. This method already has been introduced in chapter 3.1.2 for waiting times drawn from an exponential distribution. For those, it is equivalent to the first reaction method by Gillespie, but the algorithm is also a valid choice for algebraically (power-law) distributed waiting times.

The algorithm chooses an absolute event time for each reaction at the beginning of the simulation. Initially, the first event is executed and gets a new time from the waiting time distribution like in Gillespie's first reaction method. However, this time, all event non-executed times are stored in a list together. In each update, the next reaction, i.e. the reaction with the smallest event time, is executed and a new time drawn from the distribution and added to the current time. The reaction is then sorted into the list again referring to its absolute event time. In this way, the age is kept for each process. Gibson *et al.* showed that this method is equivalent to the first reaction method for Markov processes and that it is valid to reuse event times for their algorithm [140].

3.4 Renewal processes and residual waiting times

In this thesis, another class of stochastic processes is applied. Renewal processes are stochastic processes also referred to as arrival processes. There is an arrival event at

times S_n for a chain of renewed processes, i.e. $S_n = \sum_{i=1}^n X_i$ where X_i denotes the i th interarrival time (or duration) drawn from a waiting time distribution. The following discussion of renewal processes and residual waiting times is briefly summarized from [162].

One can easily construct a renewal process from a one-dimensional random walker. Every time the walker visits the site j , a new arrival event takes place. The interarrival time X_i can be counted by measuring the time between two visits i and $i - 1$ of that site j .

Often it is interesting to count the number of arrivals $N(t)$ which are observed since the beginning of the process. The *strong law for renewal processes* states that for a renewal process which has a mean value \bar{X} for interarrival times, the number of arrivals follow

$$\lim_{t \rightarrow \infty} N(t)/t = 1/\bar{X}. \quad (3.15)$$

This limit is meaningful for calculating the interesting measure below.

For a renewal process which has seen $N(t)$ arrivals at time $t \geq S_{N(t)} > 0$, the *residual life*, also called *residual waiting time*, $Y(t)$ defines the time that it takes until the next arrival $S_{N(t)+1} - t$. The *age* $Z(t)$ of the process refers to the time between the last arrival and time t , i.e. $t - S_{N(t)}$. The meaning of an arrival process becomes clear when regarding a random walker. Since visiting site j for the last time, the time called age $Z(t)$ has passed and it will take the residual time $Y(t)$ until the random walker visits site j again.

The distribution of the residual life is calculated in the following. In order to estimate the cumulative distribution function (CDF) of $Y(t)$, an indicator reward function $R(t)$ is expressed in terms of the interarrival time current \tilde{X} and the age $Z(t)$. The reward function estimates the fraction of time for that it holds $Y(t) \leq y$, i.e.

$$R(t) = \begin{cases} 1 & \text{for } Y(t) \leq y \\ 0 & \text{otherwise} \end{cases} = \begin{cases} 1 & \text{for } \tilde{X}(t) - Z(t) \leq y \\ 0 & \text{otherwise.} \end{cases} \quad (3.16)$$

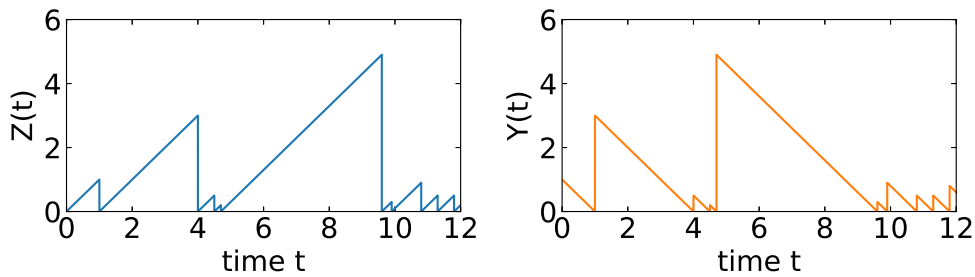


Figure 3.1: **Left:** The age for a renewal process. $Z(t)$ is growing until an arrival event $t = S_n$ and starts to grow from zero again. **Right:** The residual life $Y(t)$ is analog to the age of the renewal process but shrinks down to zero until a new arrival event occurs.

From the strong law of renewal processes, the time average of the indicator function $R(t)$ gives an estimate for the CDF for $Y(t)$ [157]

$$F_Y(y) = \lim_{t \rightarrow \infty} \frac{1}{t} \int_0^t R(\tau) d\tau = \frac{1}{\bar{X}} \int_{x=0}^{x=y} \Pr\{X > x\} dx. \quad (3.17)$$

Remarkable the distribution of the residual life is identical for an exponential distribution $Y = \lambda e^{-\lambda t}$ with $t \leq 0$. The CDF for the residual life is given by

$$\begin{aligned} F_Y(y) &= \lambda \int_0^y (1 - (1 - e^{-\lambda x})) dx \\ &= 1 - e^{-\lambda y} \end{aligned} \quad (3.18)$$

which is also the CDF of the exponential distribution itself.

However, in non-Markovian cases of a waiting time distributions function for interarrival times not following an exponential distribution, this identity does not necessarily hold. For example, power-law decays can have a residual waiting time distribution with a shifted exponent compare to the original waiting time distribution as it is shown below for the PDF

$$f_X(t) = \begin{cases} 0 & 0 < t < 1, \\ (\gamma - 1)t^{-\gamma} & t > 1. \end{cases} \quad (3.19)$$

The residual life or waiting time distribution is in this case given by

$$\begin{aligned} \frac{d}{dy} F_Y(y) &= \frac{1}{\bar{X}} \int_0^y (1 - (1 - x^{1-\gamma})\Theta(x - 1)) dx \\ &= \frac{d}{dy} \begin{cases} \frac{\gamma-2}{\gamma-1} y & y < 1 \\ \frac{\gamma-2}{\gamma-1} \left(\frac{\gamma-1}{\gamma-2} + \frac{1}{2-\gamma} y^{2-\gamma} \right) & y \geq 1. \end{cases} \\ &= \begin{cases} \frac{\gamma-2}{\gamma-1} & y < 1 \\ \frac{\gamma-2}{\gamma-1} y^{1-\gamma} & y \geq 1. \end{cases} \end{aligned} \quad (3.20)$$

3.5 Chapter summary

In this chapter, I presented stochastic processes which are the basic concept for all models in this thesis. Analytical techniques to describe the time evolution and stationary state of a system have been introduced as well as sampling techniques. Stochastic processes have been split into Markovian processes and non-Markovian processes. The Markov-property says that the future of a system is completely determined by the current state of the system. The special stochastic process discussed in this chapter is the random walker. It is widely used to model diffusive processes and stochastic motions. The RW is, hence, a useful model for describing stochastic transport processes in cell biology.

Chapter 4

Random walk models for passive transport and cell migration

Contents

4.1	Diffusion in neuronal dendrites	46
4.1.1	Diffusion in branched channels	46
4.1.2	Diffusion in spiny dendrites	47
4.2	Discrete treelike networks	49
4.3	Mapping a random walk on treelike networks to a one-dimensional random walk	51
4.4	Reconstructing network structure by transport properties	51
4.5	Persistent random walks in cell migration	52
4.6	Chapter summary	54

In the previous chapter, stochastic processes and random walk models have been presented. These techniques build the theoretical framework for the literature reviewed in this chapter. The literature and the theoretical framework of random walks provide the concepts required for my own work in projects one and two which is presented in chapter 6.

Passive intracellular transport and cell migration might seem very different from a biological point of view. On the one hand, diffusion of chemical signals happens on the molecular scale and is determined by the environment of the signal. On the other hand, the active migration of cells involves complex inner processes and energy. However, both situations can be well described by the same theoretical framework. Both transport processes are assumed to be only dependent on the environment but not on other transported signals or cells, respectively. The migration patterns of active cells can be incorporated in the random walk approach, in the same way as the environmental influences for the diffusion of chemical signals as I will present in this chapter.

For the first project of passive, intracellular transport in neuronal dendrites, I show how diffusion confined in channels has been investigated in three dimensions in section 4.1.1. Furthermore, studies of chemical signals trapping in spines and escaping from them is presented in section 4.1.2. The geometrical properties of the environment in which the diffusion takes place can be related to an effective probability move

in a given direction or being trapped in spines. This effective description enables a coarse-grained point of view, in which the three-dimensional dendritic structure is not explicitly modeled anymore. In order to prepare the reader to a coarse-grained RW model in dendrites, I present studies on RW performed on discrete, treelike networks in section 4.2. If trees are regular, transport on them can be modeled as a one-dimensional RW. This enables the analytical description shown in section 4.3. As a result, transport characteristics can be mapped by the environmental structure. Finally, the knowledge of how transport properties of random walkers are affected by an underlying treelike structure, the opposite point of view is taken in section 4.4: how to extract structural information of the network from measuring transport properties such as first-passage times.

For the second project of modeling cell search processes in migration, relevant internal processes are analyzed and incorporated in a RW approach similar to the environmental influences above in section 4.5. I will concentrate on the persistence observed in the migration resulting from the polarized state of the cell. In a second step, studies on search strategies for random walkers are discussed.

4.1 Diffusion in neuronal dendrites

Diffusion is heavily influenced by the environment in which it takes place such as environmental topology or geometrical properties [163]. For diffusive transport of chemical signals in dendrites, the key aspects are confinement by branched and narrowing channels as well as confinement by spines that act as traps along the tree [15, 16, 19, 36, 164, 165] (see section 2.4). Both aspects are addressed in the following.

4.1.1 Diffusion in branched channels

Diffusion in branched, treelike channels can be modeled by random walkers in continuous three-dimensional space that is confined by the channel. The RWs are confined by the explicit geometry of the neuronal dendrite. The focus is on a single dendritic branch that starts at the soma and extends up to the dead-ends. In such a branching treelike structure the shape of the branching points can have complicated influences in principle, especially if the tree is highly inhomogeneous. A model for a full neuronal dendrite with the structure explicitly taken into account is, however, computationally very expensive and furthermore specialized to one realization of a dendrite.

I start with diffusion confined in a channel for which the diameter shrinks when approaching from one end to the other. This is in particular interesting because neuronal dendrites have a wider diameter close to the soma than close to the growth cones for example (see section 2.4). Narrowing of the tube induces a bias to the random walker towards the wider side of the tube [166]. If the tube is regular, the bias has been related to the narrowing angle and it is, therefore, possible to use the results of the three-dimensional description to calculate an effective drift that depends on

the narrowing of a tube [166]. If one is only interested in the displacement along the tube axis, the process can be described by a one-dimensional random walker with an effective bias that comes from the narrowing. Simulations are computationally more efficient in such a coarse-grained approach.

4.1.2 Diffusion in spiny dendrites

Many studies deal with the diffusion of chemical signals in spines. The comb-like structure of spines influences the overall transport in the dendrite and can lead to localization of chemical signals in a part of the dendrite [17]. The search process of a Brownian particle from spines been investigated by calculating the mean first passage time [18] in the context of narrow escape problems.

In the study of Santamaria *et al.* [17], the authors find that spines may trap chemical signals and slow down diffusion in dendrites. In the experiment, diffusion of fluorescein dextran is tracked in dendrites of Purkinje cells that have segments of high and low spine densities. The diffusion significantly differs for the two segments.

In the same publication, simulations of diffusion in a tube without spines have been compared to analytical predictions of the geometry. The two results match but cannot explain the slow anomalous diffusion found experimentally in spiny segments. The results change when introducing compartment structures to the model dendrite (see

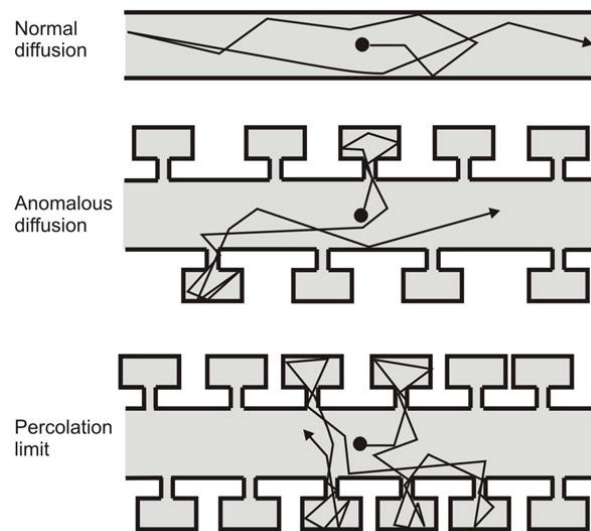


Figure 4.1: The different densities of spines along a channel affect the diffusive behavior of random walkers. **Top:** Normal diffusion in the tube without trapping in spines. **Center:** Trapping in spines causes anomalous diffusion. **Bottom:** High spine density can lead to effective localization in the percolation limit. Cropped and reprinted from *Neuron*, 52, F. Santamaria *et al.*, Anomalous Diffusion in Purkinje Cell Dendrites Caused by Spines, 635-648, Copyright (2006), with permission from Elsevier.

figure 4.1). These structures are modeling spines in the biologically relevant parameter range [17]. Depending on the spine density, the MSD shows a non-linear behavior and different asymptotic slopes which are consistent with experiments [17].

The reason for anomalous diffusion found in the experiments by Santamaria *et al.* [17] is given by the following argument. Molecules that leave spines have a high probability to enter an other spine which is near to the exit location. The displacement inside the dendrite is thereby reduced so that molecules almost remain located. The localization is called *percolation limit* [151] (see section 3.2 and figure 4.1).

Anomalous diffusion and non-Markovian descriptions have been used to model the environmental influence on diffusion [14]. Anomalous diffusion in spiny, dendritic channels has further been investigated in the theoretical study by Mendez *et al.* [165]. Here, diffusion has been related to the fractal geometry of spines as well as the fractional kinetics of chemical signals inside spines. With the approach, the authors related the MSD to the density of spines in accordance with the results of Santamaria *et al.* [17, 165]. In Fedotov *et al.* [15], anomalous diffusion has been modeled by power law escape time PDFs. This non-Markovian description (see section 3.3) also led to subdiffusion in the dendrite and signal accumulation inside spines.

The trapping inside spines may be advantageous when providing high concentrations of signals close to synapses. In Kusters *et al.* [16], mushroom-like spines are considered to be effective at retaining receptors inside the head of the spine. In this work, diffusion was simulated on a curved surface to model spine morphology.

The probability of a RW to be trapping in dendritic spine structures can be quantified by incorporating the biological morphology and structural parameters. For example, Santamaria *et al.* did investigate the influence of the shape of spines, such as the neck diameter, head diameter, spine length, and bottleneck structures. By using the neck length L_{neck} , the volume of the spine head V_{head} and neck V_{neck} as well as the radius of the neck R_{neck} , the mean escape time from spines has been estimated to be [167]

$$\langle t \rangle_{\text{spine}} = \frac{L_{\text{neck}}^2}{2D} + \frac{L_{\text{neck}}^2 V_{\text{head}}}{D V_{\text{neck}}} + \frac{V_{\text{head}}}{4 D R_{\text{neck}}}. \quad (4.1)$$

Also the probability q for a particle being trapped in spines in the stationary state can be estimated by comparing volumes of the dendritic tube and the spines in the long time limit [168]

$$q \simeq \frac{V_{\text{tube}}}{V_{\text{tube}} + V_{\text{spines}}} = \frac{1}{1 + \frac{\rho}{\pi R_{\text{tube}}^2} (V_{\text{head}} + V_{\text{neck}})}. \quad (4.2)$$

As a final remark, I discuss how these results can be used in a coarse-grained and effective description of diffusion in the complex environment of neuronal dendrites. In section 4.1.1, diffusion in a channel is influenced by the channel geometry. The thickening tube induces an effective bias to the diffusive particles. In a

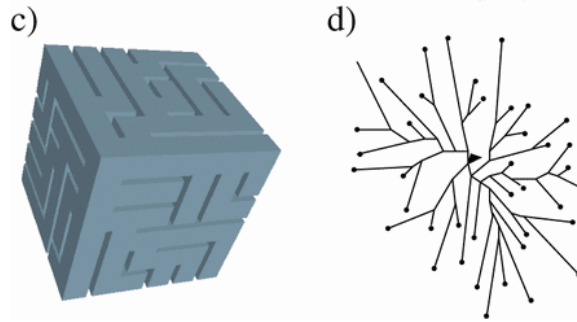


Figure 4.2: Mapping diffusive random walks on an explicit three-dimensional structure to renormalized random walks on the corresponding discrete topological graph. Cropped and reprinted from *Physical Review Letters*, 92, M. Felici *et al.*, Renormalized Random Walk Study of Oxygen Absorption in the Human Lung, 1-4, Copyright (2004), with permission from American Physical Society.

one-dimensional RW model, this effective bias can be given to the RW so that the net movement along the channel axis equals the three-dimensional diffusion model in the channel. Similarly, the trapping in spines can be coarse-grained. Instead of explicitly modeling the three-dimensional diffusion between the channel and the spines, the estimate in equation 4.2 in the stationary state well describes the ratio of a RW being located in a spine or in the channel. By carefully including the structural parameters of the three-dimensional geometry, the effective bias and trapping probability is still maintained in a coarse-grained RW model. Three-dimensional modeling of detailed spine structures along extended channels is numerically expensive on the large scale of a neuron. It is, therefore, an interesting alternative to model the coarse-grained scenario.

4.2 Discrete treelike networks

The numerically expensive three-dimensional simulations make it difficult to explicitly model diffusion in a full dendrite. In this section, different approaches for modeling diffusion will be discussed.

Theoretical modeling of diffusion on treelike structures is widely applied to systems such as random walks dendrimer molecules [169–172]. In order to build a coarse-grained model for neuronal dendrites, I first give an example for a coarse-grained model of oxygen diffusion in the branched structure of the lung [173, 174]. Subsequently, the theoretical framework for diffusion of a discrete network is given.

The mapping between three-dimensional diffusion on a tree structure and random walks on a discrete symmetric tree has been investigated in the context of oxygen transport in the lung [173, 174]. This coarse-grained model can be used for efficient numerical calculations of large trees. The complete structure of the oxygen exchange unit in the lung is a large environment for explicitly modeling three-dimensional transport. Felici *et al.* [173] did map diffusion in a three-dimensional branching struc-

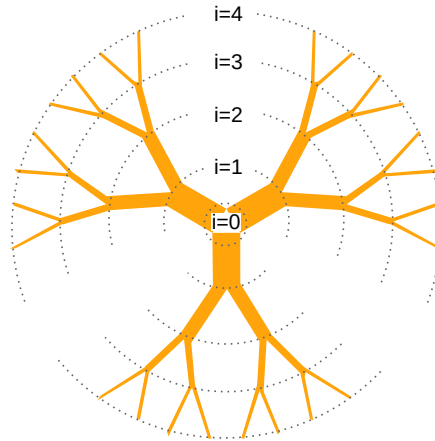


Figure 4.3: Scheme of a Cayley tree with a root ($i=0$), a coordination number $k = 3$ and 4 generations indicated by the dotted lines.

ture that is known and still small enough to handle towards the diffusive motion of random walks on the respective topological discrete treelike structure (see figure 4.2). This is possible because random walks in free space are scale-invariant, i.e. diffusion can be renormalized towards the size of the tube diameter or the branching points [173]. How the geometrical properties are translated into the parameters of the discrete treelike structure is, however, not trivial and can be achieved by detailed investigations such as it has been presented in section 4.1 for an effective bias and trapping probability.

For modeling a nerve cell that has several dendritic trees such as the lower branch in figure 4.3 a branched network without loops is needed. The focus is on such a single branched tree resembling a dendrite. The root of the tree is representing the soma of the nerve cell.

The mathematical description of the treelike network used in this thesis is the finite *Cayley tree* or the infinite *Bethe lattice*. A Cayley tree is a regular network without loops [157]. A node that is connected by k edges to neighboring nodes the node has a *coordination number* k (see figure 4.3). In order to build a Cayley tree, one can start at the root node and connect a new set of nodes to the root. This first set of nodes is called the first *generation*. By successively adding $k - 1$ nodes to each node of the last generation, a new generation is built. The nodes of the last generation are called *leaves*, and the number of generations gives the *extent* or *depth* of the treelike structure. For Cayley trees, the network has a finite extend. Cayley trees have been widely used, such as in the context of Ising models [175], quantum random walks [176], random walks in the branched molecule structures of dendrimers [169–172] and paramagnetic colloidal particle motion [177]. The infinite version of the tree-network is called Bethe lattice [178]. Random walks on these infinite lattices have been extensively studied, too [179–181].

4.3 Mapping a random walk on treelike networks to a one-dimensional random walk

Stochastic transport on a regular treelike structure can be analytically handled by mapping the tree to a one-dimensional stochastic process. Note that for the following method, the branched structure has to be regular. Inhomogeneities have to be described by more complex networks [182]. In this way, probabilities for finding a particle in a particular generation can be calculated. By first-passage times, the one-dimensional RW can be a search, or escape, problem. The required techniques to find first-passage times for a random walker on a one-dimensional lattice have been discussed in section 3.2.

The central question for mapping the tree to a one-dimensional lattice is how the transition rates of a random walker stepping between nodes is translated into stepping between generations. For a non-biased random walker on a tree with coordination number k deciding on which neighboring node to jump, the probability p is just $\frac{1}{k}$ for every neighboring node. That means that the random walker has a chance to go to a lower generation (towards the root) with probability $1 - p = \frac{k-1}{k}$ and a chance $p = \frac{1}{k}$ to go to a deeper generation in the tree (towards the leaves).

Coordination numbers of $k \geq 3$ induce a bias toward higher generations because $p \geq \frac{2}{3}$. For infinite Bethe lattices, this means that the MFPT to reach the root after the initialization diverges because of a non-vanishing probability to never visit the root again [179]. For finite extensions of the tree, an exponential decay in the distribution of the MFPT has been reported [183].

Additional weights have been given to each transition between nodes on the network [184–187]. Transitions to each node can have an additional relative weight. An effective parameter p' has been introduced by Skarpalezos *et al.* [188] that takes into account node numbers and relative weights. With this effective parameter, random walks on the treelike structure have been mapped to a one-dimensional random walk. The analytical result for the MFPT $\langle\tau\rangle$ to escape the tree of depth D has been calculated from the one-dimensional description [188] to be

$$\langle\tau\rangle = \frac{D}{2p' - 1} + \frac{1 - p'}{(2p' - 1)^2} \left[\left(\frac{1 - p'}{p'} \right)^D - 1 \right]. \quad (4.3)$$

Note that the asymptotics for large trees is determined by an exponential growth with D for $p' < \frac{1}{2}$, i.e. a bias away from the escape point and by algebraic growth for a bias towards the the escape point ($p' > \frac{1}{2}$).

4.4 Reconstructing network structure by transport properties

In the previous section, the studies investigated how transport is influenced by the geometrical structure of its environment. By means of knowing the structure, there

can be estimates for transport properties such as mean first-passage and escape times, mean square displacement and diffusion exponents. The reverse point of view is how to extract structural information of the environment of stochastic transport by measuring characteristics of the transport instead of directly measuring the structural properties.

Some examples of structural analysis by diffusive transport are presented in the following. Mitra *et al.* related the diffusion of fluid molecules that are confined in a porous medium to the pore-space structure factor [189]. Similar work by Mair *et al.* continued in the direction and found ratios between surface area and volume for pores and tortuosity, the ratio between curve length and the distance between the endpoints of the curve, in relation to gas diffusion nuclear magnetic resonance [190]. Mair *et al.* applied this technique to packs of glass beads, sandstone, and carbonate rocks. In Chen *et al.*, the permeability of a heterogeneous multi-component system has been analyzed with a random walker approach without knowing the detailed microstructure [191]. An other example is the exploration of foam structures from light scattering methods by Durian *et al.* [192]. In the study, propagation of light has been approximated by diffusive motion and is described by the diffusion equation of light and the dynamics of the average size of the foam bubbles has been identified [192].

Recap that random walk models do not have to be carried out in three dimensions but can be applied to a network structure. In discrete networks, there is a wide possibility to gain structural information out of the characteristics of random walks. Cooper *et al.* estimated properties of large, connected graphs by first passage times of random walkers and adjusting the weights of the RW that is choosing between nodes by the properties of interest [193]. The numbers of vertices or edges have been investigated by theoretical and experimental methods on two example graphs.

4.5 Persistent random walks in cell migration

So far, in this chapter, passive transport has been related to the characteristics of its environment. RW models have been presented to describe the passive transport. This environment influences on a random walker can also be utilized to extract information about the environment walker. In this section, additional features are introduced to a RW model. These enable the RW model to mimic the active character of cell migration to eventually determine search efficiency in the second project of this thesis.

Migration trajectories of dendritic cells (DCs) show a tendency to keep moving in a given direction, called *persistence* (see section 2.5). Stankevics *et al.* have observed DCs switching between diffusive and persistent states during migration [22]. The authors conclude from their experimental and theoretical analysis that the two different states, and switching between them, are created by actin polymerization waves and that by changing the actin network dynamics, it is possible to adapt migration patterns to the environment [22, 194]. The results are consistent with earlier findings in which migration is driven by activating and deactivating cell

protrusions [195].

One can define persistence as a measure of how long a random walker will move in a given direction until it will turn into the other direction. Consider a one-dimensional random walker with probability p to move from position i to $i + 1$ and probability $1 - p$ to step from i to $i - 1$. In case of a random walker with probability p to continue stepping in a direction, the probability to make l consecutive steps in a row is given by $P(l) = p^{l-1}(1 - p)$. The mean value of this PDF is a useful tool for measuring persistence and is given by the persistence length [21]

$$l_p = \sum_{l=1}^{\infty} lP(l) = 1/(1 - p). \quad (4.4)$$

Persistence has drawn attention in the field of random walkers for several decades. MFPTs have been calculated for a persistent random walker in one dimension [196]. The analysis has later been generalized for two dimensions [197, 198] and for three-dimensional walks of light scattering in thin slabs [199] for example. Furthermore, persistence has been introduced in the context of Ising models [200] in order to describe the fraction of spins that have not flipped in a given time interval.

Persistence is also applied to directed motion in biological physics. Shaebani *et al.* [201] modeled long runs of motor proteins along the complex filament network in cells by persistent random walkers. In the model, motors walk along a filament until they reach a node connecting different filaments. At each node, the walker has a choice to switch to the crossing filament. This behavior has been included in a master-equation approach of a Markov process that at each time step has knowledge of the position and the direction. Persistence is implemented by a probability p to continue in the given direction. This approach leads to anomalous diffusion for short and intermediate times [201] (see section 3.2). The method has been further developed by adding pause states [202].

As a reminder, in section 2.5 it has been discussed that dendritic cells perform searches for antigens. Search efficiency, however, can be heavily influenced by the type of motion (*search strategy*) which has been found for theoretical random walks [150]. An example has been given by Viswanathan *et al.* [203, 204] with Lévy flights performing more efficiently in search problems than simple diffusive random walkers. Another example is given by intermittent random walks (see section 3.2). Also, the environment such as bystander cells have been found to reduce search times of natural killer cells [205]. The fraction of time spent in each of the two different states of motion can be adjusted to optimize the search problem [150]. However, for the example of the DCs it is worth understanding more about the influence of the persistence on the search efficiency itself before combining intermittent walks.

Tejedor *et al.* optimized search by finding the optimal persistence in a persistent random walk model on a two-dimensional grid [21]. In the study, the authors calculated MFPTs for a target on a grid with periodic boundary conditions. The MFPT is

minimized for a non-trivial persistence length defining the optimal search strategy. Persistent random walks have been found to perform more efficiently than any Lévy walk [21]. Tejedor *et al.* found that it is crucial for the result of a search problem how the targets are distributed. A special type of search problem is to find the time that is needed to visit every site of a lattice, the *cover time*. In a consecutive study Chupeau *et al.* [206] compared different random search strategies in terms of cover times. The authors show that the mean cover time is minimized by the same search strategy as for a single target in their example search processes, i.e. Lévy strategies, intermittent walks, and persistent random walks.

4.6 Chapter summary

In this chapter, the concepts for the project about passive intracellular transport and the project about cell migration have been discussed. For both applications, random walk models are useful to describe the stochastic motion of independent cargo, i.e., chemical signals or a whole dendritic cell. With the analytical and numeric framework, transport properties such as first-passage times can be calculated. This is especially useful in escape or search problems.

In the beginning, studies have been presented that investigate diffusive motion confined in a narrowing tube and in comb-like structures of spines. Effective probabilities for a directional bias and trapping in spines have been found, which are determined by the environment of the transport. Such effective descriptions can be used to define coarse-grained models. I presented a stochastic motion on a discrete and regular treelike network and mapped it to RWs in one dimension. An relation between structure and transport properties can also be used to investigate the underlying structure. The structural influences on transport properties have been analyzed in many systems similar to neuronal dendrites and parts of them. An effective description of a complete dendritic tree was, however, lacking before this thesis.

Furthermore, the RW approach can be adjusted to describe active motion such as for molecular motors on filaments or migration of cells. For the persistent motion of dendritic cells, not only the environment but also internal processes influence the effective description in a random walk model.

Chapter 5

Lattice gas models for active transport

Contents

5.1	Unidirectional exclusion processes	55
5.1.1	The totally asymmetric simple exclusion process	56
5.1.2	TASEP with Langmuir kinetics	58
5.1.3	Local irregularities	59
5.1.4	Conservation of particles in the reservoir	60
5.1.5	Unidirectional multi-lane models	62
5.1.6	Non-Markovian exclusion processes	62
5.2	Bidirectional exclusion processes	64
5.2.1	Site-exchange models	65
5.2.2	Bidirectional multi-lane models	67
5.3	Chapter summary	71

In this chapter, the literature relevant to the third project on active intracellular transport by molecular motors is presented. The spatial interactions of cargoes with other cargoes and the environment require a many-body description. The focus in this chapter is on lattice gas models and their applications on intracellular transport.

A *lattice gas* is based on several particles, modeled as random walkers, moving on a (one-dimensional) lattice. The important element of the model is the spatial exclusion of particles which takes hardcore volume exclusion between particles into account. As a consequence, lattice gas models with volume exclusion are also named *exclusion processes*.

In this thesis, I will focus on exclusion processes in which particles are driven in a direction. This *asymmetric simple exclusion process* (ASEP) serves as a fundamental model class for non-equilibrium physics and has been extensively studied [9,141,207–210]. For particles that exclusively move in one direction, the ASEP is called *totally asymmetric simple exclusion process* (TASEP) [207]. The TASEP will serve as a reference system for transport models.

5.1 Unidirectional exclusion processes

In the first section of this chapter, the focus is on unidirectional versions of the TASEP with one or more types (species) of particles that all move in the same direction on

the lattice. I start by introducing the rules of the TASEP in the following.

5.1.1 The totally asymmetric simple exclusion process

The TASEP has a discrete and one-dimensional lattice of length L . Each of the lattice sites can be occupied by a particle or be empty, also referred to as holes. Exclusion between particles forbids more than one particle on a given lattice site. In the TASEP, particles have a constant hopping rate p in one direction which often determines the time scale by expressing all other rates in terms of p . Therefore, the simulation update can be done in discrete time steps $\Delta t = 1/p$ by a random-sequential update with effective rate $p_{\text{eff}} = 1$. There is a symmetry between particles and holes because a step of a particle from site i to site $i + 1$ also moves a hole to from $i + 1$ to i .

Different boundary conditions can be distinguished. With *periodic boundary conditions* (PBC), the lattice is closed to a ring, i.e. particles do move from site L to site 1 when performing a step on the end of the lattice and the number of particles is thereby conserved. With *open boundary conditions* (OBC), particles are inserted in the system on site 1 with rate α and escape the lattice on site L with a rate β .

The *occupation configuration* C is used in order to describe the state of the system over time. An occupation number n_i tells for every site i of the lattice if it is occupied ($n_i = 1$) by a particle or empty ($n_i = 0$). The set of these occupation numbers determines the configuration $C = \{n_1, n_2, \dots, n_L\}$. For each time t , the state of the system is described by the master equation [9] for constant transition rates ω :

$$\frac{dP(C, t)}{dt} = \sum_{C' \neq C} [\omega(C' \rightarrow C)P(C', t) - \omega(C \rightarrow C')P(C, t)], \quad (5.1)$$

where ω denotes the hopping (p) process, the insertion from the boundary at site 1 (α) or the detachment at the boundary at site L (β).

The density of particles $\rho_i = \langle n_i \rangle$ of site i in the bulk, and sites 1 and L at the

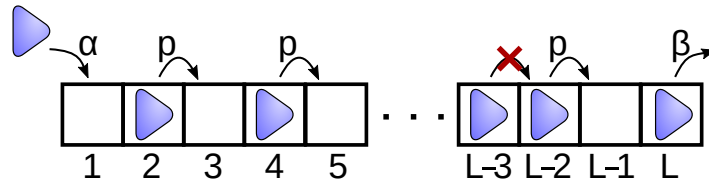


Figure 5.1: Schematics of the TASEP. Particles can hop with rate p to the right on a one-dimensional lattice of length L with spatial exclusion. In a realization of open boundaries, particles are inserted on site 1 with rate α and escape on site L with rate β .

boundaries is then [9]

$$\begin{aligned}
 \frac{d\langle n_i \rangle}{dt} &= \langle n_{i-1}(1 - n_i) \rangle - \langle n_i(1 - n_{i+1}) \rangle \\
 \frac{d\langle n_1 \rangle}{dt} &= -\langle n_1(1 - n_2) \rangle + \alpha\langle 1 - n_1 \rangle \\
 \frac{d\langle n_L \rangle}{dt} &= \langle n_{L-1}(1 - n_L) \rangle - \beta\langle n_L \rangle.
 \end{aligned}
 \tag{5.2}$$

Often it is not only important to know the configuration at time t , but also how efficient the exclusion process can transport actively driven particles. Therefore, the measure called *flux* J is introduced as the number of particles that pass from one specific site to its neighboring site per unit time. That means that from equation 5.2, the flux is given for a bond i in the bulk by $J = \langle n_i(1 - n_{i+1}) \rangle$, for the entrance $J = \alpha\langle (1 - n_1) \rangle$ and $J = \beta\langle n_L \rangle$ for the end of the lattice.

A solution of equation 5.2 is depending on successive correlations between occupation states along the lattice. A method used to find a solution is a *mean-field model* which decouples pair correlations $\langle n_i n_j \rangle = \langle n_i \rangle \langle n_j \rangle = \rho_i \rho_{i+1}$ [211, 212]. Equations (5.2) are then viewed in the continuum limit and evaluated by solving the remaining differential equations. An exact solution was later found by applying the *matrix product ansatz* [207] or recursion relations [213].

For PBC, the flux has to be constant along the lattice in the stationary state which then leads to exact results in the continuum limit for the flux

$$J(\rho) = p\rho(1 - \rho) \tag{5.3}$$

with maximum value $J_{\max} = 1/4$ for $\rho = 1/2$ [207]. This relation is regarded as a reference value for unidirectional transport systems modeled by lattice gases. The flux J plotted versus the particle density ρ is called a *fundamental diagram*.

In case of OBC, three phases can be distinguished [207, 211] that define the reference system of an open boundary exclusion process:

- (A) Low-density (LD) phase with $J = \alpha(1 - \alpha)$ for $\alpha < 1/2$ and $\beta > \alpha$,
- (B) High-density (HD) phase with $J = \beta(1 - \beta)$ for $\beta < 1/2$ and $\alpha > \beta$,
- (C) Maximum-current (MC) phase with $J = 1/4$ for $\alpha \geq 1/2$ and $\beta \geq 1/2$.

By the recursion method [213], it has been shown that the LD phase (A) and the HD phase (B) are separated into two phases each. By considering local correlations, different density profiles can be identified. This is not possible in the mean-field analysis which neglects correlations along the lattice. The phase diagram of the TASEP is shown in figure 5.2.

Regions of high density on the lattice can also be denoted as *traffic jams*. The local flux is decreased in a jam region, due to exclusion blocking many hopping attempts. Open boundaries lead to rich behaviors of density variations along the lattice which

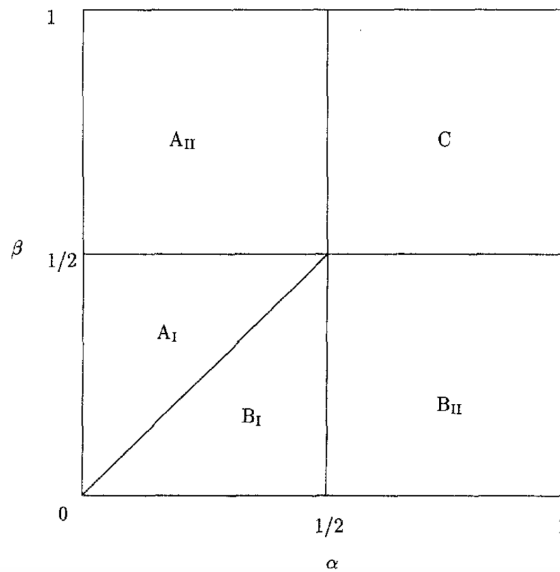


Figure 5.2: Phase diagram of the TASEP in the α, β parameter space which is scaled to units of p . A_I and A_{II} denote low-density phases (LD), B_I and B_{II} denote high-density (HD), and C the maximal-current phase (MC). Reprinted from *Journal of Statistical Physics*, 72, G. Schütz and E. Domany. Phase transitions in an exactly soluble one-dimensional exclusion process. 277-296, Copyright (1993) by Springer Nature.

are described by dynamics of shock waves in local densities [212,214–216].

The focus of this thesis is on the behavior in the bulk. As discussed for the TASEP, boundary conditions have a huge influence on the stationary state in the system. To be able to investigate the principle of many-particle interaction in a system that models the long, narrow extension of the axon, periodic boundary conditions are better suited because they do not introduce additional complexity. However, one should keep in mind that boundary effects can play a role in the axon and that periodic boundaries are an approximation to a long system only. In the following models, the focus is therefore on PBC. OBC are discussed for reasons of completeness. Recap that the periodic TASEP has a rather simple solution. In order to adjust the TASEP to the situation in intracellular transport, some modifications have to be done. Those modifications can, however, lead to complicated situations in which the solution is not found analytically anymore.

5.1.2 TASEP with Langmuir kinetics

In a modified version of the TASEP, also the bulk of the lattice is coupled to a reservoir. In Parmeggiani *et al.*, *Langmuir kinetics* have been added to the bulk [212,217,218]. Langmuir kinetics describe adsorption and desorption as reversible processes [219].

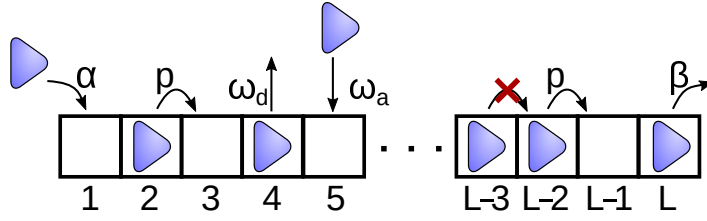


Figure 5.3: Schematics of the TASEP with Langmuir kinetics. Particles can hop with rate p to the right on a one-dimensional lattice of length L with spatial exclusion, or detach from the lattice into the reservoir with rate ω_d . Empty sites in the bulk can be occupied by particles from the reservoir with rate ω_a . Open boundaries allow insertion of a particle on site 1 with rate α and particle escape on site L with rate β .

Essentially, the lattice is coupled to a grand canonical reservoir of constant particle density. A scheme of the model is given in figure 5.3. An additional reservoir is included in the model that belongs to the bulk of the lattice, not only the boundaries. particles can detach from each site into the reservoir with rate ω_d or attach to a non-occupied site with rate ω_a from the reservoir. To distinguish between boundaries and bulk, the dynamics at site 1 and L is again described by α and β as in the ordinary open boundary condition TASEP.

Equation 5.2 is simply extended by the processes of attachment to a site in the bulk (ω_a) and detachment from the bulk (ω_d)

$$\begin{aligned} \frac{d\langle n_i \rangle}{dt} &= \langle n_{i-1}(1 - n_i) \rangle - \langle n_i(1 - n_{i+1}) \rangle + \omega_a \langle 1 - n_i \rangle - \omega_d \langle n_i \rangle \\ \frac{d\langle n_1 \rangle}{dt} &= - \langle n_1(1 - n_2) \rangle + \alpha \langle 1 - n_1 \rangle - \omega_d \langle n_1 \rangle \\ \frac{d\langle n_L \rangle}{dt} &= \langle n_{L-1}(1 - n_L) \rangle + \omega_a \langle 1 - n_L \rangle - \beta \langle n_L \rangle. \end{aligned} \quad (5.4)$$

Note that the ordinary TASEP is a non-equilibrium process since particles are actively driven but pure Langmuir kinetics represent an equilibrium process. In the stationary state, the density of particles bound to the lattice with periodic boundary conditions is simply

$$\rho_b = \frac{\omega_a}{\omega_a + \omega_d}. \quad (5.5)$$

Parmeggiani *et al.* showed that if Langmuir kinetics are combined with the open boundaries at site 1 and L , the complexity of density regimes is further increased and phenomena such as phase coexistence between all the three classic TASEP phases above appear [217,218].

5.1.3 Local irregularities

One method to calculate the stationary state is a mean-field analysis which assumes homogeneous conditions for particles and the lattice. However, in order to model

intracellular transport, this homogeneity can be questioned. Local irregularities can be taken into account in the model. Motivation is given by tau proteins that compete with molecular motors for binding sites on MTs (see section 2.2.3). This can lead to blocked binding sites and therefore to locally modified hopping rates.

Irregularities can be categorized in site-based defects or particle-based defects [10]. The three processes included in the model, i.e. hopping, binding and unbinding can be affected. Modified particle-based hopping has been studied by Evans *et al.* and Krug *et al.* [220, 221], where quenched random variables are assigned to each particle's hopping rate. Since a single slow particle obviously slows down other particles behind it, an other model has been considered where particles can take over the slow leader [209]. Nevertheless, traffic jams have been observed behind the slow leader particle if the take over is not fast enough. Similarly, if two species of particles with different hopping speeds interact on an exclusion process, the flux is decreased in comparison to the TASEP. In Chai *et al.*, it is shown that the fundamental diagram exhibits a plateau behavior for intermittent densities [222]. Remember that for a regular TASEP with PBC, the graph has the form of a parabola $J = \rho(1 - \rho)$.

A site-based irregularity has been considered in the model of Janowsky *et al.* [223], where a *slow bond* reduces the hopping rate at a single site. The System can then be separated in a HD phase in front of the defect and a LD phase behind it. The flux of the complete system is effectively determined by that single slow site. For this reason the slow site is also called *bottleneck*, as for example in Pierobon *et al.* [224].

A defect in binding and unbinding of particles on a special site has been introduced by Chai *et al.* [222]. While decreased hopping and increased unbinding rates have been found to heavily reduce the transport efficiency of the exclusion process, increased local binding had less effect on the transport.

5.1.4 Conservation of particles in the reservoir

In the section before, defects have been discussed that locally affect dynamics. The environment of the axon leads requires additional rules for a TASEP. First, it is reasonable to keep a fixed number of particles which are a finite resource in the cell. Second, as discussed in section 2.4, the MT network already is a dense structure for cargo such as vesicles that are transported by molecular motors on the filaments. The infinite diffusion that required for constant attachment rates from the reservoir and finite numbers of particles is also arguable.

To mimic the constraints of the axon, modeling the filament lattice has been embedded in a confined geometry in the theoretical work by Klumpp, Lipowsky and Müller *et al.* for different boundary conditions [225–227]. In the case of periodic boundary conditions, the result of the flux of bound particles is calculated by a mean-field analysis. Results are in accordance to the TASEP $J = p\rho_b(1 - \rho_b)$ with adjusted effective density of the bound particles as in equation 5.5. Note that there is no particle-hole symmetry anymore if particles are attracted to the filament more than holes are. The optimal particle number for reaching a high flux depends on the attachment and detachment kinetics.

Three-dimensional diffusion of motors in a closed environment has been coarse-grained by Müller *et al.* [227] in an effective two-state model with particles being bound or unbound. The difference compared to the model by Parmeggiani *et al.* with simple Langmuir kinetics is that the position along the filament axis is kept. Essentially, the two-state model can be considered as a two-lane model with one driven lane and one diffusive lane without exclusion.

Another boundary condition has been taken into account in the model by Klumpp and Müller *et al.* [225, 227]. In axons, kinesin based transport is driven from the minus-end and can be restricted by the synaptic region of the axon near the plus-end of MTs (see chapter 2). For the results of this thesis, however, I focus on the bulk behavior and, thus, on periodic boundary conditions.

The second point that questions the infinite diffusion rates in the simple TASEP with Langmuir kinetics by Parmeggiani *et al.* [217, 218] is also addressed in the next models. Particles on a two-dimensional (and three-dimensional) lattice modeling both, the filament and the cytoplasmic environment called reservoir here, have been introduced by Lipowsky *et al.* [228] and Nieuwenhuizen *et al.* [229, 230]. By explicitly hopping on this network, the particle number is conserved and diffusion can be limited to finite values.

On the one hand, dynamics of the particles on the filament sites match the implementation in the models before, i.e. hopping in one direction and exclusion by hard-core interaction. On the other hand, particles in the reservoir now also hop between sites in the lattice, still under exclusion. However, in this approach, hopping rates are equal to go to any neighboring node in the reservoir [230]. Hopping from the filament to neighbor sites is determined by detachment rate ω_d and from neighboring sites to the filament by the attachment rate ω_a . In the work of Lipowsky *et al.* [228], rates have been adjusted to experimentally measured parameters in order to reach higher comparability to the biological system of an axon than the abstract models with pure Langmuir dynamics coupled to a TASEP [217, 218].

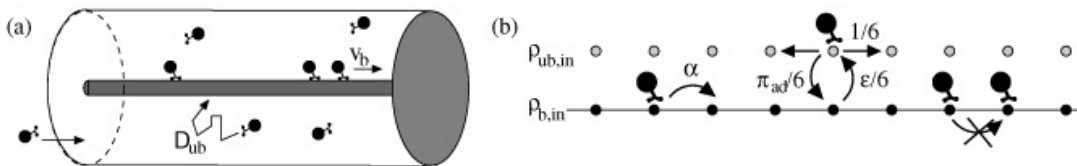


Figure 5.4: **a)** Scheme of the motion of particles in the axon confined in a half-open, tube-like geometry that mimics the axon. Particles can diffuse if unbound or actively walk if bound to the filament embedded in the cylinder. **b)** Corresponding two-lane model with a driven lane and a diffusive lane for half open boundary conditions. Müller *et al.*, *Journal of Physics: Condensed Matter*, 17, S3839-S3850, 2005. Copyright (2005) by IOP Publishing.

5.1.5 Unidirectional multi-lane models

As mentioned, the two-state model by Müller *et al.* [227] could also be seen as a two-lane model, i.e. a driven lane for the filament and a diffusive lane for the environment. The concept of a multi-lane model has widely been studied. Similar to the model by Müller *et al.*, Tsekouras *et al.* investigated a driven lane that is coupled to a single symmetric reservoir lane serving as a coarsened environment [227, 231]. However, the spatial exclusion is included for both lanes. This model has been mapped to a partially asymmetric exclusion process on one lane so that the complexity can be reduced as a consequence. Similarly, a mapping of a multi-lane TASEP has been achieved which shows that by inventing more complex rules, a single lane system, can be suitable in order to describe transport taking place on a many-lane network [232].

Complexity usually increases by adding more lanes [233]. Also by tuning transition rates between lanes, transport efficiency varies for different lanes, i.e. the optimal choice for the global density differs among the lanes [234].

5.1.6 Non-Markovian exclusion processes

In the exclusion processes reviewed so far, transition rates have been constant over time, i.e. the stochastic process is a Markov process. More complex interactions with the environment [14] such as the escape from spine cavities (see section 4.1.2) and traps from cages with exponentially distributed depth [181, 235] may lead to event times that are distributed by algebraic power laws. In section 3.3, it is discussed how modeling of non-Markovian random walkers can be handled. In this section, literature on non-Markovian versions of the TASEP is presented.

Rules of the non-Markovian TASEP

Concannon *et al.* investigated a TASEP with PBC and algebraically distributed waiting times [236]. Similar to Gillespie's first reaction method, the authors use the next reaction method to execute hopping events. The event time W is drawn from an algebraic power law PDF

$$p(W) = \begin{cases} 0 & 0 < W < 1, \\ (\gamma - 1)W^{-\gamma} & W > 1 \end{cases} \quad (5.6)$$

with exponent $\gamma > 2$.

The power-law decay of $p(W)$ has the consequence that the age of the stochastic process is relevant for the transition probabilities at a given time t . Hence, it does make a difference whether waiting times for events in the future are deleted after a hopping event or kept. Note that the particle-hole symmetry known for the Markovian TASEP is broken in this model. In this model, a particle i keeps a sequence of times $\{t_i^0, t_i^1, t_i^2 \dots\}$, that determines all attempts to hop. The authors introduce a *clock*

for each particle on which their future events, the age and residual time of a current process are given. The hopping times are determined by adding up the relative waiting times W_i^j which are distributed by the PDF $p(W)$.

In order to evolve the system, the next hopping event is chosen by searching the particle which has the lowest hopping time. The event is executed if the neighboring site on the lattice is empty and rejected otherwise.

Results for the particle flux in the non-Markovian TASEP

To compare the results of this model to the Markovian TASEP, Concannon *et al.* show a fundamental diagram for the relation between the flux J and the density of particles on the lattice ρ (see section 5.1.1). In the Markovian TASEP with periodic boundary conditions, this relation is given in the form $J = p\rho(1 - \rho)$. Furthermore, the average time of hopping events is simply $\bar{W} = 1/p$. Concannon *et al.* used the average hopping time to scale the measured flux in order to compare the Markovian TASEP with the non-Markovian TASEP. The fundamental diagram of [236] is shown in figure 5.5 (a). It is remarkable that the shape of the graph and the position of the maximum of the flux is depending on the exponent γ . In particular, the flux is not symmetric around the density which leads to the optimal flux. Second, the flux is below the estimate from the Markovian relation for exponents γ smaller than approximately 3.5.

In addition, Concannon *et al.* report that the flux is decreasing with the system length L for $\gamma < 3$ (see figure 5.5 (b)). This leads to vanishing fluxes in the limit of infinite system sizes. This differs from the results of the Markovian TASEP for which

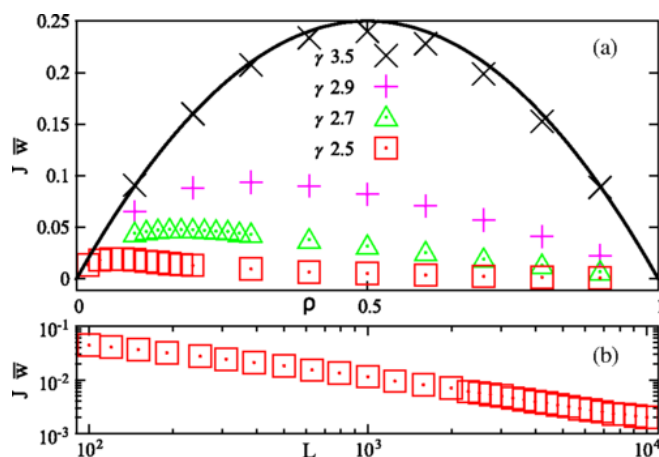


Figure 5.5: Results for the non-Markovian TASEP by Concannon *et al.*. **a)** In the fundamental diagram, the flux is shown for exponents $\gamma \in [2.5, 3.5]$ and compared to the result of the Markovian TASEP (black line) for $L = 500$. **b)** For $\gamma = 2.5$ and $\rho = 0.1$, the flux is shown as a function of the system length L . Reprinted from Concannon, Robert J. and Blythe, Richard A., Physical Review Letters, 112, 050603, 2014. Copyright (2014) by the American Physical Society.

the flux is finite in the thermodynamic limit (see section 5.1.1).

The authors discuss the length dependency by arguing the effect of aging inside a cluster of particles as follows. A first, particle in a cluster that has no obstacle on its target site is called a pack leader. Behind the pack leader, other particles wait in the queue until the pack leader hops. The new pack leader of the remaining cluster is now no longer blocked. Since the last hopping attempt of the new pack leader is some time ago, the current waiting process has an age and a residual waiting time until the next hopping attempt.

From examining renewal processes in chapter 3.4, it is plausible that this aging process influences the effective hopping time of the new pack leader. If the renewal process has been renewed for a large enough period of time to apply reasonable time averages in the calculation of the residual waiting time distribution, the density of the residual waiting time differs from the density of the original waiting times ($p(W)$) when using algebraic power-law distributions. For a particle that is finally a pack leader, the chance is high to have a large residual waiting time if the tail of $p(W)$ has a high statistical weight. In Concannon *et al.*, the exponent of the effective hopping time PDF shows a shift from $-\gamma$ to $1 - \gamma$ which means that the residual waiting time has a diverging mean at $\gamma = 3$. As a consequence, the effective flux vanishes at this critical value $\gamma = 3$ in the limit of large system lengths.

A second work about non-Markovian exclusion processes has been reported by Khoromskaia *et al.* [237]. It deals with a TASEP with hopping event times generated by algebraic Pareto tail distributions and delayed exponential distributions. In contrast to the model of Concannon *et al.*, this model conserves particle-hole symmetry by assigning times to each lattice site instead of each particle. The model is therefore referred to as *site-based* model. Results for the fundamental diagram are, however, very similar to the model by Concannon *et al.*. In the site-based model, the exponent for which the non-Markovian TASEP leads to lower fluxes than in the Markovian TASEP is calculated to be $\gamma = \gamma_M \approx 3.414$, which is consistent with results the previous results by Concannon *et al.* [236]. Furthermore, higher exponents $\gamma > 3.414$ lead to higher fluxes. The density at which the maximum is reached depends on γ . The optimal density is larger than $1/2$ for $\gamma > 3.414$ and below $1/2$ for smaller γ [237]. In comparison, the periodic Markovian TASEP always finds the maximum flux at density $1/2$. The Markovian fundamental diagram is similar to the fundamental diagram at $\gamma = \gamma_M$. Also in the site-based model, the flux has been estimated to vanish in an infinite system for exponents $\gamma < 3$ because of the diverging mean value of the residual waiting time.

5.2 Bidirectional exclusion processes

In chapter 2 it has been pointed out that for MT based transport in neurons, two species of molecular motors can be included, i.e. kinesin and dynein. Since these species mostly walk in opposite directions on the MT, transport is not restricted to

one direction. To adapt the model of an exclusion process to bidirectional transport, a second particle species can be introduced in the TASEP. Motivated by the MT-polarity, those species are named *plus-particles* (moving to the right in the following) and *minus-particles* (moving to the left). The coarse-grained approach allows assuming a particle as a single motor protein as well as a complete motor-cargo complex.

The central question for such a two-species exclusion process is how the interaction of particles is carried out in order to have efficient transport in the system that is inspired by the axon. Without any bypassing mechanism, particles would just collide in a simple exclusion process with two particle species.

Two approaches have been proposed: First, *site-exchange* models where particles pass by each other and thus exchanging positions on the lattice. Second, bidirectional *multi-lane* models in which transport could be organized in lanes which support transport in different directions. Representatives of both model classes are presented in the following.

5.2.1 Site-exchange models

A site-exchange denotes the exchange of positions of two neighboring particles on the lattice (see figure 5.6). A similar mechanism has been discussed already in section 5.1.3 where normal particles can take over a single slow particle [209]. The two-species model established by Evans *et al.* [27, 238] has a probability p (set to $p = 1$) for particle hopping for both species as well as a second probability $q \leq 1$ to exchange positions if a plus- and a minus-particle are opposing each other on sites i and $i + 1$

$$\begin{aligned}
 (+)_i(0)_{i+1} &\Rightarrow (0)_i(+)_i && \text{with rate } 1, \\
 (0)_i(-)_{i+1} &\Rightarrow (-)_i(0)_{i+1} && \text{with rate } 1, \\
 (+)_i(-)_{i+1} &\Rightarrow (-)_i(+)_i && \text{with rate } q.
 \end{aligned}
 \tag{5.7}$$

By use of mean-field calculations and MC-simulations, Evans *et al.* give phase diagrams for open boundary conditions. Plus-particles are inserted at site 1 and escape the lattice at L as for the unidirectional TASEP (hopping to the right), minus-particles have symmetrical rules for entering the lattice at site L (hopping to the left). An interesting result of the analysis is that the model exhibits spontaneous symmetry

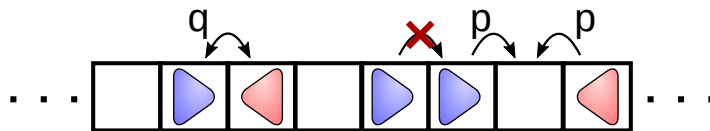


Figure 5.6: Schematics of the TASEP with site-exchange dynamics. Plus-particles (blue triangles) can hop with rate p to the right on a one-dimensional lattice of length L with spatial exclusion, minus-particles (red triangles) hop to the left with the same conditions. If a plus-particle and a minus-particle stand in front of each other, site-exchange is performed with rate q .

breaking between the two species. The density of particles on the lattice has been found to switch between low and high density phases so that the difference in fluxes $\Delta J = J_+ - J_-$ flips between positive and negative values.

For periodic boundary conditions, an exchange probability $q < p$ simply leads to slowing down transport. Particles act as obstacles for each other, in other words as defects similar to the irregularities discussed in section 5.1.3. The slow process inside the high-density area is related to the one species TASEP with irregularities [223] because, essentially, the exchange processes with particles of the other species act as bottlenecks on the particles of the first species. Free particles will follow and eventually catch up to a leading particle that is standing in front of an obstacle and therefore particle clusters and traffic jams may emerge. Within these clusters, the particle exchange is the dominant process and determines the flux of particles that come out of the cluster. Consequently, the flux in the low-density area on the lattice is also determined by the outflow of a high-density area since the flux is balanced over the whole lattice in the stationary state.

A second study by Arndt *et al.* [239, 240] has been investigating a model with site-exchange in both directions. An additional rule for backward site-exchange has been added to the set of equations in equation 5.7



By exchanging backwards faster than forwards ($q < 1$), the system forms three blocks [239, 240]. One for each of the two particle species and one for vacancies. These macroscopic blocks of the size in the order of the system size break the translation invariance than is observed for a unidirectional TASEP. The system is even less efficient for transport as it is without the backward exchange. The effective flux breaks down totally when it becomes very rare that a particle travels through the complete block of opposing particles against its backward bias.

In case of fast forward exchanges ($q > 1$), the authors identified two different *phases*, called *mixed* and *disordered*. Blocks of a macroscopic, mixed structure of plus-particles and minus-particles have been found in the mixed scenario leading to algebraically increasing the flux when increasing q [239, 240]. For even larger q , no such structures have been observed and the flux is exponentially converging to an asymptotic value. The transition between the phases has been examined for finite systems by Arndt *et al.* [241]. This separation in two phases, however, has been identified as a finite size effect later [242], which can be applied to very large systems but that is not valid in the limit of infinite system length.

Considering the models in this section, the approach of site-exchange is in principle applicable to model bidirectional intracellular transport. It has to be further clarified which physical event is modeled by a coarse-grained site-exchange. For particles referring to single motor proteins, exclusion takes the competition of binding on the MT into account. For taking over, molecular motors first have to unbind and

diffuse around each other to bind again after the obstacle. Such processes can then be described with an abstract stochastic event with a rate $q < p$, which can result in reduced transport depending on the motor density on the filament.

Modeling even more complex motor-cargo combinations, the site-exchange also has to take the description of spatial interactions of cargo-motor complexes into account. In a confined system such as the crowded environment of MT network in axons, it is questionable if a site-exchange due to diffusing around each other is possible for larger objects such as vesicles and organelles. The spatial interactions can lead to forming *cages* by particles surrounding others which results in very long escape times from these cages as it has been investigated to particles in glass theory [235]. In order to find a mechanism for efficient bidirectional transport, it is therefore also important to examine the second class of models, the multi-lane models.

5.2.2 Bidirectional multi-lane models

The second, complementary approach to bidirectional intracellular transport modeled by exclusion processes is a multi-lane system. The idea is that two or more coupled one-dimensional lattices carry out transport for one species of particles each. The many-lane version is essentially represented by several unidirectional exclusion processes transporting particles in different directions.

The first example of a one-dimensional two-species TASEP with two coupled lattices (*tracks*) has been studied by Korniss *et al.* [26]. This model has a hopping probability p and a site-exchange probability q that is related to p by a factor, i.e. $q = \gamma p$ with $\gamma = 0.1$. Furthermore, a coupling rate for hopping between sites with the same index of the two tracks is included. While the authors focus on the ordering of upcoming clusters, transport is always determined by the exchange rate q . Note that in such a site-exchange model it is not important for the flux if the exchange process slows down transport in a single, big cluster or in many smaller clusters. No lane-formation into a plus-particle carrying lattice and a minus-particle carrying lattice has been observed in the study by Korniss *et al.* [26]. Essentially, this multi-lane model does not improve transport efficiency compared to the single-track system.

In accordance, it has been shown that particles that are walking on two adjacent lattices are slowed down by inter-track interaction [243]. Hopping rate modification in presence of another particle on the site of the same index on the neighboring track is producing plateau effects in the flux-density fundamental diagram, similar to the two species of different speed on a single lane [222].

So far, inventing a second lane does not enhance transport efficiency as long as there is still interaction decreasing the hopping. Main achievements in the direction of modeling stable bidirectional transport have been made by two approaches, i.e. suppressing local density fluctuations and ordering the particles by species on the different filaments.

Inspired by the model of Müller *et al.* [227], Ebbinghaus *et al.* investigated a periodic, two-species TASEP by adding a diffusive lane to a single filament track [25].

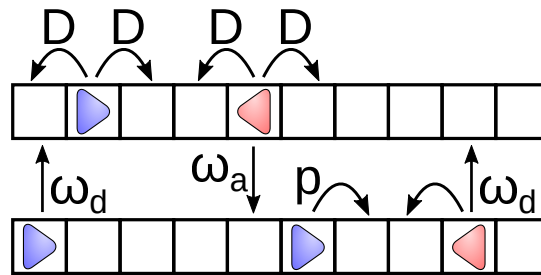


Figure 5.7: Schematic drawing of a two-track bidirectional exclusion process with one actively driven track (bottom) and one diffusive track (top). The schematics represent the model by Ebbinghaus *et al.* [25].

Both particle species are modeled identically up to the hopping direction. Direct site-exchange is not considered, hence, particles pass each other by detaching from the filament into the diffusive lane and rebinding again. A finite diffusion rate D determines the speed of particle movement without exclusion in the reservoir lane until the particle eventually reattaches to the filament. This bypassing mechanism is different from the site-exchange probability such as in the multi-lane model by Korniss *et al.* [26] or Evans *et al.* [27]. In the diffusive lane, particles are not moving in a biased direction and hence, the chance to find a site to reattach to the filament track depends on the length of the cluster. As a consequence, the flux depends on the system size [25].

The model clearly supports cluster formation that lowers the particle flux. Clustering can be reduced by increasing the detachment rate that leads to a lower density of bound particles ρ_b . Transport is enhanced until the low affinity reverses the effect due to the low number of particles on the track. Furthermore, long run lengths of molecular motors [34] indicate smaller detachment rates.

The model by Ebbinghaus *et al.* that includes one driven track and a diffusive track has also been extended to a doubled version, i.e. two driven tracks with a passive reservoir track for each driven track [25]. The filament tracks model protofilaments on an MT and the reservoirs model the cytoplasm near the protofilaments. These two sub-systems are coupled by two processes, a rate for switching between the reservoirs and a rate to switch between neighbor sites on the driven tracks. The track switching is thereby motivated by sidestepping that can be observed for dynein motors (see section 2.2). The authors found that this version with two driven tracks and reservoirs does not improve transport efficiency because clustering is even increased over the single-track version [25].

Ebbinghaus *et al.* concluded that the biologically relevant affinity to the filament and the finite diffusion leads to a strong tendency for clustering in the system compared to Langmuir kinetics such as in Parmeggiani *et al.* [217,218]. For modeling the biological system of motor-driven transport in the axon, neglecting any memory about the position along the filament is, however, highly questionable. For a confined

system such as the axon (see section 2.4), caging effects slow down diffusion. The effect is even more present considering motor-cargo complexes instead of single motor proteins. The size of cargo decreases diffusion and leads to spatial interactions between several cargoes and the environment. The model by Ebbinghaus *et al.* does not include volume exclusion for particles in the reservoir. Even though the model still simplifies essential key aspects of the interactions it does already lead to clustering and thereby transport cannot be efficient. The authors conclude that there might be another mechanism involved in intracellular transport in axons [25].

In subsequent work, Ebbinghaus *et al.* [244] reacted on the difficulty of dissolving high local densities on the filament and in the reservoir. Starting from the model in [25], the static lattice for the filament lane is replaced by several versions including dynamics, which is inspired by the MT dynamic instability reviewed in chapter 2.1. Sites in the filament lane are stochastically removed and added. Particles that occupy the removed sites switch to the reservoir lane. This leads to lowering density fluctuations and consequently smaller cluster sizes. It has been shown that a transition between a dependency on the system size and independence of the size for the flux can be achieved by increasing the depolymerization rate of filament sites. The optimal effect is thereby reached for a finite depolymerization rate. The flux vanishes in the limit of infinite depolymerization rates because the particles find no filament sites anymore to actively move in their bias direction. Besides the fact that the dynamic lattice successfully enhances the flux by avoiding length-dependent clustering, the spatial interaction in the reservoir lane is still neglected. It is questionable if the mechanism is applicable in the crowded environment of the axon [244].

Another approach toward organizing transport of particles in sub-systems has been made by Klumpp and Lipowsky [245]. A single driven track exclusion process includes modified Langmuir kinetics and a finite total density. The modified Langmuir kinetics eventually lead to symmetry-breaking, i.e. one species of particles

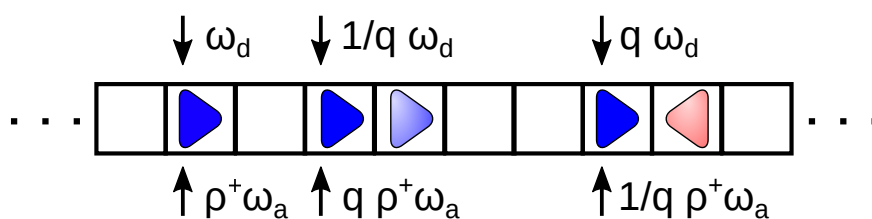


Figure 5.8: Schematic drawing of the model by Klumpp *et al.* [245], which includes particle attraction in a bidirectional two-species TASEP. Plus-particles (blue triangles) can hop with rate p to the right on a one-dimensional lattice of length L with spatial exclusion, minus-particles (red triangles) hop to the left with the same conditions. Attachment for a plus-particle (dark blue) is enhanced by the presence of other plus-particles (light blue), detachment is decreased. In presence of minus-particles (light red) the effect is reversed. The rules are analog for minus-particles.

is dominant on the filament whereas the other species is pushed into the reservoir. Motivated by the observation that motor proteins have been found to bind in attractive cooperative effects on filaments [84, 85], the binding and unbinding of particles is modified in the presence of another particle bound to the neighboring lattice site such that particles of same species attract each other when binding and lower the rate of unbinding. A factor $q > 1$ is used to adjust binding and unbinding rates in the following way for the three different local configurations of a plus-particle

$$\begin{array}{lll}
 \text{no neighbor} & \omega_a \rho_u^+ & \omega_d, \\
 \text{plus neighbor} & q \omega_a \rho_u^+ & 1/q \omega_d, \\
 \text{minus neighbor} & 1/q \omega_a \rho_u^+ & q \omega_d
 \end{array} \tag{5.9}$$

and vice versa for minus-particles (see figure 5.8). By mean-field calculations and MC-simulations, the authors did show a transition between a symmetric state and an asymmetric state for a critical attraction value $q_c(\rho)$. The symmetry is broken for $q > q_c$ so that one species is winning the competition and the flux is generated only by the bound species. The authors also state that this mechanism might lead to lane-formation in a multi-lane system [245] and show numerical results in a subsequent work [246]. However, a discussion of the multi-lane version of the model has not been published to my knowledge.

For modeling bidirectional MT-based transport with the model by Klumpp *et al.* [245], it is remarkable that new results of Shima *et al.* [34] (see section 2.2.3) show similar cooperative effects for kinesin. However, kinesin run lengths and therefore detachment rates have not been significantly affected in the experiments [34], which questions the implementation of the cooperative effect in the model. In addition, the model assumes infinite diffusion rates in the reservoir. As discussed, strong diffusion is highly questionable for particles modeling not only motor proteins but motor-cargo complexes of larger size in the confined environment of the axon.

Floor-field models

The last class of models I want to present in this thesis in the context of bidirectional transport lead to lane-formation in pedestrian dynamics. To avoid collisions, interactions between pedestrians and their environment can be way more complicated than just spatial interactions which is kept in a simple exclusion process. In an anticipation *floor-field*, models incorporate pedestrians estimating the movement of other pedestrians and adapting their direction in order to avoid collisions, also referred to as *social force* [247]. The floor-field is considered as virtual information for a specific position that influences the particle dynamics. Such models have successfully shown lane-formation in bidirectional counter flow in periodic boundary conditions [247–249]. In between a fluid phase and a complete cluster in the system, there is a distorted regime as well as a state where lanes of counterflow are formed in self-organization that has also been found in experimental studies [250]. The pedestrian interactions can become very complicated to mimic different scenarios such as evacuation [251].

A second floor-field approach does not use long-range interactions such as the anticipation of directions [252]. This idea is close to a local floor-field denoting a virtual trace left by particles walking over a particular site. The particle movement is modified by the floor-field found by a particle on that site. The effect is that particles tend to follow the *foot steps* of other particles [252]. The floor-field is increased by the presence of particles and decays over time towards neutral again, i.e. the floor-field, therefore, induces a memory in the system. In [252], lane-formation has been found in a corridor with periodic boundary conditions and a floor-field trace.

The experiments by Shima *et al.* [34] about kinesin leaving a trace on microtubules that affects the binding affinity of kinesin motors can be regarded as a realization of a floor-field mechanism in biology.

5.3 Chapter summary

In this chapter, driven lattice gases have been presented. They provide the framework for the modeling in the third project in this thesis, active and bidirectional intracellular transport by molecular motors in axons. The fundamental model that the studies of this chapter have been build on is the TASEP.

In the first part, I reviewed unidirectional exclusion processes. After introducing the TASEP, additional rules can tune the exclusion process towards the biological system of motor-based transport. Langmuir kinetics in the bulk model the attachment and detachment of molecular motors on MTs. Furthermore, defects and local irregularities have been discussed as well as conservation of particles. For these models, it is then possible to estimate the flux and particle densities on the lattice. The flux is thereby not depending on the system size. However, this independence is not guaranteed in a non-Markovian version of the TASEP. Instead of exponentially distributed hopping times, algebraically distributed times have been found to lead to fluxes that depend on the system size. Non-Markovian behavior can be expected if complex interactions

In the second part of this chapter, bidirectional exclusion processes have been discussed. Two species of particles walk in opposite directions on a quasi-one-dimensional lattice. Some kind of bypassing mechanism is needed for such a system to avoid total blockages. The first option discussed is a site-exchange mechanism on the lattice. Constant exchange probabilities lead to a stable constant flux from clusters which does only depend on local dynamics but not on the system size. The second option involves more than one lattice. The second lattice can model the cytosol around the MT, a second MT or a second protofilament. With a diffusive bypassing of unbound cargo, high local densities could be reduced, however only with large diffusivity. An alternative is to organize the transport of different species among the lattices, i.e., lane-formation. Unidirectional sub-systems can then transport efficiently without bidirectional collisions. Lane-formation has for example been observed when particle attraction has been introduced or when the track has been modified in floor-field models in pedestrian dynamics.

Chapter 6

Own work

Contents

6.1	Passive transport in treelike structures	74
6.1.1	Trapping in and escape from branched structures of neuronal dendrites	74
6.1.2	Unraveling the structure of treelike networks from first-passage times of lazy random walkers	76
6.2	Search processes in cell migration	78
6.2.1	Persistence-speed coupling enhances the search efficiency of migrating cells	78
6.3	Active bidirectional intracellular transport	79
6.3.1	Bidirectional non-Markovian exclusion processes	80
6.3.2	Self-organized lane formation in bidirectional transport of molecular motors	83

In this chapter, I will present the projects of this thesis. The results are either given as published or prefinal articles, which are attached in the appendix (Addendum I-V). Whereas the details can be found in the publications and manuscripts, this chapter sets the projects in context and relates the work with the literature review presented in chapter 4 and 5.

In the first project, the diffusive motion of small chemical signals in branched structures such as neuronal dendrites (see section 6.1) is considered. Diffusion is influenced by the confining environment of spiny and branched channels. In a random walk model on discrete networks, effective structural parameters have been related to the time that is needed to escape to the soma (first-passage time to root node). This problem is essentially a search problem in a complex geometry.

In section 6.2, the random walker search approach is adapted in order to describe the active motility patterns found in the migration of dendritic cells. The search efficiency is investigated by inducing a persistence-speed coupling for the random walker.

The third project focuses on intracellular cargo transport by molecular motors in the axon in section 6.3. It is combining the active motion with cargo-cargo interaction in a confining environment. Two principal approaches are investigated, a site-exchange TASEP and a multi-lane model.

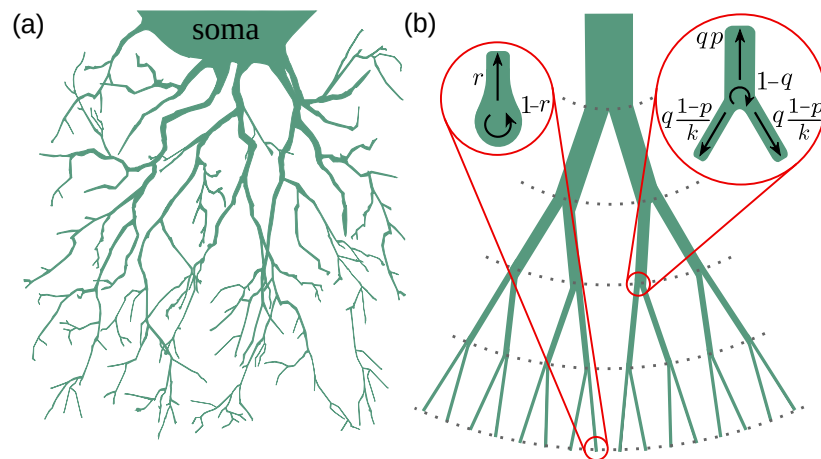


Figure 6.1: Modeling the treelike structure of dendrites by a Cayley tree. Details can be found in the **publication of Jose *et al.* in Biophysical J. 2018 (Addendum I)**. **a)** Exemplary structure dendritic trees on a nerve cell. **b)** Cayley tree with coordination number 3, a root node on top and five generations indicated by the dashed lines. Dynamical rules for particles at each node are shown in the red circles. Reprinted from *Biophysical Journal*, 115, R. Jose *et al.*, Trapping in and Escape from Branched Structures of Neuronal Dendrites, 2014-2025, Copyright (2018), with permission from Elsevier.

6.1 Passive transport in treelike structures

This section is about the random walk model on treelike structures. Theoretical background for RWs are given in section 3.2. Previous literature on diffusion in channels (spiny structures) is discussed in section 4.1.1 and 4.1.2. Random walks (RW) on networks are discussed in section 4.2 and mapping these RW to one-dimensional processes is presented in section 4.3. The model has been applied to two fields in this thesis. Results for diffusion in neuronal dendrites have been published in the **publication of Jose *et al.* in Biophysical J. 2018 (Addendum I)**. Results for the task of predicting hidden tree structures in the **publication of Shaebani *et al.* in Physical Review E 2018 (Addendum II)**.

6.1.1 Trapping in and escape from branched structures of neuronal dendrites

Biological background on diffusion in neuronal dendrites is presented in section 2.4.2. In this section, the focus is on modeling the influence of the key structural properties of dendritic trees on the transmission of chemical signals. The structure and changes in it are especially important since structural key parameters are affected during neurodegenerative diseases and aging (see section 2.4).

An estimate of transport properties such as the MSD and the escape time from a complete dendritic tree (first-passage times) has to include many aspects. Spines

vary in their shape and density, whereas dendritic channels change their diameter, branching morphology or extend (see section 2.4.2). Moreover, biological dendrites can have a heavily inhomogeneous structure (see figure 6.1 (a)). Hence, transport is performed in a complex environment. By explicitly modeling the three-dimensional structure of neuronal dendrites including the shape and variations in spines, simulations become computationally very expensive. Therefore, the modeled systems are rather small such as segments [17] or single spines [167] and a complete description of a dendritic tree is lacking.

In the **publication of Jose *et al.* in Biophysical J. 2018 (Addendum I)**, the tree morphology and the trapping of signals in spines are addressed in a stochastic coarse-grained model. Diffusive transport of ions and molecules in dendrites is modeled by random walks (see figure 6.1 (b)). The tree structure is more accessible with this approach for the following two reasons. First, analytical calculations can be done by mapping the diffusion on the tree to diffusion on a one-dimensional lattice (see section 4.2). The stochastic process is described by a system of master equations as presented in section 3.2 and 4.3. Second, numerical simulations are efficient in the coarse-grained model even for a complete treelike structure from the soma to the dead-ends of the dendrite.

The model for treelike structures is based on Cayley trees (see figure 6.1 (b)) which are discussed in section 4.2. Structural key parameters to describe the system are first, the depth d (or extend of the tree), second, the total bias parameter p that describes the chance to hop toward a lower or deeper layer of the tree, third, the trapping parameter q that defines the probability of a RW to be trapped inside spines along the segment of the tree and fourth, the trapping parameter r that gives the respective probability for being trapped at the dead-ends of the tree. In this homogeneous form, branching is regular and the parameters are constant among the nodes.

The results of the model have been deduced analytically and by numerical MC-simulations. By a set of master equations for the occupation probabilities of the RW for a given generation, first-passage times have been calculated (see section 3.2.3). Furthermore, MFPTs have been found analytically in a closed form for the regular trees. The result is consistent with equation 4.3 found by Skarpalezos *et al.* [188]. However, the calculations extend the result by trapping probabilities in spines q and dead-ends r .

The model is then calibrated towards measurements of neuronal dendrites. A crucial achievement of the publication is, therefore, that the model predicts of the influence of pathological changes on the chemical signal transmission. Each structural parameter has been mapped to geometrical properties as it is discussed in section 4.1. In a first step, a reference set of parameters has been found that resembles the healthy dendrite structure. In a second step, the reference set of parameters has been altered in order to incorporate pathological changes in the structure of neuronal dendrites during aging or neurodegenerative diseases. In Alzheimer's disease, for example,

dendrites show a smaller extent and loss of spines (see section 2.4.4) which results in shorter escape times from the dendritic tree into the soma (root node) in the model. As a result, the model can be calibrated to different changes during disease and predict the influence on the transmission of chemical signals.

Furthermore, simulations were performed in order to address irregularities in neuronal dendrites such as the variation in the density of spines (see section 2.4). The irregularities have been incorporated by two numerical approaches: First, by simulating explicit trees with randomly fluctuating structural parameters p , q and r on each node. Second, by constructing trees with sub-branches that have different extents for different generations, i.e. a variation of d for each dead-end.

In summary, a computationally efficient coarse-grained stochastic model for full dendritic tree structures has been developed in the **publication of Jose *et al.* in Biophysical J. 2018 (Addendum I)**. For homogeneous trees, analytical results have been found for the MFPT to reach the root node, which means to escape the tree towards the cell soma. Calibrating the effective structural parameters to healthy or diseased dendrites enables the study to relate diffusive transport to structural changes from specific diseases. Furthermore, structural irregularities have been addressed by MC-simulations in order to measure MFPTs and densities of signals in a more realistic structure.

6.1.2 Unraveling the structure of treelike networks from first-passage times of lazy random walkers

The second application of the RW model on treelike structures is presented in the **publication of Shaebani *et al.* in Physical Review E 2018 (Addendum II)**. The modeling approach allows it to generalize it for different tree-structures. In this section, I present how the model that is used to find escape times from neuronal dendrites is adapted to predict the hidden structure of a regular tree by measuring MFPTs of random walkers. The essential difference is that here, the waiting probability is controlled by random walkers. In contrast, for modeling neuronal dendrites, the waiting probability has been associated with trapping in spines which is controlled by the environment. A RW that has a tendency to wait on a node is here called *lazy* random walkers.

In section 4.4, several examples are given in which the dynamics of diffusive motion is used to determine an underlying structure. Foam structure, for instance, has been evaluated by diffusive light propagation [192] and permeability of a heterogeneous multi-component system [191] has been investigating.

In the setup of the **publication of Shaebani *et al.* in Physical Review E 2018 (Addendum II)**, only the root node and the number of leaves are known. The structural parameters defining the tree, i.e. the coordination number k and depth L of the tree, are unknown. One can think of a tree hidden in a black box (see figure 6.2). A given number of leaves can result from several combinations of $\{k, L\}$. This means that the tree is not uniquely determined by the number of leaves.

The method to determine the missing information is as follows: Random walkers

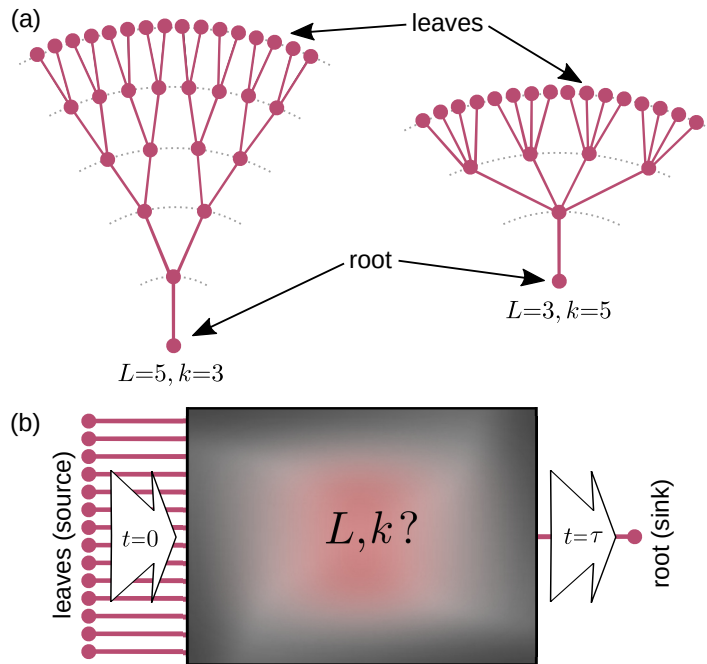


Figure 6.2: Schematic drawing regular treelike structures that are hidden in a black box. **a)** Two Cayley trees that have an equal number of leaves but differ in structure because of different coordination numbers k and depths L . **b)** Only the number of leaves and the root node are known, whereas the branching structure is hidden. Reprinted from Physical Review E, 98, M. R. Shaebani *et al.*, Unraveling the structure of treelike networks from first-passage times of lazy random walkers, Copyright (2018), with permission from American Physical Society.

are inserted at the leaves of the tree, stochastically move between nodes with a given waiting probability and eventually reach the root node that acts as a sink (see figure 6.2 (b)). The time between insertion and escape is measured as the first-passage time. From the relation between the MFPT and structural parameters, however, it is not possible to simply calculate the set $\{k, L\}$ since the equation is underdetermined. A single measurement of a MFPT fits to several possible solutions for the treelike structure that sit on a line in the $k - L$ space. This means the method has to be further developed to get all information.

This problem is solved by having two ensembles of random walkers with different laziness. As a result, the two lines in the $k - L$ space can be compared and the intersection of both solutions uniquely determines the set of parameters k and L of the network structure.

In addition to this two-point measurement method, the results are tested for variations in the parameter space of L and k . Similar to the version for neuronal dendrites, an effective hopping bias p (generated by the coordination number and additional weighting the branches as discussed in section 4.4) has been introduced. Parameters p and L were allowed to fluctuate around mean values. Similarly, fluctuations in

laziness are considered. From these simulations in irregular systems, the capability of the model to determine the hidden structure has been investigated if defects are included in the hidden structure.

All in all, a method has been discussed that enables to predict a hidden tree structure by measuring transport properties of random walkers moving on the tree in the **publication of Shaebani *et al.* in Physical Review E 2018 (Addendum II)**. By tuning the waiting probability, different measurements of random walks on a regular tree can give a unique and analytically derived prediction of the structural key parameters, i.e., the depth of the tree and the coordination number. By MC-simulations, it has been investigated how far the prediction based on regular trees is applicable to irregular trees.

6.2 Search processes in cell migration

So far, I discussed the use of the random walk model on a Cayley tree. Random walks were performed until they eventually reach the root node to escape. The root node works as a target in the search process. Also in this project, a search problem is formulated. Here, the work is inspired by the migration of dendritic cells searching for pathogens (see section 2.5). The theoretical background is again given in section 3.2. Furthermore, previous literature of search processes, persistent random walks, and cell migration is presented in section 4.5. A detailed description of the work and results of the following project is given in the **manuscript of Shaebani *et al.* (Addendum III)**. Methods shown in the manuscript are experimental and theoretical.

6.2.1 Persistence-speed coupling enhances the search efficiency of migrating cells

The motility of dendritic cells (DCs) differs heavily between different environments [11]. For this reason, the theoretical modeling of this project concentrates on the experimental setup that allows free movement by generating friction between two parallel planes as discussed in the manuscript. In contrast to the diffusive transport in the treelike structures, cell migration can change the speed and shows an internal persistence. This persistence is expected to result from the polarization state of the cell (see sections 2.5 and 4.5). In particular, a correlation has been found between cell speed and persistence [23,24].

In the manuscript, the persistence-speed coupling has been confirmed by *in vitro* experiments. The experimental trajectories expose that coupling decreases the search time of cells for randomly distributed virtual targets. These results motivate the theoretical modeling by leaving it unclear how a persistence-speed coupling influences search efficiency. In the manuscript, a search problem is formulated on a two-dimensional lattice. Typical search problems focus on optimizing the search (MFPT) as a function of one or more of the involved parameters [21, 253–256], such as persistence [21] but not the correlation between them. The objective of the work in the manuscript is the following: A new class of search problems is formulated where the

coupling between persistence and speed is varied in order to minimize the MFPT to find a target.

By a master equation approach, similar to the RWs on trees, an analytical relation has been derived that links the MFPT to the mean persistence length and the correlation strength between speed and persistence. The results are compared to numerical results from MC-simulations. In the numerical part, the RW has, in addition to the persistence-speed coupling, a speed-autocorrelation (see section 3.1.2 for sampling methods). For a low mean persistence, the coupling leads to smaller MFPTs, whereas for a high mean persistence, the effect is reversed. In the manuscript, a further discussion of parameters is given such as the range of the persistence-speed coupling.

Finally, in the manuscript **manuscript of Shaebani *et al.* (Addendum III)**, a new class of search problems is investigated. It is motivated by experimental findings that dendritic cells show a persistence-speed coupling which is able to reduce search time in the analysis of the manuscript. In the stochastic model of a migrating cell, this coupling has been incorporated. Results show that this coupling can decrease the search time if the mean persistence is low compared to the system size. This result has been found analytically for a linear coupling between persistence and speed. For a correlation between persistence and speed, as well as autocorrelated speeds, the model has been confirmed by MC-simulations.

6.3 Active bidirectional intracellular transport

An important difference between the diffusive motion of chemical signals in dendrites and the migration of cells is that the signals diffuse passively but cell migration is an active process, i.e. the supply of energy is needed. However, both processes have been described by stochastic modeling and in particular, both processes can lead to directed motion.

As discussed in chapter 2, intracellular transport can be carried out passively by diffusion or actively by driven motor proteins. I focus on active, bidirectional motor-driven transport on microtubule networks in the axon. The stochastic motion of molecular motor proteins needs a supply of ATP in order to move with the directed motility pattern along the MT (see section 2.2).

This transport is however very much influenced by the network and its environment [3]: First, the MT network is constantly rebuilding and changing its structure in the process of dynamic instability (see section 2.1). Second, there is a large class of MAPs that have an impact on the dynamics and structure of MTs and motor-filament interaction (see section 2.2.3). Third, the assumption that particles can be regarded independently that has been made for the diffusion of chemical signals is highly questionably for the transport of large cargoes. The spatial extension, as found in motor-driven transport of vesicles or organelles, indicates that cargo-cargo interactions, as well as interactions with the crowded and highly confining environment in the axon, play a crucial role (see section 2.4.1). In addition, motor-driven transport is very often carried out bidirectionally along MTs (see section 2.3. Hence, interacting

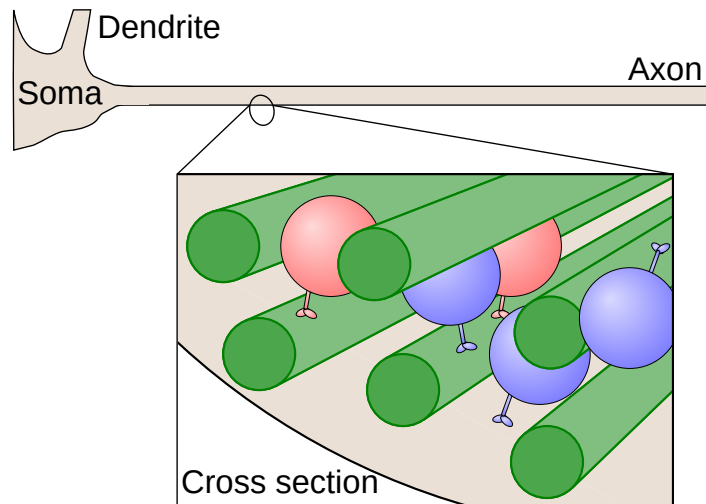


Figure 6.3: Schematic drawing of motor-driven cargo transport in the axon. In the cross section, minus directed motor-cargo complexes are red, plus directed ones blue. The narrow MT network is colored green. Reprinted from the **manuscript of Jose *et al.* (Addendum V) (2020)**, Self-organized lane-formation in bidirectional transport of molecular motors.

particles eventually meet and collide if the transport is not organized in separated sub-systems. The spatial interaction of cargoes should, therefore, be considered in a model. The crowded environment is indicated in the schematic drawing in figure 6.3.

Transport of interacting particles in (quasi) one-dimensional systems is often modeled by exclusion processes. The theoretical background for exclusion processes and a review of relevant literature for stochastic transport are presented in chapter 5. First unidirectional exclusion processes are examined and then adapted to bidirectional systems. Two general approaches have been made for efficient bidirectional transport. First bypassing mechanisms such as site-exchange and second, organization of transport in sub-systems. Both approaches have been addressed in this thesis.

In this section, I first discuss a model that focuses on a site-exchange mechanism with respect to cargo-cargo interactions. The results have been published in the **publication of Jose *et al.* in JSTAT 2020 (Addendum IV)**. Afterward, the second approach is addressed in a multi-lane model in which single lanes can act as a sub-system. Here, the objective is to find a stable mechanism for lane-formation in bidirectional transport applicable to intracellular transport. The results of this model are outlined in the **manuscript of Jose *et al.* (Addendum V)**.

6.3.1 Bidirectional non-Markovian exclusion processes

A standard model of interacting particles in bidirectional transport is the two-species TASEP with site-exchange. Variations of this model have been discussed in section 5.2.1. For site-exchange processes that are slower than free hopping particles, typi-

cally clusters and traffic jams have been observed [27, 239]. It has been found that the particle flux emerging from a cluster, and, as a consequence, the overall flux in the system is not depending on the system size. It is fully determined by the local exchange rate in such a model with site-exchange [27, 238]. An alternative approach does not use site-exchange on the track but binding and unbinding of motors (Langmuir kinetics) along the track [217, 218]. This quasi-one-dimensional system can also lead to a bypassing mechanism of unbound particles diffuse around bound particles in bidirectional transport [225–227]. For particles that have to diffuse around clusters, the flux has been shown to depend on the system size [25]. The contrasting results of size-independent flux in a site-exchange and a size-dependent flux in systems describing the biological situation in more detail question the applicability of a site-exchange in the biological set up.

The possibility to use a site-exchange mechanism as a coarse-grained point of view is, however, a favorable idea. Similar to the description of diffusion in neuronal dendrites discussed above, the abstract modeling of interactions allows efficient simulation performances. This is crucial in extended systems which already for small densities include many particles. An alternative is to modify the site-exchange dynamics so that it suits better with complex interactions.

Since the Markovian description of site-exchange is questionable, a non-Markovian model is motivated by the assumption that a strong interaction with the environment induces memory effects [14]. Such an approach has for instance been studied in the context of signal trapping in spines [15], where the complicated diffusion in the comb-like spine was approximated by a non-Markovian escape process. Similar in glass theory, a particle is considered to be trapped inside a cage created by neighbor particles which eventually can lead to non-Markovian escape times [181, 235] (see section 3.3). The objective of this section is, therefore, to use a non-Markovian description for exchange times instead of the Markovian approach with exponential times.

The analysis started with a three-state version. Each site is occupied by a plus-particle (walking toward the plus-end of the filament), a minus-particle or is empty (see figure 6.4). Also in this model, particle clusters determine the flux for the full system such as in Markovian models. Therefore, we focus on the clusters and go over to a pure two-state system in which vacancies are neglected.

In the **publication of Jose *et al.* in JSTAT 2020 (Addendum IV)**, the non-Markovian two-species exclusion process is studied. The work is based on the publications by Concannon *et al.* [236] and Khoromskaia *et al.* [237] in which unidirectional non-Markovian exclusion processes are studied (see section 5.1.6). The exchange time PDF used for exchange events of two particles of different species is modeled by an algebraic power law such as in Concannon *et al.* [236]

$$p(t) = \begin{cases} 0 & 0 < t < 1, \\ (\gamma - 1)t^{-\gamma} & t > 1. \end{cases} \quad (6.1)$$

As discussed in section 3.3, for a given step in the sampling algorithm of a non-Markovian TASEP, renewing times (direct method) for not yet executed events is

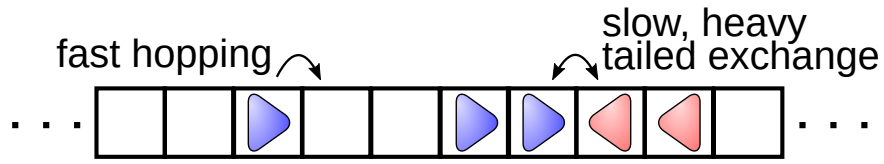


Figure 6.4: Schematic drawing of a bidirectional two-species exclusion process. Fast Markovian hopping processes are compared to a non-Markovian site-exchange between plus-particles (blue) and minus-particles (red). Exchange times are drawn from an algebraic heavy-tailed distribution (equation 6.1).

different from keeping the times (next reaction method). The residual waiting time distribution for exchange times coming from equation 6.1, will be different than $p(t)$ that governs fresh exchange times. The model is built with the next reaction method that keeps the event times and preserves the age of the process as it is implemented in Concannon *et al.* [236]. For a bidirectional exchange that keeps event times for each particle, two times are suggested for an exchange process, one from each particle. It is therefore needed to define rules for the exchange processes. In the **publication of Jose *et al.* in JSTAT 2020 (Addendum IV)**, four model types of different exchange rules are compared, i.e. *asymmetric particle based rule*, *particle-based symmetrical minimum rule*, *particle-based symmetrical maximum rule* and *site-based rule*. The site-based rule is essentially equivalent to the model by Khoromskaia *et al.* [237] due to particle hole symmetry and the asymmetric particle based rule to the work of Concannon *et al.* [236].

Results have been found for PDFs of effective exchange times by MC-simulations and analytically. To achieve analytical results, residual lifetimes are calculated as introduced in section 3.4. For the minimum (maximum) rule, PDF have been calculated by finding the PDF of the minimum (maximum) of two random times associated with neighboring particles.

The exponent of the effective exchange time PDF determines a transition between a regime in which the flux depends on the system size and a regime in which the flux is independent. This has been found by MC-simulations and is supported by the critical exponent $\gamma_{\text{crit}} = 3$ for which mean values of effective exchange-times diverge. The results are compared to the results of the unidirectional models. It shows that the bidirectional process can be mapped to the unidirectional version in most of the cases investigated.

To relate the study to the transport problem in axons, it is interesting to point out that there are two crucial values for the exponent. The first one is the critical value for which the transport transitions between size-dependence and independence $\gamma_{\text{crit}} = 3$. The second exponent has been found in the unidirectional TASEP [236, 237] (see section 5.1.6). For this exponent $\gamma_M \approx 3.5$, the non-Markovian TASEP with algebraic waiting times leads fluxes comparable to the Markovian case. Below this value, the flux is smaller, i.e. the exchange process is slower. Above, the flux is higher and the process is actually faster. Bypassing mechanism of motor-cargo complexes in the crowded environment are expected to be rather slow compared to free walking

velocities. The memoryless modeling for non-interacting walking is usually assuming Markovian dynamics. As a result, biologically relevant slow exchange processes should be modeled by exponents $\gamma < \gamma_M$. This, however, means that most transport bidirectional transport by a non-Markovian site-exchange is likely to lead to size-dependent fluxes for $\gamma < \gamma_{\text{crit}} = 3$.

In summary, a bidirectional non-Markovian exclusion process has been investigated. High interactions between transport and the confining environment are expected to cause non-Markovian dynamics. In the **publication of Jose *et al.* in JS-TAT 2020 (Addendum IV)**, different bidirectional realizations have been discussed and mapped to the unidirectional case. The results show that coarse-grained site-exchange models can lead to complex behavior and length-dependent transport. In the context of axonal transport, this may not be a problem for short systems but is highly problematic in the long extend of an axon. Next to studies such as Ebbinghaus *et al.* [25,244,257], the results of the paper can be seen as an additional indicator that, in intracellular transport by molecular motors in axons, a mechanism could be involved which leads to organization.

6.3.2 Self-organized lane formation in bidirectional transport of molecular motors

In order to find a biologically relevant mechanism that could lead to efficient bidirectional transport in axons, an organization in lanes of opposite transport directions is investigated here. This approach has previously been discussed in section 5.2 in the context of multi-lane models. Lane-formation has for example been observed in pedestrian transport [250] or for ants [258]. In bidirectional TASEP models, it has been found that simple symmetric switching between tracks is, however, not sufficient to generate lane-formation in a two-lane bidirectional TASEP [25,26]. Hence, for a biological system, it is required to search for relevant mechanisms which could provide asymmetry and organization leading to lane-formation.

Separation of oppositely directed transport among different MTs indeed has been observed in dendrites [31] and in the cilium [32] (see section 2.4.3). In dendrites, bundles of microtubules with the same polarization point in opposite directions. Such a system could transport cargo in both directions of the channel with only one type of motor [31]. In axons, however, this is not possible since all MTs are uniformly polarized [20]. The MT doublet structure in the cilium on which lane formation of motor-driven transport was found is organized in a way that the MTs appear in doublets. The two filaments (A and B microtubules) in such a doublet are equally polarized but can be differentiated by posttranslational modifications [32,259] so that molecular motors of different types might prefer one type over the other. A recent hypothesis is that the organization of MTs structure and functionality is strongly coordinated by the complex interactions between motor proteins, other MAPs and the filaments (see section 2.2.3 and *tubulin code* [29,30,43]).

For the homogeneous MT network inside the axon, not much is known about mechanisms that could support lane-formation. However, the interaction between

microtubules and motor proteins might generate a mechanism itself. Studies by Shima *et al.* [34] and Peet *et al.* [83] show that the tubulin lattice of MTs is elongated by kinesin motor proteins. Remarkably, kinesin motors have been reported to show a higher affinity to the elongated state of the MT lattice [34] (see section 2.2.3). This circle of kinesins modifying the MT and eventually attracting other kinesins generates a feedback mechanism, eventually leading to cooperative effects between kinesins [34]. The question is if such an effect is able to lead to lane-formation in active bidirectional transport in the axon.

In the model by Klumpp and Lipowsky [245], cooperative effects have been taken into account that have been reported for molecular motors before [84,85] (see section 4.2). In their approach, molecular motor particles attract other motors of the same species (direction) on the filament lattice by increasing the local binding probability on their neighbor sites. Also, they increase the chance to detach from the filament if neighbored motors have a different species. In the study, Klumpp and Lipowsky reported self-organization and symmetry breaking on a single lattice (see section 5.2.2). However, the experiments by Shima *et al.* [34] do not support the model's assumption that kinesins increase the run length of other kinesins since the affinity modification was only present for binding. Also, particle densities cannot be too small due to the short-ranged particle-particle interactions.

In the **manuscript of Jose *et al.* (Addendum V)**, the mechanism found by Shima *et al.* is implemented in a two-species, bidirectional exclusion process of two weakly coupled filament lattices. The affinity modification of motor proteins is governed by a floor-field which has been used to model pedestrian dynamics (see section 5.2.2). Particles in the model represent a coarse-grained motor-cargo complex. The floor-field allows that particles of both species leave a trace along the lattice tracks and therefore induces a memory effect. The trace then influences the binding affinity of other particles on each site. The modification strength is controlled by the affinity modification parameter μ . The detachment from the lattice is not affected by the floor-field. This realization of the affinity modification via the floor-field leads to long-range interactions emerging from the memory in the lattice. This approach is different from the short range modifications implemented in Klumpp and Lipowsky [245].

Stochastic realizations of the model are performed by MC-simulations and the stationary state is approximated by a mean-field analysis (see section 5.1.1). Above a critical modification parameter μ_{crit} , the particles self-organize into lanes of opposed stable transport in the stationary state in the simulations. It is remarkable that the mean-field analysis neglects the particle correlations along the filament axis. However, it well predicts the critical parameter μ_{crit} found in the simulations. In the mean-field model, a pitchfork bifurcation is found at the critical value where the system state changes from a symmetric distribution of the plus directed and minus directed particles to an asymmetric particle distribution.

In the manuscript, the range of densities for which lane-formation is observed is shown in fundamental diagrams. The maximum densities that support lane-formation depend on the modification parameter. However, the length independence of the flux was robust in the observed parameter regime. This means that transport

was stable on the length scale of MTs in axons.

Note that the self-organized affinity modification has been reported for kinesin [34] but not for dynein motors to my knowledge. In the **manuscript of Jose *et al.* (Addendum V)**, the influence of the motor asymmetry is investigated. It has been found that plus directed and minus directed particles do not have to be symmetric, i.e. smaller affinity modifications for minus-particles can still lead to lane-formation. However, the simulations and the mean-field analysis showed that the modification of only plus-particles is not sufficient for self-organized lane formation.

Finally, the **manuscript of Jose *et al.* (Addendum V)** addresses the question of how bidirectional intracellular transport by molecular motors can be efficient. A self-organized mechanism that modifies the binding affinity of particles by leaving a trace on the filament has been motivated by the experiments by Shima *et al.* [34]. In the stochastic model, the mechanism did lead to symmetry breaking and lane-formation. Results have been found for a mean-field analysis and MC-simulations. By the lane-formation, stable bidirectional transport has been established in the system. The results indicate that the complex interactions between MTs, molecular motors, and other MAPs might lead to efficient bidirectional intracellular transport.

Chapter 7

Conclusion & Outlook

In this thesis, applications for stochastic modeling of transport processes in cell biology have been presented. The work can be separated into three main topics, i.e. random walks on a treelike network such as diffusion in neuronal dendrites, stochastic description of cell migration and bidirectional intracellular transport on MT networks in axons. Whereas results are discussed in detail in the publications and manuscripts (Addendum I-V), this chapter summarizes the main conclusions from a more general point of view.

Within the first project, a direct link between structural characteristics of dendrites and the performance of diffusive signal transmission has been established in the **publication of Jose *et al.* in Biophysical J. 2018 (Addendum I)**. The random walker model on treelike structures provides an analytic framework for homogeneous trees, which is supported by MC-simulations for irregularities along the tree. In the search problem, random walks escape the soma by finding the root-node of the network. From the thickening of channels, trapping in spines and dead-ends, and the depth of the tree, an effective coarse-grained stochastic approach has been developed for the complex environment. The model enables an efficient description of a full neuronal dendrite, which was not available in literature before. The link between the coarse-grained model on networks and explicit, three-dimensional spiny channels has been established by calibrating structural parameters to the parameterized geometry. Knowledge about the structural changes during disease progressions enables not only to investigate transport in a healthy dendrite but, furthermore, to compare transport in dendrites affected by various diseases.

The link between structure parameters and transport properties has also been considered in the opposite scenario. From measuring MFPTs of lazy random walkers hopping on a hidden treelike network, the structure of the network has been predicted in the **publication of Shaebani *et al.* in Physical Review E 2018 (Addendum II)**. By comparing two ensemble measurements of different laziness, the structures have been uniquely determined. Thereby the method of controlling diffusivity and waiting probability of the random walkers is experimentally possible and easier to access than alternatively using noisy higher moments. Also in this application, the stability of the model predictions against structural inhomogeneities has been analyzed in the publication.

In the second project, the random walk method has further been used on the larger scale to describe complete cell trajectories. In the **manuscript of Shaebani *et al.* (Addendum III)**, the search strategy of dendritic cells in a quasi-two-dimensional confined environment has been investigated. The correlation between speed and persistence found for dendritic cells [23,24] has been confirmed in the manuscript. In the theoretical model, the phase space of persistence-speed and speed auto-correlations has been analyzed. The study invents a new kind of search problem in which search times are minimized by varying the correlation strength of two essential parameters rather than varying the parameters themselves. In the analysis of the experimental trajectories and the theoretical model, the correlation lead to increased search times if the average persistence is high. However in the biologically relevant regime of low average persistence, the search efficiency was enhanced.

Finally, the third project deals with interacting particles in bidirectional transport on MT networks in axons. Similar to the diffusion on treelike structures, the environment of the transport heavily influences the particle dynamics. However, due to the larger spatial extension of the motor-driven cargoes and the strong confinement in axons, it is required to include particle-particle interactions in the description. The quasi-one-dimensional system with particle volume exclusion has been modeled by variations of the class of TASEP models in order to investigate how efficient bidirectional transport in the axon can be realized. Two modeling approaches have been proposed in the literature, i.e. site-exchange and organization of transport in subsystems. In this project, both approaches have been used to build models for the specific axonal transport environment.

The **publication of Jose *et al.* in JSTAT 2020 (Addendum IV)** deals with several variants of a non-Markovian version of a bidirectional site-exchange TASEP. It has been investigated which requirements for an effective exchange process, independent of how it is realized in detail, have at least to be given in order to lead to efficient transport. Here, it has been shown that the efficiency of the exchange process determines the homogeneity and efficiency of the transport. Remarkably, the bidirectional version can be mapped to a simpler process, a method that is often used in theoretical physics. The bidirectional process shows the same universal behavior as the unidirectional versions [236,237], i.e. it holds $\gamma_{\text{crit}} = 3$ in both cases. At the critical exponent, a transition between a traffic jam state in which flux depends on the system size and a free-flowing state which is independent of system size has been found.

The result of size-dependent transport is consistent with results found in Ebbinghaus *et al.* [25,244]. The density fluctuations leading to traffic jams might be reduced if diffusivity is high [25]. In the crowded environment of axons, this is however not likely. As discussed before in chapter 5 and chapter 6, it is questionable how a size-dependent flux can lead to efficient transport if the environment is as crowded as in the axon. The **publication of Jose *et al.* in JSTAT 2020 (Addendum IV)** further indicates that there might be an alternative mechanism involved in intracellular transport.

The second approach has been shown to provide such an alternative by organizing

transport in sub-systems as it can be seen in nature [31, 32]. Lane-formation can be achieved by short ranged particle-particle interactions [245] or with the floor-field approach used in the **manuscript of Jose *et al.* (Addendum V)**. The study, shows a stable mechanism for self-organized lane-formation and efficient bidirectional transport under strong confinement, which is based on the affinity modification for kinesin [34]. Even if it is not totally clear how the mechanism based on PTM, molecular motors and other MAPs is realized in detail, the model proves that it can lead to a self-organization of stable transport. The lane-formation has been found in MC-simulations of the stochastic model and was retrieved in an analytical mean-field model, both finding the same critical affinity modification. Symmetry-breaking is stable against density fluctuations along the filament. The results show an organization in lanes for a combination of low densities on the filament and low diffusivity for unbound cargoes. For densities in which site-exchange already leads to traffic jams, lane-formation can still provide coexistence of stable, efficient transport in both directions on a length scale of several micrometers. Finally, the results indicate that a self-organized bidirectional transport is in principle possible to obtain by PTM on the MTs.

The models developed in this thesis have been applied to transport processes with the focus on cell biology. They can further be adapted or combined in order to address future questions.

The model of random walkers networks, for example, does not have to be limited to treelike structures but could also be adjusted to more complex network, which, for example, include loops. Furthermore, interactions, such as exclusion, of random walkers could be considered. Actively driven particles can be combined with diffusive transport, for example, for chemical signals inside vesicles or organelles [35, 260]. By actively transporting sources of chemical signals to different locations in the dendrite, there could arise interactions between the different transport mechanisms. The active transport could also be included in the master equations of the random walker model by adding inputs and persistency. For continual work with the random walker model on treelike structures, it would be interesting to incorporate real dendrite structures as an inhomogeneous network. Images of dendrites could be parameterized specifically so that the random walk model can give results for the example structures.

Volume exclusion and complex environments is also interesting in the context of cell migration. There might be different results for the optimal search strategy in the presence of complex interactions with the cell's environment and other cells.

For lane-formations inside neuronal axons, modeling would benefit from a deeper understanding of the microscopic processes. The interactions between kinesin and tubulin in the MT lattice and eventually the cooperative effects for the tubulin defects in the network are still poorly understood. In addition, *in vitro* experiments could show if a similar affinity modification mechanism can be found for dynein motors and eventually if a lane-formation can be observed in an experiment with kinesin and dynein motors. Also, filament dynamics could play a role in the initializing

process. A growing filament might favor plus-particles in the floor-field model so that thereby symmetry breaking could be supported even more. For open boundary conditions, the dynamics in exclusion processes such as the TASEP [207, 211, 213] are strongly affected by the boundaries. For intracellular transport, it would be important to understand the intersection regions between cell filaments. It is for example known that transport pauses at MT intersections [3]. A better understanding of the dynamics in these regions would be crucial for introducing biologically relevant boundary conditions.

All in all, the results developed in this work focus on different transport processes in cell biology. Mechanisms have been investigated that determine search and transport efficiency. The principle effects of the respective environment of the transport has been shown to heavily affect its efficiency by traps, blockages or organization. However, the environment of intracellular transport is very complex, so that an even broader but also deeper knowledge would be desired in the future. The long term goal would be to gain deeper understanding in these transport processes in order to know which requirements are needed for efficiency in search processes and intracellular transport. With this knowledge, studies can contribute to the research of disease progressions related to the transport processes.

Bibliography

- [1] Christopher Jarzynski. Diverse phenomena, common themes. *Nature Physics*, 11(2):105–107, 2015.
- [2] Ronald D Vale. The molecular motor toolbox for intracellular transport, feb 2003.
- [3] Shaul Yogev, Roshni Cooper, Richard Fetter, Mark Horowitz, and Kang Shen. Microtubule Organization Determines Axonal Transport Dynamics. *Neuron*, 92(2):449–460, 2016.
- [4] Jeffrey J Nirschl, Amy E Ghiretti, and Erika L F Holzbaur. The impact of cytoskeletal organization on the local regulation of neuronal transport. *Nature Reviews Neuroscience*, 18(10):585–597, 2017.
- [5] Kurt J. De Vos, Andrew J. Grierson, Steven Ackerley, and Christopher C.J. Miller. Role of Axonal Transport in Neurodegenerative Diseases. *Annual Review of Neuroscience*, 31(1):151–173, 2008.
- [6] Stéphanie Millecamps and Jean Pierre Julien. Axonal transport deficits and neurodegenerative diseases. *Nature Reviews Neuroscience*, 14(3):161–176, 2013.
- [7] Donna L. Smith, Julio Pozueta, Bing Gong, Ottavio Arancio, and Michael Shelanski. Reversal of long-term dendritic spine alterations in Alzheimer disease models. *Proceedings of the National Academy of Sciences of the United States of America*, 106(39):16877–16882, 2009.
- [8] Tara L. Spires, Melanie Meyer-Luehmann, Edward A. Stern, Pamela J. McLean, Jesse Skoch, Paul T. Nguyen, Brian J. Bacskai, and Bradley T. Hyman. Dendritic spine abnormalities in amyloid precursor protein transgenic mice demonstrated by gene transfer and intravital multiphoton microscopy. *Journal of Neuroscience*, 25(31):7278–7287, 2005.
- [9] Paul C. Bressloff and Jay M. Newby. Stochastic models of intracellular transport. *Reviews of Modern Physics*, 85(1):135–196, 2013.
- [10] Cecile Appert-Rolland, Maximilian Ebbinghaus, and Ludger Santen. Intracellular transport driven by cytoskeletal motors: General mechanisms and defects. *Physics Reports*, 593:1–59, 2015.

- [11] Mélina L. Heuzé, Pablo Vargas, Mélanie Chabaud, Maël Le Berre, Yan Jun Liu, Olivier Collin, Paola Solanes, Raphaël Voituriez, Matthieu Piel, and Ana Maria Lennon-Duménil. Migration of dendritic cells: Physical principles, molecular mechanisms, and functional implications. *Immunological Reviews*, 256(1):240–254, 2013.
- [12] William O. Hancock. Bidirectional cargo transport: Moving beyond tug of war. *Nature Reviews Molecular Cell Biology*, 15(9):615–628, 2014.
- [13] Edward A. Codling, Michael J. Plank, and Simon Benhamou. Random walk models in biology. *Journal of the Royal Society Interface*, 5(25):813–834, 2008.
- [14] T. Guérin, N. Levernier, O. Bénichou, and R. Voituriez. Mean first-passage times of non-Markovian random walkers in confinement. *Nature*, 534(7607):356–359, 2016.
- [15] Sergei Fedotov and Vicenç Méndez. Non-Markovian model for transport and reactions of particles in spiny dendrites. *Physical Review Letters*, 101(21):1–4, 2008.
- [16] Remy Kusters, Lukas C. Kapitein, Casper C. Hoogenraad, and Cornelis Storm. Shape-induced asymmetric diffusion in dendritic spines allows efficient synaptic AMPA receptor trapping. *Biophysical Journal*, 105(12):2743–2750, dec 2013.
- [17] Fidel Santamaria, Stefan Wils, Erik De Schutter, and George J. Augustine. Anomalous Diffusion in Purkinje Cell Dendrites Caused by Spines. *Neuron*, 52(4):635–648, nov 2006.
- [18] Z. Schuss, A. Singer, and D. Holcman. The narrow escape problem for diffusion in cellular microdomains. *Proceedings of the National Academy of Sciences of the United States of America*, 104(41):16098–16103, 2007.
- [19] P. C. Bressloff and B. A. Earnshaw. Diffusion-trapping model of receptor trafficking in dendrites. *Physical Review E - Statistical, Nonlinear, and Soft Matter Physics*, 75(4):1–7, 2007.
- [20] Walter P. Alberts B., Johnson A., Lewis J., Raff M., Roberts K. *Molecular Biology of Bruce the cell*. 2002.
- [21] Vincent Tejedor, Raphael Voituriez, and Olivier Bnichou. Optimizing persistent random searches. *Physical Review Letters*, 108(8):1–5, 2012.
- [22] Luiza Stankevics, Nicolas Ecker, Emmanuel Terriac, Paolo Maiuri, Rouven Schoppmeyer, Pablo Vargas, Ana Maria Lennon-Duménil, Matthieu Piel, Bin Qu, Markus Hoth, Karsten Kruse, and Franziska Lautenschläger. Deterministic actin waves as generators of cell polarization cues. *Proceedings of the National Academy of Sciences of the United States of America*, 117(2):826–835, 2020.

-
- [23] Paolo Maiuri, Emmanuel Terriac, Perrine Paul-Gilloteaux, Timothée Vignaud, Krista McNally, James Onuffer, Kurt Thorn, Phuong A. Nguyen, Nefeli Georgoulia, Daniel Soong, Asier Jayo, Nina Beil, Jürgen Beneke, Joleen Chooi Hong Lim, Chloe Pei-Ying Sim, Yeh Shiu Chu, Andrea Jiménez-Dalmaroni, Jean François Joanny, Jean Paul Thiery, Holger Erfle, Maddy Parsons, Timothy J. Mitchison, Wendell A. Lim, Ana Maria Lennon-Duménil, Matthieu Piel, and Manuel Théry. The first World Cell Race, sep 2012.
- [24] Paolo Maiuri, Jean François Rupprecht, Stefan Wieser, Verena Ruprecht, Olivier Bénichou, Nicolas Carpi, Mathieu Coppey, Simon De Beco, Nir Gov, Carl Philipp Heisenberg, Carolina Lage Crespo, Franziska Lautenschlaeger, Maël Le Berre, Ana Maria Lennon-Dumenil, Matthew Raab, Hawa Racine Thiam, Matthieu Piel, Michael Sixt, and Raphaël Voituriez. Actin flows mediate a universal coupling between cell speed and cell persistence. *Cell*, 161(2):374–386, apr 2015.
- [25] Maximilian Ebbinghaus and Ludger Santen. A model for bidirectional traffic of cytoskeletal motors. *Journal of Statistical Mechanics: Theory and Experiment*, 2009(3), 2009.
- [26] G Korniss, B Schmittmann, and R K P Zia. Long-range order in a quasi one-dimensional non-equilibrium three-state lattice gas. *Europhys. Letters*, 45:431, 1999.
- [27] M R Evans, D P Foster, C Godreche, and D Mukamel. Asymmetric exclusion model with two species: spontaneous symmetry breaking. *Journal of statistical physics*, 80(1-2):69–102, 1995.
- [28] Andreas Schadschneider, Debashish Chowdhury, and Katsuhiko Nishinari. *Stochastic transport in complex systems: from molecules to vehicles*. Elsevier, 2010.
- [29] Carsten Janke. The tubulin code: Molecular components, readout mechanisms, functions. *Journal of Cell Biology*, 206(4):461–472, 2014.
- [30] Sudarshan Gadadhar, Satish Bodakuntla, Kathiresan Natarajan, and Carsten Janke. The tubulin code at a glance. *Journal of Cell Science*, 130(8):1347–1353, 2017.
- [31] Roderick P. Tas, Anaël Chazeau, Bas M.C. Cloin, Maaike L.A. Lambers, Casper C. Hoogenraad, and Lukas C. Kapitein. Differentiation between Oppositely Oriented Microtubules Controls Polarized Neuronal Transport. *Neuron*, 96(6):1264–1271.e5, 2017.
- [32] Ludek Stepanek and Gaia Pigino. Microtubule doublets are double-track railways for intraflagellar transport trains. *Science*, 352(6286):721–724, 2016.
- [33] Daniel A. Fletcher and R. Dyche Mullins. Cell mechanics and the cytoskeleton. *Nature*, 463(7280):485–492, 2010.

- [34] Tomohiro Shima, Manatsu Morikawa, Junichi Kaneshiro, Taketoshi Kambara, Shinji Kamimura, Toshiki Yagi, Hiroyuki Iwamoto, Sotaro Uemura, Hideki Shigematsu, Mikako Shirouzu, Taro Ichimura, Tomonobu M. Watanabe, Ryo Nitta, Yasushi Okada, and Nobutaka Hirokawa. Kinesin-binding–triggered conformation switching of microtubules contributes to polarized transport. *Journal of Cell Biology*, 217(12):4164–4183, 2018.
- [35] Mei Yao Lin and Zu Hang Sheng. Regulation of mitochondrial transport in neurons, 2015.
- [36] Brenda L. Bloodgood and Bernardo L. Sabatini. Neuronal activity regulates diffusion across the neck of dendritic spines. *Science*, 310(5749):866–869, 2005.
- [37] Sonia Cohen and Michael E. Greenberg. Communication Between the Synapse and the Nucleus in Neuronal Development, Plasticity, and Disease. *Annual Review of Cell and Developmental Biology*, 24(1):183–209, 2008.
- [38] Jennifer L. Ross, M. Yusuf Ali, and David M. Warshaw. Cargo transport: molecular motors navigate a complex cytoskeleton. *Current Opinion in Cell Biology*, 20(1):41–47, 2008.
- [39] Michael A Welte. Bidirectional transport along microtubules, 2004.
- [40] Gwendalyn J. Randolph. Dendritic cell migration to lymph nodes: Cytokines, chemokines, and lipid mediators. *Seminars in Immunology*, 13(5):267–274, 2001.
- [41] Tim Worbs, Swantje I. Hammerschmidt, and Reinhold Förster. Dendritic cell migration in health and disease. *Nature Reviews Immunology*, 17(1):30–48, 2017.
- [42] Cecilia Conde and Alfredo Cáceres. Microtubule assembly, organization and dynamics in axons and dendrites. *Nature Reviews Neuroscience*, 10(5):319–332, 2009.
- [43] Carsten Janke and Jeannette Chloë Bulinski. Post-translational regulation of the microtubule cytoskeleton: Mechanisms and functions. *Nature Reviews Molecular Cell Biology*, 12(12):773–786, 2011.
- [44] Anna Akhmanova and Michel O Steinmetz. Tracking the ends: A dynamic protein network controls the fate of microtubule tips, 2008.
- [45] Kah Wai Yau, Sam F.B. VanBeuningen, Inês Cunha-Ferreira, Bas M.C. Cloin, Eljo Y. VanBattum, Lena Will, Philipp Schätzle, Roderick P. Tas, Jaap VanKrugten, Eugene A. Katrukha, Kai Jiang, Phebe S. Wulf, Marina Mikhaylova, Martin Harterink, R. Jeroen Pasterkamp, Anna Akhmanova, Lukas C. Kapitein, and Casper C. Hoogenraad. Microtubule minus-end binding protein CAMSAP2 controls axon specification and dendrite development. *Neuron*, 82(5):1058–1073, 2014.

- [46] Nobutaka Hirokawa, Yasuko Noda, and Yasushi Okada. Kinesin and dynein superfamily proteins in organelle transport and cell division. *Current Opinion in Cell Biology*, 10(1):60–73, feb 1998.
- [47] Robert Fletterick, Ron Vale, Elena Sablin, and Jon Kull. The design plan of kinesin motors. *FASEB Journal*, 11(9):745, 1997.
- [48] Günther Woehlke and Manfred Schliwa. Walking on two heads: The many talents of kinesin. *Nature Reviews Molecular Cell Biology*, 1(1):50–58, 2000.
- [49] Ronald D. Vale and Ronald A Milligan. The way things move: Looking under the hood of molecular motor proteins, 2000.
- [50] Adrian N Fehr, Charles L Asbury, and Steven M Block. Kinesin steps do not alternate in size. *Biophysical Journal*, 94(3):L20, 2008.
- [51] Arne Gennerich and Ronald D Vale. Walking the walk: how kinesin and dynein coordinate their steps, feb 2009.
- [52] Manfred Schliwa. *Molecular Motors*, pages 1160–1174. Springer Berlin Heidelberg, Berlin, Heidelberg, 2006.
- [53] Joe Howard. Molecular motors: Structural adaptations to cellular functions. *Nature*, 389(6651):561–567, 1997.
- [54] Arne Seitz and Thomas Surrey. Processive movement of single kinesins on crowded microtubules visualized using quantum dots. *EMBO Journal*, 25(2):267–277, 2006.
- [55] N. J. Carter and R. A. Cross. Mechanics of the kinesin step. *Nature*, 435(7040):308–312, 2005.
- [56] Andrzej A. Kasprzak and Łukasz Hajdo. Directionality of kinesin motors. *Acta Biochimica Polonica*, 49(4):813–821, 2002.
- [57] Elena P. Sablin, Ryan B. Case, Shirleko C. Dai, Cynthia L. Hart, Aaron Ruby, Ronald D. Vale, and Robert J. Fletterick. Direction determination in the minus-end-directed kinesin motor ncd. *Nature*, 395(6704):813–816, 1998.
- [58] Peter Höök and Richard B. Vallee. The dynein family at a glance. *Journal of Cell Science*, 119(21):4369–4371, 2006.
- [59] Anthony J. Roberts, Takahide Kon, Peter J. Knight, Kazuo Sutoh, and Stan A. Burgess. Functions and mechanics of dynein motor proteins. *Nature Reviews Molecular Cell Biology*, 14(11):713–726, 2013.
- [60] Julia R Kardon and Ronald D Vale. Regulators of the cytoplasmic dynein motor, 2009.

- [61] Gina A. Monzon, Lara Scharrel, Ludger Santen, and Stefan Diez. Activation of mammalian cytoplasmic dynein in multimotor motility assays. *Journal of Cell Science*, 132(4):1–9, 2019.
- [62] Z Wang, S Khan, and M P Sheetz. Single cytoplasmic dynein molecule movements: characterization and comparison with kinesin. *Biophysical Journal*, 69(5):2011–2023, 1995.
- [63] Roop Mallik, Brian C Carter, Stephanie A Lex, Stephen J King, and Steven P. Gross. Cytoplasmic dynein functions as a gear in response to load. *Nature*, 427(6975):649–652, 2004.
- [64] Samara L Reck-Peterson, Ahmet Yildiz, Andrew P Carter, Arne Gennerich, Nan Zhang, and Ronald D Vale. Single-Molecule Analysis of Dynein Processivity and Stepping Behavior. *Cell*, 126(2):335–348, 2006.
- [65] Jennifer L Ross, Karen Wallace, Henry Shuman, Yale E Goldman, and Erika L.F. Holzbaur. Processive bidirectional motion of dynein-dynactin complexes in vitro. *Nature Cell Biology*, 8(6):562–570, 2006.
- [66] Zhaohui Wang and Michael P Sheetz. One-dimensional diffusion on microtubules of particles coated with cytoplasmic dynein and immunoglobulins. In *Cell Structure and Function*, volume 24, pages 373–383, 1999.
- [67] Satish Bodakuntla, Anne Schnitzler, Cristopher Villablanca, Christian Gonzalez-Billault, Ivan Bieche, Carsten Janke, and Maria M Magiera. Tubulin polyglutamylation is a general traffic control mechanism in hippocampal neurons. *Journal of Cell Science*, (January):jcs.241802, 2020.
- [68] Szymon W. Manka and Carolyn A. Moores. Microtubule structure by cryo-EM: Snapshots of dynamic instability. *Essays in Biochemistry*, 62(6):737–751, 2018.
- [69] Carolyn A Moores, Ming Yu, Jun Guo, Christophe Beraud, Roman Sakowicz, and Ronald A Milligan. A mechanism for microtubule depolymerization by KinI kinesins. *Molecular Cell*, 9(4):903–909, 2002.
- [70] Carolyn A. Moores, Mylène Perderiset, Caroline Kappeler, Susan Kain, Douglas Drummond, Stephen J. Perkins, Jamel Chelly, Rob Cross, Anne Houdusse, and Fiona Francis. Distinct roles of doublecortin modulating the microtubule cytoskeleton. *EMBO Journal*, 25(19):4448–4457, 2006.
- [71] Kenneth G. Campellone and Matthew D. Welch. A nucleator arms race: Cellular control of actin assembly. *Nature Reviews Molecular Cell Biology*, 11(4):237–251, 2010.
- [72] Carolyn A Moores, Mylène Perderiset, Fiona Francis, Jamel Chelly, Anne Houdusse, and Ronald A Milligan. Mechanism of microtubule stabilization by doublecortin. *Molecular Cell*, 14(6):833–839, jun 2004.

- [73] Arne Seitz, Hiroaki Kojima, Kazuhiro Oiwa, Eva Maria Mandelkow, Young Hwa Song, and Eckhard Mandelkow. Single-molecule investigation of the interference between kinesin, tau and MAP2c. *EMBO Journal*, 21(18):4896–4905, 2002.
- [74] Ram Dixit, Jennifer L Ross, Yale E Goldman, and Erika L.F. Holzbaur. Differential regulation of dynein and kinesin motor proteins by tau. *Science*, 319(5866):1086–1089, 2008.
- [75] B Trinczek, A Ebner, E. M. Mandelkow, and E Mandelkow. Tau regulates the attachment/detachment but not the speed of motors in microtubule-dependent transport of single vesicles and organelles. *Journal of Cell Science*, 112(14):2355–2367, 1999.
- [76] A. Ebner, R. Godemann, K. Stamer, S. Illenberger, B. Trinczek, E. M. Mandelkow, and E. Mandelkow. Overexpression of tau protein inhibits kinesin-dependent trafficking of vesicles, mitochondria, and endoplasmic reticulum: Implications for Alzheimer’s disease. *Journal of Cell Biology*, 143(3):777–794, 1998.
- [77] Brigette Y. Monroy, Danielle L. Sawyer, Bryce E. Ackermann, Melissa M. Borden, Tracy C. Tan, and Cassandra M. Ori-Mckenney. Competition between microtubule-associated proteins directs motor transport. *Nature Communications*, 9(1):1–12, 2018.
- [78] V. V. Mustyatsa, A. V. Boyakhchyan, F. I. Ataulakhanov, and N. B. Gudimchuk. EB-family proteins: Functions and microtubule interaction mechanisms. *Biochemistry (Moscow)*, 82(7):791–802, 2017.
- [79] Rui Zhang, Gregory M. Alushin, Alan Brown, and Eva Nogales. Mechanistic origin of microtubule dynamic instability and its modulation by EB proteins. *Cell*, 162(4):849–859, aug 2015.
- [80] Gregory M. Alushin, Gabriel C. Lander, Elizabeth H. Kellogg, Rui Zhang, David Baker, and Eva Nogales. High-Resolution microtubule structures reveal the structural transitions in $\alpha\beta$ -tubulin upon GTP hydrolysis. *Cell*, 157(5):1117–1129, may 2014.
- [81] Szymon W. Manka and Carolyn A. Moores. The role of tubulin–tubulin lattice contacts in the mechanism of microtubule dynamic instability. *Nature Structural and Molecular Biology*, 25(7), 2018.
- [82] Rui Zhang, Benjamin LaFrance, and Eva Nogales. Separating the effects of nucleotide and EB binding on microtubule structure. *Proceedings of the National Academy of Sciences of the United States of America*, 115(27):E6191–E6200, 2018.

- [83] Daniel R. Peet, Nigel J. Burroughs, and Robert A. Cross. Kinesin expands and stabilizes the GDP-microtubule lattice. *Nature Nanotechnology*, 13(5):386–391, 2018.
- [84] Andrej Vilfan, Erwin Frey, Franz Schwabl, Manfred Thormählen, Young Hwa Song, and Eckhard Mandelkow. Dynamics and cooperativity of microtubule decoration by the motor protein kinesin. *Journal of Molecular Biology*, 312(5):1011–1026, 2001.
- [85] Albina Orlova and Edward H. Egelman. Cooperative rigor binding of myosin to actin is a function of F-actin structure, 1997.
- [86] Etsuko Muto, Hiroyuki Sakai, and Kuniyoshi Kaseda. Long-range cooperative binding of kinesin to a microtubule in the presence of ATP. *Journal of Cell Biology*, 168(5):691–696, 2005.
- [87] Robert H Miller and Raymond I. Lasek. Cross-bridges mediate anterograde and retrograde vesicle transport along microtubules in squid axoplasm. *Journal of Cell Biology*, 101(6):2181–2193, 1985.
- [88] A Ashkin, Karin Schütze, J M Dziedzic, Ursula Euteneuer, and Manfred Schliwa. Force generation of organelle transport measured in vivo by an infrared laser trap. *Nature*, 348(6299):346–348, 1990.
- [89] Naoko Mizuno, Shiori Toba, Masaki Edamatsu, Junko Watai-Nishii, Nobutaka Hirokawa, Yoko Y Toyoshima, and Masahide Kikkawa. Dynein and kinesin share an overlapping microtubule-binding site. *EMBO Journal*, 23(13):2459–2467, 2004.
- [90] Andrew P Carter, Joan E Garbarino, Elizabeth M Wilson-Kubalek, Wesley E Shipley, Carol Cho, Ronald A Milligan, Ronald D Vale, and I R Gibbons. Structure and Functional Role of Dynein’s Microtubule-Binding Domain. *Science*, 322(5908):1691 LP – 1695, dec 2008.
- [91] Olga I. Kahn and Peter W. Baas. Microtubules and Growth Cones: Motors Drive the Turn, jul 2016.
- [92] P W Baas, J S Deitch, M M Black, and G A Banker. Polarity orientation of microtubules in hippocampal neurons: Uniformity in the axon and nonuniformity in the dendrite. *Proceedings of the National Academy of Sciences of the United States of America*, 85(21):8335–8339, 1988.
- [93] M. Reza Shaebani, Aravind Pasula, Albrecht Ott, and Ludger Santen. Tracking of plus-ends reveals microtubule functional diversity in different cell types. *Scientific Reports*, 6(March):1–9, 2016.
- [94] A Brown, Y Li, T Slaughter, and M M Black. Composite microtubules of the axon: Quantitative analysis of tyrosinated and acetylated tubulin along individual axonal microtubules. *Journal of Cell Science*, 104(2):339–352, 1993.

-
- [95] J. Chen, Y. Kanai, N. J. Cowan, and N. Hirokawa. Projection domains of MAP2 and tau determine spacings between microtubules in dendrites and axons. *Nature*, 360(6405):674–677, 1992.
- [96] Elea Prezel, Auréliane Elie, Julie Delaroche, Virginie Stoppin-Mellet, Christophe Bosc, Laurence Serre, Anne Fourest-Lieuvin, Annie Andrieux, Marylin Vantard, and Isabelle Arnal. Tau can switch microtubule network organizations: from random networks to dynamic and stable bundles. *Molecular Biology of the Cell*, 29(2):154–165, jan 2018.
- [97] Jack Waters, Andreas Schaefer, and Bert Sakmann. Backpropagating action potentials in neurones: Measurement, mechanisms and potential functions, jan 2005.
- [98] D Bray. BRANCHING PATTERNS OF INDIVIDUAL SYMPATHETIC NEURONS IN CULTURE. 56:702–712, 1973.
- [99] Concha Bielza, Ruth Benavides-Piccione, Pedro López-Cruz, Pedro Larrañaga, and Javier Defelipe. Branching angles of pyramidal cell dendrites follow common geometrical design principles in different cortical areas. *Scientific Reports*, 4:1–7, 2014.
- [100] M. Rapp, I. Segev, and Y. Yarom. Physiology, morphology and detailed passive models of guinea-pig cerebellar Purkinje cells. *The Journal of Physiology*, 474(1):101–118, 1994.
- [101] Nelson Spruston. Pyramidal neurons: Dendritic structure and synaptic integration. *Nature Reviews Neuroscience*, 9(3):206–221, 2008.
- [102] Heike Hering and Morgan Sheng. <_DENDRITIC SPINES STRUCTURE DYNAMICS AND REGULATION-hering and shen.pdf>. *Nature Reviews Neuroscience*, 2(December):880–888, 2001.
- [103] Jun-ichi Tanaka, Yoshihiro Horiike, Masanori Matsuzaki, Takashi Miyazaki, Graham C. R. Ellis-Davies, and Haruo Kasai. Protein Synthesis and Neurotrophin-Dependent Structural Plasticity of Single Dendritic Spines Jun-ichi. *Science*, 319(5870):1683–1688, 2008.
- [104] Kaja Ewa Moczulska, Juliane Tinter-Thiede, Manuel Peter, Lyubov Ushakova, Tanja Wernle, Brice Bathellier, and Simon Rumpel. Dynamics of dendritic spines in the mouse auditory cortex during memory formation and memory recall. *Proceedings of the National Academy of Sciences of the United States of America*, 110(45):18315–18320, 2013.
- [105] Haruo Kasai, Masahiro Fukuda, Satoshi Watanabe, Akiko Hayashi-Takagi, and Jun Noguchi. Structural dynamics of dendritic spines in memory and cognition, mar 2010.

- [106] Ran Su, Changming Sun, Chao Zhang, and Tuan D. Pham. A novel method for dendritic spines detection based on directional morphological filter and shortest path. *Computerized Medical Imaging and Graphics*, 38(8):793–802, dec 2014.
- [107] Jan Tønnesen, Gergely Katona, Balázs Rózsa, and U. Valentin Nägerl. Spine neck plasticity regulates compartmentalization of synapses. *Nature Neuroscience*, 17(5):678–685, 2014.
- [108] Ruth Benavides-Piccione, Isabel Fernaud-Espinosa, Victor Robles, Rafael Yuste, and Javier Defelipe. Age-based comparison of human dendritic spine structure using complete three-dimensional reconstructions. *Cerebral Cortex*, 23(8):1798–1810, 2013.
- [109] I. Ballesteros-Yáñez, R. Benavides-Piccione, G. N. Elston, R. Yuste, and J. DeFelipe. Density and morphology of dendritic spines in mouse neocortex. *Neuroscience*, 138(2):403–409, jan 2006.
- [110] Yi Zheng, Jill Wildonger, Bing Ye, Ye Zhang, Angela Kita, Susan H. Younger, Sabina Zimmerman, Lily Yeh Jan, and Yuh Nung Jan. Dynein is required for polarized dendritic transport and uniform microtubule orientation in axons. *Nature Cell Biology*, 10(10):1172–1180, 2008.
- [111] K. m. Harris and P. Sultan. Variation in the number, location and size of synaptic vesicles provides an anatomical basis for the nonuniform probability of release at hippocampal CA1 synapses. *Neuropharmacology*, 34(11):1387–1395, 1995.
- [112] Lukas C. Kapitein, Max A. Schlager, Marijn Kuijpers, Phebe S. Wulf, Myrre van Spronsen, Frederick C. MacKintosh, and Casper C. Hoogenraad. Mixed Microtubules Steer Dynein-Driven Cargo Transport into Dendrites. *Current Biology*, 20(4):290–299, feb 2010.
- [113] Christophe Leterrier and Bénédicte Dargent. No Pasaran! Role of the axon initial segment in the regulation of protein transport and the maintenance of axonal identity, mar 2014.
- [114] Gorazd B Stokin, Concepción Lillo, Tomás L Falzone, Richard G Bruschi, Edward Rockenstein, Stephanie L Mount, Rema Raman, Peter Davies, Eliezer Masliah, David S Williams, and Lawrence S.B. Goldstein. Axonopathy and transport deficits early in the pathogenesis of Alzheimer’s diseases. *Science*, 307(5713):1282–1288, 2005.
- [115] D. M.A. Mann, P. Q. Sumpter, C. A. Davies, and P. O. Yates. Glycogen accumulations in the cerebral cortex in Alzheimer’s disease. *Acta Neuropathologica*, 73(2):181–184, 1987.

- [116] A D Cash, G Aliev, S L Siedlak, A Nunomura, H. Fujioka, X Zhu, A K Raina, H V Vinters, M Tabaton Johnson, A B, M Paula-Barbosa, J Avila, P K Jones Castellani, R J, M A Smith, and G Perry. Microtubule Reduction in Alzheimer's Disease and Aging Is Independent of Tau Filament Formation. *Am. J. Path.*, 162:1623, 2003.
- [117] D. P. Purpura, N. Bodick, K. Suzuki, I. Rapin, and S. Wurzelmann. Microtubule disarray in cortical dendrites and neurobehavioral failure. I. Golgi and electron microscopic studies. *Developmental Brain Research*, 5(3):287–297, nov 1982.
- [118] David A. Orner, Chia Chien Chen, Daniella E. Orner, and Joshua C. Brumberg. Alterations of dendritic protrusions over the first postnatal year of a mouse: an analysis in layer VI of the barrel cortex. *Brain structure & function*, 219(5):1709–1720, 2014.
- [119] Zdravko Petanjek, Miloš Judaš, Goran Šimić, Mladen Roko Rašin, Harry B.M. Uylings, Pasko Rakic, and Ivica Kostović. Extraordinary neoteny of synaptic spines in the human prefrontal cortex. *Proceedings of the National Academy of Sciences of the United States of America*, 108(32):13281–13286, 2011.
- [120] Julia Tsai, Jaime Grutzendler, Karen Duff, and Wen Biao Gan. Fibrillar amyloid deposition leads to local synaptic abnormalities and breakage of neuronal branches. *Nature Neuroscience*, 7(11):1181–1183, 2004.
- [121] Jaime Grutzendler, Kathryn Helmin, Julia Tsai, and Wen Biao Gan. Various dendritic abnormalities are associated with fibrillar amyloid deposits in Alzheimer's disease. *Annals of the New York Academy of Sciences*, 1097:30–39, 2007.
- [122] Tim Lämmermann, Jörg Renkawitz, Xunwei Wu, Karin Hirsch, Cord Brakebusch, and Michael Sixt. Cdc42-dependent leading edge coordination is essential for interstitial dendritic cell migration. *Blood*, 113(23):5703–5710, 2009.
- [123] Yosuke Harada, Yoshihiko Tanaka, Masao Terasawa, Markus Pieczyk, Katsuyoshi Habiro, Tomoya Katakai, Hanawa Suetsugu Kyoko, Kukimoto Niino Mutsuko, Tomoko Nishizaki, Mikako Shirouzu, Xuefeng Duan, Takehito Uruno, Akihiko Nishikimi, Fumiyuki Sanematsu, Shigeyuki Yokoyama, Jens V. Stein, Tatsuo Kinashi, and Yoshinori Fukui. DOCK8 is a Cdc42 activator critical for interstitial dendritic cell migration during immune responses. *Blood*, 119(19):4451–4461, 2012.
- [124] Sandrine Etienne-Manneville. Actin and microtubules in cell motility: Which one is in control? *Traffic*, 5(7):470–477, 2004.
- [125] Anna Huttenlocher, Rebecca R Sandborg, and Alan F Horwitz. Adhesion in cell migration. page 2013, 2013.

- [126] Bernhard Wehrle-Haller and Beat A Imhof. Actin, microtubules and focal adhesion dynamics during cell migration, jan 2003.
- [127] C. Ballestrem, B. Wehrle-Haller, B. Hinz, and B. A. Imhof. Actin-dependent lamellipodia formation and microtubule-dependent tail retraction control-directed cell migration. *Molecular Biology of the Cell*, 11(9):2999–3012, 2000.
- [128] Kathrin Schumann, Tim Lämmermann, Markus Brückner, Daniel F. Legler, Julien Polleux, Joachim P. Spatz, Gerold Schuler, Reinhold Förster, Manfred B. Lutz, Lydia Sorokin, and Michael Sixt. immobilized chemokine fields and soluble chemokine gradients cooperatively shape migration patterns of dendritic cells. *Immunity*, 32(5):703–713, may 2010.
- [129] Hugues Lelouard, Sandrine Henri, Béatrice De Bovis, Bénédicte Mugnier, Alexandre Chollat-Namy, Bernard Malissen, Stéphane Méresse, and Jean Pierre Gorvel. Pathogenic Bacteria and Dead Cells Are Internalized by a Unique Subset of Peyer’s Patch Dendritic Cells That Express Lysozyme. *Gastroenterology*, 138(1):173–184.e3, jan 2010.
- [130] Hugues Lelouard, Mathieu Fallet, Béatrice De Bovis, Stéphane Méresse, and Jean-Pierre Gorvel. Peyer’s patch dendritic cells sample antigens by extending dendrites through M cell-specific transcellular pores. *Gastroenterology*, 142(3):592–601.e3, mar 2012.
- [131] Julia Farache, Idan Koren, Idan Milo, Irina Gurevich, Ki Wook Kim, Ehud Zigmond, Glaucia C. Furtado, Sergio A. Lira, and Guy Shakhar. Luminal Bacteria Recruit CD103+ Dendritic Cells into the Intestinal Epithelium to Sample Bacterial Antigens for Presentation. *Immunity*, 38(3):581–595, mar 2013.
- [132] Melanie Chabaud, Melina L. Heuze, Marine Bretou, Pablo Vargas, Paolo Maiuri, Paola Solanes, Mathieu Maurin, Emmanuel Terriac, Maël Le Berre, Danielle Lankar, Tristan Piolot, Robert S. Adelstein, Yingfan Zhang, Michael Sixt, Jordan Jacobelli, Olivier Benichou, Raphaël Voituriez, Matthieu Piel, and Ana Maria Lennon-Dumenil. Cell migration and antigen capture are antagonistic processes coupled by myosin II in dendritic cells. *Nature Communications*, 6(May):1–16, 2015.
- [133] Yaneer Bar-yam. *Dynamics Of Complex Systems*. CRC Press, 1 edition, 1999.
- [134] Van N G Kampen. *Stochastic Processes in Physics and Chemistry*. Elsevier, 3rd edition, 2007.
- [135] C. W. Gardiner. *Stochastic Methods A Handbook For The Natural And Social Sciences 2010*, 2010.
- [136] Daniel T. Gillespie. A general method for numerically simulating the stochastic time evolution of coupled chemical reactions. *Journal of Computational Physics*, 1976.

- [137] Sheehan Olver and Alex Townsend. Fast inverse transform sampling in one and two dimensions. pages 24–29, 2013.
- [138] Philip A. Desautels. A method to generate autocorrelated uniform random numbers. *Journal of Statistical Computation and Simulation*, 45(1-2):23–31, 1993.
- [139] Jung Tai Chen. Using the sum-of-uniforms method to generate correlated random variates with certain marginal distribution. *European Journal of Operational Research*, 167(1):226–242, 2005.
- [140] Michael A Gibson and Jehoshua Bruck. Efficient exact stochastic simulation of chemical systems with many species and many channels. *The journal of physical chemistry A*, 104(9):1876–1889, 2000.
- [141] N Rajewsky, L Santen, A Schadschneider, and M Schreckenberg. The asymmetric exclusion process: Comparison of update procedures. *Journal of Statistical Physics*, 92(1-2):151–194, 1998.
- [142] Mark Kac. Random Walk and the Theory of Brownian Motion. *The American Mathematical Monthly*, 54(7P1):369–391, aug 1947.
- [143] L. V. Bogachev. Random Walks in Random Environments. *Encyclopedia of Mathematical Physics: Five-Volume Set*, pages 353–371, 2006.
- [144] Ralf Metzler and Joseph Klafter. The random walk’s guide to anomalous diffusion: A fractional dynamics approach, dec 2000.
- [145] A. Einstein. Über die von der molekularkinetischen Theorie der Wärme geforderte Bewegung von in ruhenden Flüssigkeiten suspendierten Teilchen (On the Motion of Small Particles Suspended in a Stationary Liquid, as Required by the Molecular Kinetic Theory of Heat). *Ann. d. Phys.*, (17):549–560, 1905.
- [146] Ralf Metzler and Joseph Klafter. The restaurant at the end of the random walk: Recent developments in the description of anomalous transport by fractional dynamics. *Journal of Physics A: Mathematical and General*, 37(31), 2004.
- [147] Jean Philippe Bouchaud and Antoine Georges. Anomalous diffusion in disordered media: Statistical mechanisms, models and physical applications, nov 1990.
- [148] Michael J. Saxton. A biological interpretation of transient anomalous subdiffusion. I. Qualitative model. *Biophysical Journal*, 92(4):1178–1191, feb 2007.
- [149] Alexander M. Berezhkovskii, Leonardo Dagdug, and Sergey M. Bezrukov. Discriminating between anomalous diffusion and transient behavior in microheterogeneous environments. *Biophysical Journal*, 106(2):L09–L11, jan 2014.

- [150] O. Bénichou, C. Loverdo, M. Moreau, and R. Voituriez. Intermittent search strategies. *Reviews of Modern Physics*, 83(1):81–129, 2011.
- [151] Michael J. Saxton and Ken Jacobson. Single-particle tracking: Applications to membrane dynamics. *Annual Review of Biophysics and Biomolecular Structure*, 26:373–399, 1997.
- [152] Ignacio Gomez Portillo, Daniel Campos, and Vicenç Méndez. Intermittent random walks: Transport regimes and implications on search strategies. *Journal of Statistical Mechanics: Theory and Experiment*, 2011(2), 2011.
- [153] Felix Thiel, Lutz Schimansky-Geier, and Igor M. Sokolov. Anomalous diffusion in run-and-tumble motion. *Physical Review E - Statistical, Nonlinear, and Soft Matter Physics*, 86(2):1–4, 2012.
- [154] Karsten Schwarz, Yannick Schröder, and Heiko Rieger. Numerical analysis of homogeneous and inhomogeneous intermittent search strategies. *Physical Review E*, 94(4):1–31, 2016.
- [155] J. Shlesinger, M. F. and West, B. J. and Klafter. Lévy dynamics of enhanced diffusion: Application to turbulence. *Phys. Rev. Lett.*, 58(11):1100—1103, 1987.
- [156] Sergei Fedotov, Hamed Al-Shamsi, Alexey Ivanov, and Andrey Zubarev. Anomalous transport and nonlinear reactions in spiny dendrites. *Physical Review E - Statistical, Nonlinear, and Soft Matter Physics*, 82(4):20–22, 2010.
- [157] Sidney Redner. *A Guide to First-Passage Processes*. Cambridge University Press, 2001.
- [158] Gunter M. Schütz and Steffen Trimper. Elephants can always remember: Exact long-range memory effects in a non-Markovian random walk. *Physical Review E - Statistical Physics, Plasmas, Fluids, and Related Interdisciplinary Topics*, 70(4):4, 2004.
- [159] Loïc Turban. On a random walk with memory and its relation with Markovian processes. *Journal of Physics A: Mathematical and Theoretical*, 43(28), 2010.
- [160] Zeinab Sadjadi, M. Reza Shaebani, Heiko Rieger, and Ludger Santen. Persistent-random-walk approach to anomalous transport of self-propelled particles. *Physical Review E - Statistical, Nonlinear, and Soft Matter Physics*, 91(6):1–13, 2015.
- [161] Marian Boguñá, Luis F. Lafuerza, Raúl Toral, and M. Ángeles Serrano. Simulating non-Markovian stochastic processes. *Physical Review E - Statistical, Nonlinear, and Soft Matter Physics*, 2014.
- [162] Robert G Gallager. *Stochastic processes: theory for applications*. Cambridge University Press, 2013.

-
- [163] Daniel Ben-Avraham and Shlomo Havlin. *Diffusion and reactions in fractals and disordered systems*. Cambridge university press, 2000.
- [164] Lu Li, Nicolas Gervasi, and Jean Antoine Girault. Dendritic geometry shapes neuronal cAMP signalling to the nucleus. *Nature Communications*, 6, 2015.
- [165] Vicenç Méndez and Alexander Iomin. Comb-like models for transport along spiny dendrites. *Chaos, Solitons and Fractals*, 53:46–51, aug 2013.
- [166] A. M. Berezhkovskii, M. A. Pustovoit, and S. M. Bezrukov. Diffusion in a tube of varying cross section: Numerical study of reduction to effective one-dimensional description. *Journal of Chemical Physics*, 126(13), 2007.
- [167] Alexander M Berezhkovskii, Alexander V Barzykin, and Vladimir Yu Zitserman. Escape from cavity through narrow tunnel. *The Journal of chemical physics*, 130(24):06B625, 2009.
- [168] Leonardo Dagdug, Alexander M. Berezhkovskii, Yurii A. Makhnovskii, and Vladimir Yu Zitserman. Transient diffusion in a tube with dead ends. *Journal of Chemical Physics*, 127(22), 2007.
- [169] Panos Argyrakis and Raoul Kopelman. Random walks and reactions on dendrimer structures. *Chemical Physics*, 261(3):391–398, 2000.
- [170] Dimitris Katsoulis, Panos Argyrakis, Alexander Pimenov, and Alexei Vitukhnovsky. Diffusion and trapping in dendrimer structures. *Chemical Physics*, 275(1-3):261–269, 2002.
- [171] Dirk-Jan Heijs, Victor A Malyshev, and Jasper Knoester. Trapping time statistics and efficiency of transport of optical excitations in dendrimers. *The Journal of Chemical Physics*, 121(10):4884–4892, aug 2004.
- [172] Bin Wu, Yuan Lin, Zhongzhi Zhang, and Guanrong Chen. Trapping in dendrimers and regular hyperbranched polymers. *The Journal of Chemical Physics*, 137(4):44903, jul 2012.
- [173] M. Felici, M. Filoche, and B. Sapoval. Renormalized Random Walk Study of Oxygen Absorption in the Human Lung. *Physical Review Letters*, 92(6):1–4, 2004.
- [174] D. S. Grebenkov, M. Filoche, B. Sapoval, and M. Felici. Diffusion-reaction in branched structures: Theory and application to the lung acinus. *Physical Review Letters*, 94(5):2–5, 2005.
- [175] Colin J. Thompson. Local properties of an Ising model on a Cayley tree. *Journal of Statistical Physics*, 27(3):441–456, 1982.
- [176] E Agliari, A Blumen, and O Mülken. Dynamics of continuous-time quantum walks in restricted geometries. *Journal of Physics A: Mathematical and Theoretical*, 41(44):445301, 2008.

- [177] Pietro Tierno and M Reza Shaebani. Enhanced diffusion and anomalous transport of magnetic colloids driven above a two-state flashing potential. *Soft Matter*, 12(14):3398–3405, 2016.
- [178] H.A. Bethe and William Lawrence Bragg. Statistical theory of superlattices. *Proc. R. Soc. Lond. A*, 150(871), 1935.
- [179] Barry D. Hughes and Muhammad Sahimi. Random walks on the Bethe lattice. *Journal of Statistical Physics*, 29(4):781–794, 1982.
- [180] D Cassi. Random Walks on Bethe Lattices. *Europhysics Letters (EPL)*, 9(7):627–631, 1989.
- [181] Cécile Monthus and Jean-Philippe Bouchaud. Models of traps and glass phenomenology. *Journal of Physics A: Mathematical and General*, 29(14):3847, 1996.
- [182] Nicola Perra, Andrea Baronchelli, Delia Mocanu, Bruno Gonçalves, Romualdo Pastor-Satorras, and Alessandro Vespignani. Random walks and search in time-varying networks. *Physical Review Letters*, 109(23):1–5, 2012.
- [183] M. Khantha and V. Balakrishnan. First passage time distributions for finite one-dimensional random walks. *Pramana*, 21(2):111–122, 1983.
- [184] S. H. Yook, H. Jeong, A. L. Barabási, and Y. Tu. Weighted evolving networks. *Physical Review Letters*, 86(25):5835–5838, 2001.
- [185] E. Almaas, P. L. Krapivsky, and S. Redner. Statistics of weighted treelike networks. *Physical Review E - Statistical, Nonlinear, and Soft Matter Physics*, 71(3):1–9, 2005.
- [186] A. Barrat, M. Barthélemy, R. Pastor-Satorras, and A. Vespignani. The architecture of complex weighted networks. *Proceedings of the National Academy of Sciences of the United States of America*, 101(11):3747–3752, 2004.
- [187] Ann E. Krause, Kenneth A. Frank, Doran M. Mason, Robert E. Ulanowicz, and William W. Taylor. Compartments revealed in food-web structure. *Nature*, 426(6964):282–285, 2003.
- [188] Loukas Skarpalezos, Aristotelis Kittas, Panos Argyrakis, Reuven Cohen, and Shlomo Havlin. Anomalous biased diffusion in networks. *Physical Review E - Statistical, Nonlinear, and Soft Matter Physics*, 88(1):1–7, 2013.
- [189] Partha P Mitra, Pabitra N Sen, Lawrence M Schwartz, and Pierre Le Doussal. Diffusion propagator as a probe of the structure of porous media. *Physical Review Letters*, 68(24):3555–3558, jun 1992.
- [190] R W Mair, G P Wong, D Hoffmann, M D Hürlimann, S Patz, L M Schwartz, and R L Walsworth. Probing Porous Media with Gas Diffusion NMR. *Physical Review Letters*, 83(16):3324–3327, oct 1999.

-
- [191] F. F. Chen and Y. S. Yang. Microstructure-based characterization of permeability using a random walk model. *Modelling and Simulation in Materials Science and Engineering*, 20(4), 2012.
- [192] D. J. Durian, D. A. Weitz, and D. J. Pine. Multiple light-scattering probes of foam structure and dynamics. *Science*, 252(5006):686–688, 1991.
- [193] Colin Cooper, Tomasz Radzik, and Yiannis Siantos. Fast Low-Cost Estimation of Network Properties Using Random Walks. *Internet Mathematics*, 12(4):221–238, 2016.
- [194] A. Dreher, I. S. Aranson, and K. Kruse. Spiral actin-polymerization waves can generate amoeboidal cell crawling. *New Journal of Physics*, 16, 2014.
- [195] David Caballero, Raphaël Voituriez, and Daniel Riveline. Protrusion fluctuations direct cell motion. *Biophysical Journal*, 107(1):34–42, jul 2014.
- [196] George H. Weiss. First passage time problems for one-dimensional random walks. *Journal of Statistical Physics*, 24(4):587–594, 1981.
- [197] Jaume Masoliver, Josep M. Porrà, and George H. Weiss. The continuum limit of a two-dimensional persistent random walk. *Physica A: Statistical Mechanics and its Applications*, 182(4):593–598, 1992.
- [198] Marián Boguñá, Josep M. Porrà, and Jaume Masoliver. Generalization of the persistent random walk to dimensions greater than 1. *Physical Review E - Statistical Physics, Plasmas, Fluids, and Related Interdisciplinary Topics*, 58(6):6992–6998, 1998.
- [199] Marián Boguñá, Josep M. Porrà, and Jaume Masoliver. Persistent random walk model for transport through thin slabs. *Physical Review E - Statistical Physics, Plasmas, Fluids, and Related Interdisciplinary Topics*, 59(6):6517–6526, 1999.
- [200] Bernard Derrida, Vincent Hakim, and Reuven Zeitak. Persistent spins in the linear diffusion approximation of phase ordering and zeros of stationary Gaussian processes. *Physical Review Letters*, 77(14):2871–2874, 1996.
- [201] M. Reza Shaebani, Zeinab Sadjadi, Igor M. Sokolov, Heiko Rieger, and Ludger Santen. Anomalous diffusion of self-propelled particles in directed random environments. *Physical Review E - Statistical, Nonlinear, and Soft Matter Physics*, 90(3):1–5, 2014.
- [202] Anne E. Hafner, Ludger Santen, Heiko Rieger, and M. Reza Shaebani. Run-and-pause dynamics of cytoskeletal motor proteins. *Scientific Reports*, 6(October):1–12, 2016.
- [203] G. M. Viswanathan, Sergey V. Buldyrev, Shlomo Havlin, M. G.E. Da Luz, E. P. Raposo, and H. Eugene Stanley. Optimizing the success of random searches. *Nature*, 401(6756):911–914, 1999.

- [204] G. M. Viswanathan, V. Afanasyev, Sergey V. Buldyrev, Shlomo Havlin, M. G.E. Da Luz, E. P. Raposo, and H. Eugene Stanley. Levy flights in random searches, 2000.
- [205] Xiao Zhou, Renping Zhao, Karsten Schwarz, Matthieu Mangeat, Eva C. Schwarz, Mohamed Hamed, Ivan Bogeski, Volkhard Helms, Heiko Rieger, and Bin Qu. Bystander cells enhance NK cytotoxic efficiency by reducing search time. *Scientific Reports*, 7:1–12, 2017.
- [206] Marie Chupeau, Olivier Bénichou, and Raphaël Voituriez. Cover times of random searches. *Nature Physics*, 11(10):844–847, 2015.
- [207] B Derrida, S A Janowsky, J L Lebowitz, and E R Speer. Exact solution of the totally asymmetric simple exclusion process: Shock profiles. *Journal of Statistical Physics*, 73(5-6):813–842, 1993.
- [208] Debashish Chowdhury, Ludger Santen, and Andreas Schadschneider. Statistical physics of vehicular traffic and some related systems. *Physics Report*, 329(4-6):199–329, 2000.
- [209] K Mallick. Shocks in the asymmetry exclusion model with an impurity. *Journal of Physics A: Mathematical and General*, 29(17):5375–5386, 1996.
- [210] Steven A Janowsky and Joel L Lebowitz. Finite-size effects and shock fluctuations in the asymmetric simple-exclusion process. *Physical Review A*, 45(2):618–625, 1992.
- [211] B Derrida, E Domany, and D Mukamel. An exact solution of a one-dimensional asymmetric exclusion model with open boundaries. *Journal of Statistical Physics*, 69(3):667–687, 1992.
- [212] M R Evans, R Juhász, and L Santen. Shock formation in an exclusion process with creation and annihilation. *Physical Review E - Statistical Physics, Plasmas, Fluids, and Related Interdisciplinary Topics*, 68(2):8, 2003.
- [213] Phase transitions in an exactly soluble one-dimensional exclusion process. *Journal of Statistical Physics*, 72(1-2):277–296, 1993.
- [214] Joachim Krug. Boundary-induced phase transitions in driven diffusive systems. *Physical Review Letters*, 67(14):1882–1885, 1991.
- [215] L Jonathan Cook and R. K.P. Zia. Feedback and fluctuations in a totally asymmetric simple exclusion process with finite resources. *Journal of Statistical Mechanics: Theory and Experiment*, 2009(2), 2009.
- [216] Róbert Juhász and Ludger Santen. Dynamics of an exclusion process with creation and annihilation. *Journal of Physics A: Mathematical and General*, 37(13):3933–3944, 2004.

- [217] A Parmeggiani, T Franosch, and E Frey. Phase Coexistence in Driven One-Dimensional Transport. *Physical Review Letters*, 90(8):4, 2003.
- [218] A. Parmeggiani, T. Franosch, and E. Frey. Totally asymmetric simple exclusion process with Langmuir kinetics. *Physical Review E - Statistical Physics, Plasmas, Fluids, and Related Interdisciplinary Topics*, 70(4):20, 2004.
- [219] Irving Langmuir. THE ADSORPTION OF GASES ON PLANE SURFACES OF GLASS, MICA AND PLATINUM. *Journal of the American Chemical Society*, 40(9):1361–1403, sep 1918.
- [220] M. R. Evans. Bose-Einstein condensation in disordered exclusion models and relation to traffic flow. *Europhysics Letters*, 36(1):13–18, 1996.
- [221] Joachim Krug and Pablo A Ferrari. Phase transitions in driven diffusive systems with random rates. *Journal of Physics A: Mathematical and General*, 29(18):L465, 1996.
- [222] Yan Chai, Reinhard Lipowsky, and Stefan Klumpp. Transport by molecular motors in the presence of static defects. *Journal of Statistical Physics*, 135(2):241–260, 2009.
- [223] Steven A. Janowsky and Joel L. Lebowitz. Finite-size effects and shock fluctuations in the asymmetric simple-exclusion process. *Physical Review A*, 45(2):618–625, 1992.
- [224] Paolo Pierobon, Mauro Mobilia, Roger Kouyos, and Erwin Frey. Bottleneck-induced transitions in a minimal model for intracellular transport. *Physical Review E - Statistical, Nonlinear, and Soft Matter Physics*, 74(3):31906, 2006.
- [225] Stefan Klumpp and Reinhard Lipowsky. Traffic of Molecular Motors through Tube-Like Compartments. *Journal of Statistical Physics*, 113(1-2):233–268, 2003.
- [226] Stefan Klumpp, Theo M Nieuwenhuizen, and Reinhard Lipowsky. Self-organized density patterns of molecular motors in arrays of cytoskeletal filaments. *Biophysical Journal*, 88(5):3118–3132, 2005.
- [227] Melanie J I Müller, Stefan Klumpp, and Reinhard Lipowsky. Molecular motor traffic in a half-open tube. *Journal of Physics Condensed Matter*, 17(47):S3839, 2005.
- [228] Reinhard Lipowsky, Stefan Klumpp, and Theo M Nieuwenhuizen. Random walks of cytoskeletal motors in open and closed compartments. *Physical Review Letters*, 87(10):108101/1–108171/3, 2001.
- [229] T M Nieuwenhuizen, S Klumpp, and R Lipowsky. Walks of molecular motors in two and three dimensions. *Europhysics Letters*, 58(3):468–474, 2002.

- [230] Theo M Nieuwenhuizen, Stefan Klumpp, and Reinhard Lipowsky. Random walks of molecular motors arising from diffusional encounters with immobilized filaments. *Physical Review E - Statistical Physics, Plasmas, Fluids, and Related Interdisciplinary Topics*, 69(6):19, 2004.
- [231] K Tsekouras and A B Kolomeisky. Parallel coupling of symmetric and asymmetric exclusion processes. *Journal of Physics A: Mathematical and Theoretical*, 41(46):465001, 2008.
- [232] A I Curatolo, M R Evans, Y Kafri, and J Tailleur. Multilane driven diffusive systems. *Journal of Physics A: Mathematical and Theoretical*, 49(9):95601, 2016.
- [233] Zhong-Pan Cai, Yao-Ming Yuan, Rui Jiang, Mao-Bin Hu, Qing-Song Wu, and Yong-Hong Wu. Asymmetric coupling in multi-channel simple exclusion processes. *Journal of Statistical Mechanics: Theory and Experiment*, 2008(07):P07016, 2008.
- [234] Yu-Qing Wang, Bin Jia, Rui Jiang, Zi-You Gao, Wan-He Li, Ke-Jie Bao, and Xian-Ze Zheng. Dynamics in multi-lane TASEPs coupled with asymmetric lane-changing rates. *Nonlinear Dynamics*, 88(3):2051–2061, 2017.
- [235] Jean-Philippe Bouchaud. Weak ergodicity breaking and aging in disordered systems. *Journal de Physique I*, 2(9):1705–1713, 1992.
- [236] Robert J Concannon and Richard A Blythe. Spatiotemporally complete condensation in a non-poissonian exclusion process. *Physical review letters*, 112(5):50603, 2014.
- [237] Diana Khoromskaia, Rosemary J Harris, and Stefan Grosskinsky. Dynamics of non-Markovian exclusion processes. *Journal of Statistical Mechanics: Theory and Experiment*, 2014(12):P12013, 2014.
- [238] M R Evans, D P Foster, C Godrèche, and D Mukamel. Spontaneous symmetry breaking in a one dimensional driven diffusive system. *Physical Review Letters*, 74(2):208–211, 1995.
- [239] Peter F Arndt, Thomas Heinzl, and Vladimir Rittenberg. Spontaneous breaking of translational invariance in one-dimensional stationary states on a ring. *Journal of Physics A: Mathematical and General*, 31(2):L45, 1998.
- [240] Peter F Arndt, Thomas Heinzl, and Vladimir Rittenberg. Stochastic models on a ring and quadratic algebras. The three-species diffusion problem. *Journal of Physics A: Mathematical and General*, 31(3):833–843, 1998.
- [241] Peter F Arndt. Yang-Lee theory for a nonequilibrium phase transition. *Physical Review Letters*, 84(5):814–817, 2000.

- [242] N Rajewsky, T Sasamoto, and E R Speer. Spatial particle condensation for an exclusion process on a ring. *Physica A: Statistical Mechanics and its Applications*, 279(1):123–142, 2000.
- [243] Rui Jiang, Katsuhiko Nishinari, Mao-Bin Hu, Yong-Hong Wu, and Qing-Song Wu. Phase Separation in a Bidirectional Two-Lane Asymmetric Exclusion Process. *Journal of Statistical Physics*, 136(1):73–88, jul 2009.
- [244] M Ebbinghaus, C Appert-Rolland, and L Santen. Bidirectional transport on a dynamic lattice. *Physical Review E - Statistical, Nonlinear, and Soft Matter Physics*, 82(4):040901(R), 2010.
- [245] S Klumpp and R Lipowsky. Phase transitions in systems with two species of molecular motors. *Europhysics Letters*, 66(1):90–96, 2004.
- [246] Reinhard Lipowsky, Yan Chai, Stefan Klumpp, Steffen Liepelt, and Melanie J.I. Müller. Molecular motor traffic: From biological nanomachines to macroscopic transport. *Physica A: Statistical Mechanics and its Applications*, 372(1 SPEC. ISS.):34–51, 2006.
- [247] Dirk Helbing and Péter Molnár. Social force model for pedestrian dynamics. *Physical Review E*, 51(5):4282–4286, 1995.
- [248] Yushi Suma, Daichi Yanagisawa, and Katsuhiko Nishinari. Anticipation effect in pedestrian dynamics: Modeling and experiments. *Physica A: Statistical Mechanics and its Applications*, 391(1-2):248–263, 2012.
- [249] Stefan Nowak and Andreas Schadschneider. Quantitative analysis of pedestrian counterflow in a cellular automaton model. *Physical review E*, 85(6):66128, 2012.
- [250] Claudio Feliciani and Katsuhiko Nishinari. Empirical analysis of the lane formation process in bidirectional pedestrian flow. *Physical Review E*, 94(3), 2016.
- [251] Ren Yong Guo and Hai Jun Huang. A modified floor field cellular automata model for pedestrian evacuation simulation. *Journal of Physics A: Mathematical and Theoretical*, 41(38), 2008.
- [252] Carsten Burstedde, Kai Klauck, Andreas Schadschneider, and Johannes Zittartz. Simulation of pedestrian dynamics using a two-dimensional cellular automaton. *Physica A: Statistical Mechanics and its Applications*, 295(3-4):507–525, 2001.
- [253] Karsten Schwarz, Yannick Schröder, Bin Qu, Markus Hoth, and Heiko Rieger. Optimality of Spatially Inhomogeneous Search Strategies. *Physical Review Letters*, 117(6):68101, aug 2016.

- [254] Anne E. Hafner and Heiko Rieger. Spatial organization of the cytoskeleton enhances cargo delivery to specific target areas on the plasma membrane of spherical cells. *Physical Biology*, 13(6), 2016.
- [255] C Loverdo, O Bénichou, M Moreau, and R Voituriez. Robustness of optimal intermittent search strategies in one, two, and three dimensions. *Physical Review E*, 80(3):31146, sep 2009.
- [256] O Bénichou, M Coppey, M Moreau, P-H. Suet, and R Voituriez. Optimal Search Strategies for Hidden Targets. *Physical Review Letters*, 94(19):198101, may 2005.
- [257] Maximilian Ebbinghaus. Stochastic modeling of intracellular processes : bidirectional transport and microtubule dynamics, 2010.
- [258] I. D. Couzin and N. R. Franks. Self-organized lane formation and optimized traffic flow in army ants. *Proceedings of the Royal Society B: Biological Sciences*, 270(1511):139–146, 2003.
- [259] Karl A. Johnson. The axonemal microtubules of the *Chlamydomonas* flagellum differ in tubulin isoform content. *Journal of Cell Science*, 111(3):313–320, 1998.
- [260] D. Zenisek, J. A. Steyer, and W. Almers. Transport, capture and exocytosis of single synaptic vesicles at active zones. *Nature*, 406(6798):849–854, 2000.

Publications and manuscripts

Publications

R. Jose, L. Santen and M. R. Shaebani. Trapping in and escape from branched structures of neuronal dendrites. *Biophys. J.* 115.10 (2018): 2014-2025.

M. R. Shaebani, R. Jose, C. Sand and L. Santen. Unraveling the structure of treelike networks from first-passage times of lazy random walkers. *Physical Review E* 98.4 (2018): 042315.

R. Jose, C. Arita and L. Santen (2020). Bidirectional non-Markovian exclusion processes. *Journal of Statistical Mechanics: Theory and Experiment*. Forthcoming.

Manuscripts

R. Jose and L. Santen (2020). Self-organized lane formation in bidirectional transport of molecular motors. Manuscript submitted for publication.

M. R. Shaebani, R. Jose, L. Santen, L. Stankevics and F. Lautenschläger (2020). Persistence-speed coupling enhances the search efficiency of migrating cells. Manuscript in preparation.

Addendum I Trapping in and Escape from Branched Structures of Neuronal Dendrites

Authors: R. Jose, L. Santen and M. R. Shaebani

Department of Theoretical Physics & Center for Biophysics, Saarland University, 66123 Saarbrücken, Germany

Biophysical Journal, Volume 115, Issue 10, 20 November 2018, Pages 2014-2025
DOI: <https://doi.org/10.1016/j.bpj.2018.09.029>
arXiv: 1901.05334

Author contributions:

Corresponding author: M. R. Shaebani.

L. Santen and M. R. Shaebani designed the research. R. Jose and M. R. Shaebani developed the theory and generated the figures. R. Jose implemented and performed the simulations. All authors contributed to the analysis and interpretation of the results. M. R. Shaebani wrote the manuscript. All authors contributed to the revision of the manuscript.

Abstract:

We present a coarse-grained model for stochastic transport of noninteracting chemical signals inside neuronal dendrites and show how first-passage properties depend on the key structural factors affected by neurodegenerative disorders or aging: the extent of the tree, the topological bias induced by segmental decrease of dendrite diameter, and the trapping probabilities in biochemical cages and growth cones. We derive an exact expression for the distribution of first-passage times, which follows a universal exponential decay in the long-time limit. The asymptotic mean first-passage time exhibits a crossover from power-law to exponential scaling upon reducing the topological bias. We calibrate the coarse-grained model parameters and obtain the variation range of the mean first-passage time when the geometrical characteristics of the dendritic structure evolve during the course of aging or neurodegenerative disease progression (a few disorders for which clear trends for the pathological changes of dendritic structure have been reported in the literature are chosen and studied). We prove the validity of our analytical approach under realistic fluctuations of structural parameters by comparison to the results of Monte Carlo simulations. Moreover, by constructing local structural irregularities, we analyze the resulting influence on transport of chemical signals and formation of heterogeneous density patterns. Because neural functions rely on chemical signal transmission to a large extent, our results open the possibility of establishing a direct link between the disease progression and neural functions.

Trapping in and Escape from Branched Structures of Neuronal Dendrites

Robin Jose,¹ Ludger Santen,¹ and M. Reza Shaebani^{1,*}¹Department of Theoretical Physics and Center for Biophysics, Saarland University, Saarbrücken, Germany

ABSTRACT We present a coarse-grained model for stochastic transport of noninteracting chemical signals inside neuronal dendrites and show how first-passage properties depend on the key structural factors affected by neurodegenerative disorders or aging: the extent of the tree, the topological bias induced by segmental decrease of dendrite diameter, and the trapping probabilities in biochemical cages and growth cones. We derive an exact expression for the distribution of first-passage times, which follows a universal exponential decay in the long-time limit. The asymptotic mean first-passage time exhibits a crossover from power-law to exponential scaling upon reducing the topological bias. We calibrate the coarse-grained model parameters and obtain the variation range of the mean first-passage time when the geometrical characteristics of the dendritic structure evolve during the course of aging or neurodegenerative disease progression (a few disorders for which clear trends for the pathological changes of dendritic structure have been reported in the literature are chosen and studied). We prove the validity of our analytical approach under realistic fluctuations of structural parameters by comparison to the results of Monte Carlo simulations. Moreover, by constructing local structural irregularities, we analyze the resulting influence on transport of chemical signals and formation of heterogeneous density patterns. Because neural functions rely on chemical signal transmission to a large extent, our results open the possibility of establishing a direct link between the disease progression and neural functions.

INTRODUCTION

The complex behavior of advanced nervous systems mainly originates from the elaborate structure of neuronal dendrites (1,2). The functions of the nervous system substantially rely on the diffusion of chemical signals, which is strongly affected by the dendrite structure. The branching morphology of dendrites allows the neurons to control the transmission time of signals and construct a complex network of signaling pathways. Although dendritic trees share some structural features, e.g., branching at acute angles or decreasing in their diameter when moving distally from soma, their morphology varies widely in different neuronal types and regions, reflecting their diverse functions (3). Moreover, the presence of small protrusions along dendrites, called spines, adds to the complexity of the system. Spines receive excitatory synaptic inputs, temporarily compartmentalize them, and undergo dynamic structural changes regulated by neuronal activity (4–6). Bidirectional communication between the spines and the soma (via, e.g., Ca^{2+} , soluble intracellular domains, and subunits of the nuclear import machinery) is critical for long-term

plasticity, neuronal development, and information processing capabilities (7–10). Additionally, synaptic activation can trigger signaling pathways that spread locally in the dendritic channel and influence neighboring synapses (11–13).

Understanding how signal transmission is governed by the structure is becoming more important because pervasive changes of dendritic structure due to aging (14–16) or neurodegenerative disorders (17,18) such as Alzheimer's disease (19–22) have been reported: 1) the population and spatial extent of branches (16,19); 2) the thickness, length, and even curvature of dendritic channels (14,17,19); or 3) the density, shape, and spatial distribution of spines (14–22) can be affected. To establish a link between the structural changes and subsequent alterations of neural functions, a deep understanding of the role of structure on transport of ions or molecules is still lacking. The attempts have been mainly limited to the determination of the impact of spine shape on diffusional and first-passage properties of signals inside spines (7,23–29). The role of spine density has also been studied by considering comb-like structures or (periodically) distributed traps along a channel (30–34). However, the precise estimation of escape time from dendritic trees to reach soma is a difficult task. The complication arises because of complex branching morphology, presence of

Submitted December 4, 2017, and accepted for publication September 26, 2018.

*Correspondence: shaebani@lusi.uni-sb.de

Editor: Ruth Baker.

<https://doi.org/10.1016/j.bpj.2018.09.029>

© 2018 Biophysical Society.

2014 Biophysical Journal 115, 2014–2025, November 20, 2018



spines along the tree, irregular shape of junctions, and varying cross-sectional radius of dendritic channels.

Here, we propose a coarse-grained approach to map the stochastic transport of ions and molecules inside neuronal dendrites to an effective one-dimensional random walk of noninteracting particles in a confined geometry. Coarse-grained random-walk models have been previously employed to successfully describe the influence of topological and geometrical characteristics of the structure on diffusion in labyrinthine environments (see, e.g., (35) for oxygen absorption in the human lung). Our effective one-dimensional (1D) random-walk model enables us to obtain insightful analytical results for mean first-passage times (MFPTs) in complex structures of neuronal dendrites. Various types of 1D random walks have been previously studied, including biased (36–39) and persistent (37–40) walks as well as the walks with absorption along the path (36) or at the boundaries (41). Here, in view of the morphological differences between the dendrites of healthy and degenerate brain tissues, we concentrate on the major characteristics affected by neurodegenerative diseases: the overall extent of dendritic trees, the thicknesses of channels, and the structure and density of spines. By combining appropriate boundary conditions at the two ends of a finite 1D system, partial absorption along the path, and biased motion in an effective 1D random-walk model, we construct a suitable framework to study signal transmission in dendrites. We disentangle the contributions of key structural features to first-passage properties and verify that the scaling behavior of the asymptotic MFPT changes below a threshold value of the topological bias induced by hierarchical reduction of branch diameter. We evaluate the variation range of the mean time required for chemical signals to travel from the synapses to the soma in the course of some specific neurodegenerative disease progression. Moreover, the applicability of our theoretical approach to realistic dendritic structures with spatial heterogeneities is addressed, and the role of local structural changes on signal transmission and formation of heterogeneous density patterns is discussed.

METHODS

By adopting a mesoscopic perspective for transmission of ions and molecules inside dendrites, we consider the motion of a noninteracting random walker

on the nodes of a tree-like regular network with a finite depth d , parameterizing the extent of branches (Fig. 1 b). Each node is identified by its depth n , ranging from 0 (soma) to d (dead ends). After entering the network, the walker randomly jumps to the neighboring nodes until it is absorbed in the target, i.e., soma. To take into account the stochastic trapping events in spines, we assume that the walker either moves in the channel or resides inside biochemical cages with probabilities q or $1 - q$, respectively. This way, we map the problem to a stochastic two-state model. Such models have been widely employed to describe altering phases of motion in biological systems (42–44). Typically, the density of spines (i.e., the number of spines per unit length along the dendritic channel) quickly saturates after a distance of about 50–100 μm from soma (14,45,46). Therefore, we suppose that the residence probability in cages is simply depth independent. The waiting probability at each node is an effective measure of the importance of spines in compartmentalizing the signals: it increases with increasing the density or head volume of spines or decreasing their neck size. To consider the directional preference due to, e.g., hierarchical reduction of branch diameter, a topological bias parameter p is introduced for adopting the direction of motion at each node. Jumping toward soma or a dead end occurs, respectively, with probabilities p or $(1 - p)/k$ (with $k = 2$ for the structure of neuronal dendrites). More generally, one can adopt a persistent random-walk approach (47,48) to include active transport on microtubules or consider passive motion in crowded dendritic channels (the effective persistency of the motion can be characterized by the turning-angle distribution $P(\theta)$ of the particle. Introducing $\varepsilon = \int d\theta \cos(\theta) P(\theta)$, one obtains a negative ε for motion in a crowded environment in which the particle is frequently reflected from obstacles and experiences sharp turns (i.e., a higher chance of motion to the backward directions), whereas one gets a positive ε for active motion along microtubules, in which the walker continues along the previous direction of motion unless when it switches to another filament with opposite polarity. In (anti)persistent random walks, the stochastic equations of motion are generalized by introducing the parameter ε to take the previous direction of motion into account). When arriving at a dead end, the walker either returns to the previous junction with probability r or explores the connecting channel and the growth cone at the tip of the branch with probability $1 - r$.

We estimate the mean time required for a particle to escape the dendrite structure (characterized by the set of parameters $\{d, q, p, r\}$) and reach the soma by treating the soma as an absorbing boundary. However, one can follow the proposed approach to investigate the first-passage time for the inverse direction (i.e., soma-to-spine signaling) as well by distributing the absorbing boundaries along the tree. Let us introduce the probability distribution $P_n(t)$ of being at depth level n at time step t (in an irregular structure, the probability of being at each node can be considered instead). The signals initially enter the system via spines, which are almost uniformly distributed along dendritic trees. As a result, the input rate may even exponentially grow with depth, corresponding to the initial condition $P_n(0) = 2^{n-1}/(2^d - 1)$ ($n \geq 1$). Here, for simplicity, we consider entering from the dead ends $P_n(0) = \delta_{n,d}$, which gives the major contribution to the signal input (see the inset of Fig. 2). The analytical procedure is, however, similar for other initial conditions. We construct a set of coupled master equations for the dynamical evolution of $P_n(t)$ within the framework of our stochastic model:

$$\begin{cases} P_0(t) &= P_0(t-1) + qpP_1(t-1), \\ P_1(t) &= (1-q)P_1(t-1) + qpP_2(t-1), \\ \vdots & \\ P_n(t) &= q(1-p)P_{n-1}(t-1) + (1-q)P_n(t-1) + qpP_{n+1}(t-1), \\ \vdots & \\ P_{d-1}(t) &= q(1-p)P_{d-2}(t-1) + (1-q)P_{d-1}(t-1) + rP_d(t-1), \\ P_d(t) &= q(1-p)P_{d-1}(t-1) + (1-r)P_d(t-1) + \delta(t). \end{cases} \quad (1)$$

Jose et al.

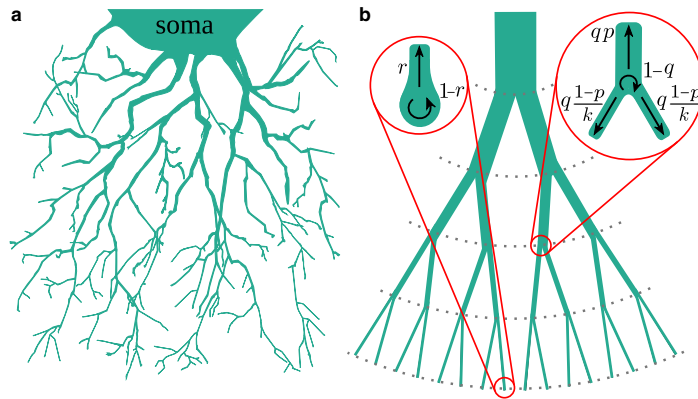


FIGURE 1 (a) Schematic drawing of neuronal dendrites. (b) An illustration of the model. An example tree structure with $d = 5$ and $p = 0.5$ is shown. The arrows indicate possible choices at junctions or dead ends described by Eq. 1. As a visual guide, the ratio between the diameters of parent and child branches is taken to be $p/((1-p)/k)$ (with $k = 2$ in dendritic trees). To see this figure in color, go online.

The detailed calculations to obtain an expression for the escape-time distribution $F(t)$ by solving the above set of equations are presented in the Appendix.

First-passage properties

The overall shape of the escape-time distribution is shown in Fig. 2. Notably, $F(t)$ exhibits an exponential tail. We checked that the exponential decay holds independently of the choice of the trapping factor q , the boundary condition r at the deepest branch level, or the chance p of hopping to shallower layers. The slope, however, varies with q , p , r , and d . Importantly, the inset of Fig. 2 shows that although the initial conditions of entering the tree may considerably influence the overall shape of $F(t)$, the slope of the exponential tail remains independent of the way the signals enter the system (49). It is technically difficult to extract the tail behavior of $F(t)$ from Eq. 8 (see Appendix) in general; however, for a given set of parameter values, one can deduce

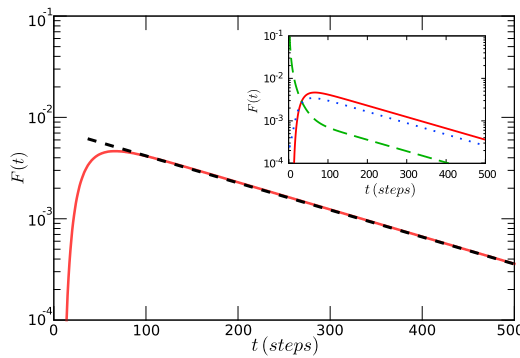


FIGURE 2 First-passage time distribution $F(t)$ for $p = q = r = 1/2$ and $d = 10$. The solid line shows the analytical result via Eq. 8, and the dashed line represents the leading exponential term of Eq. 8 for $t \gg 1$. The inset shows $F(t)$ for the same set of parameter values as in the main panel but for different initial conditions of entering the tree. The solid, dashed, and dotted lines correspond to the initial conditions $P_n(0) = \delta_{n,d}$ (i.e., entering from the dead ends), $P_n(0) = \delta_{n,1}$ (entering from the soma), and $P_n(0) = (2^n - 1)/(2^d - 1)$ (entering uniformly along the tree), respectively. To see this figure in color, go online.

the exponential asymptotic scaling. The resulting dashed line in Fig. 2 fully captures the asymptotic slope. As a proof of the existence of exponential tail, one can show from Eq. 8 that the z transform of the first-passage time distribution can be written as $F(z) = (2^{d+1}(pqz)^d / \Phi_d(z))$, where $\Phi_d(z)$ is a polynomial of maximal degree d . By evaluating the roots k of the polynomial, it can be verified that $F(z) \sim (1/\prod_{k=1}^d (1 - \alpha_k z)^{\beta_k})$, where α_k is a function of the structural parameters and $d^{\beta_k}, \beta_k \leq d$. Then, after partial fraction decomposition of $F(z)$ and inverse z transform, $F(t)$ can be represented as a sum of α_k^t terms and thus can be approximated by the leading exponential term $\alpha_{k,\max}^t$ in the limit $t \rightarrow \infty$.

The MFPT $\langle t \rangle$ of chemical signals to reach the soma, which is our main quantity of interest, can be evaluated from $F(t)$ as explained in details in the Appendix. The analytical Eq. 9 in the Appendix represents the MFPT in terms of the coarse-grained model parameters. Although the expression is continuous, it is indeterminate at $p = 1/2$. By taking the limit, we get $\langle t \rangle = (qd - rd + rd^2)/(qr)$ for the specific choice $p = 1/2$.

Crossover in asymptotic scaling behavior

To clarify how $\langle t \rangle$ varies with the model parameters, we exclude the indeterminate point $p = 1/2$ to simplify the MFPT expression. For $p \neq 1/2$, Eq. 9 of the Appendix reduces to the sum of a linear and an exponential function of d ,

$$\langle t \rangle = \frac{d}{q(2p-1)} + \frac{p r - p q (2p-1)}{q r (2p-1)^2} \left(\left(\frac{1}{p} - 1 \right)^d - 1 \right). \quad (2)$$

Hence, $\langle t \rangle$ in the limit $d \gg 1$ scales exponentially (linearly) for $0 < p < 1/2$ ($1/2 < p < 1$) as the exponential term on the right-hand side of Eq. 2 dominates (vanishes). It can be also seen that $\langle t \rangle$ for the specific choice $p = 1/2$ scales as a power-law d^γ with $\gamma = 2$. Thus, the crossover of the asymptotic mean escape time from a power-law to an exponential scaling can be summarized as

$$\langle t \rangle \sim \begin{cases} \frac{1}{q(2p-1)} d, & 1/2 < p < 1, \\ q^{-1} d^2, & p = 1/2, \\ \frac{p r - p q (2p-1)}{q r (2p-1)^2} e^{d \ln(\frac{1}{p} - 1)}, & 0 < p < 1/2. \end{cases} \quad (3)$$

2016 Biophysical Journal 115, 2014–2025, November 20, 2018

The first (last) case indeed grows logarithmically (linearly) with the number of nodes in regularly branched trees (50). Fig. 3 indicates that the asymptotic slopes are properly captured by the analytical prediction of Eq. 3. The change in the scaling behavior of $\langle t \rangle$ from linear to exponential at the threshold value $p_c = 1/2$ in a 1D random walk can be understood because the effective direction of flow (with respect to the target) is inverted. This also induces a transition from recurrent to transient random walks in infinite trees (51). At $p = 1/2$, the balance between the two directions of diffusive transport holds, and it is expected that the bias parameter p in a healthy neuron is around this threshold value.

RESULTS AND DISCUSSION

Coarse-grained model calibration

In the following, we compare our analytical results to those obtained from ordinary diffusion at microscopic scales in dendritic spines and other relevant geometries such as thickening tubes to verify the applicability of our coarse-grained approach and to calibrate the model parameters. Note that the diffusion problem with a constant diffusion coefficient across the structure is basically a linear differential equation. If the trend of the first-passage time versus one of the model parameters or as a function of a related geometrical characteristic of actual dendrite structures match, then our model parameter can be calibrated into the dendritic structure through a fit to microscale computations for pure diffusion.

The structure of neuronal dendrites primarily depends on the nervous system and varies in different neuronal regions and cell types. However, as a reference for comparison, here we have chosen typical cerebellar Purkinje cells of guinea pigs, which extend nearly 200 μm from the soma and have ~ 450 dendritic terminals (52). Thus, there are nearly 10 generations of junctions in such a structure (corresponding to $d = 10$ in our coarse-grained view), and they branch out every 20 μm on average.

The bias parameter p

The problem of diffusion in a tube of varying cross sections has been thoroughly studied both theoretically and numerically in the literature (53–55). Particularly, Brownian dynamics simulations at microscopic scales were employed in (56) to explore the range of validity of an effective one-dimensional description of diffusion in uniformly thickening or thinning tubes. Denoting the opening angle of the tube with θ (see the inset of Fig. 4 a), they approximated the MFPT $\langle t \rangle$ between the two ends of a tube of length L_{tube} and initial radius R_{tube} , scaled by $\langle t \rangle$ of a tube of uniform cross section, as

$$\langle t \rangle / \langle t \rangle_{\text{uniform}} \simeq \begin{cases} \frac{\sqrt{1+\lambda^2}}{3} (3+2\lambda\bar{L}), & \lambda < 0, \\ \frac{\sqrt{1+\lambda^2}}{3} \frac{3+\lambda\bar{L}}{1+\lambda\bar{L}}, & 0 < \lambda, \end{cases} \quad (4)$$

where $\lambda = \tan\theta$ and $\bar{L} = L_{\text{tube}}/R_{\text{tube}}$. Their analytical and simulation results match for opening angles $\theta < 10^\circ$. Even such small thickening rates are still larger than what is typically observed in neuronal dendrites. For example, the thickness of the dendritic channel varies from nearly 0.5 around the dead ends to less than 8 μm close to soma in cerebellar Purkinje cells of guinea pigs, which have a typical extent of 200 μm , i.e., an opening angle of less than 2° (52). Therefore, within the validity range of their analytical expressions, we compare $\langle t \rangle$ obtained from our coarse-grained approach Eq. 9 to their results in Fig. 4 a. We set $q = r = 1$ to avoid trapping because Eq. 4 is valid for smooth tubes with reflecting walls. We also consider our reference dendritic structure (see Fig. 4, b and e) for ease of comparison. The scaled MFPTs obtained via Eqs. 4 and 9 fit very well using a simple linear map between λ and p as $\lambda \sim 0.5p - 0.25$. We checked that, within biologically relevant parameter

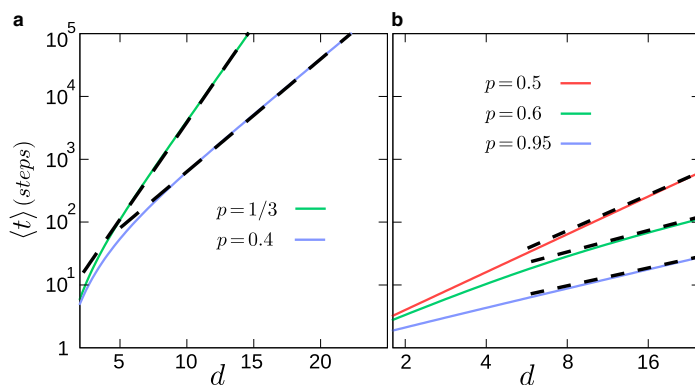


FIGURE 3 Mean escape time versus the depth of the tree for (a) $p < 1/2$ (log-lin scales) and (b) $p \geq 1/2$ (log-log scales) at $q = r = 1$. The analytical results of Eq. 9 are shown with solid lines, and the dashed lines represent the asymptotic exponential or power-law scaling of $\langle t \rangle$ via Eq. 3. To see this figure in color, go online.

Jose et al.

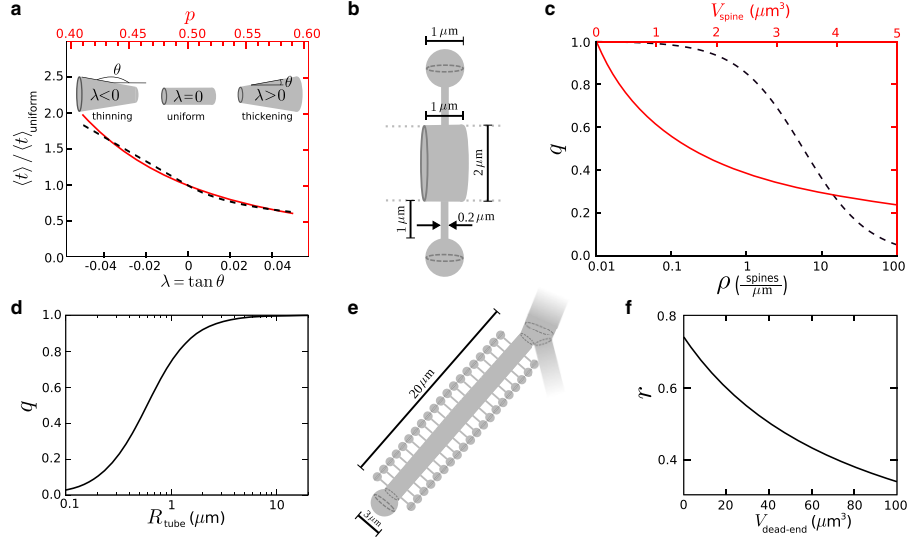


FIGURE 4 (a) The MFPT between the two ends of a tube, scaled by the result of a uniform tube, versus $\lambda = \tan\theta$ or the bias parameter p . The results of Eqs. 4 and 9 are shown with solid and dashed lines, respectively. The inset shows a schematic drawing of tubes of varying cross sections. (b) Typical size scales taken as the reference values in healthy dendrites. (c) The parameter q versus the spine density ρ (dashed line) or the spine volume $V_{\text{spine}} = V_{\text{head}} + V_{\text{neck}}$ (solid line). (d) q versus the radius of the dendritic tube. (e) The regularized geometry of the segment of the dendritic tube connecting the dead end to the last branch point. (f) The coarse-grained parameter r in terms of the volume of the dead end. The parameter values (unless varied) are taken to be $\rho = 2$ (spines/ μm), $R_{\text{tube}} = 1$ μm , $V_{\text{spine}} \approx 0.55$ μm^3 , and $L_{\text{tube}} = 20$ μm in (c), (d), and (f). To see this figure in color, go online.

ranges and weakly thickening regime $\theta < 5^\circ$, one can obtain similar satisfactory agreement between the MFPTs by treating the coefficients of the linear transformation as fit parameters. In the following, we choose $p = 0.55$ as the reference value for our coarse-grained bias parameter in a typical healthy dendrite (corresponding to $\theta \approx 1.4^\circ$). Note that the geometry of the junctions may affect the first-passage results in general; however, we expect that it causes minor variations because the cross-sectional area at the branch point is conserved.

The trapping parameter q

The coarse-grained parameter q in our model indeed represents the fraction of time spent in the dendritic channel in the steady state, which is set by the probabilities κ_w and κ_m of switching from motion in the channel to waiting in the spines and vice versa. κ_w is proportional to the density of spines and the mean entrance area of the spine neck and inversely proportional to the cross-sectional area of the dendritic channel. Thus, one obtains $\kappa_w \propto \rho R_{\text{neck}}^2 / R_{\text{tube}}^2$, where R_{neck} , ρ , and R_{tube} denote the neck radius, spine density, and radius of the dendritic channel, respectively. κ_m is inversely proportional to the mean escape time from spines $\langle t \rangle_{\text{spine}}$, which obeys (29)

$$\langle t \rangle_{\text{spine}} = \frac{L_{\text{neck}}^2}{2D} + \frac{L_{\text{neck}}^2 V_{\text{head}}}{D V_{\text{neck}}} + \frac{V_{\text{head}}}{4D R_{\text{neck}}}, \quad (5)$$

with D being the diffusion coefficient and L_{neck} , V_{neck} , and V_{head} denoting, respectively, the neck length and volume and the head volume of the spines. The diffusion coefficient depends on the size of the diffusing object. For example, the typical value of D in dendritic spines for Ca^{2+} ions and green fluorescent protein (GFP) variants (that are much smaller in size) were reported to be ~ 100 and 20 $\mu\text{m}^2/\text{s}$, respectively (57). Inside the dendrite channel, $D \sim 37$ $\mu\text{m}^2/\text{s}$ was obtained for a specific photoactivatable GFP (paGFP) (23). Similar results were reported for diffusion in other cell types. For comparison, D was found to be ~ 23.5 and ~ 25.2 $\mu\text{m}^2/\text{s}$ for the motion of enhanced GFP (eGFP) inside the nucleus and in the cytoplasm of HeLa cells, respectively (58). For a typical thin spine (59) with $R_{\text{neck}} = 100$ nm, $L_{\text{neck}} = 1$ μm , and a head diameter of 1 μm (thus, with $V_{\text{neck}} \approx 0.03$ μm^3 and $V_{\text{head}} \approx 0.52$ μm^3) as shown in Fig. 4 b, one gets $\langle t \rangle_{\text{spine}} \approx 0.19$, 0.48 , and 0.77 s for the escape time of Ca^{2+} , paGFP, and eGFP from spines (using $D_{\text{Ca}} = 100$, $D_{\text{paGFP}} = 40$, and $D_{\text{eGFP}} = 25$ $\mu\text{m}^2/\text{s}$). Moreover, the mean travel time of signals from synapses to soma in smooth dendritic channels of length x can be estimated from Eq. 5 as

2018 Biophysical Journal 115, 2014–2025, November 20, 2018

$t \approx x^2/(2D)$. By choosing $x = 20 \mu\text{m}$ as an example, one obtains 2.0, 5.0, and 8.0 s for the travel time of Ca^{2+} , paGFP, and eGFP, respectively.

The transitions between the two states of motility are non-Markovian in general; however, one can estimate the asymptotic value of q in the limit $t \rightarrow \infty$ as a function of the volumes of the dendritic tube and spines as (30)

$$q = \frac{\kappa_m}{\kappa_m + \kappa_w} \approx \frac{V_{\text{tube}}}{V_{\text{tube}} + V_{\text{spines}}} = \frac{1}{1 + \frac{\rho}{\pi R_{\text{tube}}^2} (V_{\text{head}} + V_{\text{neck}})}. \quad (6)$$

Fig. 4 c shows how the q parameter varies with the spine density and volume. Although increasing ρ or V_{spine} enhances the trapping probability and thus reduces q , increasing the volume of the dendritic tube leads to longer excursion times in the tube and increases q , as shown in Fig. 4 d. By choosing $\rho = 2$ (spines/ μm), $R_{\text{tube}} = 1 \mu\text{m}$, and $V_{\text{head}} + V_{\text{neck}} \approx 0.55 \mu\text{m}^3$ (59), we obtain the healthy reference value $q \approx 0.74$ for further comparisons.

The boundary-condition parameter r

Finally, we calibrate the parameter r via a similar procedure as explained for q . The coarse-grained parameter r effectively represents the probability of motion inside the segment of the dendritic tube that connects the last branch point to the dead end (see the schematic in Fig. 4 e). By ignoring the minor corrections due to the negligible thickening along such a short tube segment, the asymptotic value of r can be approximated as

$$r \approx \frac{V_{\text{tube}}}{V_{\text{tube}} + V_{\text{spines}} + V_{\text{dead-end}}} = \frac{1}{1 + \frac{\rho}{\pi R_{\text{tube}}^2} (V_{\text{head}} + V_{\text{neck}}) + \frac{V_{\text{dead-end}}}{\pi R_{\text{tube}}^2 L_{\text{tube}}}}. \quad (7)$$

Let us consider a spherical dead end with a typical diameter of $3 \mu\text{m}$ and assume that the tree branches out every $20 \mu\text{m}$ on average. Then, using the rest of the reference parameter values used for the determination of the q parameter, we get $r \approx 0.63$. The variation of r as a function of the volume of the dead end is shown in Fig. 4 f. Even in the absence of the dead end (i.e., $V_{\text{dead-end}} = 0$), the signals may be still trapped in the spines distributed between the dead end and the last junction, leading to $r \neq 1$.

Influence of pathological changes on transmission of chemical signals

After adopting the set of model parameter values $p = 0.55$, $q = 0.7$, $r = 0.6$, and $d = 10$ as the reference for healthy structures of dendrites, next, we investigate how far the

MFPT varies when the geometrical characteristics of the dendritic structure evolve during the course of aging or neurodegenerative disease progression. Here, we choose aging and a few examples of neurodegenerative disorders (such as Alzheimer's disease, schizophrenia, and fragile X and Down syndromes) for which clear trends for the pathological changes of dendritic structure have been reported in the literature (60). In the course of aging or Alzheimer's progression, both the density of spines and the extent of the dendritic tree reduce (14,20,22,61) (the spine density of the apical dendrites of pyramidal neurons in the cingulate cortex of humans may decrease to less than 60% with aging (14)). These changes are equivalent to the increase of q and reduction of d in our coarse-grained perspective. It is also known that schizophrenia and Down syndrome progression leads to reduction of the spine size (62,63), corresponding to the enhancement of our q parameter. The pathology of fragile X makes the prediction of MFPT variations complicated. In the course of fragile X progression, although the spine density increases (enhancement of q), their shapes become more elongated and the spine head volume reduces (reduction of q) (64–66). Therefore, we expect that the variation of q (and thus of the MFPT) is less pronounced in fragile X compared to the other examples. The competition between the variations of spine density and shape determines whether q effectively decreases or increases in the course of fragile X progression.

In Fig. 5, we show the trends of the MFPTs upon the dendritic structure changing because of aging or diseases, as explained above. The combined effects of the reduction of tree extent and spine density due to aging or Alzheimer's disease can dramatically decrease the MFPT of chemical signals from the synapses to the soma (Fig. 5 a). To calculate the MFPT, we used Eq. 9 with q inserted from Eq. 6 and $d = L(\mu\text{m})/20$. The reduction of both spine density and tree extent to half of their healthy reference values decreases the relative MFPT to $\langle t \rangle / \langle t \rangle_{\text{healthy}} \approx 0.3$. Thus, the system gradually loses the ability to compartmentalize ions and molecules and maintain chemical concentrations to a wide extent. The shrinkage of the spine size in schizophrenia and Down syndrome leads to a similar trend for the variation of MFPT; however, the effect is less pronounced. In the extreme case of zero head volume, the MFPT reduces to nearly 80% of its reference value (see Fig. 5 b). As a result of the competition between the increase of spine density (up to $\rho \approx 10$ (spines/ μm)) and reduction of spine head volume (down to $R_{\text{head}} = 0$) in fragile X syndrome, the relative MFPT, $\langle t \rangle / \langle t \rangle_{\text{healthy}}$, may vary within the range of [0.6, 1.9]. If the reduction rate of spine head volume equals the growth rate of spine density, the two effects compensate each other and the MFPT remains unchanged, as shown by the contour line in Fig. 5 c. In other neurodegenerative disorders, the pathology of spine and dendrite structure is more complicated. For example, distortion of spine shape in most mental retardations (18)

Jose et al.

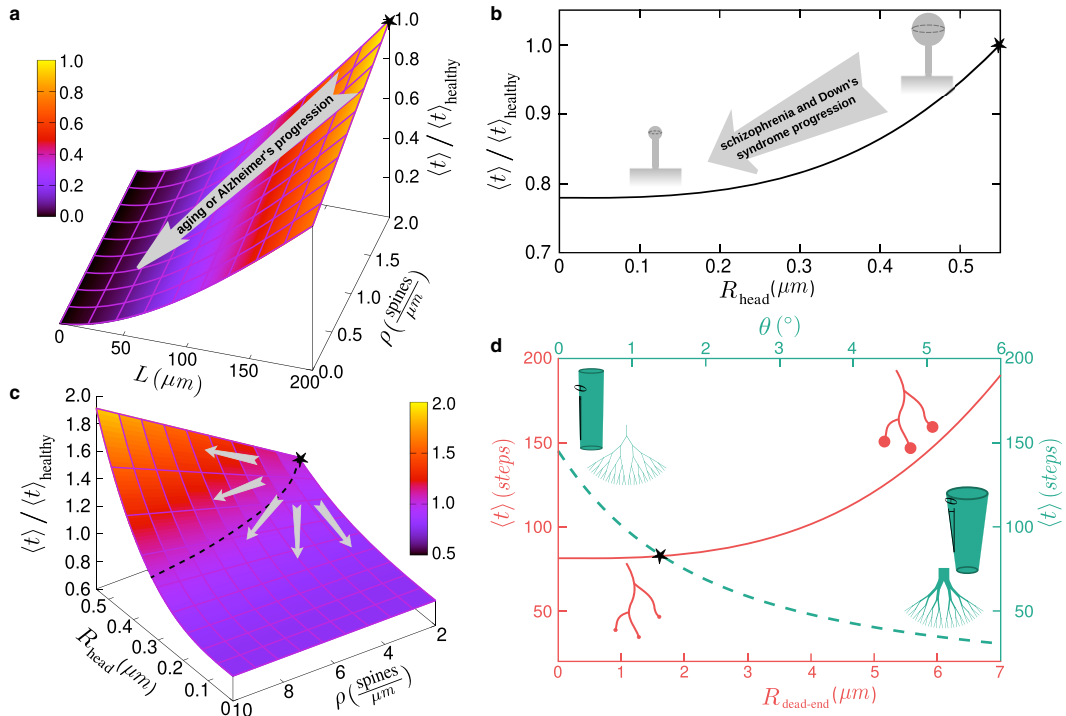


FIGURE 5 Influence of the pathologies of spines and dendrites on chemical signal transmission. The MFPT $\langle t \rangle$, scaled by the MFPT of the reference healthy structure $\langle t \rangle_{\text{healthy}}$, is shown versus the structural characteristics affected in the course of (a) aging and Alzheimer's disease (spine density ρ and extent of the dendritic tree L), (b) schizophrenia and Down syndrome (spine head radius R_{head}), and (c) fragile X syndrome (ρ and R_{head}). The stars mark the corresponding point for the reference healthy structure. In (c), the arrows represent the possible directions of fragile X progression, and the dashed contour line marks the path along which $\langle t \rangle / \langle t \rangle_{\text{healthy}} = 1$. (d) Variation of the MFPT with changing the opening angle θ of the dendritic tube (dashed line) or the radius $R_{\text{dead-end}}$ of the spherical growth cones (solid line) is shown. To see this figure in color, go online.

makes the prediction of the MFPT trend difficult. Another point is that there is currently a lack of quantitative studies to clarify the impact of diseases or aging on the thickening of dendritic tubes (corresponding to the variation of our p parameter) or on the morphological changes of growth cones (variation of r). In Fig. 5 d, we calculate the MFPTs within reasonable variation ranges of the opening angle of the dendritic tube or the radius of spherical growth cones. Here, we use Eq. 9 with q inserted from Eq. 9 and p from the linear relation $\tan(\theta) \approx 0.5p - 0.25$. One obtains up to threefold increase or reduction in $\langle t \rangle$ compared to the healthy reference $\langle t \rangle_{\text{healthy}}$.

The mean travel time of chemical signals in dendrites reflects the ability to preserve local concentrations or induce concentration gradients of ions and molecules; thus, it is tightly connected to neural functions. Therefore, the quantitative evaluation of the first-passage times in different diseases is a step forward toward linking the disease progression to neural functions and draw physiological conclusions.

Structural irregularities

In our analytical formalism, we consider constant coarse-grained parameters along the entire tree. This corresponds to the assumption of a spatially homogeneous structure, i.e., if the dendritic tree is regularly branched, the channels thicken with the same rate throughout the tree, the spine density and size are spatially uniform, and all the growth cones are of the same size. From a coarse-grained perspective, such a regular structure can be described by a few major parameters, which allows for the calculation of the MFPTs. Taking into account that our coarse-grained parameters indeed represent the key structural features that undergo pathological changes in the course of neurodegenerative disease progression, the model enables us to connect the disease progression to signal transmission, as discussed in the previous section. However, realistic dendritic structures are spatially heterogeneous. For example, the density of spines may vary even up to 40% around the global mean value in dendritic trees (14,45). The spines

also undergo dynamic structural changes regulated by neuronal activity (4–6).

In view of the realistic structural fluctuations, the basic question is whether the analytical predictions via our coarse-grained approach remain valid when the structural parameters of a given dendritic tree are allowed to spatially vary around their global mean values. In the following, we compare the analytical result for the reference set of parameter values with the simulation results in which the structural parameters spatially fluctuate around the reference values. For comparison, the fluctuation range $\Delta q/\langle q \rangle \approx 0.2$ is comparable to the realistic variations in spine head size and density in pyramidal neurons in the cingulate cortex of humans (14). Similar fluctuation ranges are considered for d , r , and p parameters in the absence of quantitative studies to explore the variation ranges of the extent of dendritic trees, the size of growth cones, and the thickening rate of dendritic channels.

In each of the Monte Carlo simulations, we vary only one of the coarse-grained parameters, whereas the rest of them are fixed at their mean values $\langle d \rangle = 10$, $\langle p \rangle = 0.55$, $\langle q \rangle = 0.7$, or $\langle r \rangle = 0.6$. Let us first consider the parameters p , q , and r . A new value is assigned to the variable parameter at each random-walk step, which is randomly taken from a uniform distribution in the interval $[p - \Delta p, p + \Delta p]$, $[q - \Delta q, q + \Delta q]$, or $[r - \Delta r, r + \Delta r]$ for parameter p , q , or r , respectively. The upper panels of Fig. 6 represent the variation ranges of the geometrical characteristics of dendritic structures as the width of the uniform distributions for coarse-grained parameters varies from 0 up to 20% around the reference (healthy) values. In the upper panel of Fig. 6 *b*, we present the extreme values of the spine head volume as a function of $\Delta q/\langle q \rangle$. However, one can alternatively fix the head volume (e.g., at $V_{\text{head}} = 1 \mu\text{m}^3$) and consider the changes in the spine density and get [1.3, 1.3], [1.1, 1.6], [0.9, 1.8], and [0.6, 2.5] intervals for the number of spines per micron at $\Delta q/\langle q \rangle = 0, 0.05, 0.1$, and

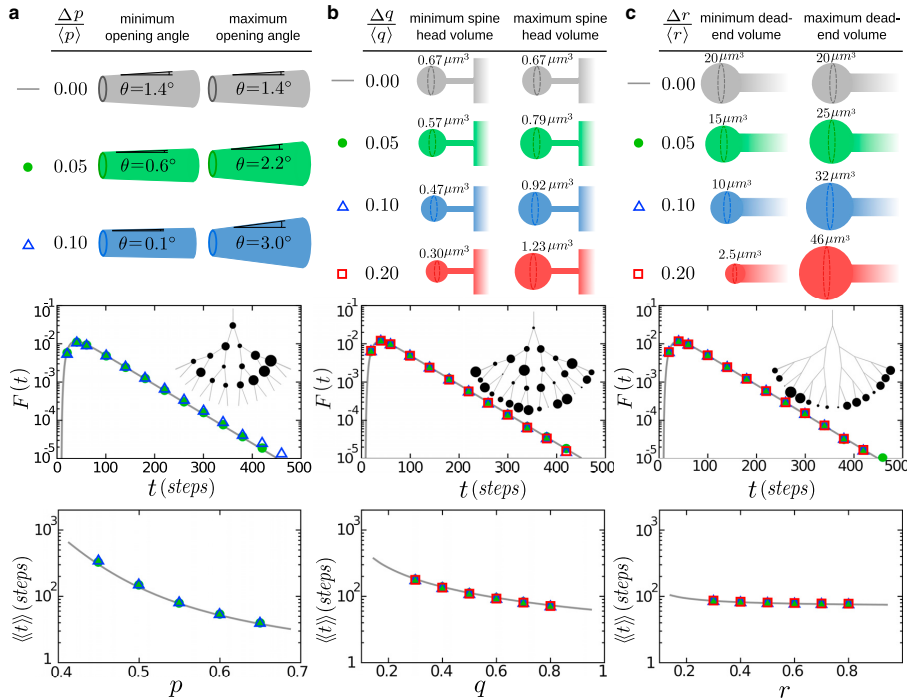


FIGURE 6 Comparison between the analytical predictions for constant parameter values and simulation results for dynamically varying (a) p , (b) q , or (c) r parameter across the dendritic structure. The reference parameter values are taken to be $p = 0.55$, $q = 0.7$, $r = 0.6$, and $d = 10$. Upper panels show schematic representations of the variations in the realistic dendritic geometry when the coarse-grained model parameters vary 5, 10, or 20% around their mean reference values. Middle panels show log-lin plots of the escape-time distribution. The analytical curve via Eq. 8 (solid line) is compared to the simulation results (symbols). The insets are schematic diagrams of typical trees with $d = 5$ and 10% fluctuations in the corresponding model parameter. The radii of the circles are proportional to the relative deviations from the minimal values. Lower panels show the mean escape time versus the model parameters. The solid line represents the analytical prediction of Eq. 9, and the symbols correspond to the simulation results. $\langle\langle \dots \rangle\rangle$ denotes averaging over both the ensemble of realizations for a given disorder and the ensemble of possibilities for the stochastic particle dynamics. To see this figure in color, go online.

Jose et al.

0.2, respectively. The middle panels show that the resulting escape-time distributions $F(t)$ invisibly deviate from the analytical prediction (*solid line*) for q and r parameters, whereas the tail of $F(t)$ starts deviating from the theory line when p varies up to 10% around $\langle p \rangle = 0.55$. However, such tail deviations have an insignificant impact on the MFPT $\langle t \rangle$, as shown in the lower panel of Fig. 6 *a* at $p = 0.55$. We also repeated the simulations for other sets of reference parameters to check whether $\langle t \rangle$ deviates from the analytical prediction. According to the results shown in the lower panels of Fig. 6, we conclude that our analytical results are robust against realistic fluctuations of the structural characteristics across the dendritic trees (even up to 20% around the mean) over a wide range around the reference set of coarse-grained parameter values.

Next, we investigate the variations in the extent of the tree around the mean value $\langle d \rangle$. To this aim, in Monte Carlo simulations, we construct stochastic tree structures by randomly allowing the nodes to have their child nodes in a hierarchical manner starting from the root node. The procedure continues until the tree consists of a given number of dead ends. A few examples of the resulting structures with 32 dead ends are shown in Fig. 7 *a*. We characterize the depth of the irregular tree by the average of its dead-ends depths $\langle d \rangle$ and its variation by $\sigma(d)/\langle d \rangle$, with $\sigma(d)$ being the SD. As shown in Fig. 7 *a*, the ensemble of structures corresponding to a given $\sigma(d)/\langle d \rangle$ contains globally heterogeneous configurations as well as highly asymmetric ones. In Fig. 7 *b*, we show how the deviation from our analytical prediction grows with increasing the fluctuation range of the dead-end depths. It can be seen that the error of the analytical expression remains below 10% even in considerably heterogeneous structures with $\sigma(d)/\langle d \rangle \approx 20\%$. For lower variations in the extent of the tree ($\sigma(d)/\langle d \rangle < 10\%$), the error is less than 5%. Thus, our analytical approach is applicable to dendritic structures with moderate heterogeneity in their branching pattern.

So far, we have investigated the influence of global dynamic irregularities of structure on the first-passage times. However, static local irregularities may also exist in real dendrites, induced by pathological changes. For example, various dendritic abnormalities associated with fibrillar amyloid deposits in the transgenic mouse model of Alzheimer's disease and in the human brain were reported in (67). Extensive spine-density loss, shaft atrophy (i.e., decline in the radius of the dendritic tube), and formation of varicosity (which consists of an enlarged, tortuous, and crumpled part of the dendritic channel) were observed in the vicinity of amyloid deposits. From our coarse-grained perspective, the local varicosity formation, shaft atrophy, and spine-density reduction correspond, respectively, to the decrease of q and p and increase of q in a specific region of the tree such as a sub-branch. To elucidate the impact of static local irregularities on signal transmis-

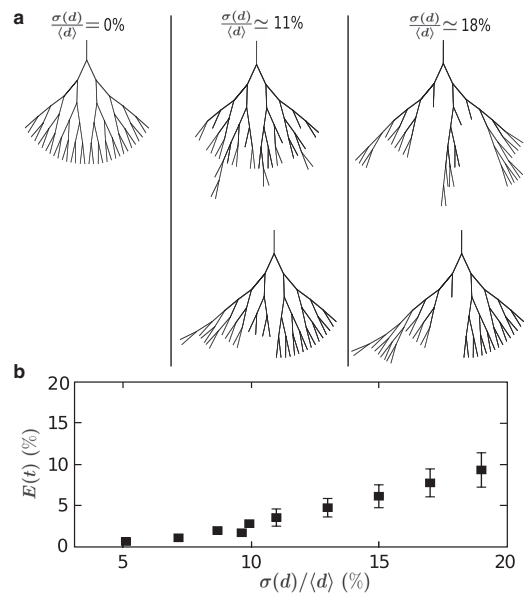


FIGURE 7 (a) Schematic drawings of typical heterogeneous trees with 32 dead ends and a global variation of the order of $\sigma(d)/\langle d \rangle = 11$ or 18% in their extent. The lower trees are examples of highly asymmetric structures, with a regularly branched right wing and an irregular left wing. (b) The deviation of the analytical MFPT $\langle t \rangle_{\text{theory}}$ (calculated for the average depth $\langle d \rangle$) from the simulation result $\langle t \rangle$, characterized by $E(t) = \left| \langle t \rangle - \langle t \rangle_{\text{theory}} \right| / \langle t \rangle$, in terms of the fluctuation range of the dead-end depths. $\langle \langle \dots \rangle \rangle$ denotes averaging over both the ensemble of configurations for a given disorder and the ensemble of possibilities for the stochastic particle dynamics. The parameter values are taken to be $p = 0.55$ and $q = r = 1$. The data points without error bars represent single realizations, whereas those with error bars are averages of $E(t)$ over bins of size 2 along the x axis. Error bars represent the SD of $E(t)$.

sion, our effective 1D analytical description based on the depth levels does not help. Therefore, we construct the entire tree structure in Monte Carlo simulations again (similar to the procedure to construct asymmetric configurations in Fig. 7 but this time for q or p parameters). Fig. 8 shows a few samples of coarse-grained dendritic trees with an affected sub-branch. We change q or p parameter in the affected sub-branch while keeping the rest of parameters the same as the entire tree. By imposing a constant entrance rate (one particle from one of the randomly chosen dead ends at each time step), we eventually obtain the spatial distribution of noninteracting particles in the steady state. The results shown in Fig. 8 reveal that local structural irregularities influence the transport of particles and lead to the formation of heterogeneous density patterns in the system. Reduction of q or p in the affected sub-branch to $q_i = 0.1$ or $p_i = 0.3$ imposes a local trap and leads to a local population that is, respectively, 43 or 28% higher than the homogeneous case. On the other

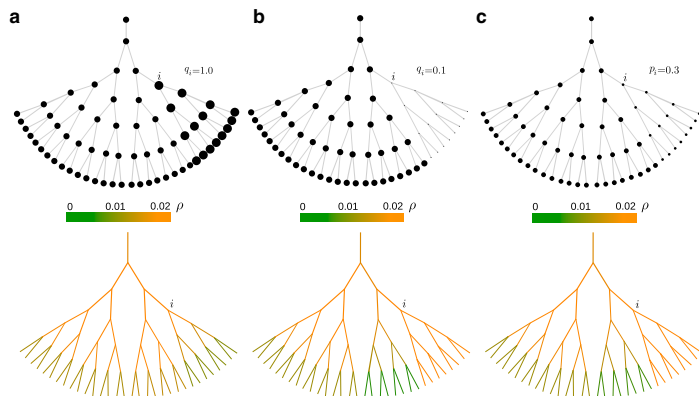


FIGURE 8 Upper panels: schematic diagrams of example trees with local structural irregularities in the sub-branch starting from junction i . Common parameters (unless locally varied) are $d = 6$, $p = 0.55$, $q = 0.7$, and $r = 0.6$. The modified coarse-grained parameter in the sub-branch is denoted by q_i or p_i . The radii of the circles are proportional to the local q (a and b) or p (c) values. Lower panels show heat maps of the stationary density of particles in each branch in simulations performed for the corresponding asymmetric structures. To see this figure in color, go online.

hand, increasing the local q to $q_i = 1$ reduces the population in the sub-branch to 88% compared to the regular tree. Such uneven distributions of signaling ions and molecules may have dramatic consequences on neural activities such as neuronal firing and the ability to maintain chemical concentrations and gradients.

CONCLUSIONS

In summary, an analytical framework has been developed to obtain first-passage times of chemical signals in neuronal dendrites in terms of the structural factors that undergo pathological changes in the course of neurodegenerative disease progression. By quantitatively connecting the dendritic structure to signal transmission, our results open the possibility of establishing a direct link between the disease progression and neural functions, which allows us to draw important physiological conclusions.

To consider structural inhomogeneities and dynamical variations of real dendrites, the master Eq. 1 can be generalized by introducing uncorrelated probability distributions for the key structural parameters p , q , and r and calculating the first-passage properties in terms of their first two moments. The fluctuation of depth d can be also taken into account by distributing the dead-end conditions among the master equations that belong to a given range of the deepest levels of the tree. Moreover, the MFPT of passive particles in crowded dendritic channels or active ones along microtubules (68) can be taken into account in our master equations by introducing a (anti)

persistent random walker. The interparticle interactions at high-density regimes affect the transport through the narrow necks of spines, which influences the waiting time distribution in spines and the first-passage properties. The investigation of these aspects calls for additional research efforts. The proposed approach provides an analytical route into a variety of search and transport phenomena on complex networks (e.g. weighted time-varying trees), branched macromolecules and polymers, various energy landscapes, and more generally biased random walks with absorbing boundaries (69–71). Our calculations can be adapted to real labyrinthine environments by introducing node-degree distribution and closed paths.

APPENDIX: FIRST-PASSAGE TIME CALCULATIONS

To derive an expression for the first-passage time distribution, we start from the master Eq. 1 and obtain a set of equations for $P_n(z)$ at different depth levels by defining the z transform $P_n(z) = \sum_{t=0}^{\infty} P_n(t) z^t$ (with $|z| < 1$). For example, the transformation of the last equation in the set of master Eq. 1 reads $P_d(z) = q(1-p)zP_{d-1}(z) + (1-r)zP_d(z) + 1$, where the constant term results from the z transform of the δ function. The challenge is that the number of equations $d + 1$ is arbitrary. However, after some algebra, we solve this set of equations to obtain $P_n(z)$, from which the z transform of the first-passage time distribution to reach the soma can be evaluated as $F(z) = \sum_{t=0}^{\infty} F(t) z^t = qpzP_1(z)$ (72). Let us define $\lambda_{\pm} = (1/qpz)[1 + (q-1)z \pm A(z, q, p)]$, where $A(z, q, p) = [1 + 2(q-1)z + [1 - 2q + (1-2p)^2 q^2 z^2]^{1/2}]^{1/2}$. We derive the following exact expression for the z transform of the escape-time distribution,

$$F(z) = \frac{2^{d+1} r A(z, q, p)}{(\lambda_+^d - \lambda_-^d)[r(1 - (q-1)z) + pq(-2 + 2z - rz)] + (\lambda_+^d + \lambda_-^d)r A(z, q, p)}. \quad (8)$$

Jose et al.

Next, by inverse z transforming of $F(z)$, one gets an explicit lengthy expression for $F(t)$ in terms of the number of time steps t . We confirmed the correctness of our calculations by comparing the analytical predictions via Eq. 8 to the results of extensive Monte Carlo simulations obtained from 10^6 realizations of the same stochastic process. The MFPT $\langle t \rangle$ can be evaluated as $\langle t \rangle = \sum_{t=0}^{\infty} t F(t) = z \frac{d}{dz} F(z)|_{z \rightarrow 1}$. By expanding Eq. 8 around $z = 1$ up to first-order terms, $F(z) \sim F(z)|_{z \rightarrow 1} + (z - 1)(d/dz)F(z)|_{z \rightarrow 1} + \mathcal{O}((z - 1)^2)$, and defining $\gamma_{\pm} = (1/p)(1 \pm |2p - 1|)$, we arrive at the following expression for the mean escape time,

$$\langle t \rangle = 2^{d+1} \frac{(\gamma_-^d - \gamma_+^d)[(2pq + dr)(1 - 2p) + 2pr] + (\gamma_-^d + \gamma_+^d)dr |2p - 1|}{qr[(\gamma_-^d - \gamma_+^d)(1 - 2p) + (\gamma_-^d + \gamma_+^d)|2p - 1|]^2} \Theta(1 - 2p), \quad (9)$$

where $\Theta(x) = \begin{cases} +1 & 0 \leq x \\ -1 & x < 0 \end{cases}$. In the limit $d \rightarrow \infty$, $\langle t \rangle$ diverges as expected for infinite Cayley trees (72) and Bethe lattices (51,73,74).

AUTHOR CONTRIBUTIONS

L.S. and M.R.S. designed the research. R.J. and M.R.S. performed the research. All authors contributed to the analysis and interpretation of the results. M.R.S. wrote the manuscript.

ACKNOWLEDGMENTS

This work was funded by the Deutsche Forschungsgemeinschaft through Collaborative Research Center SFB 1027 (Projects A7 and A8).

REFERENCES

1. Spruston, N. 2008. Pyramidal neurons: dendritic structure and synaptic integration. *Nat. Rev. Neurosci.* 9:206–221.
2. Hering, H., and M. Sheng. 2001. Dendritic spines: structure, dynamics and regulation. *Nat. Rev. Neurosci.* 2:880–888.
3. Waters, J., A. Schaefer, and B. Sakmann. 2005. Backpropagating action potentials in neurones: measurement, mechanisms and potential functions. *Prog. Biophys. Mol. Biol.* 87:145–170.
4. Tanaka, J., Y. Horiike, ..., H. Kasai. 2008. Protein synthesis and neurotrophin-dependent structural plasticity of single dendritic spines. *Science*. 319:1683–1687.
5. Moczulska, K. E., J. Tinter-Thiede, ..., S. Rumpel. 2013. Dynamics of dendritic spines in the mouse auditory cortex during memory formation and memory recall. *Proc. Natl. Acad. Sci. USA*. 110:18315–18320.
6. Kasai, H., M. Fukuda, ..., J. Noguchi. 2010. Structural dynamics of dendritic spines in memory and cognition. *Trends Neurosci.* 33:121–129.
7. Li, L., N. Gervasi, and J. A. Girault. 2015. Dendritic geometry shapes neuronal cAMP signalling to the nucleus. *Nat. Commun.* 6:6319.
8. Zhai, S., E. D. Ark, ..., R. Yasuda. 2013. Long-distance integration of nuclear ERK signaling triggered by activation of a few dendritic spines. *Science*. 342:1107–1111.
9. Cohen, S., and M. E. Greenberg. 2008. Communication between the synapse and the nucleus in neuronal development, plasticity, and disease. *Annu. Rev. Cell Dev. Biol.* 24:183–209.

10. Jordan, B. A., and M. R. Kreutz. 2009. Nucleocytoplasmic protein shuttling: the direct route in synapse-to-nucleus signaling. *Trends Neurosci.* 32:392–401.
11. Harvey, C. D., and K. Svoboda. 2007. Locally dynamic synaptic learning rules in pyramidal neuron dendrites. *Nature*. 450:1195–1200.
12. Murakoshi, H., H. Wang, and R. Yasuda. 2011. Local, persistent activation of Rho GTPases during plasticity of single dendritic spines. *Nature*. 472:100–104.
13. Harvey, C. D., R. Yasuda, ..., K. Svoboda. 2008. The spread of Ras activity triggered by activation of a single dendritic spine. *Science*. 321:136–140.

14. Benavides-Piccione, R., I. Fernaund-Espinosa, ..., J. DeFelipe. 2013. Age-based comparison of human dendritic spine structure using complete three-dimensional reconstructions. *Cereb. Cortex*. 23:1798–1810.
15. Petanjek, Z., M. Judaš, ..., I. Kostovic. 2011. Extraordinary neurogenesis of synaptic spines in the human prefrontal cortex. *Proc. Natl. Acad. Sci. USA*. 108:13281–13286.
16. Ormer, D. A., C. C. Chen, ..., J. C. Brumberg. 2014. Alterations of dendritic protrusions over the first postnatal year of a mouse: an analysis in layer VI of the barrel cortex. *Brain Struct. Funct.* 219:1709–1720.
17. Purpura, D. P., N. Bodick, ..., S. Wurzelmann. 1982. Microtubule disarray in cortical dendrites and neurobehavioral failure. I. Golgi and electron microscopic studies. *Brain Res.* 281:287–297.
18. Purpura, D. P. 1974. Dendritic spine “dysgenesis” and mental retardation. *Science*. 186:1126–1128.
19. Smith, D. L., J. Pozueta, ..., M. Shelanski. 2009. Reversal of long-term dendritic spine alterations in Alzheimer disease models. *Proc. Natl. Acad. Sci. USA*. 106:16877–16882.
20. Tsai, J., J. Grutzendler, ..., W. B. Gan. 2004. Fibrillar amyloid deposition leads to local synaptic abnormalities and breakage of neuronal branches. *Nat. Neurosci.* 7:1181–1183.
21. Tackenberg, C., A. Ghori, and R. Brandt. 2009. Thin, stubby or mushroom: spine pathology in Alzheimer’s disease. *Curr. Alzheimer Res.* 6:261–268.
22. Spire, T. L., M. Meyer-Luehmann, ..., B. T. Hyman. 2005. Dendritic spine abnormalities in amyloid precursor protein transgenic mice demonstrated by gene transfer and intravital multiphoton microscopy. *J. Neurosci.* 25:7278–7287.
23. Bloodgood, B. L., and B. L. Sabatini. 2005. Neuronal activity regulates diffusion across the neck of dendritic spines. *Science*. 310:866–869.
24. Tønnesen, J., G. Katona, ..., U. V. Nägerl. 2014. Spine neck plasticity regulates compartmentalization of synapses. *Nat. Neurosci.* 17:678–685.
25. Takasaki, K., and B. L. Sabatini. 2014. Super-resolution 2-photon microscopy reveals that the morphology of each dendritic spine correlates with diffusive but not synaptic properties. *Front. Neuroanat.* 8:29.
26. Santamaria, F., S. Wils, ..., G. J. Augustine. 2006. Anomalous diffusion in Purkinje cell dendrites caused by spines. *Neuron*. 52:635–648.
27. Kusters, R., L. C. Kapitein, ..., C. Storm. 2013. Shape-induced asymmetric diffusion in dendritic spines allows efficient synaptic AMPA receptor trapping. *Biophys. J.* 105:2743–2750.
28. Schuss, Z., A. Singer, and D. Holcman. 2007. The narrow escape problem for diffusion in cellular microdomains. *Proc. Natl. Acad. Sci. USA*. 104:16098–16103.

2024 Biophysical Journal 115, 2014–2025, November 20, 2018

Addendum I. Trapping in and Escape from Branched Structures of Neuronal Dendrites

First-Passage Time in Neuronal Dendrites

29. Berezhkovskii, A. M., A. V. Barzykin, and V. Y. Zitserman. 2009. Escape from cavity through narrow tunnel. *J. Chem. Phys.* 130:245104.
30. Dagdug, L., A. M. Berezhkovskii, ..., V. Y. Zitserman. 2007. Transient diffusion in a tube with dead ends. *J. Chem. Phys.* 127:224712.
31. Berezhkovskii, A. M., L. Dagdug, and S. M. Bezrukov. 2014. From normal to anomalous diffusion in comb-like structures in three dimensions. *J. Chem. Phys.* 141:054907.
32. Méndez, V., and A. Iomin. 2013. Comb-like models for transport along spiny dendrites. *Chaos Solitons Fractals.* 53:46–51.
33. Fedotov, S., and V. Méndez. 2008. Non-Markovian model for transport and reactions of particles in spiny dendrites. *Phys. Rev. Lett.* 101:218102.
34. Bressloff, P. C., and B. A. Earnshaw. 2007. Diffusion-trapping model of receptor trafficking in dendrites. *Phys. Rev. E Stat. Nonlin. Soft Matter Phys.* 75:041915.
35. Felici, M., M. Filoche, and B. Sapoval. 2004. Renormalized random walk study of oxygen absorption in the human lung. *Phys. Rev. Lett.* 92:068101.
36. Benichou, O., A. M. Cazabat, ..., G. Oshanin. 1999. Biased diffusion in a one-dimensional adsorbed monolayer. *J. Stat. Phys.* 97:351–371.
37. Weiss, G. H. 2002. Some applications of persistent random walks and the telegrapher's equation. *Physica A.* 311:381–410.
38. Pottier, N. 1996. Analytical study of the effect of persistence on a one-dimensional biased random walk. *Physica A.* 230:563–576.
39. Garcia-Pelayo, R. 2007. Solution of the persistent, biased random walk. *Physica A.* 384:143–149.
40. Masoliver, J., K. Lindenberg, and G. H. Weiss. 1989. A continuous-time generalization of the persistent random walk. *Physica A.* 157:891–898.
41. Kantor, Y., and M. Kardar. 2007. Anomalous diffusion with absorbing boundary. *Phys. Rev. E Stat. Nonlin. Soft Matter Phys.* 76:061121.
42. Hafner, A. E., L. Santen, ..., M. R. Shaebani. 2016. Run-and-pause dynamics of cytoskeletal motor proteins. *Sci. Rep.* 6:37162.
43. Theves, M., J. Taktikos, ..., C. Beta. 2013. A bacterial swimmer with two alternating speeds of propagation. *Biophys. J.* 105:1915–1924.
44. Pinkoviezky, I., and N. S. Gov. 2013. Transport dynamics of molecular motors that switch between an active and inactive state. *Phys. Rev. E Stat. Nonlin. Soft Matter Phys.* 88:022714.
45. Ballesteros-Yáñez, I., R. Benavides-Piccione, ..., J. DeFelipe. 2006. Density and morphology of dendritic spines in mouse neocortex. *Neuroscience.* 138:403–409.
46. Rothnie, P., D. Kabaso, ..., S. L. Wearne. 2006. Functionally relevant measures of spatial complexity in neuronal dendritic arbors. *J. Theor. Biol.* 238:505–526.
47. Shaebani, M. R., Z. Sadjadi, ..., L. Santen. 2014. Anomalous diffusion of self-propelled particles in directed random environments. *Phys. Rev. E Stat. Nonlin. Soft Matter Phys.* 90:030701.
48. Sadjadi, Z., M. R. Shaebani, ..., L. Santen. 2015. Persistent-random-walk approach to anomalous transport of self-propelled particles. *Phys. Rev. E Stat. Nonlin. Soft Matter Phys.* 91:062715.
49. Tejedor, V., O. Bénichou, and R. Voituriez. 2011. Close or connected: distance and connectivity effects on transport in networks. *Phys. Rev. E Stat. Nonlin. Soft Matter Phys.* 83:066102.
50. Wu, B., Y. Lin, ..., G. Chen. 2012. Trapping in dendrimers and regular hyperbranched polymers. *J. Chem. Phys.* 137:044903.
51. Cassi, D. 1990. Dynamical phase transition of biased random walks on Bethe lattices. *Europhys. Lett.* 13:583–586.
52. Rapp, M., I. Segev, and Y. Yarom. 1994. Physiology, morphology and detailed passive models of guinea-pig cerebellar Purkinje cells. *J. Physiol.* 474:101–118.
53. Petersen, E. E. 1958. Diffusion in a pore of varying cross section. *AICHE J.* 4:343–345.
54. Berezhkovskii, A. M., A. V. Barzykin, and V. Y. Zitserman. 2009. One-dimensional description of diffusion in a tube of abruptly changing diameter: boundary homogenization based approach. *J. Chem. Phys.* 131:224110.
55. Kalinay, P., and J. K. Percus. 2010. Mapping of diffusion in a channel with abrupt change of diameter. *Phys. Rev. E.* 82:031143.
56. Berezhkovskii, A. M., M. A. Pustovoi, and S. M. Bezrukov. 2007. Diffusion in a tube of varying cross section: numerical study of reduction to effective one-dimensional description. *J. Chem. Phys.* 126:134706.
57. Yasuda, R., and H. Murakoshi. 2011. The mechanisms underlying the spatial spreading of signaling activity. *Curr. Opin. Neurobiol.* 21:313–321.
58. Chen, Y., J. D. Müller, ..., E. Gratton. 2002. Molecular brightness characterization of EGFP in vivo by fluorescence fluctuation spectroscopy. *Biophys. J.* 82:133–144.
59. Harris, K. M., F. E. Jensen, and B. Tsao. 1992. Three-dimensional structure of dendritic spines and synapses in rat hippocampus (CA1) at postnatal day 15 and adult ages: implications for the maturation of synaptic physiology and long-term potentiation. *J. Neurosci.* 12:2685–2705.
60. Fiala, J. C., J. Spacek, and K. M. Harris. 2002. Dendritic spine pathology: cause or consequence of neurological disorders? *Brain Res. Brain Res. Rev.* 39:29–54.
61. Giannakopoulos, P., E. Kövari, ..., C. Bouras. 2009. Pathological substrates of cognitive decline in Alzheimer's disease. *Front. Neurol. Neurosci.* 24:20–29.
62. Roberts, R. C., R. Conley, ..., D. J. Chute. 1996. Reduced striatal spine size in schizophrenia: a postmortem ultrastructural study. *Neuroreport.* 7:1214–1218.
63. Marin-Padilla, M. 1972. Structural abnormalities of the cerebral cortex in human chromosomal aberrations: a Golgi study. *Brain Res.* 44:625–629.
64. He, C. X., and C. Portera-Cailliau. 2013. The trouble with spines in fragile X syndrome: density, maturity and plasticity. *Neuroscience.* 251:120–128.
65. Irwin, S. A., B. Patel, ..., W. T. Greenough. 2001. Abnormal dendritic spine characteristics in the temporal and visual cortices of patients with fragile-X syndrome: a quantitative examination. *Am. J. Med. Genet.* 98:161–167.
66. Wisniewski, K. E., S. M. Segan, ..., R. D. Rudelli. 1991. The Fra(X) syndrome: neurological, electrophysiological, and neuropathological abnormalities. *Am. J. Med. Genet.* 38:476–480.
67. Grutzendler, J., K. Helmin, ..., W. B. Gan. 2007. Various dendritic abnormalities are associated with fibrillar amyloid deposits in Alzheimer's disease. *Ann. N. Y. Acad. Sci.* 1097:30–39.
68. Newby, J. M., and P. C. Bressloff. 2009. Directed intermittent search for a hidden target on a dendritic tree. *Phys. Rev. E Stat. Nonlin. Soft Matter Phys.* 80:021913.
69. Perra, N., A. Baronchelli, ..., A. Vespignani. 2012. Random walks and search in time-varying networks. *Phys. Rev. Lett.* 109:238701.
70. Tierno, P., and M. R. Shaebani. 2016. Enhanced diffusion and anomalous transport of magnetic colloids driven above a two-state flashing potential. *Soft Matter.* 12:3398–3405.
71. Hansen, A., and J. Kertész. 2004. Phase diagram of optimal paths. *Phys. Rev. Lett.* 93:040601.
72. Redner, S. 2001. *A Guide to First-Passage Processes.* Cambridge University Press, New York.
73. Hughes, B. D., and M. Sahimi. 1982. Random walks on the Bethe lattice. *J. Stat. Phys.* 29:781–794.
74. Cassi, D. 1989. Random walks on Bethe lattices. *Europhys. Lett.* 9:627–631.

Addendum II Unraveling the structure of treelike networks from first-passage times of lazy random walkers

Authors: M. R. Shaebani[†], R. Jose[†], C. Sand and L. Santen

Department of Theoretical Physics & Center for Biophysics, Saarland University, 66123 Saarbrücken, Germany

Physical Review E, Volume 98, Issue 4, 31 October 2018, Pages 042315
DOI: <https://doi.org/10.1103/PhysRevE.98.042315>
arXiv: 1811.03602

Author contributions:

Corresponding author: M. R. Shaebani.

[†] *M. R. Shaebani and R. Jose contributed equally to this work.*

L. Santen and M. R. Shaebani designed the research. R. Jose and M. R. Shaebani developed the theory and generated the figures. R. Jose, C. Sand and M. R. Shaebani performed the simulations. All authors contributed to the analysis and interpretation of the results. M. R. Shaebani wrote the manuscript. R. Jose, L. Santen and M. R. Shaebani contributed to the revision of the manuscript.

Abstract:

We study the problem of random search in finite networks with a tree topology, where it is expected that the distribution of the first-passage time $F(t)$ decays exponentially. We show that the slope α of the exponential tail is independent of the initial conditions of entering the tree in general, and scales exponentially or as a power law with the extent of the tree L , depending on the bias parameter p to jump toward the target node. It is unfeasible to uniquely determine L and p from measuring α or the mean first-passage time (MFPT) of an ordinary diffusion along the tree. To unravel the structure, we consider lazy random walkers that take steps with probability m when jumping on the nodes and return with probability q from the leaves. By deriving an exact analytical expression for the MFPT of the intermittent random walk, we verify that the structural information of the tree can be uniquely extracted by measuring the MFPT for two randomly chosen types of tracer particles with distinct parameters m and q . We also address the applicability of our approach in the presence of disorder in the structure of the tree or statistical uncertainty in the experimental parameters.

Unraveling the structure of treelike networks from first-passage times of lazy random walkers

M. Reza Shaebani,^{*} Robin Jose, Christian Sand,[†] and Ludger Santen

Department of Theoretical Physics & Center for Biophysics, Saarland University, 66123 Saarbrücken, Germany

 (Received 24 July 2018; revised manuscript received 27 September 2018; published 31 October 2018)

We study the problem of random search in finite networks with a tree topology, where it is expected that the distribution of the first-passage time $F(t)$ decays exponentially. We show that the slope α of the exponential tail is independent of the initial conditions of entering the tree in general, and scales exponentially or as a power law with the extent of the tree L , depending on the tendency p to jump toward the target node. It is unfeasible to uniquely determine L and p from measuring α or the mean first-passage time (MFPT) of an ordinary diffusion along the tree. To unravel the structure, we consider lazy random walkers that take steps with probability m when jumping on the nodes and return with probability q from the leaves. By deriving an exact analytical expression for the MFPT of the intermittent random walk, we verify that the structural information of the tree can be uniquely extracted by measuring the MFPT for two randomly chosen types of tracer particles with distinct experimental parameters m and q . We also address the applicability of our approach in the presence of disorder in the structure of the tree or statistical uncertainty in the experimental parameters.

DOI: [10.1103/PhysRevE.98.042315](https://doi.org/10.1103/PhysRevE.98.042315)

I. INTRODUCTION

Diffusion and transport in complex environments are strongly influenced by the geometrical and topological properties of the underlying structures [1]. For example, the topology of the tree structure of human lung affects the absorption efficiency of diffusing oxygen [2], the obstacle size and density determines the mean free path of light in turbid media [3], the topology of Cayley trees influences the average displacement of quantum or classical random walkers [4,5], or the arrangement of magnetic bubbles in flashing potentials controls the anomalous behavior of the mean square displacement of paramagnetic colloidal particles [6].

Conversely, reconstructing the structure by means of the information obtained from the transport properties of tracer particles also constitutes an interesting subject. The idea of extracting the structural information of labyrinthine environments (or indirect evaluation of other quantities of interest in general) from the diffusional properties has attracted attention for a few decades [7–15]: (i) It was suggested [7] that the geometry of the boundaries of a drum can be determined from the eigenvalues of the diffusion equation in a cage surrounded by absorbing walls; (ii) in porous structures, the porosity [8], surface-to-volume ratio of the voids [9], degree of confinement and absorption strength [10], and permeability [11] were shown to be calculable from the diffusion propagator (more simply from the asymptotic diffusion coefficient in special cases); (iii) the temporal changes in the structure of foams and turbid media can be probed by the diffusive propagation of light [12,13]; (iv) the geometrical properties of complex networks such as the number of triangles, loops, and sub-

graphs can be estimated from the first return time of random walks [14]; and (v) as the last example, the time required for autocatalytic reactions on inhomogeneous substrates can be obtained from the mean time taken for the reactants to reach a reaction center or to encounter each other [15].

In this paper, we verify that the mean first-passage time (MFPT) of tracer particles to reach a target, as a conceptually simple and easily accessible transport quantity, can be

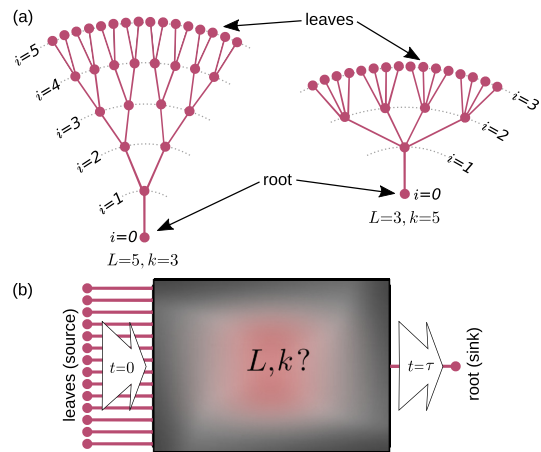


FIG. 1. (a) Examples of finite regular trees with the same number of leaves but different structure. (b) Schematic illustration of the measurement design. The tracer particle enters a tree, with unknown structural characteristics L and k (more generally p), from a leaf. It performs a random walk and eventually reaches the root after a first-passage time τ . The mean first-passage time $\langle \tau \rangle$ is obtained by repeating the measurement for an ensemble of noninteracting tracer particles.

^{*}Corresponding author: shaebani@lusi.uni-sb.de

[†]Present address: Heidelberg Institut für Theoretische Studien, 69118 Heidelberg, Germany.

employed to extract useful structural information. While we consider a treelike network in the present study, the idea can be extended to other complex networks and structures. Branching morphologies constitute an important subset of complex structures, ranging from real systems (e.g., dendrimer macromolecules [16–20], neuronal dendrites [21–23], and rivers [24]) to virtual ones such as treelike graphs [25,26]. To investigate diffusion on branched structures, they have been often modeled as regular treelike networks with, e.g., a given degree of the node k representing the number of links connected to each node [see Fig. 1(a)]. Well-studied examples include finite Cayley trees [16–20,27] and infinite Bethe lattices [28–30]. A weight can be also assigned to each link [31,32], as the real-world networks exhibit heterogeneity in the capacity of their links [33,34]. The advantage of regular trees is that the stochastic transport of particles along such structures can be mapped onto effective one-dimensional (1D) random walk models. By mapping Bethe lattices and Cayley trees onto 1D random walks, some basic quantities such as the mean square displacement, the probability of returning to the origin, and the first-passage times were calculated [16–20,28–30]. For example, the MFPT to reach a target node in finite trees was shown to depend on the extent L of the tree as well as the degree k of the node (more generally on the probability p to hop toward the target) [17,18,35,36]. Thus, the structural parameters L and k [shown in Fig. 1(a)] cannot be uniquely determined from the measurement of the MFPT of an ordinary random walk on the tree. The question arises of whether the prediction of the structural properties of trees from the MFPTs of other types of random walks is feasible. It is also not clear how far the possible predictions are robust in the presence of disorder in the extent of the tree, the degree of the nodes, or the capacity of the links.

To be able to unravel the structure, we increase the complexity of the dynamics of the tracer particles by introducing lazy random walkers that intermittently jump along the tree. We derive an exact analytical expression for the MFPT in terms of the waiting probabilities at nodes and dead ends (leaves), which enables us to uniquely determine the structure by measuring the MFPTs [see the schematic sketch in Fig. 1(b)]. To identify the validity range of the theoretical results, we compare the analytical predictions to the simulation results in the presence of disorder in the structure of the tree or statistical uncertainty in the experimental parameters. Our results are also applicable to ordinary random walks along specific structures which induce temporal absorption along the path or at the dead ends. This is particularly relevant to transport in neuronal dendrites in the presence of biochemical cages along the dendritic tubes [21–23].

This paper is organized as follows. We first review biased random walks on bounded 1D domains and ordinary random walks on regularly branched trees in Sec. II, and present an expression for the MFPT to travel from the leaves to the root of a finite tree. Next we introduce lazy random walkers in Sec. III and demonstrate how the structure of the tree can be uniquely determined from the MFPTs of such tracer particles. In Sec. IV, we show how the deviation of the MFPT from that of a regular tree enhances as the structural disorder or the experimental uncertainty grows. Section V concludes the paper.

II. FIRST-PASSAGE TIMES OF BIASED RANDOM WALKS ON FINITE 1D DOMAINS

Stochastic motion of biased [37–40] or persistent [37–39,41,42] walkers in one dimension has been thoroughly investigated in the literature. Several aspects of 1D random walks, such as the influence of waiting [43] or absorption [40] along the path or at the boundaries [44] on transport properties, has been studied. These studies also help understand the transport in other systems. For example, mapping of Bethe lattices and Cayley trees onto 1D random walks facilitates the calculation of the transport quantities of interest such as the first-passage times. While the MFPT to visit any specific target node on the Bethe lattice (i.e., an unlimited Cayley tree) is infinite, the MFPT in bounded domains such as Cayley trees is finite [17,18,35,36]. For instance, it was shown that the MFPT of traveling from the leaves to the root of a finite regular tree obeys the following relation [35,36]:

$$\langle \tau \rangle = \frac{L}{2p-1} + \frac{1-p}{(2p-1)^2} \left[\left(\frac{1-p}{p} \right)^L - 1 \right], \quad (1)$$

where L denotes the extent of the tree and p represents the tendency to hop toward the root at each node (corresponding to an effective bias toward the target in a 1D system). Here, the parameter p equals to $p = \frac{1}{k}$ in trees with uniform links, where k is the coordination number (i.e., the degree of the nodes) as shown in Fig. 1(a). More generally, p can represent the effective tendency to move toward the target, including all the effects of branching at nodes, relative weights of the links, tendency to follow the shortest path toward the target, etc. The relevant systems are, e.g., weighted treelike networks [32], neuronal dendrites where the branches tend to taper toward the dead ends [23], and stochastic packet transport in the Internet preferably along the shortest path [45,46] (though the last structure contains loops). In deriving Eq. (1), it was assumed that the reflection probability at the dead ends (leaves) equals the hopping probability toward the root at the bulk nodes [35,36].

According to Eq. (1), the MFPT depends on both L and p parameters. Therefore, having access to the MFPT via the experiment illustrated in Fig. 1(b) does not provide sufficient information to uniquely determine the structure, i.e., the tree extent L and the node degree k (or the effective upward tendency p). As shown in Fig. 2, for a given measured value of the MFPT, one obtains a monotonic iso-MFPT contour line in the (L, p) phase space as the set of possible solutions.

III. FIRST-PASSAGE TIMES OF INTERMITTENT RANDOM WALKS

We propose that the structural properties of an unknown tree can be deduced from the mean first-passage times of specific tracer particles with a tunable tendency to move along the tree. We consider random walks with waiting probabilities at nodes and leaves. When such lazy random walkers enter a tree from the leaves, explore the unknown structure, and exit from the root, the MFPT can be obtained in terms of the waiting probabilities. We show that having access to the MFPT for only two different random choices of the waiting probabilities enables us to uniquely determine the structure of

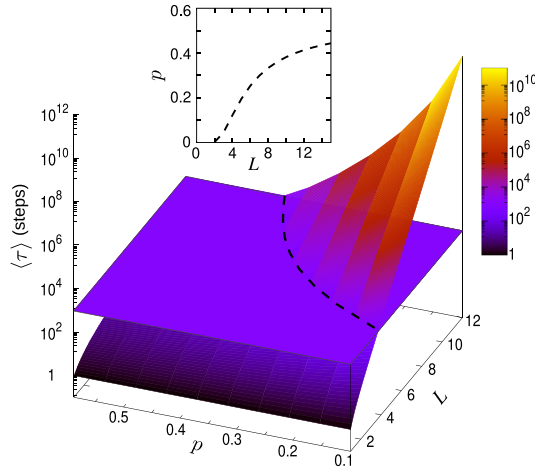


FIG. 2. Mean first-passage time $\langle \tau \rangle$ of traveling from the leaves to the root, obtained via Eq. (1), versus the extent of the tree L and the effective tendency p to jump toward the target. The flat plane represents a constant MFPT, $\langle \tau \rangle \simeq 1000$ steps, as an example of the measured MFPT in experiments. The dashed contour line marks the intersection of the two surfaces, i.e., the path along which the MFPT equals the measured value. Inset: The contour line in the (L, p) phase space.

the regular tree via the analytical framework developed in this section.

Let us consider the stochastic motion of an individual random walker on the nodes of a regular tree with the extent L . We can identify each node by its generation (i.e., its distance from the root) in regular trees. The generation of the nodes ranges from 0 at the root to L at the leaves. The number of nodes belonging to the same generation i equals k^{i-1} (for $i > 0$), with k being the coordination number of the nodes. Each tracer particle initially enters the tree from one of the leaves. When the tracer is on a bulk node, it either jumps to one of the neighboring nodes with probability m or waits at its current node with probability $1 - m$ at each time step. The dynamics is, however, different at the boundaries. At the leaves, the particle either returns to the interior of the tree with probability q or waits with probability $1 - q$. The other boundary, i.e., the root node with generation $i = 0$, is treated as a trap. When the particle eventually reaches the root after a first-passage time τ , it is not allowed to return to the tree (which corresponds to $m = 0$ for the specific generation $i = 0$).

In trees with uniform links and in the absence of other sources which induce preference toward the target, k determines the probability $\frac{m}{k}$ to jump to one of the neighboring nodes, thus the relative tendency to move toward the target equals $p = \frac{1}{k}$. More generally, there can exist an additional net probability m' to choose the root direction ($0 \leq m' \leq m$), induced by other possible effects (such as the hierarchical reduction of branch diameter toward the leaves or tendency to travel along the shortest path). In such a case, the total probability to jump from a bulk node toward the root or each

of the leaves is $\frac{m-m'}{k} + m'$ or $\frac{m-m'}{k}$, respectively. Therefore, the relative tendency to move toward the root effectively equals $p = \frac{m-m'}{m} \frac{1}{k} + \frac{m'}{m}$ and the tendency to hop to any of the nodes toward the leaves is $\frac{m-m'}{m} \frac{1}{k}$.

In the following, we solve the problem of the first-passage time from leaves to root for the set of parameters $\{L, p, m, q\}$. However, one can straightforwardly follow the proposed approach to calculate the MFPT between two arbitrary generations of the tree. By introducing the probability distribution $P_i(t)$ of being on a node with generation i at time step t , we practically map the problem onto an effective biased random walk on a 1D domain in the presence of temporal absorption along the path and at one of the boundaries. Using the initial condition $P_i(0) = \delta_{i,L}$, we construct a set of master equations for the dynamical evolution of $P_i(t)$. The probability evolves at the root ($i = 0$) and leaves ($i = L$) as $P_0(t) = P_0(t-1) + mpP_1(t-1)$ and $P_L(t) = m(1-p)P_{L-1}(t-1) + (1-q)P_L(t-1) + \delta_{0,t}$. At a bulk node with generation i , the evolution of $P_i(t)$ follows $P_i(t) = m(1-p)P_{i-1}(t-1) + (1-m)P_i(t-1) + mpP_{i+1}(t-1)$. By defining the z transform $P_i(z) = \sum_{t=0}^{\infty} P_i(t)z^t$, we obtain the following set of coupled equations:

$$P_0(z) = zP_0(z) + mpzP_1(z),$$

$$P_1(z) = (1-m)zP_1(z) + mpzP_2(z),$$

$$\vdots$$

$$P_i(z) = m(1-p)zP_{i-1}(z) + (1-m)zP_i(z) + mpzP_{i+1}(z),$$

$$\vdots$$

$$P_{L-1}(z) = m(1-p)zP_{L-2}(z) + (1-m)zP_{L-1}(z) + qzP_L(z),$$

$$P_L(z) = m(1-p)zP_{L-1}(z) + (1-q)zP_L(z) + 1. \quad (2)$$

After some algebra we obtain $P_i(z)$ in the general form. Then, the z transform of the FPT distribution to reach the root can be evaluated as $F(z) = mpzP_1(z)$ [27]. We derive an exact expression for the z transform of the FPT distribution [23]:

$$F(z) = \frac{2^{L+1}qA(z, m, p)}{(H_+^L - H_-^L)B(z, q, m, p) + (H_+^L + H_-^L)qA(z, m, p)}, \quad (3)$$

with

$$A(z, m, p) = \sqrt{1 + 2(m-1)z + [1 - 2m + (1-2p)^2m^2]z^2},$$

$$B(z, q, m, p) = q[1 - (m-1)z] + pm(-2 + 2z - qz),$$

and

$$H_{\pm} = \frac{1}{mpz} [1 + (m-1)z \pm A(z, m, p)].$$

The first-passage time distribution $F(\tau)$ can be obtained by inverse z transformation of $F(z)$. In order to check our lengthy analytical results for correctness, we compare them with the results of Monte Carlo simulations in Fig. 3, and we find them to be in perfect agreement.

Figure 3 shows that the tail of $F(\tau)$ decays exponentially with a slope α , which is independent of the initial conditions of entering the tree. Expectedly, α varies with the structural

Addendum II. Unraveling the structure of treelike networks from first-passage times of lazy random walkers

SHAEBANI, JOSE, SAND, AND SANTEN

PHYSICAL REVIEW E **98**, 042315 (2018)

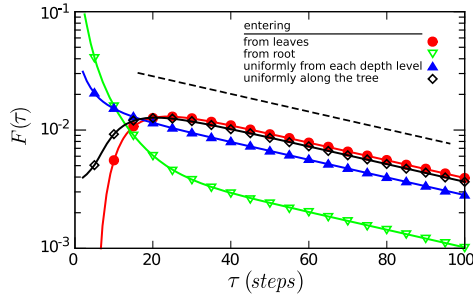


FIG. 3. First-passage time distribution for $L = 6$ and $p = m = q = 0.5$ and for different initial conditions of entering the tree. The solid lines are the analytical prediction of Eq. (3) and the symbols denote the simulation results. The exponential dashed line is given by Eq. (4).

properties L and p as well as the waiting probabilities m and q . While the tail behavior of the lengthy expression $F(\tau)$ cannot be necessarily expressed in a closed form in general, at least the existence of an exponential tail can be proved. $F(z)$ can be represented as the inverse of a polynomial $g(z, p, m, q, L)$ with j roots ($j \leq L$), thus it can be written as

$$F(z) = \frac{1}{(1 - a_1 z)^{b_1} \cdots (1 - a_j z)^{b_j}},$$

where the prefactors of z are functions of the parameter set $\{L, p, m, q\}$ and $b_1, \dots, b_j \leq L$. As a result, $F(\tau)$ can be written as a sum of a_k^t terms by partial fraction decomposition of $F(z)$ and applying inverse z transform. Therefore, one can approximate $F(\tau)$ by the leading exponential term $a_{k, \max}^t$ in the long-time limit. In view of the difficulty of extracting the roots of the polynomial and deducing a general form for the exponential asymptotic scaling, we choose the given set of parameter values in Fig. 3 and reconstruct the master equations (2) for the four different initial conditions of entering the tree introduced in the figure. It can be shown that the leading term of $F(\tau)$ follows

$$F(\tau) \sim \exp \left[- \ln \left(\frac{4}{2 + \sqrt{2 + \sqrt{3}}} \right) t \right] \quad (4)$$

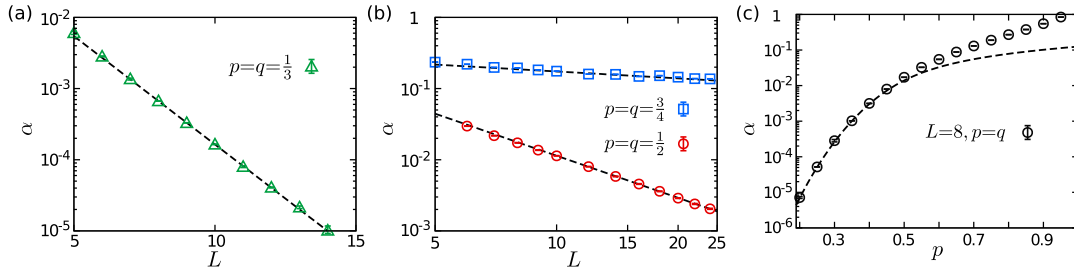


FIG. 4. The slope α of the exponential tail versus the extent of the tree for (a) $p < \frac{1}{2}$ (log-linear scales) and (b) $p \geq \frac{1}{2}$ (log-log scales) at $m = 1$. The dashed lines represent exponential or power-law fits. (c) α versus p at $L = 8$ and $m = 1$. The dashed line represents $\alpha = 1/(\tau)$ for the MFPTs obtained for different values of p at $L = 8$, $m = 1$, and $q = p$.

for all the initial conditions. Thus, the slope α of the exponential tail can be deduced as $\alpha = \ln [4/(2 + \sqrt{2 + \sqrt{3}})]$ for the given set of parameters in Fig. 3.

By extracting α for other values of the structural parameters L and p , we find that α scales exponentially with the extent of the tree L if $p < \frac{1}{2}$. However, a crossover to power-law scaling occurs for $p \geq \frac{1}{2}$, as shown in Figs. 4(a) and 4(b). The overall shape of $F(\tau)$ exhibits a plateau or even develops a peak at short times in general. The characteristic time to converge to the exponential tail behavior is reduced with decreasing p , such that the entire distribution $F(\tau)$ follows an exponential form in the limit $p \rightarrow 0$. Consequently, the mean value of $F(\tau)$ (i.e., the MFPT $\langle \tau \rangle$) is inversely related to the slope α at small values of p , as expected for exponential distributions. With increasing p , the form of $F(\tau)$ changes, thus the deviations from $\alpha = \frac{1}{\langle \tau \rangle}$ grow, as shown in Fig. 4(c).

The MFPT can be calculated as $\langle \tau \rangle = z \frac{d}{dz} F(z)|_{z \rightarrow 1}$. We expand Eq. (3) around $z = 1$ up to first-order terms, as $F(z) \sim F(z)|_{z \rightarrow 1} + (z - 1) \frac{d}{dz} F(z)|_{z \rightarrow 1} + \mathcal{O}((z - 1)^2)$, and obtain the following exact expression for the MFPT:

$$\langle \tau \rangle = \begin{cases} \frac{(m-q)L + qL^2}{mq}, & p = \frac{1}{2}, \\ \frac{L}{m(2p-1)} + \frac{pq - pm(2p-1)}{mq(2p-1)^2} \left[\left(\frac{1}{p} - 1 \right)^L - 1 \right], & p \neq \frac{1}{2}. \end{cases} \quad (5)$$

The MFPT diverges in the limit $L \rightarrow \infty$ as expected for infinite structures. It can be also seen that the MFPT scales linearly (exponentially) with the extent of the tree L in the limit $p \rightarrow 1$ ($p \rightarrow 0$), as the exponential term on the right-hand side of Eq. (5) vanishes (dominates). In the absence of waiting ($m = 1$) and assuming that the reflection probability q at the leaves equals the hopping probability p toward the root at the bulk nodes ($q = p$), Eq. (5) for $p \neq \frac{1}{2}$ reduces to Eq. (1). It is also notable that the total number of nodes N in a regular tree is given as $N = 2^L$. Thus, the first (last) term of $\langle \tau \rangle$ for $p \neq \frac{1}{2}$ grows logarithmically (linearly) with the number of nodes [17].

According to Eq. (5), the MFPT of an intermittent random walk to travel from the leaves to the root depends on the set of parameters $\{L, p, m, q\}$. Let us suppose that the intrinsic dynamics of the lazy random walkers, characterized by m and q parameters, can be tuned before they start to explore the structure as tracer particles. For a given set of m and

042315-4

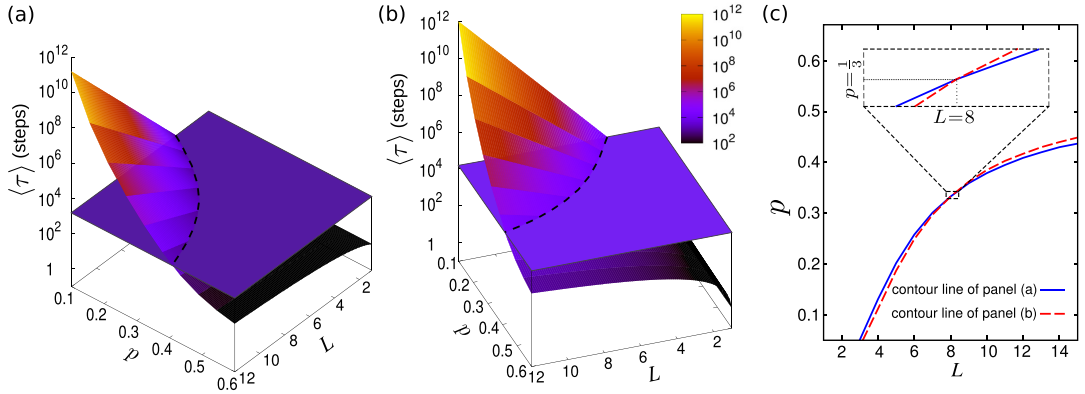


FIG. 5. Mean first-passage time via Eq. (5) versus the effective tendency p to jump toward the target and the tree extent L at (a) $m = 1$, $q = \frac{1}{3}$ and (b) $m = 0.05$, $q = 0.8$. The flat (constant MFPT) planes correspond to the MFPTs measured by tracer particles in experiments [chosen to be $\langle \tau \rangle \simeq 1500$ and $15\,000$ steps in panels (a) and (b), respectively]. The dashed line marks the intersection of the two surfaces, i.e., the contour line along which the MFPT equals the measured value. (c) Intersected contour lines in the (L, p) phase space. Inset: A zoomed view of the same plot near the intersection, which determines the unknown values of the structural parameters.

q , one obtains a surface in the $(L, p, \langle \tau \rangle)$ phase space via Eq. (5). The intersection of this surface with a flat plane representing the measured MFPT results in an iso-MFPT contour line in the (L, p) plane. An example is presented in Fig. 5(a) for $m = 1$ and $q = \frac{1}{3}$, assuming that the measured MFPT is $\langle \tau \rangle \simeq 1500$ steps. By repeating this procedure for a different set of m and q (with a different $\frac{m}{q}$ ratio), we can obtain another contour line in the (L, p) plane which intersects the previous one and, thus, uniquely determines the structure (i.e., L and p parameters). Figure 5(b) shows an example, where new parameter values $m = 0.05$ and $q = 0.8$ are chosen. Assuming that the measured MFPT for this lazy random walker is $\langle \tau \rangle \simeq 15\,000$ steps, we obtain the second contour line. The intersected contour lines in Fig. 5(c) reveal that the unknown tree has the extent $L = 8$ and the effective tendency $p \simeq \frac{1}{3}$ to move toward the root (corresponding to the node degree $k = 3$ in the case of uniform links). Therefore, having access to the MFPTs of lazy random walkers provides sufficient information to unravel the structure.

IV. DISORDERED NETWORKS AND EXPERIMENTAL UNCERTAINTIES

In derivation of the MFPT in the previous section, we considered a regular tree with the same tree extent along all branches and the same effective tendency to jump toward the target at every node. However, the real or virtual tree structures of interest are disordered. Particularly, heterogeneity in the degree of the nodes or in the capacity of the links has been widely studied in the context of complex networks. If the degree of the nodes or the weight of the links follow probability distributions, the effective tendency to move toward the target varies from node to node. The question arises of how far our analytical predictions for a regular tree remain valid when the network connectivity pattern becomes more and more diverse. To answer this question, we compare the analytical result of the MFPT for the constant p across the

tree, via Eq. (5), with the Monte Carlo simulation results where p dynamically fluctuates at each node around the mean global value. Before each jump, we assign a new value to the effective tendency to move toward the target, which is randomly taken from a uniform probability distribution in the interval $[p - \delta p, p + \delta p]$.

Figure 6(a) shows that the deviations of the MFPT from the analytical expression (5) grow with increasing the variation range δp . It can be seen that the significance of the impact on the MFPTs depends on the mean value of p . The higher the tendency to jump toward the target node, the more robust the analytical predictions become. For comparison, we define an upper threshold of 10% deviations of the MFPT from the theory and measure the critical value δp_c for the variation range of the parameter p in simulations, at which the fluctuations of the MFPT reach the 10% threshold. As shown in Fig. 6(b), broader fluctuations in p can be tolerated with increasing p . For example, even a broad range of 15% variations of p around the mean value $p = 0.7$ does not cause 10% deviations in the measured MFPT from the predicted value. In regular trees with node degree $k \gg 1$, $p \rightarrow 0$ and the analytical predictions are only applicable in the limit of small variations in the degree of the nodes across the tree. As mentioned above, we have chosen a uniform distribution for p . In order to clarify whether the form of the probability distribution influences the MFPT results, we compare uniform and normal distributions of p with the same mean and variance in Fig. 6(c). The mean value is fixed at $\langle p \rangle = \frac{1}{2}$ and a few examples for δp have been examined. It can be seen that the differences between the FPT distributions are negligible when the first two moments of the distributions of the parameter p are equal.

Next we investigate the influence of the structural disorder on the estimation of L and p , as the main objective of the present study. We perform simulations where either p or L is allowed to fluctuate around its mean value. Let us first consider a tree with $L = 10$ and allow p to dynamically vary around $\langle p \rangle = \frac{1}{2}$ in Monte Carlo simulations through the

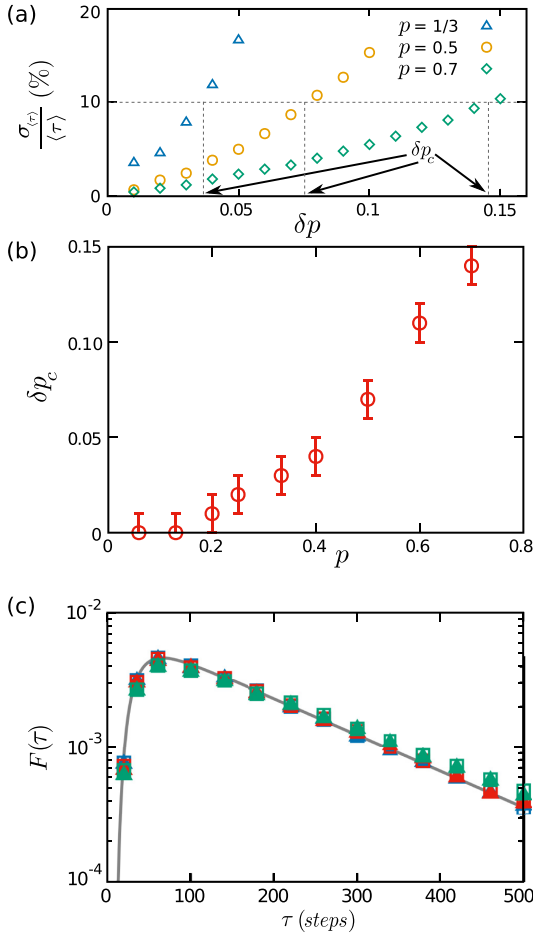


FIG. 6. (a) The standard deviation of the MFPT in simulations, scaled by the analytical prediction for $\langle \tau \rangle$ via Eq. (5), in terms of the variation range δp around its mean value p at $L = 10$ and $m = q = 1$. The results are shown for three different values of p . The horizontal dashed line corresponds to 10% error in the measured MFPT in simulations compared to the analytical prediction. (b) The critical variation range of the effective tendency δp_c (which causes 10% differences between simulation and theory) in terms of p . (c) The FPT distribution obtained via Eq. (3) (solid line) or simulations with $\delta p \sim 0.02$ (blue symbols), 0.04 (red symbols), and 0.10 (green symbols). The results of uniform probability distributions of p (full triangles) are compared to those obtained from normal distributions (open squares).

procedure which was previously explained in this section. By obtaining the MFPT from simulations and inserting it in Eq. (5), one can predict the structural parameters for a given standard deviation $\sigma(p)$. Assuming that one of the structural parameters L or p is known, we estimate the other one via Eq. (5) and compare it to its actual value in Fig. 7(a). The deviation from the analytical prediction grows with increasing

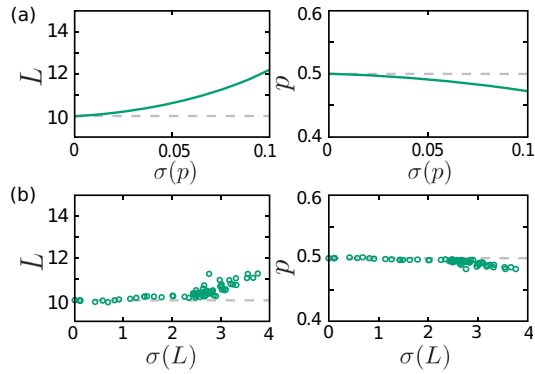


FIG. 7. The estimated values of the structural parameters L and p versus the structural disorder characterized by the variance of the parameters (a) p and (b) L . The horizontal dashed lines indicate the actual parameter values (unless varied). The parameter values (unless varied) are taken to be $L = 10$ and $p = m = q = \frac{1}{2}$. Each data point in panel (b) represents the result for a given static tree with a stochastic irregular branching pattern.

$\sigma(p)$; however, the effect is less pronounced for estimation of p compared to L . We also note that the deviations are smaller for higher values of $\langle p \rangle$ (not shown). Our theoretical approach is thus applicable to treelike networks with moderate disorder in their connectivity pattern. We remind that according to Eq. (5) the MFPT approaches a linear scaling when $p \rightarrow 1$, while it grows almost exponentially when p decreases toward zero. Therefore, it is expected that the variation of p around a mean value in the linear regime ($\langle p \rangle > \frac{1}{2}$) induces less deviations in the measured MFPTs, leading to a more accurate estimation of the structural parameters. On the other hand, fluctuations of p around a mean value in the exponential regime ($\langle p \rangle < \frac{1}{2}$) causes an overestimation of the MFPT on average, which increases the errors of the estimated structural parameters.

In order to study disorder in the extent of the tree, we generate static irregular trees with $\langle L \rangle = 10$ and standard deviation $\sigma(L)$ in the following way: we randomly allow the nodes to have their child nodes in a hierarchical manner starting from the root node. The procedure continues until the average extent of the tree reaches $\langle L \rangle = 10$. In Fig. 7(b), we have presented the results for a tree with $p = \frac{1}{2}$ and for $m = q = \frac{1}{2}$ as an example. The deviations from analytical predictions remain below 10% even in considerably heterogeneous trees with $\frac{\sigma(L)}{\langle L \rangle} \approx 40\%$.

In addition to disorder in the structure of the network, one may introduce uncertainty in tuning the experimental parameters m and q . For example, intermittent random walks induced by random trapping and release in cages or by stochastic temporal absorption along the path lead to statistical errors for the resulting waiting probabilities m and q . In order to assess the robustness of our analytical estimation of L and p in the presence of experimental uncertainties, we perform simulations where the structure is regular but the parameters m and q fluctuate around their mean values. In each of the Monte

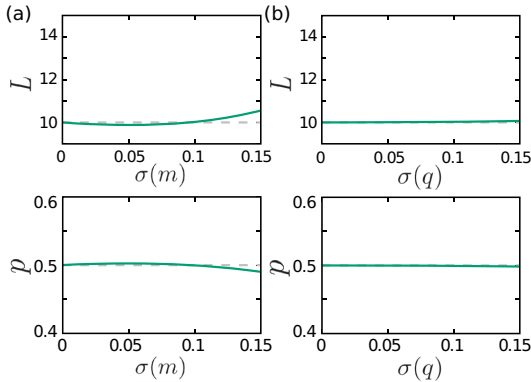


FIG. 8. The estimated values of the structural parameters L and p versus the experimental uncertainty characterized by the variance of the parameters (a) m and (b) q . The horizontal dashed lines indicate the actual parameter values. The parameter values (unless varied) are taken to be $L = 10$ and $p = m = q = \frac{1}{2}$. The mean values of the variable parameters are $\langle m \rangle = \frac{1}{2}$ and $\langle q \rangle = \frac{1}{2}$ in panels (a) and (b), respectively.

Carlo simulations, we vary only one of the experimental parameters m or q while the other one is fixed at its mean value. A new value is assigned to the variable parameter at each random walk step, which is randomly taken from a uniform distribution with standard deviation $\sigma(m)$ or $\sigma(q)$. For a given fluctuation range [either $\sigma(m)$ or $\sigma(q)$], we obtain the MFPT from simulations. Next, we insert the resulting MFPT (as well as $\langle m \rangle$, $\langle q \rangle$), and one of the structural parameters L or p in Eq. (5) to predict the remaining structural parameter. In Fig. 8, we compare the analytical estimations with the actual values to demonstrate the impact of uncertainty in the experimental parameters on the prediction of L and p . It can be seen that the predicted values of p or L insignificantly deviate from the actual values for moderate (even up to 15%) experimental uncertainties.

V. DISCUSSION AND CONCLUSION

We presented an analytical framework to calculate the first-passage properties of intermittent random walks on treelike networks in terms of the waiting probabilities at the bulk nodes and leaves as well as the structural properties of the network such as its connectivity and extent. We proposed

simple measurements of the mean-first-passage times of tracer particles entering the tree at the leaves and exiting from the root, to uniquely determine the structural properties. In regular trees, having access to the MFPT for only two different sets of waiting probabilities would be enough to unravel the structure. The idea of tuning the waiting probabilities of the random walkers to unravel the structure can be extended to other intrinsic dynamic properties such as the persistency of the walker [47,48]. Persistent random walkers can be employed to explore the structure of 1D domains and obtain their length and the effective bias to hop toward the target, even though assigning a persistency to the particle dynamics on a network topology is not well defined in general. Calculating the higher moments of the FPT distribution is another possibility. Since the i th moment $\langle \tau^i \rangle = (z \frac{d}{dz})^i F(z)|_{z \rightarrow 1}$ can be straightforwardly obtained, having access to the first two moments of the FPT distribution also enables one to uniquely determine the structure via our analytical framework. However, the resulting set of equations may be redundant in special cases and it is considerably more difficult to evaluate variance or higher moments of the FPT distribution in experiments.

We addressed the validity range of the analytical predictions in networks with diverse connectivity patterns or heterogeneous branching morphologies. In the presence of disorder in the structural parameters L and p or uncertainty in the experimental parameters m and q , even more measurements are required to determine the MFPT itself with a given accuracy. Therefore, it is naturally expected that the evaluation of the second moment of the FPT distribution with a given accuracy would be extremely time consuming in such cases. The advantage of considering intermittent random walks is that equipping particles with different diffusivity in experiments is possible, which makes our proposed measurements feasible in practice. The final remark is that the results obtained in this study are equivalently applicable to ordinary random walks on treelike structures which induce temporal absorption along the path or at the dead ends. A particularly relevant example is the transport in neuronal dendrites in the presence of biochemical cages along the dendritic tube.

ACKNOWLEDGMENTS

We thank Z. Sadjadi and J. Kertész for fruitful discussions. This work was funded by the Deutsche Forschungsgemeinschaft (DFG) through Collaborative Research Center SFB 1027 (Projects A7 and A8).

M.R.S. and R.J. contributed equally to this work.

- [1] D. ben-Avraham and S. Havlin, *Diffusion and Reactions in Fractals and Disordered Systems* (Cambridge University Press, Cambridge, 2000).
- [2] M. Felici, M. Filoche, and B. Sapoval, *Phys. Rev. Lett.* **92**, 068101 (2004).
- [3] Z. Sadjadi, M. F. Miri, M. R. Shaebani, and S. Nakhaee, *Phys. Rev. E* **78**, 031121 (2008).
- [4] E. Agliari, A. Blumen, and O. Mülken, *J. Phys. A* **41**, 445301 (2008).

- [5] E. Agliari and D. Cassi, *First-Passage Phenomena and Their Applications* (World Scientific, Singapore, 2014), pp. 96–121.
- [6] P. Tierno and M. R. Shaebani, *Soft Matter* **12**, 3398 (2016).
- [7] M. Kac, *Am. Math. Mon.* **73**, 1 (1966).
- [8] P. P. Mitra, P. N. Sen, L. M. Schwartz, and P. Le Doussal, *Phys. Rev. Lett.* **68**, 3555 (1992).
- [9] R. W. Mair, G. P. Wong, D. Hoffmann, M. D. Hürlimann, S. Patz, L. M. Schwartz, and R. L. Walsworth, *Phys. Rev. Lett.* **83**, 3324 (1999).

Addendum II. Unraveling the structure of treelike networks from first-passage times of lazy random walkers

SHAEBANI, JOSE, SAND, AND SANTEN

PHYSICAL REVIEW E **98**, 042315 (2018)

- [10] R. Krishna, *J. Phys. Chem. C* **113**, 19756 (2009).
- [11] F. F. Chen and Y. S. Yang, *Modell. Simul. Mater. Sci. Eng.* **20**, 045005 (2012).
- [12] D. J. Durian, D. A. Weitz, and D. J. Pine, *Science* **252**, 686 (1991).
- [13] G. Maret, *Curr. Opin. Colloid Interface Sci.* **2**, 251 (1997).
- [14] C. Cooper, T. Radzik, and Y. Siantos, *Internet Math.* **12**, 221 (2016).
- [15] E. Agliari, R. Burioni, D. Cassi, and F. M. Neri, *Theor. Chem. Acc.* **118**, 855 (2007).
- [16] E. Helfand and D. S. Pearson, *J. Chem. Phys.* **79**, 2054 (1983).
- [17] B. Wu, Y. Lin, Z. Zhang, and G. Chen, *J. Chem. Phys.* **137**, 044903 (2012).
- [18] D.-J. Heijs, V. A. Malyshev, and J. Knoester, *J. Chem. Phys.* **121**, 4884 (2004).
- [19] D. Katsoulis, P. Argyrakakis, A. Pimenov, and A. Vitukhnovsky, *Chem. Phys.* **275**, 261 (2002).
- [20] P. Argyrakakis and R. Kopelman, *Chem. Phys.* **261**, 391 (2000).
- [21] N. Spruston, *Nat. Rev. Neurosci.* **9**, 206 (2008).
- [22] H. Hering and M. Sheng, *Nat. Rev. Neurosci.* **2**, 880 (2001).
- [23] R. Jose, L. Santen, and M. R. Shaebani, *Biophys. J.*, doi:10.1016/j.bpj.2018.09.029.
- [24] V. Fleury, J.-F. Gouyet, and M. Leonetti, *Branching in Nature: Dynamics and Morphogenesis of Branching Structures, from Cell to River Networks* (Springer-Verlag, Berlin, 2001).
- [25] G. Szabó, M. Alava, and J. Kertész, *Phys. Rev. E* **66**, 026101 (2002).
- [26] B. Bollobás and O. Riordan, *Phys. Rev. E* **69**, 036114 (2004).
- [27] S. Redner, *A Guide to First-Passage Processes* (Cambridge University Press, New York, 2001).
- [28] B. D. Hughes and M. Sahimi, *J. Stat. Phys.* **29**, 781 (1982).
- [29] C. Monthus and C. Texier, *J. Phys. A* **29**, 2399 (1996).
- [30] D. Cassi, *Europhys. Lett.* **9**, 627 (1989).
- [31] S. H. Yook, H. Jeong, A.-L. Barabási, and Y. Tu, *Phys. Rev. Lett.* **86**, 5835 (2001).
- [32] E. Almaas, P. L. Krapivsky, and S. Redner, *Phys. Rev. E* **71**, 036124 (2005).
- [33] A. Barrat, M. Barthélemy, R. Pastor-Satorras, and A. Vespignani, *Proc. Natl. Acad. Sci. U.S.A.* **101**, 3747 (2004).
- [34] A. E. Krause, K. A. Frank, D. M. Mason, R. E. Ulanowicz, and W. W. Taylor, *Nature (London)* **426**, 282 (2003).
- [35] M. Khantha and V. Balakrishnan, *Pramana* **21**, 111 (1983).
- [36] L. Skarpalezos, A. Kittas, P. Argyrakakis, R. Cohen, and S. Havlin, *Phys. Rev. E* **88**, 012817 (2013).
- [37] R. Garcia-Pelayo, *Physica A* **384**, 143 (2007).
- [38] N. Pottier, *Physica A* **230**, 563 (1996).
- [39] G. H. Weiss, *Physica A* **311**, 381 (2002).
- [40] O. Benichou, A. M. Cazabat, A. Lemarchand, M. Moreau, and G. Oshanin, *J. Stat. Phys.* **97**, 351 (1999).
- [41] M. R. Shaebani, Z. Sadjadi, I. M. Sokolov, H. Rieger, and L. Santen, *Phys. Rev. E* **90**, 030701 (2014).
- [42] J. Masoliver, K. Lindenberg, and G. H. Weiss, *Physica A* **157**, 891 (1989).
- [43] A. E. Hafner, L. Santen, H. Rieger, and M. R. Shaebani, *Sci. Rep.* **6**, 37162 (2016).
- [44] Y. Kantor and M. Kardar, *Phys. Rev. E* **76**, 061121 (2007).
- [45] T. Huisinga, R. Barlovic, W. Knospe, A. Schadschneider, and M. Schreckenberg, *Physica A* **294**, 249 (2001).
- [46] A. D. Kachhah and N. Gupte, *Phys. Rev. E* **86**, 026104 (2012).
- [47] Z. Sadjadi, M. R. Shaebani, H. Rieger, and L. Santen, *Phys. Rev. E* **91**, 062715 (2015).
- [48] J. M. Newby and P. C. Bressloff, *Phys. Rev. E* **80**, 021913 (2009).

Addendum III Persistence-Speed Coupling Enhances the Search Efficiency of Migrating Cells

Authors: M. R. Shaebani^{1,2*†}, R. Jose^{1,†}, L. Stankevics³, F. Lautenschläger^{2,3,4} and L. Santen^{1,2}

¹ Department of Theoretical Physics, Saarland University, 66123 Saarbrücken, Germany

² Center for Biophysics, Saarland University, 66123 Saarbrücken, Germany

³ INM-Leibniz Institute for New Materials, 66123 Saarbrücken, Germany

⁴ Department of Experimental Physics, Saarland University, 66123 Saarbrücken, Germany

Manuscript in preparation

Author contributions:

* *Corresponding author: M. R. Shaebani.*

† *M. R. Shaebani and R. Jose contributed equally to this work.*

M. R. Shaebani and F. Lautenschläger designed the research. L. Stankevics and F. Lautenschläger performed the experiments. M. R. Shaebani developed the analytical model. R. Jose performed the simulations. All authors contributed to the analysis and interpretation of the results. M. R. Shaebani wrote the manuscript.

Abstract:

Migration of immune cells within the human body allows them to fulfill their main function of detecting pathogens. Adopting an optimal navigation and search strategy by these cells is of crucial importance to achieve an efficient immune response. Analyzing the dynamics of dendritic cells in our in vitro experiments reveals that the directional persistence of these cells is highly correlated with their migration speed, and that the persistence-speed coupling enables the migrating cells to reduce their search time. We theoretically introduce a new class of random search optimization problems by minimizing the mean first-passage time (MFPT) with respect to the strength of the coupling between influential parameters such as speed and persistence length. We derive an analytical expression for the MFPT in a confined geometry and verify that the correlated motion improves the search efficiency if the mean persistence length $\langle l_p \rangle$ is sufficiently shorter than the confinement size. In contrast, a positive persistence-speed correlation even increases the MFPT at long $\langle l_p \rangle$ regime, thus, such a strategy is disadvantageous for highly persistent active agents.

Persistence-Speed Coupling Enhances the Search Efficiency of Migrating Immune Cells

M. Reza Shaebani,^{1,2,*} Robin Jose,^{1,†} Ludger Santen,^{1,2} Luiza Stankevics,³ and Franziska Lautenschläger^{2,3,4}

¹Department of Theoretical Physics, Saarland University, 66123 Saarbrücken, Germany

²Center for Biophysics, Saarland University, 66123 Saarbrücken, Germany

³INM-Leibniz Institute for New Materials, 66123 Saarbrücken, Germany

⁴Department of Experimental Physics, Saarland University, 66123 Saarbrücken, Germany

Migration of immune cells within the human body allows them to fulfill their main function of detecting pathogens. Adopting an optimal navigation and search strategy by these cells is of crucial importance to achieve an efficient immune response. Analyzing the dynamics of dendritic cells in our *in vitro* experiments reveals that the directional persistence of these cells is highly correlated with their migration speed, and that the persistence-speed coupling enables the migrating cells to reduce their search time. We theoretically introduce a new class of random search optimization problems by minimizing the mean first-passage time (MFPT) with respect to the strength of the coupling between influential parameters such as speed and persistence length. We derive an analytical expression for the MFPT in a confined geometry and verify that the correlated motion improves the search efficiency if the mean persistence length $\langle \ell_p \rangle$ is sufficiently shorter than the confinement size. In contrast, a positive persistence-speed correlation even increases the MFPT at long $\langle \ell_p \rangle$ regime, thus, such a strategy is disadvantageous for highly persistent active agents.

A successful immune response crucially depends on its first steps: finding harmful pathogens. In general search and transport efficiency of random processes have been quantified by observables such as the diffusivity of randomly moving particles [1], the reactivity of transport-limited chemical reactions [2], the cover time to visit all sites of a confined domain [3, 4], or often by the mean first-passage time (MFPT) that a searcher needs to find a target [5, 6]. Optimal search strategies considered so far minimize the MFPT or equivalently the cover time with respect to one of the key parameters of the problem. This can be either a structural property of the environment in which the particle moves [7, 8] or a parameter of the stochastic motion (e.g., the persistency in active random searches [9], the resetting rate in diffusion processes with stochastic resetting to the initial position [10, 11], the ratio between the durations of diffusive and directed motion in intermittent searches [5, 12, 13], or the speed of the searcher when passing over a target location [14]). However, the influential factors governing the search efficiency are correlated in general. For instance, a universal coupling between migration speed and directional persistence has been recently reported for various cell lines mediated by retrograde actin flows [15]. Alternative optimal search strategies for such correlated stochastic processes need to be developed.

Adopting an efficient search and navigation strategy is of particular importance in biological systems as, for example, in search for specific target sites over a DNA strand by proteins [16–18], escape through small absorbing boundaries and targeted intracellular transport [7, 19], delivery of chemical signals in neurons [20–22], bacterial swimming and chemotaxis [5, 23–25], and animal foraging [14, 26, 27]. It is often hypothesized that the motility of mammalian cells enables them to effec-

tively fulfill their biological functions. Of particular interest is the migration of immune cells [28–30], which is expected to be optimized in the course of evolution to achieve an efficient immune response. Nevertheless, the optimality of the search for pathogens and other targets by immune cells has neither been precisely verified nor systematically studied. Understanding the mechanisms of adaptive search and clearance in the immune system opens the way toward more effective cancer immunotherapies and vaccine design.

In this Letter, we consider theoretically a correlated stochastic process and introduce, for the first time, a new

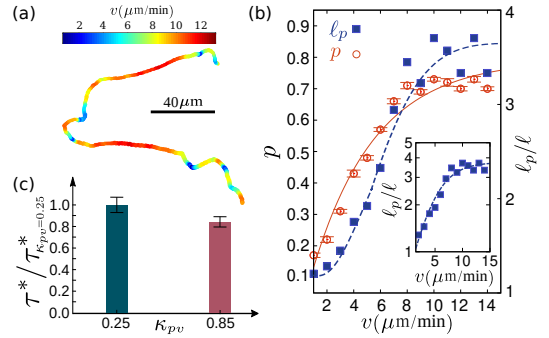


FIG. 1. (a) Sample cell trajectory, color coded with respect to speed. (b) Cell persistence p and persistence length ℓ_p (scaled by the mean distance ℓ between successive recorded positions) in terms of migration speed v . The solid line indicates an exponential saturation fit. The dashed line shows the fit via Eq. (1). Inset: Log-lin plot of ℓ_p/ℓ vs v . (c) Comparison between the conditional MFPT τ^* of two categories of cells with low and high p - v coupling strength κ_{pv} .

class of optimal search strategies based on tuning the strength of coupling between key parameters. Inspired by the dynamics of dendritic cells [15, 31], we consider the correlation between the migration speed v and directional persistence p of the searcher. The optimization is achieved by analytically calculating the MFPT and minimizing it with respect to the strength κ_{pv} of p - v coupling. The success of the scheme in improving the MFPT nontrivially depends on the ratio between the mean persistence length $\langle \ell_p \rangle$ of the searcher and the system size L ; in the regime $\langle \ell_p \rangle \ll L$ ($\langle \ell_p \rangle \sim L$), the correlated motion is advantageous (disadvantageous) for reducing the search time. We experimentally investigate the dynamics of dendritic cells (responsible for tissue patrolling and antigen capture [30, 32]) and expectedly observe a significant p - v correlation [15, 31] (see Fig. 1). Our data analysis also reveals an interesting inverse dependence of the MFPT on the coupling strength, in agreement with our analytical predictions for the low persistence regime.

Migration of dendritic cells.— To study the dynamics of migrating cells in our *in vitro* experiments, we tracked the two-dimensional motion of primary mouse immature dendritic cells with typical size of nearly ten micrometers derived from bone marrow of LifeAct-GFP knock-in mice. The motion was confined between the cell culture dish and a roof held by microfabricated pillars made out of Polydimethylsiloxane (PDMS) as described in [33] at a height of $3 \mu\text{m}$. Both surfaces were coated with PLL-PEG (0.5 mg/mL), a non-adhesive material to exclude movement by cell adhesion. The cell concentration was low enough to treat the cells as non-interacting. Cell nuclei were stained with Hoechst 34580 (200 ng/mL for 30 min) (Sigma Aldrich, St Louis, USA) and migration was recorded by epifluorescence microscopy for at least 6h at 37° with a camera of $6.5 \mu\text{m}$ pixel size and sampling rate of 20 frames/h.

A typical cell trajectory is shown in Fig. 1(a), evidencing that the path is more straight when the migration speed is higher. We quantify the cell persistence—the ability of the cell to maintain its current direction of motion— by $p = \cos\theta$ with θ being the orientational change at each recorded position [34–36], from which the instantaneous persistence length ℓ_p can be estimated as $\ell_p = \frac{\ell}{\ln|p|}$ (ℓ is the mean distance between two successive recorded positions) [37]. The leading contribution goes as $\mathcal{O}(\frac{\ell}{1-p})$. After averaging over all trajectories and speed binning intervals of $\Delta v = 1 \mu\text{m}/\text{min}$, we observe a clear coupling between the cell persistence p and the migration speed v , which can be fitted by an exponential saturation $p = p_\infty(1 - e^{-\gamma v})$, with $p_\infty \simeq 0.76$ and $\gamma \simeq 0.26$ [Fig. 1(b)]. The behavior of ℓ_p is well fitted by a logistic function

$$\ell_p = \frac{\ell_{p_\infty}}{1 + \left(\frac{\ell_{p_\infty} - \ell_{p_0}}{\ell_{p_0}}\right)e^{-\gamma v}}, \quad (1)$$

where ℓ_{p_0} is the persistence length of a nonpersistent

motion and $\ell_{p_\infty} \sim \frac{\ell_{p_0}}{1 - p_\infty}$. ℓ_p initially grows exponentially as $\ell_p \propto e^{\gamma v}$ [15] but eventually saturates to ℓ_{p_∞} at high speeds. To describe the overall coupling strength for individual cells we calculate the p - v correlation coefficient $\kappa_{pv} = \frac{\text{cov}(p,v)}{\sigma_p \sigma_v}$ for each cell. When averaged over all trajectories, a strong correlation $\bar{\kappa}_{pv} \simeq 0.9$ is obtained.

The key question is whether such a correlated random motion helps the immune cells to improve their search efficiency. To answer this, we selected two subpopulations of cells with distinct mean correlation coefficients $\kappa_{pv} = 0.25 \pm 0.05$ and $\kappa_{pv} = 0.85 \pm 0.05$. By calculating the conditional MFPT τ^* — i.e. over successful trials to reach a random hidden target— for each category (scaled by their mean speeds) and various target sizes we obtain 10–15% lower search times at higher correlations, as shown in Fig. 1(c). In order to understand these MFPT results we develop a stochastic model for correlated persistent search in the following, and prove that p - v coupling strategy is only beneficial for relatively weak persistencies, as in the case of dendritic cells.

Correlated persistent search model.— We consider a discrete-time persistent random walk on a two-dimensional square lattice of size L with periodic boundary conditions [Fig. 2(a)]. At each time step, the searcher moves v steps drawn from a speed distribution $f(v)$. It either continues along the previous direction of motion with probability $q+p$ or chooses a new direction, each

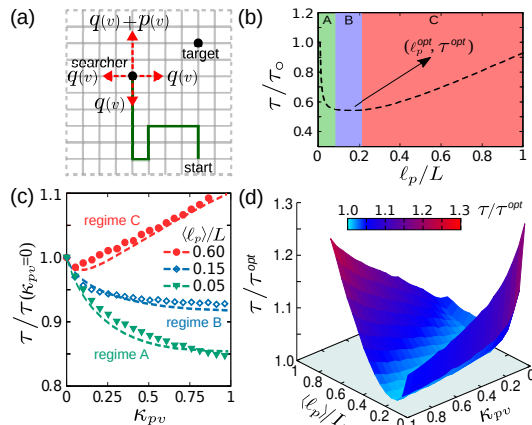


FIG. 2. (a) Sketch of the correlated persistent random search on a square lattice. (b) MFPT of a constant ℓ_p and v process, scaled by the MFPT of a diffusive searcher, vs ℓ_p normalized by $L=200$. (c) MFPT of a correlated p - v process, scaled by the MFPT when $\kappa_{pv}=0$, vs the coupling strength κ_{pv} . Each curve belongs to a different regime of $\langle \ell_p \rangle$ shown in panel (b). The dashed lines represent analytical predictions and the symbols are simulation results. (d) MFPT scaled by the optimal search time of the constant ℓ_p process vs κ_{pv} and scaled $\langle \ell_p \rangle$.

with a probability q , so that $4q+p=1$. The persistency parameter p (and thus q) depends on the instantaneous speed v and ranges from 0 (ordinary diffusion) to 1 (ballistic motion). The instantaneous persistence length can be obtained as $\ell_p = \sum_{\ell=1}^{\infty} \ell(q+p)^{\ell-1}(1-q-p) = \frac{4}{3} \frac{1}{1-p(v)}$.

Assuming that a single target of one lattice-unit size is located at \mathbf{r}_T (equivalent to regularly spaced targets on an infinite plane with $\frac{1}{L^2}$ density), we introduce $\tau(\mathbf{r}, v, \sigma)$ as the MFPT of reaching the target starting at position \mathbf{r} ($\neq \mathbf{r}_T$) with speed v and orientation $\sigma \in \{\rightarrow, \leftarrow, \uparrow, \downarrow\}$. The evolution of $\tau(\mathbf{r}, v, \sigma)$ can be described by the following backward master equation

$$\begin{aligned} \tau(\mathbf{r}, v, \rightarrow) = & \int dv' f(v') \left[(q+p) \tau(\mathbf{r}+v\hat{\mathbf{i}}, v', \rightarrow) + \right. \\ & \left. q \tau(\mathbf{r}-v\hat{\mathbf{i}}, v', \leftarrow) + q \tau(\mathbf{r}+v\hat{\mathbf{j}}, v', \uparrow) + q \tau(\mathbf{r}-v\hat{\mathbf{j}}, v', \downarrow) + 1 \right], \end{aligned} \quad (2)$$

and similar master equations for $\tau(\mathbf{r}, v, \leftarrow)$, $\tau(\mathbf{r}, v, \uparrow)$ and $\tau(\mathbf{r}, v, \downarrow)$. The possible velocities are limited to the integer values $v' \in [0, v_{\max}]$, which are supposed to be equally probable for simplicity. By introducing the Fourier transform $\tau(\mathbf{k}, v, \sigma) = \sum_{\mathbf{r}} \tau(\mathbf{r}, v, \sigma) e^{-i\mathbf{k} \cdot \mathbf{r}}$ and using $\int dv f(v) \tau(\mathbf{k}, v, \sigma) = \tau(\mathbf{k}, \sigma)$ for a uniform distribution $f(v)$, after some calculations we obtain

$$\tau(\mathbf{k}, \sigma) = \frac{F(\mathbf{k}) + S(\delta(\mathbf{k}) - e^{-i\mathbf{k} \cdot \mathbf{r}_T})}{1 - B_{\sigma}(\mathbf{k})}, \quad (3)$$

with $B_{\sigma}(\mathbf{k}) = \frac{1}{L^2} \sum_{v=0}^{v_{\max}} p(v) e^{ivk_{\sigma}}$, $F(\mathbf{k}) = \frac{1}{L^2} \sum_{v=0}^{v_{\max}} p(v) \sum_{\sigma} e^{ivk_{\sigma}} \tau(\mathbf{k}, \sigma)$, $S = L^2$, and $k_{\sigma} \in \{\mathbf{k} \cdot \hat{\mathbf{i}}, -\mathbf{k} \cdot \hat{\mathbf{i}}, \mathbf{k} \cdot \hat{\mathbf{j}}, -\mathbf{k} \cdot \hat{\mathbf{j}}\}$. Next we multiply Eq. (3) by $e^{ivk_{\sigma}}$ and sum over σ and v to derive a closed expression

$$F(\mathbf{k}) = \frac{A(\mathbf{k}) S (\delta(\mathbf{k}) - e^{-i\mathbf{k} \cdot \mathbf{r}_T})}{1 - A(\mathbf{k})}. \quad (4)$$

Here $A(\mathbf{k}) = \frac{1}{L^2} \sum_{v=0}^{v_{\max}} p(v) \sum_{\sigma} \frac{e^{ivk_{\sigma}}}{1 - B_{\sigma}(\mathbf{k})}$. Inserting $F(\mathbf{k})$ into Eq. (3) and averaging over all directions σ then yields

$$\tau(\mathbf{k}) = \frac{C(\mathbf{k}) S (\delta(\mathbf{k}) - e^{-i\mathbf{k} \cdot \mathbf{r}_T})}{1 - A(\mathbf{k})}, \quad (5)$$

where $C(\mathbf{k}) = \frac{1}{4} \sum_{\sigma} \frac{1}{1 - B_{\sigma}(\mathbf{k})}$. Finally, we apply the inverse Fourier transform (with the components of available modes being $k_i = \frac{2\pi n_i}{L}$, $n_i \in [0, L-1]$) and numerically average over all possible starting positions \mathbf{r} to obtain the overall MFPT τ .

In the case of constant persistence and speed, the results of a single-state persistent random search [9] are recovered, where the MFPT admits a minimum τ^{opt} at

an optimal persistence length ℓ_p^{opt} ; see Fig. 2(b). The optimal value $\frac{\ell_p^{\text{opt}}}{L}$ slightly decreases with increasing L . For correlated random searches, we consider a linear relation between ℓ_p and v for simplicity, corresponding to an expansion of Eq. (1) up to the first order term in v . We use

$$\frac{\ell_p}{\langle \ell_p \rangle} = \kappa_{pv} (\tilde{v} - 1) + 1, \quad (6)$$

with \tilde{v} being the scaled speed $\tilde{v} = \frac{v}{\langle v \rangle}$ and κ_{pv} the strength of persistence-speed coupling. The persistence length ℓ_p equals $\langle \ell_p \rangle$ for zero coupling coefficient and ranges within $[0, 2\langle \ell_p \rangle]$ for $\kappa_{pv} = 1$. By inserting the resulting persistence parameter $p(v)$ in the above formalism, we obtain $\tau(\langle \ell_p \rangle, \kappa_{pv})$. We checked that using Eq. (1) instead of Eq. (6) yields qualitatively analogous results to those reported in the following.

Combined effects of $\langle \ell_p \rangle$ and κ_{pv} on search efficiency.— Interestingly, Fig. 2(c) reveals different dependencies of the MFPT on the coupling strength κ_{pv} for choices of $\langle \ell_p \rangle$ taken from low, intermediate, and high persistence-length regimes A, B, C, as specified in Fig. 2(b). While τ is a decreasing function of κ_{pv} at low $\langle \ell_p \rangle$, the search efficiency at high mean persistence lengths even reduces with increasing κ_{pv} . Compared with the optimal choice of the constant persistence length strategy, the $p-v$ correlated search is always less efficient but approaches the search time τ^{opt} of the former strategy at $\langle \ell_p \rangle$ values around ℓ_p^{opt} ; see Fig. 2(d). Note that even at $\kappa_{pv} = 0$ the two strategies are not equivalent as the velocity is a variable quantity in the correlated search strategy (uniformly distributed within $[0, 2\langle v \rangle]$). The fact that the search time for the optimal choice of constant persistence length ℓ_p^{opt} is the absolute minimum over all correlated and uncorrelated persistent searches provides a qualitative explanation for the observed behavior in correlated random searches; inducing $p-v$ coupling at low $\langle \ell_p \rangle$ regime A helps to effectively increase the persistence of motion

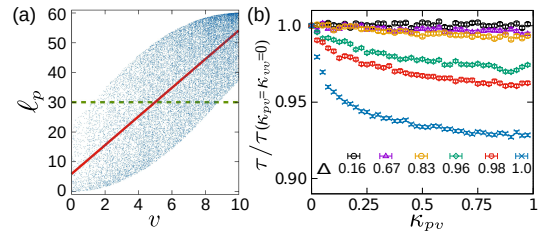


FIG. 3. (a) Example of correlated (v, ℓ_p) pairs generated in simulations with the coupling strength $\kappa_{pv} = 0.8$, drawn from a distribution with $\langle \ell_p \rangle = 30$ (dashed line) and width $\Delta = 1$. The solid line represents the $p-v$ coupling according to Eq. (6). $L = 200$. (b) Influence of the distribution width Δ on the MFPT as a function of the coupling strength κ_{pv} .

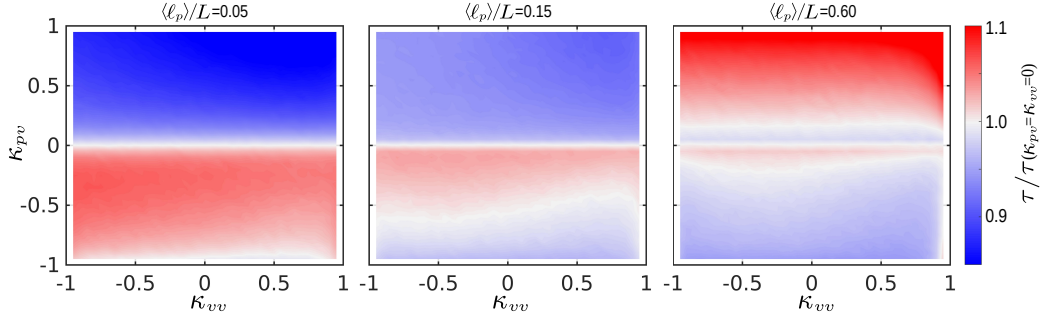


FIG. 4. Phase diagram of the MFPT in $(\kappa_{vv}, \kappa_{pv})$ plane for different values of mean persistence length $\langle \ell_p \rangle$. The search time of an uncorrelated p - v process in the absence of speed autocorrelations $\tau(\kappa_{vv}=\kappa_{pv}=0)$ is taken as the reference for comparison in each panel. The color intensity indicates the deviation from the uncorrelated-search time, with red (blue) reflecting a decrease (increase) in the search efficiency.

i.e. toward ℓ_p^{opt} . This is in sharp contrast to the high $\langle \ell_p \rangle$ regime C where the increase of effective persistence length by p - v correlations drags it away from ℓ_p^{opt} leading to a less efficient search. In the plateau regime B the p - v coupling is expectedly less influential. We can analytically verify a distinct dependency of τ on κ_{pv} at two extreme regimes $\langle \ell_p \rangle \rightarrow 0$ and $\langle \ell_p \rangle \rightarrow L$: Up to the leading order term, τ increases linearly with κ_{pv} at high persistency as $\tau(\langle \ell_p \rangle \rightarrow L) \sim \frac{1}{1-p} = a_1 \langle \ell_p \rangle \kappa_{pv} + a_2$; however, it decreases inversely with κ_{pv} when the persistency is extremely low, where it can be shown that $\tau(\langle \ell_p \rangle \rightarrow 0) \sim \frac{1-p}{1+p} = \frac{1}{b_1 \langle \ell_p \rangle \kappa_{pv} + b_2}$ ($a_1, b_1 > 0$).

Speed autocorrelations.— So far we analytically obtained the MFPT in the presence of persistence-speed correlation for a randomly varying speed at each time step. However, the successive instantaneous speeds can be correlated in general such that the searcher experiences a rather smooth speed change over time. For instance, we obtain a positive speed autocorrelation coefficient $\kappa_{vv} \approx 0.4$ for the dendritic cells in our experiments. To incorporate the speed autocorrelation in our analytical approach, one should replace the speed distribution $f(v')$ in the master equation (2) with the probability distribution of speed change $f(v-v')$. Analytical determination of the MFPT for autocorrelated speed however appears to be intractable; thus, we resort to Monte Carlo simulations to generate the desired stochastic motion.

In our simulations, we use the *sum-of-uniforms* algorithm [38–40] to correlate speed and persistence length and to include speed autocorrelation. The algorithm allows for inducing a certain degree of stochasticity in the resulting v and ℓ_p values, which is controlled by an additional parameter Δ . At each time step, first a new speed is chosen from a distribution around the current speed, which generates the demanded speed autocorrelation κ_{vv} . Then a new ℓ_p is chosen from a uniform distribution of ℓ_p values around the value determined by the

p - v coupling strength κ_{pv} and the local speed v according to Eq. (6) [red line in Fig. 3(a)]. This results in the cloud of blue dots in the figure. The parameter $\Delta \in [0, 1]$ tunes the actual slope of the cloud (the upper limit is however set by κ_{pv}) and allows for $\pm \Delta \langle \ell_p \rangle$ overall fluctuations. As shown in Fig. 3(b), τ approaches the MFPT of uncorrelated motion by decreasing the scattering parameter Δ . Here we show the simulation results for $\Delta=1$ corresponding to the widest overall range of persistence length $[0, 2\langle \ell_p \rangle]$. Once the new v and ℓ_p are determined, we extract the instantaneous persistence p of the searcher and move it v sub-steps within one time step by allowing it to change the direction of motion after each sub-step according to the persistence probability p .

The results of uncorrelated speeds $\kappa_{vv}=0$ in different regimes of $\langle \ell_p \rangle$ are shown in Fig. 2(c); the agreement between analytical predictions and simulation results is satisfactory. When speed autocorrelations are switched on, we find that the trends reported in Fig. 2(c) remain qualitatively valid. κ_{vv} plays a relatively insignificant role in determining the search time, while $\langle \ell_p \rangle$ and κ_{pv} are influential factors. We extend the range of correlation coefficients κ_{pv} and κ_{vv} to negative values for anti-correlated dynamics. Figure 4 summarizes the results in a phase diagram of search times in $(\kappa_{vv}, \kappa_{pv})$ plane. τ shows only modest dependence on κ_{vv} (subtle color intensity changes along horizontal lines) but variation of κ_{pv} may cause even up to 25% changes in the search time. Another point is that inducing p - v anticorrelation reduces the effective persistence of motion, thus, acts in the opposite direction, i.e. it improves the search time in regime C while leads to an increased search time in regime A.

The natural microenvironment for dendritic cells is the skin layers, with a density of a few hundred cells per mm^2 [41]. If each dendritic cell patrols, on average, an area of linear size $L \sim 100 \mu\text{m}$ with a persistence length of less than $10 \mu\text{m}$ (for typical speeds of 3 – $4 \mu\text{m}/\text{min}$ and

assuming even a high persistence $p \approx 0.7$ before reaching the $p-v$ saturation regime), then these cells belong to the weakly persistent regime A in Fig. 2(b) (indeed regime A is even more extended to right for such small patrolling areas); thus, $p-v$ correlations are beneficial in these systems to improve the search efficiency.

In summary, our study suggests improving the search efficiency of an active agent by inducing persistence-speed correlations and/or speed autocorrelations. Our key finding is that a correlated random motion is not necessarily an optimal search strategy in general; it is advantageous for dendritic cells moving with a persistence length much smaller than the size of the environment, however, highly persistent active agents should even adopt an anticorrelation between their speed and directional persistence to reduce their search time. By optimizing the search efficiency with respect to the strength of coupling between influential parameters, we introduced a new class of random search optimization problems with broad application to correlated stochastic processes.

This work was funded by the Deutsche Forschungsgemeinschaft (DFG) through Collaborative Research Center SFB 1027. We would like to thank A. M. Lennon Duménil for support with the dendritic cell system and Raphael Voituriez for discussions.

* corresponding author. shaebani@lusi.uni-sb.de

† equal contribution.

- [1] T. Bertrand, Y. Zhao, O. Bénichou, J. Tailleur, and R. Voituriez, *Phys. Rev. Lett.* **120**, 198103 (2018).
- [2] C. Loverdo, O. Bénichou, M. Moreau, and R. Voituriez, *Nat. Phys.* **4**, 134 (2008).
- [3] M. Chupeau, O. Bénichou, and R. Voituriez, *Phys. Rev. E* **89**, 062129 (2014).
- [4] M. Chupeau, O. Bénichou, and R. Voituriez, *Nat. Phys.* **11**, 844 (2015).
- [5] O. Bénichou, C. Loverdo, M. Moreau, and R. Voituriez, *Rev. Mod. Phys.* **83**, 81 (2011).
- [6] S. Redner, *A Guide to First-Passage Processes* (Cambridge University Press, Cambridge, 2001).
- [7] K. Schwarz, Y. Schröder, B. Qu, M. Hoth, and H. Rieger, *Phys. Rev. Lett.* **117**, 068101 (2016).
- [8] M. R. Shaebani, R. Jose, C. Sand, and L. Santen, *Phys. Rev. E* **98**, 042315 (2018).
- [9] V. Tejedor, R. Voituriez, and O. Bénichou, *Phys. Rev. Lett.* **108**, 088103 (2012).
- [10] M. R. Evans and S. N. Majumdar, *Phys. Rev. Lett.* **106**, 160601 (2011).
- [11] L. Kusmierz, S. N. Majumdar, S. Sabhapandit, and G. Schehr, *Phys. Rev. Lett.* **113**, 220602 (2014).
- [12] O. Bénichou, M. Coppey, M. Moreau, P.-H. Suet, and R. Voituriez, *Phys. Rev. Lett.* **94**, 198101 (2005).
- [13] C. Loverdo, O. Bénichou, M. Moreau, and R. Voituriez, *Phys. Rev. E* **80**, 031146 (2009).
- [14] D. Campos, V. Méndez, and F. Bartumeus, *Phys. Rev. Lett.* **108**, 028102 (2012).
- [15] P. Maiuri, J.-F. Rupprecht, S. Wieser, V. Rupprecht, O. Bénichou, N. Carpi, M. Coppey, S. D. Beco, N. Gov, C.-P. Heisenberg, et al., *Cell* **161**, 374 (2015).
- [16] M. A. Lomholt, T. Ambjörnsson, and R. Metzler, *Phys. Rev. Lett.* **95**, 260603 (2005).
- [17] J. Elf, G.-W. Li, and X. S. Xie, *Science* **316**, 1191 (2007).
- [18] M. Bauer and R. Metzler, *Biophys. J.* **102**, 2321 (2012).
- [19] Z. Schuss, A. Singer, and D. Holcman, *Proc. Natl. Acad. Sci. USA* **104**, 16098 (2007).
- [20] P. C. Bressloff and B. A. Earnshaw, *Phys. Rev. E* **75**, 041915 (2007).
- [21] R. Jose, L. Santen, and M. R. Shaebani, *Biophys. J.* **115**, 2014 (2018).
- [22] S. Fedotov and V. Méndez, *Phys. Rev. Lett.* **101**, 218102 (2008).
- [23] J. Najafi, M. R. Shaebani, T. John, F. Altegoer, G. Bange, and C. Wagner, *Sci. Adv.* **4**, eaar6425 (2018).
- [24] G. H. Wadhams and J. P. Armitage, *Nat. Rev. Mol. Cell Biol.* **5**, 1024 (2004).
- [25] E. Perez Ipiña, S. Otte, R. Pontier-Bres, D. Czerucka, and F. Peruani, *Nat. Phys.* **15**, 610 (2019).
- [26] F. Bartumeus and S. A. Levin, *Proc. Natl. Acad. Sci. USA* **105**, 19072 (2008).
- [27] G. Oshanin, O. Vasilyev, P. L. Krapivsky, and J. Klafter, *Proc. Natl. Acad. Sci. USA* **106**, 13696 (2009).
- [28] T. H. Harris, E. J. Banigan, D. A. Christian, C. Konradt, E. D. Tait Wojno, K. Norose, E. H. Wilson, B. John, W. Weninger, A. D. Luster, et al., *Nature* **486**, 545 (2012).
- [29] I. Lavi, M. Piel, A.-M. Lennon-Duménil, R. Voituriez, and N. S. Gov, *Nat. Phys.* **12**, 1146 (2016).
- [30] M. Chabaud, M. L. Heuzé, M. Bretou, P. Vargas, P. Maiuri, P. Solanes, M. Maurin, E. Terriac, M. Le Berre, D. Lankar, et al., *Nat. Commun.* **6**, 7526 (2015).
- [31] P.-H. Wu, A. Giri, S. X. Sun, and D. Wirtz, *Proc. Natl. Acad. Sci. USA* **111**, 3949 (2014).
- [32] M. L. Heuzé, P. Vargas, M. Chabaud, M. Le Berre, Y.-J. Liu, O. Collin, P. Solanes, R. Voituriez, M. Piel, and A.-M. Lennon-Duménil, *Immunol. Rev.* **256**, 240 (2013).
- [33] M. L. Berre, E. Zlotek-Zlotkiewicz, D. Bonazzi, F. Lautenschlaeger, and M. Piel, *Method. Cell Biol.* **121**, 213 (2014).
- [34] M. R. Shaebani, Z. Sadjadi, I. M. Sokolov, H. Rieger, and L. Santen, *Phys. Rev. E* **90**, 030701 (2014).
- [35] Z. Sadjadi, M. R. Shaebani, H. Rieger, and L. Santen, *Phys. Rev. E* **91**, 062715 (2015).
- [36] S. Burov, S. M. A. Tabei, T. Huynh, M. P. Murrell, L. H. Philipson, S. A. Rice, M. L. Gardel, N. F. Scherer, and A. R. Dinner, *Proc. Natl. Acad. Sci. USA* **110**, 19689 (2013).
- [37] M. R. Shaebani and Z. Sadjadi, arXiv e-prints p. arXiv:1909.05033 (2019).
- [38] V. C. Lakhan, *J. Stat. Comput. Simul.* **12**, 303 (1981).
- [39] R. T. Willemain and A. P. Desautels, *J. Stat. Comput. Simul.* **45**, 23 (1993).
- [40] J.-T. Chen, *Eur. J. Oper. Res.* **167**, 226 (2005).
- [41] L. G. Ng, A. Hsu, M. A. Mandell, B. Roediger, C. Hoeller, P. Mrass, A. Iparraguirre, L. L. Cavanagh, J. A. Triccas, S. M. Beverley, et al., *PLOS Pathog.* **4**, e1000222 (2008).

Addendum IV Bidirectional non-Markovian exclusion processes

Authors: R. Jose, C. Arita and L. Santen

Department of Theoretical Physics & Center for Biophysics, Saarland University,
66123 Saarbrücken, Germany

Journal of Statistical Mechanics: Theory and Experiment 2020, Forthcoming.
arXiv: 1912.08647

Author contributions:

Corresponding author: R. Jose.

L. Santen supervised the research. R. Jose and C. Arita developed the theory and performed the simulations. R. Jose wrote the manuscript and generated the figures. All authors contributed to the analysis and interpretation of the results. All authors contributed to the revision of the manuscript.

Abstract:

Bidirectional transport in (quasi) one-dimensional systems generically leads to cluster-formation and small particle currents. This kind of transport can be described by the asymmetric simple exclusion process (ASEP) with two species of particles. In this work, we consider the effect of non-Markovian site exchange times between particles. Different realizations of the exchange process can be considered: The exchange times can be assigned to the lattice bonds or each particle. In the latter case we specify additionally which of the two exchange times is executed, the earlier one (minimum rule) or the later one (maximum rule). In a combined numerical and analytical approach we find evidence that we recover the same asymptotic behavior as for unidirectional transport for most realizations of the exchange process. Differences in the asymptotic behavior of the system have been found for the minimum rule which is more efficient for fast decaying exchange time distributions.

20 January 2020

Bidirectional Non-Markovian Exclusion Processes

Robin Jose, Chikashi Arita and Ludger Santen

Department of Theoretical Physics & Center for Biophysics, Saarland University,
66123 Saarbrücken, Germany

E-mail: santen@lusi.uni-sb.de

Abstract. Bidirectional transport in (quasi) one-dimensional systems generically leads to cluster-formation and small particle currents. This kind of transport can be described by the asymmetric simple exclusion process (ASEP) with two species of particles. In this work, we consider the effect of non-Markovian site exchange times between particles. Different realizations of the exchange process can be considered: The exchange times can be assigned to the lattice bonds or each particle. In the latter case we specify additionally which of the two exchange times is executed, the earlier one (minimum rule) or the later one (maximum rule). In a combined numerical and analytical approach we find evidence that we recover the same asymptotic behavior as for unidirectional transport for most realizations of the exchange process. Differences in the asymptotic behavior of the system have been found for the minimum rule which is more efficient for fast decaying exchange time distributions.

1. Introduction

One of the broadly investigated fields in non-equilibrium physics is actively driven transport. These processes can be found in different topics such as pedestrian dynamics [1, 2, 3, 4], vehicle traffic [5, 6, 7, 3], and intracellular transport of molecular motors along cellular filaments [8, 9, 10, 11, 12, 13, 14].

A common tool to model active transport is a lattice gas [15, 5]. These stochastic processes are defined in a very simple way, but lead to many interesting phenomena [16]. Particles hop stochastically to their nearest neighbor sites on the lattice, but the hopping rates are spatially biased, and this asymmetry causes a non-vanishing flow of particles in a specific direction. The particular case where particles are allowed to unidirectionally hop in one dimension is called the totally asymmetric exclusion process (TASEP) [17]. One of the most basic assumptions in the TASEP is that each site of the lattice is either occupied by a particle or empty. Due to this exclusion principle, hopping is prohibited if the target site is already occupied by another particle. Therefore particles behave as an obstacle for each other, in other words, particles themselves serve as an environment and influence motility.

In bidirectional transport, however, particles have to be transported in opposite directions. Adaptation of the TASEP can be done by distinguishing two different species

arXiv:1912.08647v2 [nlin.CG] 17 Jan 2020

of particles with opposing directions on the same lattice. By introducing an position exchange rate, several intriguing scenarios have been reported, such as spontaneous symmetry breaking [18, 19]. In case of slow position exchange interactions, the particle flux is determined by the exchange times of particles from different species similar to a defect in the unidirectional TASEP [20]. Bidirectional TASEP models have been modified by introducing a second dimension to describe pedestrian dynamics [21, 22] or intracellular traffic on polar filaments by adding additional lanes [23, 24, 9]. Despite situations where symmetry is broken and the system organizes into lanes [22], particle interactions often lead to cluster formation and is therefore a limiting factor for transport [25].

In this paper, the focus is on active particles in confinement. Here, not only the aspect of non-equilibrium drive but also crowded and confined environments is expected to heavily influence transport processes. In the field of glass theory for example, a popular approach is to describe a particle trapped inside a *cage*, denoting the potential created by its neighbor particles [26]. Such interactions can affect the waiting time distribution of particle movements as it can be seen in a trap model by Bouchaud *et al.* [27]. Here, a particle falls into a trap of potential depth E which is exponentially distributed and escape from it following a Poisson process with a rate depending on the energy E . This combination leads to algebraically (power law) distributed waiting times for particles to escape from traps. It is therefore not guaranteed that in a complex environment, properties from an exponential distribution, resulting in constant rates which are typically used in TASEP models. However, the choice of waiting time distribution can be crucial for the systems phenomena because heavy tails induce a higher statistical weight for extreme values such as for the scale free family of Pareto distributions [28].

Recent studies by Concannon *et al.* [29] and Khoromskaia *et al.* [30] took a step forward to investigate transport behavior in the framework of unidirectional exclusion processes for non-Markovian waiting time distributions. It was found that, beside a fluid phase, the particles form condensates which are complete in space and time and hence a flux depending on the system size. This phenomenon differs from typical condensations appearing beside a stable current flowing out of clusters which is seen in models related to Markovian processes [25, 31].

The influence of crowded environments reflected in non-Poissonian waiting times on bidirectional transport is however not fully understood. Combining the aspects of bidirectional lattice gases and non-Poissonian waiting time distributions for exchange processes, here we will investigate two-species non-Markovian TASEPs.

This work is organized as follows. In section 2, we develop the model including three sub-versions for realizing exchange process between particles. We then show analytical estimations and simulation results for single and many particle dynamics in section 3 and compare them no simulation results. Finally we discuss our results in section 4.

2. The model

2.1. Two particle species with holes - a motivation

In order to mimic bidirectional transport on a track we first introduce plus- and minus-directed particles on a one-dimensional lattice of L sites, each of which is either occupied by a plus (“+”) particle, occupied by a minus (“-”) particle, or empty. Empty sites are denoted as holes if the particle density $\rho < 1$. Particles are identical up to their direction. We have three types of stochastic, microscopic events between two neighboring sites, i.e.

$$+0 \Rightarrow 0+, \quad (1)$$

$$0- \Rightarrow -0, \quad (2)$$

$$+- \Rightarrow -+. \quad (3)$$

This two-species TASEP has two conserved quantities, i.e. the numbers N_{\pm} of plus and minus particles, under periodic boundary conditions.

In a crowded environment, the exchange process (3) can be very different from free hopping events and turn out to be the major criterium for estimating the particle flux similar to bottlenecks in unidirectional exclusion processes [20]. In a first approach we therefore impose Poissonian stochasticity on the normal jumps (1) and (2), but a heavy tailed non-Markovian waiting time distribution on exchange processes (3) in this section. It has been observed that the particle flux is heavily influenced by particle condensates, both in a two-species Markovian TASEP [18] and in a one-species non-Markovian TASEP [29]. We see a similar phenomenon in first results of our two-species non-Markovian model, (figure 1 (a)). Macroscopic clusters block particle flow for a long time interval interrupted by short boosts of particles hopping in a free space outside the clusters. This blockage is the major inhibitor of particle flux so that the waiting time distribution for exchange processes mainly controls the transport property of our system. We therefore focus on the cluster region indicated by the green ellipse in figure 1 (a) leaving only the two states “+” and “-” for a site in the lattice in the following.

2.2. Two-species model without holes

By concentrating on clusters and therefore neglecting holes, we consider a system fully occupied by plus and minus particles without holes $N_+ + N_- = L$, for which an exemplary configuration is given in figure 1 (b).

We remark that usually the two-species TASEP with $N_+ + N_- = L$ is considered as standard TASEP below. We will explain the difference to the standard one-species TASEP in detail.

We first consider the standard one-species TASEP, where each site i takes states $\eta_i = 1$ (occupied by a particle) or $\eta_i = 0$ (empty). In most of the cases of the TASEP, the exponential distribution $p(t) = \alpha^{-1}e^{-\alpha t}$ ($t > 0$) is used to generate waiting times between two consecutive stochastic events, hence the TASEP is usually a Markov process. The

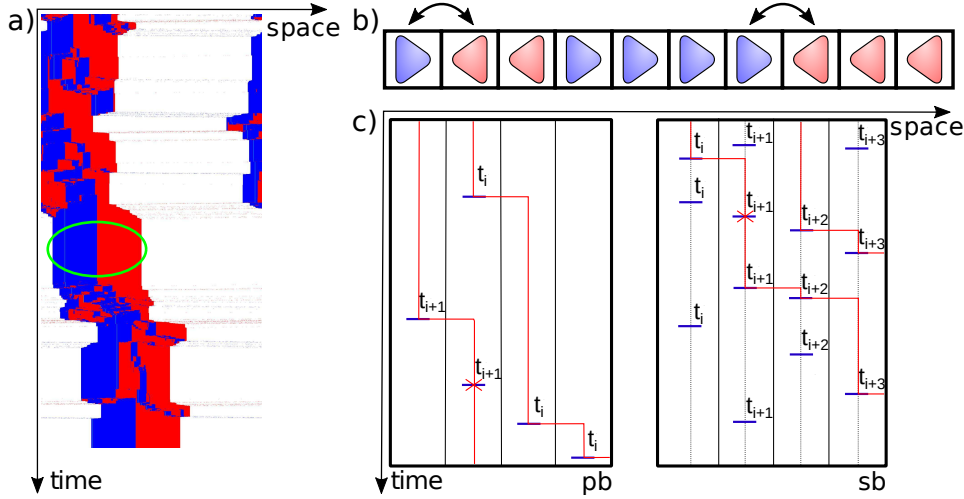


Figure 1: (a) Kymograph section of a simulation of our two-species TASEP with holes, color-coded as plus particles in blue, minus particles in red and holes in white. Hopping times (1) and (2) are distributed exponentially, exchange times (3) by a power law. The system size is $L = 1000$ with $N_+ = N_- = 200$, the shown time interval is approximately 15000 time units. In this paper, we focus on the cluster, indicated by a green ellipse in the plot, leading to the model without holes defined in chapter 2.1. (b) Scheme of the two-species model without holes. Triangles mimic particles, the tip indicates the direction. Exchange processes are only allowed for the configuration $(+-)$ (3). (c) Comparison of the two update schemes particle-based (left) and site-based (right) regarding particle trajectories (red lines). Timelines (dashed lines) for hopping events (blue bars) are carried by particles, hence identical to the red trajectory line in the left scheme or are fixed to the sites (right). Hopping events can be rejected due to exclusion (red crosses).

parameter α stands for the hopping rate and is independent of time or the current system state. A common way to assign waiting times to the Markovian TASEP is to use Gillespie's *direct method* or *first reaction method* [32]. In the latter one, times are generated from the exponential distribution for every possible hopping transition but only the smallest one determines the process which is executed and the other times are not used in the update mechanism anymore. In order to increase computational efficiency, a modified waiting time algorithm called *next reaction method* [33] is storing the assigned times for every process and realizing them successively if the transition is allowed.

Using the next reaction method, we distinguish two ways to assign waiting times to the Markovian TASEP, illustrated in figure 1 (c). The first one is a *site-based* update. We generate and store a series of times $\{t_i^1, t_i^2, \dots\}$ for each *bond* between sites i and

$i + 1$. The difference $t_i^{k+1} - t_i^k$ with $t_i^0 = 0$ must obey the exponential distribution. At time $t = t_i^k$, one checks whether the local configuration is appropriate for hopping, i.e. $\eta_i = 1, \eta_{i+1} = 0$. If this is the case, we move the particle from i to $i + 1$. If not, the move is rejected. The second one is a *particle-based* update. We give a series of times $\{t_i^1, t_i^2, \dots\}$ to each particle labeled by i . Again the difference $t_i^{k+1} - t_i^k$ should follow an exponential distribution. The particle i *attempts* to hop to its right neighbor site at time $t = t_i^k$, but the jump is again allowed only when the target site is empty. These two update schemes eventually yield equivalent dynamics to the particles, as long as we use an exponential distribution.

However, for a probability density function (PDF) $p(t)$ which belongs to a power law

$$p(t) = \begin{cases} 0 & 0 < t < 1, \\ (\gamma - 1)t^{-\gamma} & t > 1, \end{cases} \quad (4)$$

with an exponent $\gamma > 1$ this equivalence does not hold anymore. We remark that the algebraic distribution violates the Markov property so that we use the next reaction method which is not equivalent to Gillespie's methods anymore. This is similar to the method used in [29, 34] to evolve the system in time. See Appendix C for details of the algorithm to perform simulations of our model.

We recall that there are plus and minus particles, but no holes. As shown in figure 1 (b), only the local exchanges of plus and minus particles are effective stochastic events in this case. This means that particle hopping refers to position exchange between neighboring particles. Instead of hopping of a single particle to an empty site, the exchange of particles in general depends on the status of both particles. We need more detailed rules to define the exchange process.

The generalization of the site-based update to our non-Markovian TASEP is straightforward. We generate the time series $\{t_i^1, t_i^2, \dots\}$ for each bond, such that now the difference $t_i^{k+1} - t_i^k$ obeys the algebraic distribution (4). If we find $\eta_i = +$ and $\eta_{i+1} = -$ at time $t = t_i^k$, we simply exchange the positions, i.e. we get a new configuration with $\eta_i = -$ and $\eta_{i+1} = +$.

On the other hand, the particle-based update becomes a little complicated, and we need to further divide it into sub-schemes. The simplest one is considered as follows. We only assign the time series to the $+$ particles. At time $t = t_i^k$, the $+$ particle labeled by i wants to hop rightward. This is allowed only if there is a $-$ particle on the target site. In other words, $-$ particles are regarded as holes, and the systems is completely identical to the one-species non-Markovian TASEP that was introduced by Concannon *et al.* Thus, we name this rule *particle-based-asymmetrical* update, because this case does not hold plus-minus (or particle-hole after the identification) symmetry for Non-Markovian processes.

Now we wish to look for rules which do not break the plus-minus symmetry to define two-species bidirectional transport using the particle-based approach. We assign a time-series to each plus and minus particle $\{t_j^1, t_j^2, \dots\}$. At time $t = t_j^i$ the particle is

activated if a “+−” configuration is given. We now consider two different local update schemes for a plus particle i with waiting time t_i^k and a minus particle with waiting time t_j^m which are located at neighboring sites l (plus particle) and $l + 1$ (minus particle).

1) The *minimum rule*: An exchange between a pair of “+−” particles is executed if one of the two particles is active. This means that the minimum of the two waiting times determines the particle exchange.

2) The *maximum rule*: An exchange of the particles is executed if both particles are active, i.e. a particle exchange happens after $\max\{t_i^k, t_j^m\}$. In both cases, the particles become passive after exchanging positions.

Let us summarize the four types of the update rules in the following:

$$\left\{ \begin{array}{l} \text{site-based} \\ \text{particle-based} \end{array} \right\} \left\{ \begin{array}{l} \text{asymmetric} \\ \text{symmetric} \end{array} \right\} \left\{ \begin{array}{l} \text{maximum} \\ \text{minimum} \end{array} \right\} \quad (5)$$

3. Results

In this section, we show simulation results of our non-Markovian two-species TASEP, with a completely filled system, i.e. $N_+ + N_- = L$. We first discuss the site-based update from [30] as an algorithm for bidirectional transport in section 3.1 and then the previously described three types of particle-based rules in section 3.2. For each of them we evaluate dynamics by measuring the PDFs for the *effective* waiting time, i.e. the duration between two realized exchange processes of a particle. We discuss the effective waiting time distribution, in the following two situations; the system with only one plus particle and $L - 1$ minus particles called *single particle dynamics* (spd), and the equally-filled case where $N_+ = N_-$ called *many particle dynamics* (mpd). We discuss the spd as a reference in order to highlight the collective effects modifying the original PDF $p(t)$ to the PDF for effective waiting times of exchange processes. With many particle dynamics, we investigate the influence of exclusion on the effective PDF. In case of mpd, we also investigate transport efficiency by measuring particle flows. We compare the flows for the three symmetrical model rules in section 3.3.

3.1. Site-based model

The first bidirectional update we deal with is the site-based model inspired by [30]. We start with spd, i.e. the situation where there is only one plus particle, i.e. $N_+ = 1$ and $N_- = L - 1$, and we probe its motion in the environment of minus particles. We give analytical estimates for and measure by simulations the effective waiting time distribution for site-exchange events, and compare the tail exponents of this quantity.

For the site-based update scheme, analytical estimates can be deduced from renewal theory as in [30]. Let us assume that the plus particle arrives at a site i , where an internal clock is already running since the last event on that site at time t_i^k , giving the clock an

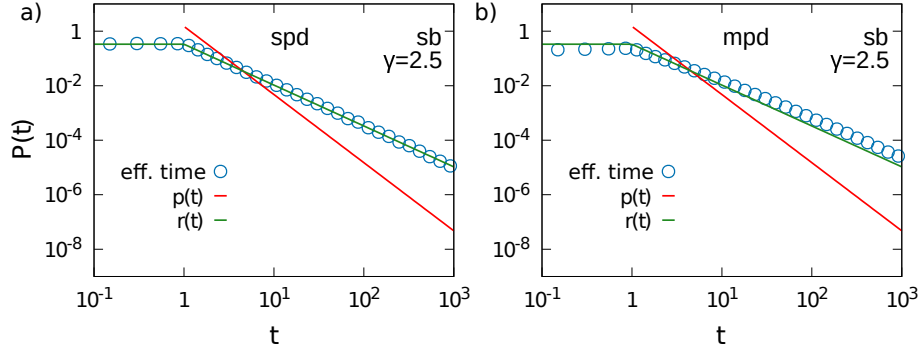


Figure 2: **Site-based rule:** PDFs of the effective exchange time for a system of $L = 100$ for the site-based rule. (a) Single-particle dynamics, i.e. $N_+ = 1$ and $N_- = L - 1$. (b) Many-particle dynamics, i.e. $N_+ = N_- = L/2$.

age $t - t_i^k$. The particle has to wait for the remaining time until t_i^{k+1} to execute the following step. This remaining time is called the *residual* waiting time distributed by the PDF $r(t)$ which in general is different from the original PDF $p(t)$. In the case where $p(t)$ is given by equation (4), one finds the residual waiting time PDF in the form

$$r(t) = \begin{cases} \frac{\gamma-2}{\gamma-1} & 0 < t < 1 \\ \frac{\gamma-2}{\gamma-1} t^{1-\gamma} & t \geq 1, \end{cases} \quad (6)$$

(see Appendix A for details). We note that $r(t) > 0$ even for $0 < t < 1$, while the original $p(t)$ is zero. More remarkably, the residual waiting time has a tail exponent shifted by 1, meaning that very large values have a higher statistical weight than the original PDF $p(t)$. In figure 2 (a), our simulation results for spd agree to the residual waiting time $r(t)$.

As a next step, we introduce $N_+ = L/2$ plus particles, to check if the exclusion between plus particles further modifies the PDF. Results are shown in figure 2 (b) where the simulation results for exchange times also follow the asymptotics of $r(t)$ calculated for a single particle. This similar result is expected since the waiting times are renewed in both cases for every site in the lattice, no matter if a plus particle or a minus particle is occupying the site.

After discussing the influence of the used update method and the particle interaction on the PDF of exchange times, we will continue by examining transport properties in a bidirectional, two-species system. As discussed of effective exchange time distributions, we will continue by examining how these effects are reflected in the transport properties in the bidirectional two-species TASEP with $N_+ = N_- = L/2$.

A common way to measure the transport efficiency of the system is the particle flux J . In [29], it was shown that for the unidirectional non-Markovian TASEP, system size has an impact on J in the clustering phase. Since we find similar shifts of the PDF for the site-based update, we also expect a transition from a size-dependent to a size-

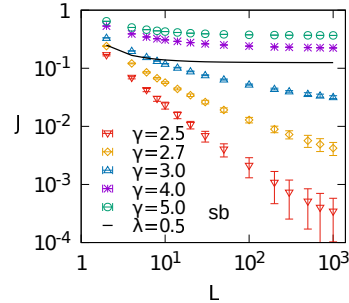


Figure 3: **Site-based rule:** Length dependency of the particle flux J for different values of γ in the PDF (4) and mpd. The black line serves as a comparison to the flux generated by an exponential distributed waiting times with exponent λ .

independent regime with growing γ . We test this transition by plotting the particle flux versus the length of the system in figure 3 for different exponents γ . Up to a finite-size effect, no significant dependency of J is observed when using a $\gamma > 3$ in the simulations. The flow converges for large L , so that no significant size-dependency is observed for $L > 100$.

However, J is decreasing with the system size for $\gamma < 3$. At the same time, the error bars are larger and it is difficult to judge the limit for infinite system size from numerical results. It is, therefore, necessary to argue with additional information about a transition from length dependency to constant fluxes. From the residual waiting time, we know that the average effective waiting time diverges at $\gamma = 3$. So we expect the flux to vanish below this critical value $\gamma_c = 3$ for infinite systems similar as pointed out in [30]. Below γ_c , the transport efficiency is determined by the asymptotics of the effective waiting time distribution. This effect induces a strong size dependence of the flow and

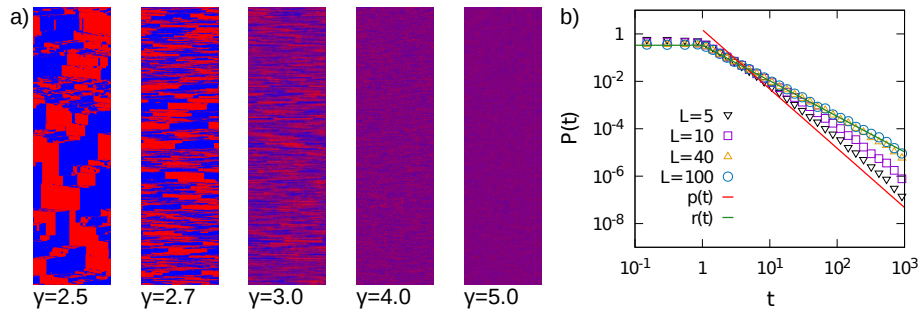


Figure 4: (a) Kymographs for the site-based model with runtime: $8 \cdot 10^{10}$ system size $L = 1000$ and equal particle numbers $N_+ = N_-$. For $\gamma < 3$ it is computationally hard to achieve stationary states. (b) Finite size effects in PDFs for spd following the site-based model with an exponent $\gamma = 2.5$.

at the same time increases the relaxation times of the system.

In order to illustrate the computational complexity, we show kymographs of a system of length $L = 1000$ which cover a time period of $8 \cdot 10^{10}$ time units for different exponents in figure 4 (a). Homogeneous spatiotemporal structures are obtained for $\gamma \geq 4$, while stable clusters emerge for $\gamma \leq 3$. In this regime, the lifetime of the clusters are comparable to the simulation time, which make it difficult to reach the stationary state of the system numerically. The slow relaxation of the system is caused by rare extreme values for the waiting times which develop in an aging phase inside a cluster and block other exchange events such as in [29]. We estimate the uncertainty of J by using the partial time averages $J_n = \left(\sum_{t=t_n}^{t_n+\Delta} J_t \right) / \left(\sum_{t=t_n}^{t_n+\Delta} t \right)$ where Δ is the complete time of measurement divided by the number of partial blocks and $t_n = n\Delta$.

For the site-based model, we expect that the residual waiting time PDF (6) describes exactly the effective exchange time distribution. The results of our simulations, however, slightly differ from this prediction. We expect that the small deviation can be attributed to a finite-size effect, since local waiting times may exceed the typical time a particle needs for a complete tour in a finite periodic system. This finite-size effect is observable in figure 4 (b) where tails differ from $r(t)$ for small system sizes.

3.2. particle-based models

3.2.1. Asymmetrical rule As a reference system for particle-based updates, we start with the asymmetrical rule, which is identical to the model of Concannon *et al.* [29]. In the paper, it was pointed out that interaction via exclusion leads to a shift of one for exponents in the hopping time PDF for a unidirectional many particle system. Again, we will show PDFs for single-particle and many-particle dynamics.

The spd under the particle-based, asymmetric update rule is much easier than for

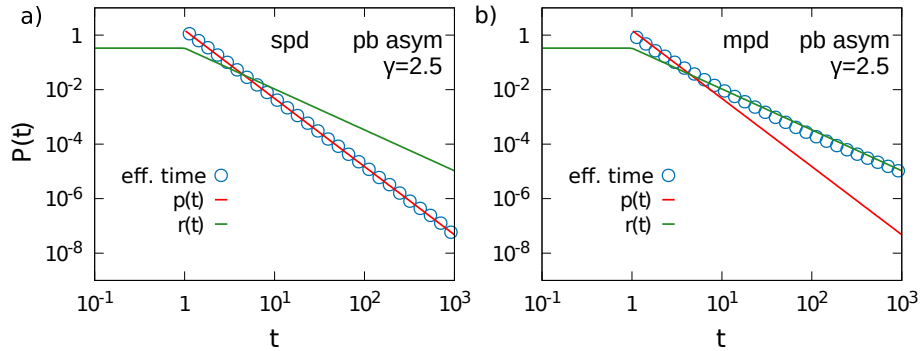


Figure 5: **Particle-based asymmetrical rule:** PDFs of the effective exchange time for a system of $L = 100$ for the asymmetrical particle-based rule. (a) Single-particle dynamics, i.e. $N_+ = 1$ and $N_- = L - 1$. (b) Many-particle dynamics, i.e. $N_+ = N_- = L/2$.

the site-based rule. The time-series $\{t_1^1, t_1^2, \dots\}$ contains the times for which the plus particle moves, since it is never blocked by other plus particles. In other words, the effective waiting time distribution is $p(t)$ itself, and we can regard the plus particle simply as a non-Markovian random walker while minus particles serve as passive holes. The motion of the particle is completely determined by $\{t_1^1, t_1^2, \dots\}$. Our simulation results for this scenario are shown in figure 5.

Now turning to the mpd realization of the asymmetric update, we get back the scenario discussed in [29], since minus particles are passive and correspond to holes of the one-species TASEP. For completeness, the results are shown in figure 5 (b). As expected, we observe that for small times near $t = 1$, the simulation data points follow the original density $p(t)$ but then the exponent of PDF changes to $\gamma - 1$ for larger times as predicted in [29]. The particle flux and its dependency on the system size for $\gamma \leq \gamma_c$ has already been discussed in [29], hence we continue with the symmetric rules for particle-based updates.

3.2.2. Maximum rule Let us turn to the first particle-based-symmetrical update, the maximum rule, which was introduced in section 2. This rule does not break the symmetry between plus and minus particles because the exchange process is triggered by both particles (with index i and j) that have to be activated for an exchange process first. Hence, one has to choose the maximum from the two next event times in the time-series t_i^k, t_j^l , in order to determine when the plus particle actually exchanges with its neighbor. We estimate PDFs for the symmetrical maximum update by calculating the density of the maximum of two random variables X and Y with density $p_1(t)$ and $p_2(t)$.

Because all particles follow to their own time series $\{t_i^1, t_i^2, \dots\}$ and $\{t_j^1, t_j^2, \dots\}$, different situations appear for neighboring pairs of plus and minus particles. There is always one particle inducing the exchange process, e.g. the one with the later time for the maximum update rule. However, the process can be induced by a plus particle or a minus particle.

Let us assume that a plus particle induced an exchange k and then becoming involved in a new exchange process $k + 1$ with a new partner. Here, the plus particle's clock has no age immediately after the last executed exchange process. In contrast, the new neighbor minus particle already is located on its position for some time meaning a clock with a non zero age. Hence, the plus particle follows the density $p_{plus}(t) = p(t)$ but we assume that the minus particle's residual waiting time is rather described by $p_{minus}(t) = r(t)$ because it is standing in the queue of other minus particles. In the single particle case, the maximum of two random times is taken from a time X that follows $p(t)$ and a time Y that follows $r(t)$ as $\max(X_{p(t)}, Y_{r(t)})$ which we call a *mixed scenario* in the following.

However, for symmetric rules, minus particles also can introduce an exchange process. Let us follow a plus particle again, but this time the exchange k was induced by its former neighboring particle. The plus particle has a new exchange partner for the

process $k + 1$ again, but this time also a non zero age, just as its new neighbor minus particle which was not involved in the former process k . In this case, we assume both residual waiting times are distributed by $p_{plus}(t) = p_{minus}(t) = r(t)$. The maximum of two random times X and Y is now chosen as $\max(X_{r(t)}, Y_{r(t)})$, called the *pure scenario*.

First, we give the cumulative distribution function (CFD) for both $p(t)$ and $r(t)$:

$$P(t) = \begin{cases} 0 & 0 < t < 1 \\ 1 - t^{1-\gamma} & t \geq 1, \end{cases} \quad (7)$$

$$R(t) = \begin{cases} \frac{\gamma-2}{\gamma-1}t & 0 < t < 1 \\ 1 - \frac{1}{\gamma-1}t^{2-\gamma} & t \geq 1. \end{cases} \quad (8)$$

With these, we can now calculate the density of the maximum X and Y , i.e.

$$f_{max}^{mix}(t) = \frac{d}{dt} [P(t)R(t)] \quad (9)$$

$$= \begin{cases} 0 & 0 < t < 1 \\ (\gamma - 1)t^{-\gamma} + \frac{\gamma-2}{\gamma-1}t^{1-\gamma} + \frac{3-2\gamma}{\gamma-1}t^{2(1-\gamma)} & t \geq 1, \end{cases} \quad (10)$$

$$f_{max}^{pure}(t) = \frac{d}{dt} [R(t)R(t)] \quad (11)$$

$$= \begin{cases} 2 \left(\frac{\gamma-2}{\gamma-1} \right)^2 t & 0 < t < 1 \\ 2 \frac{\gamma-2}{\gamma-1} t^{1-\gamma} - 2 \frac{\gamma-2}{(\gamma-1)^2} t^{3-2\gamma} & t \geq 1. \end{cases} \quad (12)$$

Both, the pure and mixed scenarios have the leading exponent $1 - \gamma$ which is equal to the exponent of $r(t)$. In the pure scenario, we get an estimate for effective waiting times smaller than 1. This expression is expected to overestimate the weight of the waiting times because also the mixed scenario is contributing to the exchange processes, always with times larger than one. However, we will use the pure scenario as an estimate for

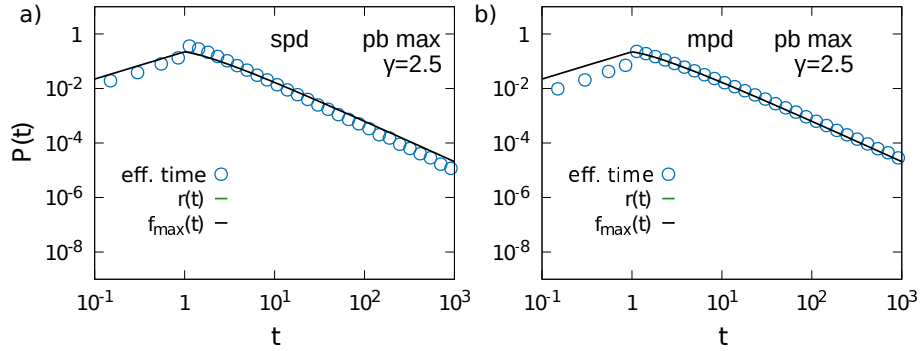


Figure 6: **Particle-based maximum rule:** PDFs of the effective exchange time for a system of $L = 100$ for the particle-based maximum rule. (a) Single-particle dynamics, i.e. $N_+ = 1$ and $N_- = L - 1$. (b) Many-particle dynamics, i.e. $N_+ = N_- = L/2$.

the spd effective waiting time density for the maximum rule in the following,

$$f_{max}(t) = f_{max}^{pure}(t) = \begin{cases} 2 \left(\frac{\gamma-2}{\gamma-1} \right)^2 t & 0 < t < 1 \\ 2 \frac{\gamma-2}{\gamma-1} t^{1-\gamma} - 2 \frac{\gamma-2}{(\gamma-1)^2} t^{3-2\gamma} & t \geq 1. \end{cases} \quad (13)$$

We compare these estimates with simulation results in figure 6 (a) for spd. Here, the tail behavior of our simulation results are in good agreement with $f_{max}(t)$. Also, short time behavior is well approximated when relating the sharp increase at $t \approx 1$ to the influence of the mixed scenario which estimates a zero probability for $t < 1$ and a higher weight at $t > 1$ for the used $\gamma = 2.5$.

We now compare $f_{max}(t)$ to simulation results of the mpd in figure 6 (b). Again we see that the tail behavior is well described by $f_{max}(t)$ and $r(t)$. The short time behavior is still close to the estimate but the tail has a higher statistical weight comparing to spd.

The shift in the exponent that is seen when comparing the original waiting time PDF and the effective exchange time PDF is also consistent with the results for the flux in the maximum rule which is shown in figure 8 (b). We observe no significant changes in the flux for system sizes larger than $L = 100$ if $\gamma > \gamma_c$ but a flux that vanishes with L for $\gamma < \gamma_c$, similar to the results found for the site-based model.

3.2.3. Minimum rule The second particle-based-symmetrical update is the minimum rule, also introduced in section 2. Also, this rule does not break the symmetry between plus and minus particles. The exchange process is triggered by the first particle that is activated for an exchange process at the minimum time of the two next event times in each particle's time-series t_i^k, t_j^ℓ . We calculate an estimates for PDFs from the minimum of two random variables X and Y with density $p_1(t)$ and $p_2(t)$.

As in the maximum model, we have plus induced and minus induced exchanges. In our analytical estimate we use again the assumption that the particle with an aged residual waiting time is distributed by $r(t)$ so that we have to calculate $\min(X_{p(t)}, Y_{r(t)})$ for the mixed scenario and $\min(X_{r(t)}, Y_{r(t)})$ for the pure scenario.

We again use the CFDs of equations (7) and (8) to calculate the minimum density in both scenarios:

$$f_{min}^{mix}(t) = p(t) [1 - R(t)] + r(t) [1 - P(t)] \quad (14)$$

$$= \begin{cases} \frac{\gamma-2}{\gamma-1} & 0 < t < 1 \\ \frac{2\gamma-3}{\gamma-1} t^{2-2\gamma} & t \geq 1, \end{cases} \quad (15)$$

$$f_{min}^{pure}(t) = 2r(t) [1 - R(t)] \quad (16)$$

$$= \begin{cases} 2 \frac{\gamma-2}{\gamma-1} \left(1 - \frac{\gamma-2}{\gamma-1} t \right) & 0 < t < 1 \\ 2 \frac{\gamma-2}{(\gamma-1)^2} t^{3-2\gamma} & t \geq 1. \end{cases} \quad (17)$$

We realize that the largest tail is $3 - 2\gamma$ which we get for the pure scenario. Since both scenarios can be observed in the exclusion process, each of them contributes to the

effective exchange time but the tail behavior is determined by the slower process that can block transport completely. We therefore set

$$f_{min}(t) = f_{min}^{pure}(t) = \begin{cases} \frac{2\gamma-2}{\gamma-1} \left(1 - \frac{\gamma-2}{\gamma-1}t\right) & 0 < t < 1 \\ \frac{2}{(\gamma-1)^2} t^{3-2\gamma} & t \geq 1. \end{cases} \quad (18)$$

Note that $f_{min}(t)$ leads to a increase in transport efficiency for $\gamma > 3$ but the exponent of $f_{min}(t)$ becomes larger than $-\gamma$ if $\gamma > 3$. This counter-intuitive result follows from the assumption that both waiting times of interfacing particles are distributed by $r(t)$ instead of $p(t)$. However, the prediction would mean a slower exchange than in the asymmetric particle-based rule where minus particles are completely passive. We will see that our estimates actually describes the simulation results for spd only for $\gamma > 3$ in figure 7 (c) but not in panel (a) where $\gamma = 2.5$. Here, the tail behavior is well represented by $p(t)$.

In order to understand the origin of this difference in tail exponents, we measure

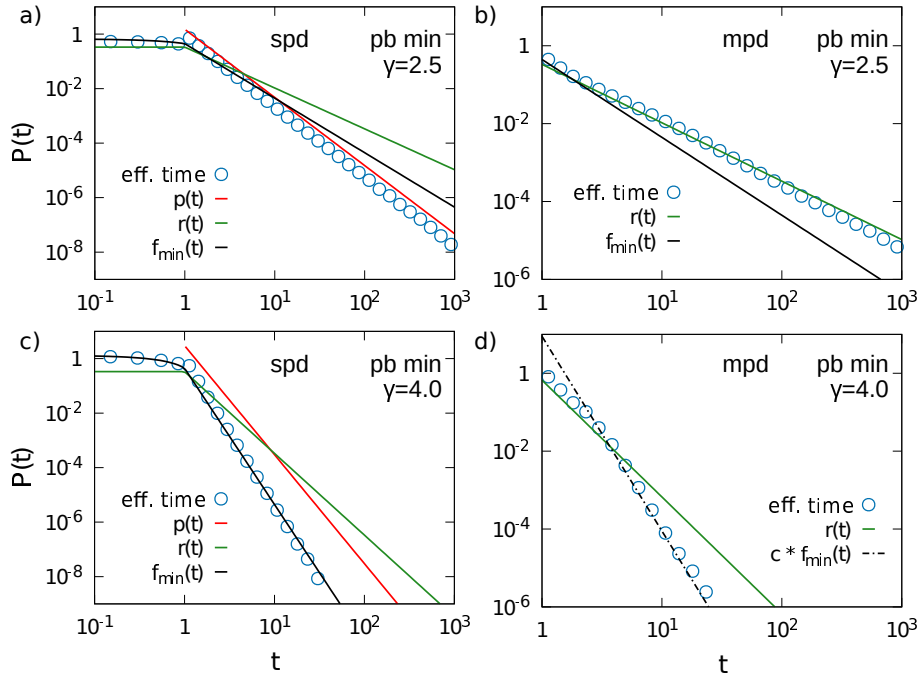


Figure 7: **Particle-based minimum rule:** PDFs of the effective exchange time for a system of $L = 100$ for the particle-based minimum rule. (a) Single-particle dynamics, i.e. $N_+ = 1$ and $N_- = L - 1$ for exponent $\gamma = 2.5$. (b) Many-particle dynamics, i.e. $N_+ = N_- = L/2$ for exponent $\gamma = 2.5$. (c) Single-particle dynamics for exponent $\gamma = 4.0$. (d) Many-particle dynamics for exponent $\gamma = 4.0$. The dashed line shows the tail behavior of $f_{min}(t)$ close to the simulation data.

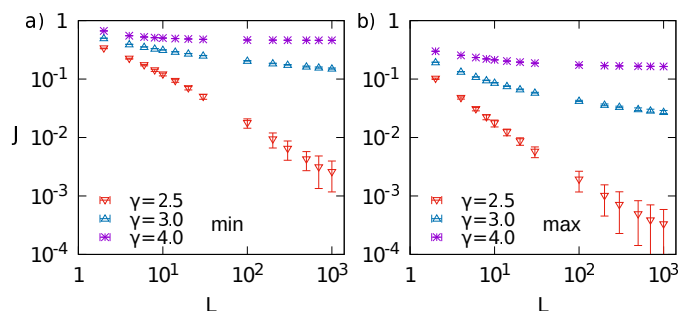


Figure 8: **(a) Minimum and (b) maximum rule:** Length dependency of the particle flux J for different values of the exponent γ in the PDF (4) and mpd.

the residual waiting time carried by the plus particle, which we call $\tilde{p}(t)$. We find that in the tail $\tilde{p}(t) \approx r(t)$ for $\gamma > 3$ but not for $\gamma < 3$ where the exponent is not exceeding values of $\gamma = -2$. Calculating the minimum with such an exponent from \tilde{p} would lead to an $f_{min}(t)$ with exponents $\leq -\gamma$, i.e. $p(t)$ serves as a upper limit (see Appendix B for details).

We can understand this deviation by realizing that the plus induced dynamics is getting more important for if γ is below the critical value γ_c . The influence of the tail in the residual waiting time is important for inducing events by minus particles that did stand in the queue for a long time. In contrast, the plus particle is more often responsible for inducing the events and consequently determines the effective exchange time. We show that the ratio of plus induced events is growing in this regime in Appendix B. The time average in the calculation of the residual waiting time in Appendix A is not valid due to temporal correlations in this scenario.

For mpd, similar behavior is observed. The estimate f_{min} is well suited to the simulation result if $\gamma > 3$, which is shown in figure 7 (d). In results for small exponents $\gamma < 3$ shown in figure 7 (b), the analytical estimate again does not describe the simulation results. Instead, the tail is determined by the residual waiting time $r(t)$. The relevance of the residual waiting time is caused by the dominance of long exchange times in long queues. Furthermore, passively exchanged particles keep their event time after an exchange process which leads to long range correlations of particles exchange times.

Similar to the results of the site-based model and the maximum model, the flux in the minimum rule does not show significant changes with L in the fast decaying regime above γ_c , which is shown in figure 8 (a). For $\gamma < \gamma_c$, again a dependency on the system length in the data supports the qualitative difference between the regimes found in results from effective exchange times above. However, the flux clearly is higher in the minimum rule than in the maximum rule (panel b)). We want to further study the difference of the applied model rules on the particle flux in the next section.

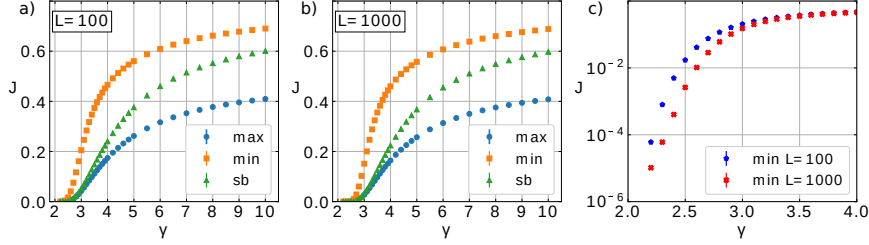


Figure 9: Particle flux depending on the exponent γ for the three different update rules (site-based green, minimum orange, maximum blue). Error bars are drawn from sem values of 10 realizations. (a) The system size is $L = 100$, (b) $L = 1000$. (c) Section for $\gamma \leq 4$ in a logarithmic scale for J for $L = 100$ (blue) and $L = 1000$ (red).

3.3. Transport efficiency of symmetric model rules

The exponents for effective exchange times found for the different model rules are summarized in table 1. We now compare the flux which is generated by the three symmetrical updates in figure 9. Even though the asymptotic behavior of the three rules are similar (except for $\gamma > \gamma_c$ in the minimum model), the short exchange times influence the value of the flux. This leads to significant differences between the site-based model, the particle-based minimum model and the particle-based maximum model for $\gamma > \gamma_c$. As expected, the maximum rule is really slower than the site-based model and the minimum rule can enhance the transport. For $\gamma < \gamma_c$ however, the flux generated in the maximum rule is close to the flux by the site-based rule. In the minimum rule, we still measure higher fluxes, both for the system size of $L = 100$ (a) and $L = 1000$ (b). Note that we observe finite-size effects in these results which is shown in panel c) where the data points deviate for the different system sizes. By the analysis of tail exponents, we expect $J = 0$ for the infinite system in the stationary state such as in the other models.

Table 1: The resulting exponent seen in the effective waiting time PDFs in the different update rules for single-particle dynamics and many-particles dynamics.

	single-particle dynamics		many-particle dynamics	
site-based	$1 - \gamma$		$1 - \gamma$	
particle-based asymmetrical	$-\gamma$		$1 - \gamma$	
particle-based maximum	$1 - \gamma$		$1 - \gamma$	
particle-based minimum	$-\gamma$ for $\gamma < 3$	$3 - 2\gamma$ for $\gamma > 3$	$1 - \gamma$ for $\gamma < 3$	$3 - 2\gamma$ for $\gamma > 3$

4. Conclusion

In our contribution, we analyzed different bidirectional variants of the TASEP with non-Markovian exchange dynamics. These models are relevant for one-dimensional transport problems in crowded environments, where the high density of particle clusters leads to small effective exchange rates of particle positions. A possible realization of the bidirectional transport model would include two oppositely moving particle species and holes. A model of this kind would combine a Markovian particle-dynamics, which would be applied when the particles move toward an empty site and a non-Markovian particle-dynamics, which governs the particle-exchange. Simulation results show strong condensation of the particles, which implies that the bidirectional transport capacity is determined by the efficiency of the exchange processes rather than by the time spent in the low density area. Therefore, we restricted our analysis to symmetric and fully-filled systems. This choice reduces considerably the corrections to scaling for small system sizes.

Modeling bidirectional transport of active particles with lattice gases allows assigning the exchange times to the particles as well as to the lattice. In the latter case, we can map the problem to the uni-directional process, since pairs of oppositely moving particles behave as particles and holes in the uni-directional case. This is even true for spd which correspond to a uni-directional system with a single hole where the dynamics of the particle is governed by the residual waiting time. Significant differences to the uni-directional case exist if the exchange times are assigned to the particles. This can be realized in a symmetric or in an asymmetric way, wherein the latter case the reaction times are assigned to only one-particle species. The asymmetric case implies that one particle species can be assumed to be passive which is why we find the asymptotics of the uni-directional non-Markovian TASEP for the single-particle as well as for the many-particle dynamics.

Assigning exchange times symmetrically to both particle species implies that two exchange times are given for a pair of oppositely moving particles. Therefore, one has to define an additional selection rule. In this work we have chosen two extreme cases that preserve the symmetry between the two types of particles, i.e. either the minimum or the maximum of the two waiting-times will be selected. In case of the maximum rule, residual waiting time and $f_{max}(t)$ show the same asymptotics. Therefore the maximum rule modifies indeed the effective exchange time distribution but to the exponent compared to the residual waiting time of the site-based model. Significant differences exist only in the $\gamma > \gamma_c$ regime for the minimum rule. In this case, we find that the asymptotics is governed by the distribution of independent residual times where the asymptotics of effective exchange time distribution is given by $3 - 2\gamma$. For $\gamma < \gamma_c$ this is not the leading contribution. Here, the asymptotic behavior is in accordance with the asymmetric particle based model which is given by the residual waiting time for mpd. This effect is the result of passively moving particles which keep the assigned exchange time. For small values of γ the dynamic is, as for the other cases, governed

by pairs of particles with long residual waiting times.

Our results underline the universality of the findings which have been discussed for the uni-directional non-Markovian TASEP [29, 30]. In this class of models, many particle effects generically lead to a dominant contribution of the residual waiting time for $\gamma < \gamma_c$. Here, the configurations are characterized by large particle clusters and a size dependent flow of particles. The transport capacity of large systems in this parameter regime is extremely low compared to their Markovian counterparts. For $\gamma > \gamma_c$ however, we observe homogeneous particle configurations and size-independent values of the flow which differ for the different implementations of the dynamics.

Our findings can be relevant for bidirectional flows under strong confinement as for example in narrow escape problems in pedestrian dynamics [5] or intracellular transport in axons and dendrites [35] where the effective exchange dynamics can be non-Markovian.

Acknowledgments

This work was funded by the Deutsche Forschungsgemeinschaft (DFG) through Collaborative Research Center SFB 1027 (Project A8).

Appendix A. Calculation of residual waiting times

The waiting time PDF for a single particle site exchange in the site-based model is calculated by using renewal theory following [36]. In particular, we will determine the residual waiting time until the next exchange event occurs if two particles are in the local (+−) configuration. We start with a renewal process for renewal waiting times X_n distributed by Eq. (4), which are given to a site in the lattice. The N -th renewal of the waiting time on this site occurs at time

$$S_N = \sum_{n=1}^N X_n, \quad (\text{A.1})$$

i.e. we can count the number of passed renewal events $N(t)$ at each time t .

For a time $t > S_{N(t)}$, the waiting times of this site are called the duration of renewal time intervals $\tilde{X}(t) = X_{N(t)+1} = S_{N(t)+1} - S_{N(t)}$ (see figure A1). The renewal process also has an age $Z(t) = t - S_{N(t)}$ as well as a residual life (residual waiting time) $Y(t) = S_{N(t)+1} - t$ until the next renewal event takes place at time $S_{N(t)+1}$. The residual waiting time is therefore also written as $Y(t) = \tilde{X}(t) - Z(t)$.

We now calculate the time averaged CDF of the residual waiting time $Y(t)$, i.e. $F_Y(y) = \Pr\{Y(t) \leq y\}$ that gives the fraction of time that the residual waiting time is smaller than a given y . We can invent an indicator reward function $R(t)$ to determine

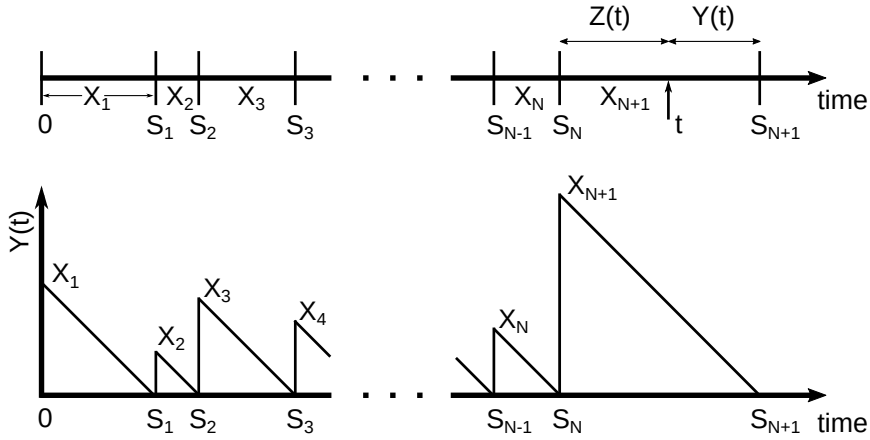


Figure A1: **Top:** The renewal process is determined by the time series X_n , $n \in \mathbb{N}$, build from the algebraic waiting time PDF in Eq. (4). Summing up these waiting times S_1, S_2, \dots, S_N gives the time for the next event at S_{N+1} . For a time $S_n \leq t \leq S_{N+1}$, the current process has the age Z and the residual life Y . **Bottom:** The residual life $Y(t)$ is a step wise function of time, decaying from X_n to 0 during the time in the interval between S_{n-1} and S_n .

if the residual waiting time is actually smaller or not, i.e.

$$R(t) = R(Z(t), \tilde{X}(t)) = \begin{cases} 1 & \text{for } \tilde{X}(t) - Z(t) \leq y \\ 0 & \text{otherwise.} \end{cases} \quad (\text{A.2})$$

The following form for the CDF of $Y(t)$ can then be found by using the time average over the indicator function

$$F_Y(y) = \lim_{t \rightarrow \infty} \frac{1}{t} \int_0^t R(\tau) d\tau = \frac{1}{\bar{X}} \int_{x=0}^{x=y} \Pr\{X > x\} dx, \quad (\text{A.3})$$

where $\bar{X} = \frac{\gamma-1}{\gamma-2}$ denotes the mean value of the renewal event duration for the PDF in Eq. (4).

We now use this framework to determine the residual waiting time for the renewal process with algebraic waiting time PDF Eq. (4), i.e.

$$f_X(x) = \begin{cases} 0 & 0 < x < 1, \\ (\gamma - 1)x^{-\gamma} & x > 1. \end{cases}$$

The CDF of the renewal time intervals is

$$F_X(x) = \begin{cases} 0 & x < 1 \\ 1 - x^{1-\gamma} & x \geq 1. \end{cases} \quad (\text{A.4})$$

We use equation A.3 to determine the CDF

$$F_Y(y) = \frac{1}{\bar{X}} \int_0^y (1 - (1 - x^{1-\gamma})\Theta(x - 1)) dx \quad (\text{A.5})$$

$$= \begin{cases} \frac{\gamma - 2}{\gamma - 1} y & y < 1 \\ \frac{\gamma - 2}{\gamma - 1} \left(\frac{\gamma - 1}{\gamma - 2} + \frac{1}{2 - \gamma} y^{2-\gamma} \right) & y \geq 1, \end{cases} \quad (\text{A.6})$$

and finally arrive at the result

$$Y(y) = \begin{cases} \frac{\gamma - 2}{\gamma - 1} & y < 1 \\ \frac{\gamma - 2}{\gamma - 1} y^{1-\gamma} & y \geq 1 \end{cases} \quad (\text{A.7})$$

for the PDF of the residual waiting time $Y(y)$.

Appendix B. Additional measurements for the minimum rule in single-particle dynamics

In this appendix, we further examine results in the single-particle dynamics, minimum update rule. As we have seen in figure 7, the effective waiting time distribution follows the estimation f_{min}^{pure} only for exponents $\gamma > 3$.

In a first step, we will compare the PDF for effective waiting times of the spd minimum rule to the case where we always assign new waiting times to the plus particle after an exchange process. In figure B1 (a), the simulation results really follow the respective estimate f_{min}^{mix} , which is expected since the plus particle always has a non-aged waiting time. This result is in contrast to the result of the bulk text, which is also shown in figure B1 (b) for comparability. For the minimum rule, effective waiting times do not follow f_{min}^{mix} , hence the age of the plus particle plays a role. However, neither do they follow f_{min}^{pure} which is expected for the minimum of two random variables distributed by the residual time $r(t)$.

In a second step, we show simulation results for residual waiting times of the plus particle in figure B2, which we call $\tilde{p}(t)$ in the following. In the fast regime of $\gamma > 3$, the measurements follow the theoretical estimate $r(t)$. However, this changes for exponents $\gamma < 3$. The simulation result do not follow $r(t)$ anymore but rather stay close to the asymptotic of $\gamma = 2$. This slope for $\tilde{p}(t)$ is consistent with the effective exchange time observed in figure 7 (a), where simulation results follow $p(t) \approx t^{-\gamma}$ in the tail, when considering the minimum out of a random variable distributed by $r(t)$ for minus particles and $\tilde{p}(t)$ for plus.

We see that the time-averaged estimate $r(t)$ is not valid anymore for the residual waiting time of a single plus particle in the minimum model for $\gamma < 3$. We further give an argument for the break down of validity by showing that the fraction of exchange

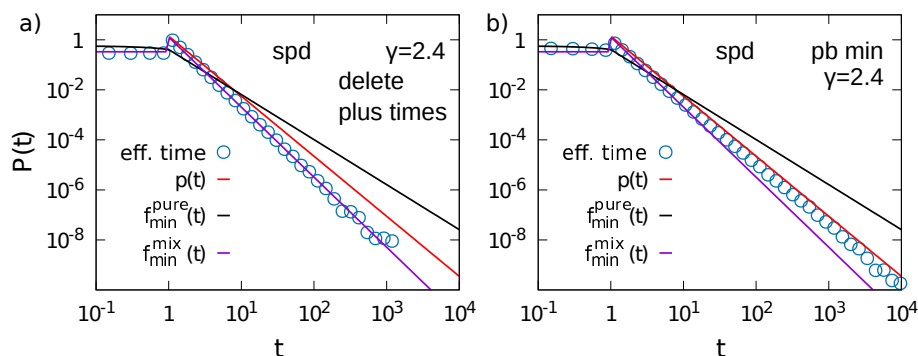


Figure B1: a) Single-particle dynamics exclusion process where residual waiting times of the plus particle is deleted after each exchange process, independent whether the plus particle was active or passive in the exchange. b) The normal spd minimum rule from the bulk text for comparison.

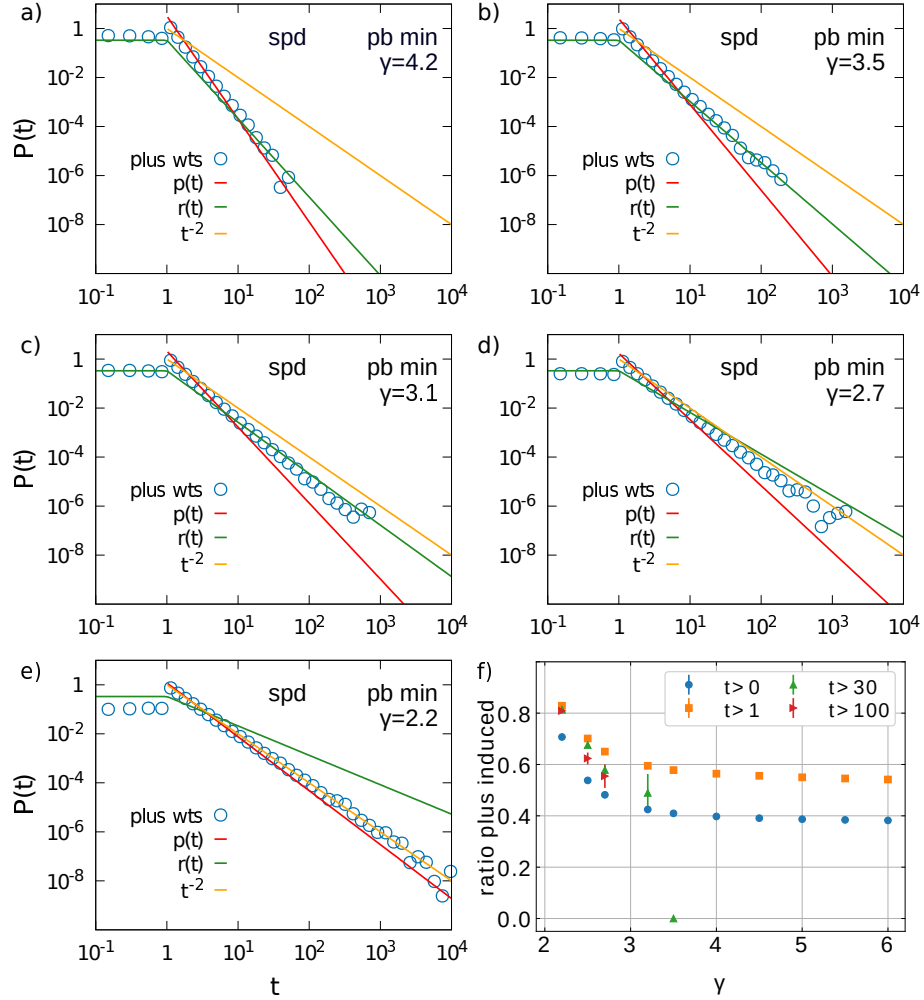


Figure B2: **Particle-based minimum rule** PDFs of the residual waiting time of a plus particle \tilde{p} for a system of $L = 100$ filled by $N_+ = 1$ and $N_- = L - 1$ (spd). (a) $\gamma = 4.2$, (b) $\gamma = 3.5$, (c) $\gamma = 3.1$, (d) $\gamma = 2.7$, (e) $\gamma = 2.2$. Blue data points show the residual waiting times of the plus particle, red $p(t)$ original waiting time distribution, green $r(t)$ residual waiting time from renewal theory, yellow a constant function t^{-2} as a reference line. f) The measured ratio of exchange processes which have been induced by an active plus particle in the spd minimum case. Statistics over all exchange events are colored blue, exchange processes with an effective waiting time of at least 1 are orange, 30 green and at least 100 red. Data points are missing if no such high waiting times have been observed in the simulation, errors bars show the sem.

events induced by the plus particle increases for $\gamma < 3$ (see figure B2 (f)). This is in particular important for large times in the tail. If most events are induced by the single plus particle the motion is more and more determined by this particle itself and hence, the dynamics are more similar to the asymmetric particle-based model of passive minus particles.

Appendix C. Update scheme

For the Markovian TASEP: We also remark that, thanks to the memoryless property of the Markovian TASEP, one can practically generate the next time t_i^{k+1} at every $t = t_i^k$. The Markov property does not hold for the algebraic distribution $p(t)$ in equation (4). To evolve the system in time, we use a modified waiting time algorithm (*next reaction method* [33]) similar to [29, 34].

Times for all events (particle-based or site-based) are initialized at the beginning of the simulation ($\tau = 0$). The shortest time t_α is then chosen from a list of all waiting times to be the absolute time for the next event α . In the realization of the event, the system time is increased up to this point in time $\tau_{i+1} = \tau_i + t_\alpha$. Anyhow, the process is only executed if the local particle configuration is appropriate. After the realization, the waiting time of the event is renewed by taking a new time t_{new} from the distribution $p(t)$ added to the current system time $t_\alpha = \tau + t_{new}$. This time is then placed into the list for the event α and the procedure is repeated.

- [1] Mohcine Chraïbi, Antoine Tordeux, Andreas Schadschneider, and Armin Seyfried. Modelling of pedestrian and evacuation dynamics. In *Complex Dynamics of Traffic Management*, pages 649–669. Springer US, New York, NY, 2019.
- [2] Livio Gibelli and Nicola Bellomo. *Crowd Dynamics, Volume 1: Theory, Models, and Safety Problems*. Springer, 2019.
- [3] Dirk Helbing. Collective phenomena and states in traffic and self-driven many-particle systems. *Selected papers of the Twelfth International Workshop on Computational Materials Science (CMS2002)*, 30(1):180–187, May 2004.
- [4] Gunnar G. Lvs. Modeling and simulation of pedestrian traffic flow. *Transportation Research Part B: Methodological*, 28(6):429–443, 1994.
- [5] Andreas Schadschneider, Debashish Chowdhury, and Katsuhiro Nishinari. *Stochastic transport in complex systems: from molecules to vehicles*. Elsevier, 2010.
- [6] Debashish Chowdhury, Ludger Santen, and Andreas Schadschneider. Statistical physics of vehicular traffic and some related systems. *Physics Reports*, 329(4):199–329, 2000.
- [7] Boris S. Kerner. Complex dynamics of traffic management, introduction to. In *Encyclopedia of Complexity and Systems Science*, pages 1177–1180. Springer New York, New York, NY, 2009.
- [8] Mithila Burute and Lukas C. Kapitein. Cellular logistics: Unraveling the interplay between microtubule organization and intracellular transport. *Annu. Rev. Cell Dev. Biol.*, 35(1):29–54, October 2019.
- [9] Cecile Appert-Rolland, Maximilian Ebbinghaus, and Ludger Santen. Intracellular transport driven by cytoskeletal motors: General mechanisms and defects. *Physics Reports*, 593:1–59, 2015.
- [10] Debashish Chowdhury. Stochastic mechano-chemical kinetics of molecular motors: A multidisciplinary enterprise from a physicists perspective. *Stochastic mechano-chemical kinetics of molecular motors: A multidisciplinary enterprise from a physicists perspective*, 529(1):1–197, August 2013.
- [11] William O. Hancock. Bidirectional cargo transport: moving beyond tug of war. *Nature Reviews Molecular Cell Biology*, 15(9):615–628, September 2014.
- [12] Nobutaka Hirokawa, Shinsuke Niwa, and Yosuke Tanaka. Molecular motors in neurons: Transport mechanisms and roles in brain function, development, and disease. *Neuron*, 68(4):610–638, November 2010.
- [13] Nobutaka Hirokawa and Reiko Takemura. Molecular motors and mechanisms of directional transport in neurons. *Nature Reviews Neuroscience*, 6:201, February 2005.
- [14] Anthony Brown. Axonal transport of membranous and nonmembranous cargoes. *J Cell Biol*, 160(6):817, March 2003.
- [15] T. Chou, K. Mallick, and R. K. P. Zia. Non-equilibrium statistical mechanics: from a paradigmatic model to biological transport. *Reports on progress in physics*, 74(11):116601, 2011.
- [16] David Mukamel. Phase transitions in nonequilibrium systems. *Soft and fragile matter*, page 237, 2000.
- [17] Bernard Derrida. An exactly soluble non-equilibrium system: the asymmetric simple exclusion process. *Physics Reports*, 301(1-3):65–83, 1998.
- [18] Martin R. Evans, Damien P. Foster, Claude Godrche, and David Mukamel. Spontaneous symmetry breaking in a one dimensional driven diffusive system. *Physical review letters*, 74(2):208, 1995.
- [19] Peter F. Arndt, Thomas Heinzl, and Vladimir Rittenberg. Spontaneous breaking of translational invariance in one-dimensional stationary states on a ring. *Journal of Physics A: Mathematical and General*, 31(2):L45, 1998.
- [20] Philip Greulich and Andreas Schadschneider. Single-bottleneck approximation for driven lattice gases with disorder and open boundary conditions. *Journal of Statistical Mechanics: Theory and Experiment*, 2008(04):P04009, 2008.
- [21] Carsten Burstedde, Kai Klauck, Andreas Schadschneider, and Johannes Zittartz. Simulation of pedestrian dynamics using a two-dimensional cellular automaton. *Physica A: Statistical Mechanics and its Applications*, 295(3-4):507–525, 2001.

- [22] Stefan Nowak and Andreas Schadschneider. Quantitative analysis of pedestrian counterflow in a cellular automaton model. *Physical Review E*, 85(6):066128, 2012.
- [23] Stefan Klumpp and Reinhard Lipowsky. Phase transitions in systems with two species of molecular motors. *EPL (Europhysics Letters)*, 66(1):90, 2004.
- [24] Maximilian Ebbinghaus and Ludger Santen. A model for bidirectional traffic of cytoskeletal motors. *Journal of Statistical Mechanics: Theory and Experiment*, 2009(03):P03030, 2009.
- [25] M. Ebbinghaus, C. Appert-Rolland, and L. Santen. Particle interactions and lattice dynamics: scenarios for efficient bidirectional stochastic transport? *Journal of Statistical Mechanics: Theory and Experiment*, 2011(07):P07004, 2011.
- [26] Jean-Philippe Bouchaud. Weak ergodicity breaking and aging in disordered systems. *Journal de Physique I*, 2(9):1705–1713, 1992.
- [27] Ceile Monthus and Jean-Philippe Bouchaud. Models of traps and glass phenomenology. *Journal of Physics A: Mathematical and General*, 29(14):3847, 1996.
- [28] Mark E. J. Newman. Power laws, pareto distributions and zipf’s law. *Contemporary physics*, 46(5):323–351, 2005.
- [29] Robert J. Concannon and Richard A. Blythe. Spatiotemporally complete condensation in a non-poissonian exclusion process. *Physical review letters*, 112(5):050603, 2014.
- [30] Diana Khoromskaia, Rosemary J. Harris, and Stefan Grosskinsky. Dynamics of non-markovian exclusion processes. *Journal of Statistical Mechanics: Theory and Experiment*, 2014(12):P12013, 2014.
- [31] Rui Jiang, Katsuhiko Nishinari, Mao-Bin Hu, Yong-Hong Wu, and Qing-Song Wu. Phase separation in a bidirectional two-lane asymmetric exclusion process. *Journal of Statistical Physics*, 136(1):73–88, July 2009.
- [32] Daniel T. Gillespie. A general method for numerically simulating the stochastic time evolution of coupled chemical reactions. *Journal of computational physics*, 22(4):403–434, 1976.
- [33] Michael A. Gibson and Jehoshua Bruck. Efficient exact stochastic simulation of chemical systems with many species and many channels. *The journal of physical chemistry A*, 104(9):1876–1889, 2000.
- [34] Mieke Gorissen and Carlo Vanderzande. Ribosome dwell times and the protein copy number distribution. *Journal of Statistical Physics*, 148(4):628–636, 2012.
- [35] O. A. Shemesh and M. E. Spira. Paclitaxel induces axonal microtubules polar reconfiguration and impaired organelle transport: implications for the pathogenesis of paclitaxel-induced polyneuropathy. *Acta Neuropathologica*, 119(2):235–248, February 2010.
- [36] Robert G. Gallager. *Stochastic processes: theory for applications*. Cambridge University Press, 2013.

Addendum V Self-organized lane-formation in bidirectional transport of molecular motors

Authors: R. Jose and L. Santen

Department of Theoretical Physics & Center for Biophysics, Saarland University, 66123 Saarbrücken, Germany

Manuscript submitted for publication (2019).
arXiv: 2002.11960

Author contributions:

Corresponding author: R. Jose.

L. Santen suggested the scientific problem and supervised the research. R. Jose and L. Santen developed the theory. R. Jose implemented and performed the simulations. R. Jose wrote the manuscript and generated the figures. R. Jose and L. Santen contributed to the analysis and interpretation of the results. R. Jose and L. Santen revised of the manuscript.

Abstract:

Within cells, vesicles and proteins are actively transported several micrometers along the cytoskeletal filaments. The transport along microtubules is propelled by dynein and kinesin motors, which carry the cargo in opposite directions. Bidirectional intracellular transport is performed with great efficiency, even under strong confinement, as for example in the axon. For this kind of transport system, one would expect generically cluster formation. In this work, we discuss the effect of the recently observed self-enhanced binding-affinity along the kinesin trajectories on the MT. We introduce a stochastic lattice-gas model, where the enhanced binding affinity is realized via a floor-field. From Monte Carlo simulations and a mean-field analysis we show that this mechanism can lead to self-organized symmetry-breaking and lane-formation which indeed leads to efficient bidirectional transport in narrow environments.

Self-organized lane-formation in bidirectional transport of molecular motors

Robin Jose and Ludger Santen
 Department of Theoretical Physics & Center for Biophysics,
 Saarland University, 66123 Saarbrücken, Germany
 (Dated: February 28, 2020)

ABSTRACT Within cells, vesicles and proteins are actively transported several micrometers along the cytoskeletal filaments. The transport along microtubules is propelled by dynein and kinesin motors, which carry the cargo in opposite directions. Bidirectional intracellular transport is performed with great efficiency, even under strong confinement, as for example in the axon. For this kind of transport system, one would expect generically cluster formation. In this work, we discuss the effect of the recently observed self-enhanced binding-affinity along the kinesin trajectories on the MT. We introduce a stochastic lattice-gas model, where the enhanced binding affinity is realized via a floor-field. From Monte Carlo simulations and a mean-field analysis we show that this mechanism can lead to self-organized symmetry-breaking and lane-formation which indeed leads to efficient bidirectional transport in narrow environments.

arXiv:2002.11960v1 [physics.bio-ph] 27 Feb 2020

INTRODUCTION

The efficiency of intracellular transport is one of the most intriguing features of biological cells. Different kinds of cellular cargo have to be transported to specific locations in order to maintain the cells' functionality. Intracellular transport can be driven by molecular motors, i.e. specialized proteins that can carry cargo along polar filaments of the cytoskeleton [2–5]. Molecular motors, such as the microtubule (MT) associated proteins (MAPS) kinesin and dynein, step stochastically along MTs in a given preferred direction: Kinesins step typically toward the plus-end and dyneins to the minus-end. Molecular motors are able to carry big (on the scale of the cell) objects through crowded environments.

We focus on bidirectional motor-driven transport under spatial confinement, which is for example relevant for intracellular transport in axons. In this kind of environment, active transport is particularly difficult to organize, since cluster formation is generically observed in spatially extended one-dimensional systems [6–10]. Clusters can either have stationary particle output [8] or can lead to long times of blockages such as for non-Markovian site-exchange [10]. The general question we address in this work is the following: How do confined systems of active particles self-organize to realize efficient bidirectional transport states?

Motor-driven transport has been described by variants of the totally asymmetric exclusion processes (TASEP) which combine the directed stochastic motion of particles on a one-dimensional lattice with hard-core exclusion and Langmuir-kinetics [6, 11, 12]. In principle, the particle exchange with a reservoir would allow for bidirectional transport, in case of large diffusivity of unbound particles. However, if the unbound particles are localized, so far no mechanism has been suggested which leads to efficient bidirectional transport. A rather direct approach is the self-organization in sub-systems each of which carries unidirectional transport. A recent hypothesis is that posttranslational modifications on MTs might organize

transport in neurons [14, 15]. This kind of organization has been observed for example in dendrites, where the MTs are oppositely oriented [16] and in MT doublets in cilia [17]. Furthermore, motor proteins can regulate MTs themselves [18], and MT-dynamics [6] and tau [13] can affect motor transport.

Recent experimental findings suggest a possible mechanism leading to efficient bidirectional transport on MT bundles where no *a priori* compartmentalization exists. Shima *et al.* [19] reported that binding affinity of MTs for

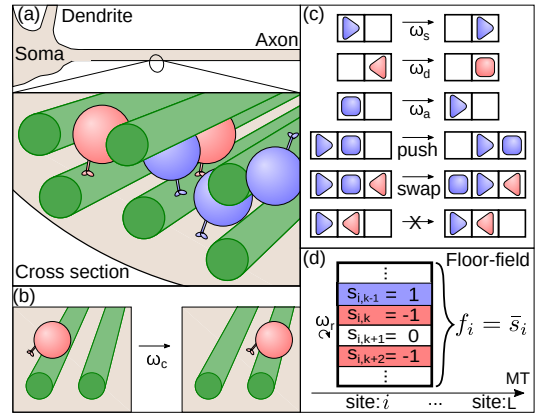


FIG. 1. (a) Scheme of a neuron, indicating the crowded environment and confinement inside axons, including MTs, plus-particles (blue) and minus-particles (red). (b) Unbound particles switch filaments with rate ω_c . (c) Particle dynamics in the exclusion process. Triangles mimic bound particles, the tip indicates the direction. Unbound particles are shown by squares. Bound particles can step or detach, unbound particles can reattach. If a particle attempts to step onto a site occupied by an unbound particle, it can either push it away or swap position. Two bound particles block each other via exclusion. (d) The floor-field state f_i is averaged over all sub-states for every site i of the lattice.

kinesin motors is self-enhanced along the kinesin trajectories which modify the MTs. This kind of self-induced preferential binding can be understood as a true realization of a floor-field, which has been successfully introduced as a virtual mechanism in order to generate e.g. lane-formation in bidirectional pedestrian flows [20–24].

In this paper, the transport problem is formulated as a TASEP with Langmuir-kinetics, where we additionally consider an explicit particle reservoir and a floor-field. Our theoretical model describes the key features of bidirectional axonal transport but considerably reduces the complexity of the biological reference system.

THE MODEL

We study a TASEP with Langmuir-kinetics of two particle species moving on a pair of parallel, identically polarized one-dimensional filaments. The model filaments (MTs) are represented as one-dimensional, static lattices. Lattice sites can either be empty or occupied by a single particle. We consider two types of particles, i.e. moving to the plus-end of the filament ($\tau = 1$, blue in Fig. 1) and to the minus-end ($\tau = -1$, red).

Particle dynamics: Both types of particles can either be bound or unbound to a filament (triangles or squares in Fig. 1(c)). Bound particles step to the neighboring site (target-site) with rate ω_s or detach from the filament with rate ω_d (Fig. 1(c)). In order to study lane-formation as a bulk effect, we are considering periodic boundary conditions. Particles which detach from the filament stay at the same lattice-site, unlike in typical models with Langmuir-kinetics where particles move to a bulk reservoir [6, 11]. This feature is crucial for modeling transport in crowded environments, where unbound particles cannot simply diffuse away from clusters.

Unbound particles can reattach to the filament with rate ω_a or change to an unbound state on the other filament with a coupling rate ω_c (Fig. 1(b)), where the position is kept. Particles interact with each other via hard-core repulsion (Fig. 1(c) bottom). For a particle which is selected to step we distinguish three cases. (i) If the target-site is free, the step is executed. (ii) If the target-site is occupied by a bound particle the step is rejected. (iii) If the target-site is occupied by an unbound particle, the unbound particle is either pushed to next site (in moving direction of the stepping particle) or exchanges position with it (swapping). If both pushing and swapping are possible, one of the two possibilities is selected with probability 1/2. If the site in moving direction next to the unbound particle is occupied, swapping is executed. (Fig. 1(c)).

Floor-field dynamics: In [19, 25] an axial elongation of the MT by kinesin has been reported. The elongation is related to a meta-stable tubulin-state which has a higher binding affinity for kinesins. This effect is implemented via a floor-field which considers the number of MT protofilaments, $N_p = 13$. A floor-field f_i is assigned

to each lattice-site i , which is given by

$$f_i = \frac{1}{N_p} \sum_{k=1}^{N_p} s_{i,k} \quad (1)$$

where k denotes the index of the protofilament which is permanently assigned to the particles until they detach from the (proto-)filament. Therefore, f_i represents the average of N_p sub-states $s_{i,k} \in \{-1, 0, 1\}$. The value of f_i is updated if particle steps to site i and thereby sets the value of a given sub-state $s_{i,k}$ to $+1(-1)$ in case of $+(-)$ directed motors. The sub-state can decay back to 0 again with rate ω_r (Fig. 1(d)). Averaging over N_p sub-states introduces a memory effect which stabilizes the preferential adsorption of a given type of particle, i.e. the amplitude of the floor-field determines the robustness of the floor-field against changes of the affinity by single oppositely directed particles. The sub-division of the floor-field into "protofilaments" is also consistent with the observation that low kinesin concentration may lead to a curvature of MTs which signifies a coexistence of excited and non-excited tubulin states ([25]).

The state f_i influences the binding affinity of particles $\omega_{a,i}$ given by

$$\omega_{a,i} = \begin{cases} \omega_a^0 \mu^{|f_i|}, & \tau = \text{sgn}(f) , \\ \omega_a^0 \frac{1}{\mu^{|f_i|}}, & \tau \neq \text{sgn}(f) , \end{cases} \quad (2)$$

where ω_a^0 is the free attachment rate and $\mu \geq 1$ is called affinity modification factor. This modification leads to higher binding rates if the floor-field state f_i was predominantly set by particles of the same type τ as well as lower rates for opposing combinations. If $\mu = 1$ or $f_i = 0$, the interaction is neutral. We consider a symmetric excitation for dynein and kinesin motors, though so far experimental evidence for a modification of the MT-structure by dynein is still lacking.

RESULTS AND DISCUSSION

We study the influence of the floor-field on the particle flux J as a measure of transport efficiency as well as symmetry-breaking and self-organized lane-formation. First, we introduce a mean-field analysis and then compare results to Monte Carlo (MC) simulations.

Mean-field analysis: As a reference, we consider TASEP models [26], two-species, bidirectional exclusion processes [8, 10, 27], as well as combinations of TASEP and Langmuir-kinetics [6, 11, 28]. From these models, a mean-field estimation [29] of the flux $J_{\text{ud}} = \rho_{\text{eff}}(1 - \rho_{\text{eff}})$ can be deduced for unidirectional one-filament systems with Langmuir-kinetics ([30]). We use J_{ud} for judging on the transport efficiency. Note that fluxes are scaled by ω_s^{-1} and the system size L .

To include the floor-field dependency in a mean-field model, we assume a simplified unbound state (u) shared

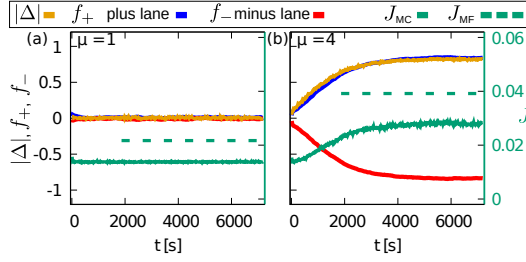


FIG. 2. Time dependence of the flux and particle densities for a system of $L = 1000$, $\rho = 0.05$, and random initial configurations. Values of the floor-fields f_+ , f_- and difference in densities Δ are given at the left axis; values of the total flux J , and the mean-field estimation J_{MF} are given at the right axis. (a) $\mu = 1$, (b) $\mu = 4$.

for both filaments called top (t) and bottom (b). The average floor-field f is represented by the normalized difference in particle densities $\Delta_{t,+} = (\rho_t^+ - \rho_t^-)/\rho^+$ for the plus-species and the top filament (bottom analog) so that we can formulate the mean-field equations exemplary for plus-particles (details in the supplemental material [30])

$$\begin{aligned} \frac{\partial \rho_t^+}{\partial t} &= \omega_a^0 \mu^{\Delta_{t,+}} \rho_u^+ - \omega_d \rho_t^+ \\ \frac{\partial \rho_u^+}{\partial t} &= \omega_d (\rho_t^+ + \rho_b^+) - (\mu^{\Delta_{t,+}} + \mu^{\Delta_{b,+}}) \omega_a^0 \rho_u^+ \\ \frac{\partial \rho_b^+}{\partial t} &= \omega_a^0 \mu^{\Delta_{b,+}} \rho_u^+ - \omega_d \rho_b^+. \end{aligned} \quad (3)$$

Additionally, we get the identity $\rho^\pm = \rho_t^\pm + \rho_b^\pm + \rho_u^\pm$ from particle conservation. In the stationary state, we find the equation for the difference in densities on the top filament Δ as

$$\Delta = \frac{(\mu^\Delta - \mu^{-\Delta})}{\frac{1}{\omega_d}(\mu^\Delta + \mu^{-\Delta}) + \frac{\omega_d}{\omega_a^0}}. \quad (4)$$

Eq. 4 is numerically solvable and shows a pitchfork bifurcation, at a critical $\mu = \mu_{crit}$. For $\mu < \mu_{crit}$ eq. 4 has only a single solution given by $\Delta_0 = 0$, while for $\mu > \mu_{crit}$ the solution $\Delta_0 = 0$ gets unstable and two stable points at Δ_\pm , depending on ω_d and ω_a^0 , occur. We also find that the floor-field has to modify the affinity for both species, otherwise only a symmetric solution can be found [30].

By solving Eq. 4, the flux is estimated by

$$J_{MF} = \rho_t^+ (1 - (\rho_t^+ + \rho_t^-)). \quad (5)$$

Parameters: We used the experimental results of [19] to select the relevant parameters of the model, given in table 1 in the supplemental material [30]. We kept the rates ω_s , ω_d , ω_a^0 and ω_r constant. The relevant density regime is rather difficult to estimate. On the one hand the fraction of occupied binding site is rather low. On the

other hand molecular motors carry rather big objects (20 nm and 50 nm for axonal vesicles [31, 32], compared to 8 nm step-size for most kinesin and dynein motors [33, 34]) such that the density in terms of the occupied volume along the MT is considerably higher. Therefore, we did not focus on the low density regime of $\rho \approx 0.01$, which has been addressed in [19] but varied the particle density in order to study the stability of the bidirectional transport in our model. The chosen lengths of approximately 1000 sites, which correspond to MTs of length $8 \mu\text{m}$, is in accordance to the typical MT-length in axons [35, 36]. The range of the affinity modification μ is motivated by different experiments in which kinesin binding affinity has been measured for different types of MTs. In [19, 37], GTP-MTs show three to four times higher affinity than GDP-MTs and comparing [38] with [39], the affinity is five times higher. The choice of coupling rates, filament number and the number of sub-states in the floor-field implementation is discussed in the supplemental material [30].

MC-Simulations: We investigate the influence of the floor-field on our stochastic model by performing MC-simulations with two filaments started with neutral floor-fields and randomly distributed particles. The total particle density is given by $\rho_{tot} = \rho_+ + \rho_- = 2\rho_+$.

A time-evolution of the system is shown in Fig. 2 averaged over 100 simulations. Yellow lines show the difference in densities Δ . A filament with average floor-field $f = 1/L \sum_{i=1}^L f_i > 0$ is called plus-lane and $f < 0$ minus-lane. The floor-field f_+ (f_-) of the plus (minus)-lane is shown in blue (red), and the total flux J in green (right axis).

Without modification, i.e. $\mu = 1$ in panel (a), no symmetry-breaking is observed. There is no significant difference between f_+ and f_- , and particles are distributed equally ($\Delta = 0$). By raising μ , the floor-field values split up and Δ increases. For $\mu = 4$, f_+ (f_-) and Δ almost reach the extreme values ± 1 , meaning a quasi separation of particles and totally asymmetric floor-fields. This lane-formation is stable and the time-evolution shows very little sample to sample fluctuations. Also the difference in the particle distribution Δ is in good agreement with the average floor-field $|f|$ which makes Δ a good representation for f in the mean-field analysis.

The stationary flux (green) increases for higher μ when the floor-field is stabilized (Fig. 2(b) with $\mu = 4$). In case of $\mu = 4$ ($\mu = 6$) an average effective velocity of ≈ 270 nm/s (350 nm/s) for a motor protein whereas the free stepping velocity of bound kinesins is presumed to be 480 nm/s in this work ([19]). As expected the mean-field solution (dashed green line in Fig. 2) overestimates the flux considerably, since a homogeneous distribution of particles is assumed, while in the full model there are strong density-correlations due to cluster formation. However, the initially symmetric two-lane system spontaneously

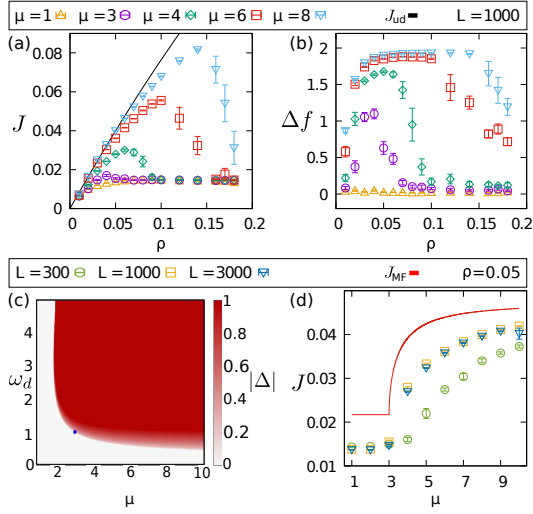


FIG. 3. Transport efficiency (a) and symmetry-breaking (b), (d)) under variation of density and affinity modification. Simulations did run for 3 hours real-time, measurements started after 1 hour. Panel (c) shows the phase-space for symmetric and asymmetric solutions in the mean-field model.

breaks symmetry so both lanes carry stationary and oppositely directed net flows.

In Fig. 3(a), we show the density dependence of the flux for different μ in comparison to the unidirectional flux. Simulation results show that the transport efficiency of the system is significantly increased for ($\mu \geq 3$) compared to the plateau obtained without floor-field ($\mu = 1$). Actually, the flux reaches almost the value of the corresponding unidirectional flux to J_{ud} until it breaks down to the traffic jam plateau value, similar for all μ . The density at which the transition to the plateau value is observed, depends on μ . Note that the stationary state is not always reached at high densities if we initialize the system with a random configuration, indicated by the larger error bars in the high density regime caused by meta-stable clusters (Fig. 3(a)), which have not been dissolved within the simulation time.

Lane-formation is well characterized by the difference in floor-field $\Delta f = f_+ - f_-$ measuring asymmetry between filaments and is shown in Fig. 3(b). The base line corresponds to symmetric fields without lane-formation for $\mu = 1$. By increasing μ , the asymmetry develops in a density dependent range before Δf drops down. Results of panel (a) and (b) indicate a lane-formation and quasi ordering the system into two sub-systems with oppositely directed flux. When the self-organization breaks down, traffic jams are forming on both lanes and transport efficiency is not enhanced anymore. This is consistent with lane-formation observed in other floor-field models [20].

The influence of μ on the symmetry-breaking is further examined in Fig. 3(c) and (d) by comparing mean-field results to MC-simulations. In panel (c), a phase diagram from mean-field analysis for $|\Delta|$ under variation of μ and ω_d is shown for fixed $\omega_a^0 = 5s^{-1}$. The blue dot marks μ_{crit} for ω_d used in simulations and agrees with Fig. 2 and Fig. 3 (b). The border of $|\Delta| > 0$ shows that $\mu_{crit} > 1$ for arbitrary ω_d . There is only a small region where $0 < |\Delta| < 1$ because the mathematical solution of Eq. 4 can be larger than the physical border of $|\Delta| = 1$, hence particles are completely separated. The transition is sharper for shorter run lengths (larger ω_d). In panel (d), J is growing under variation of μ for constant $\rho = 0.05$ and different L . Remarkably, the transition from a symmetric to a stable asymmetric solution is captured by the mean-field approach and even the predicted value μ_{crit} agrees well with simulation results. The transition is sharper for $L \geq 1000$ than for $L = 300$, hence, the larger system is better approximated by the mean-field model. Also, larger systems have higher fluxes. This is in contrast to the plateau value for $\mu = 1$ which decreases with the system size. For even larger L it is computationally hard to achieve stationary states but we expect the system to still self-organize in lanes due to stable lanes if already started in such conditions (supplemental material [30]).

CONCLUSION AND OUTLOOK

To summarize, we introduced a stable mechanism for efficient bidirectional transport of active particles in one-dimensional systems under strong confinement. This mechanism is based on self-organized lane-formation. Directed lanes may be predefined in engineered systems, however, this is not always the case for transport of animals or humans as for instance in pedestrian dynamics where self-organized lane-formation occurs [20–24]. The influence of the floor-field on particle binding was inspired by recent experimental results on self-induced strengthening of the kinesin MT-affinity, but could also be realized by other modifications of MTs. Lane-formation can be captured by a mean-field approach, which shows the mechanism is stable against local density fluctuations.

The stability of lane-formation is remarkable in several respects. First of all, lane-formation is observed in the biologically relevant low density regime. This is in contrast to other mechanisms, based on particle-particle interactions [40], which lead to symmetry-breaking at high densities and therefore low particle velocities, while *in vivo* observations of e.g. axonal vesicle transport show that vesicles transported by molecular motors reach the free stepping velocities of kinesin. Second, we observe the coexistence of transport in both directions on a coupled pair of filaments, which goes beyond symmetry-breaking mechanisms reported as discussed in e.g. [41] where symmetry-breaking leads to unidirectional trans-

port. Third, our model describes the low mobility of unbound particles, which may trigger cluster formation in bidirectional transport and illustrates the stability of the suggested mechanism. From our point of view, our results indicate that stable bidirectional flows are more easily realized by modifications of the filaments rather than interactions between particles.

The importance of the MT structure on transport has recently been pointed out [14–17]. Bidirectional intracellular transport is organized on oppositely oriented filament bundles in dendrites [16] and on parallel oriented MT doublets in cilia [17]. In axons, however, so far a similar organization of the MT network has not been identified. Our findings indicate that the posttranslational modification by motors and self-induced preferential binding of one or the other motor species could indeed lead to stable bidirectional transport in an *a priori* unipolar MT network. A self-induced amplification of the binding affinity must be given for both particle species. Otherwise, the density of oppositely oriented particles on the same filament is too high to realize efficient transport states.

Concerning the robustness and efficiency of the proposed lane-formation in our model for intracellular transport, it would be of great interest to obtain further insight to the interplay between dynein and kinesin motors, microtubules and MAPS, which might have a strong impact on the (self-)organization of intracellular transport.

ACKNOWLEDGEMENTS

This work was funded by the Deutsche Forschungsgemeinschaft (DFG) through Collaborative Research Center SFB 1027 (Project A8).

-
- [1] B. L. Bloodgood and B. L. Sabatini, *Science*, 310, 866, (2005).
- [2] N. Hirokawa and R. Takemura, *Nature Reviews Neuroscience*, 6, 201, (2005).
- [3] A. Brown, *J Cell Biol*, 160, 817, (2003).
- [4] C. Herold, C. Leduc, R. Stock, S. Diez, and P. Schwill, *ChemPhysChem*, 13, 1001, (2012).
- [5] P. J. Hollenbeck and W. M. Saxton, *Journal of cell science*, 118, 5411, (2005).
- [6] M. Ebbinghaus, C. Appert-Rolland and L. Santen, *Journal of Statistical Mechanics: Theory and Experiment*, 2011, P07004, (2011).
- [7] C. Appert-Rolland, M. Ebbinghaus and L. Santen, *Physics Reports*, 593, 1-59, (2015).
- [8] M. Evans, D. Foster, C. Godr?che and D. Mukamel, *Journal of Statistical Physics*, 80, 69, (1995).
- [9] G. Korniss, B. Schmittmann and R. Zia, *Europhys. Letters*, 45, 431, (1999).
- [10] R. Jose, C. Arita and L. Santen, accepted for publication in *JSTAT* 2020, arXiv:1912.08647
- [11] A. Parmeggiani, T. Franosch, and E. Frey, *Physical Review E*, 70(4), 046101, (2004).
- [12] I. Pinkoviezky, and N. S. Gov, *Physical review letters*, 118(1), 018102 (2017).
- [13] A. Ebnet *et al.*, *J Cell Biol* 143, 777-794, (1998).
- [14] S. Gadadhar, S. Bodakuntla, K. Natarajan, C. Janke *Journal of Cell Science*, 130, 1347-1353 (2017).
- [15] C. Janke, *J Cell Biol* 206 (4), 461-472 (2014).
- [16] R. P. Tas, A. Chazeau B. M. C. Cloin, M. L. A. Lambers, C. C. Hoogenraad and L.C. Kapitein, *Neuron*, 96, 1264, (2017).
- [17] L. Stepanek and G. Pigino, *Science*, 352, 721, (2016).
- [18] D. Johann, C. Erlenk?mper and K. Kruse, *Phys. Rev. Lett.* 108, 258103, (2012).
- [19] T. Shima, M. Morikawa, J. Kaneshiro, T. Kambara, S. Kamimura, T. Yagi, H. Iwamoto, S. Uemura, H. Shigematsu and M. Shirouzu, *J Cell Biol*, 217, 4164, (2018).
- [20] C. Burstedde, K. Klauck, A. Schadschneider J. and Zitzartz, *Physica A*, 295, 507, (2001).
- [21] S. Nowak and A. Schadschneider, *Physical Review E*, 85, 066128, (2012).
- [22] M. Chraibi, A. Tordeux, A. Schadschneider and A. Seyfried, *Complex Dynamics of Traffic Management*, pages649?669. Springer US, New York, NY, (2019).
- [23] L. Gibelli and N. Bellomo. *Crowd Dynamics, Volume 1: Theory, Models, and SafetyProblems*. Springer, (2019).
- [24] A. Schadschneider, D. Chowdhury and K. Nishinari. *Stochastic transport incomplex systems: from molecules to vehicles*. Elsevier, (2010).
- [25] D. Peet, N. Burroughs and R. Cross, *Nature Nanotechnology*, 1, (2018).
- [26] B. Derrida, *Physics Reports*, 301, 65, (1998).
- [27] P. Arndt, T. Heinzel, and V. Rittenberg, *Journal of Physics A*, 31, L45, (1998).
- [28] M. Ebbinghaus and L. Santen, *Journal of Statistical Mechanics: Theory and Experiment*, 2009, P03030, (2009).
- [29] M. Evans, R. Juh?asz and L. Santen, *Physical Review E*, 68, 026117, (2003).
- [30] See the Supplemental Material at [...] for the set of parameters, a detailed mean-field analysis and a discussion of the used reference set.
- [31] K. Harris and P. Sultan, *Neuropharmacology*, 34, 1387, (1995).
- [32] D. Hall and E. Hedgecock, *Cell*, 65, 837, (1991).
- [33] K. Svoboda, C. Schmidt, B. Schnapp and S. Block, *Nature*, 365, 721, (1993).
- [34] E. Hirakawa, H. Higuchi and Y. Toyoshima, *PNAS*, 97, 2533, (2000).
- [35] M. R. Shaebani, A. Pasula, A. Ott and L. Santen, *Scientific reports*, 6, 30285, (2016).
- [36] W. Yu and P. Baas, *Journal of Neuroscience*, 14, 2818, (1994).
- [37] M. Morikawa, H. Yajima, R. Nitta, S. Inoue, T. Ogura, C. Sato and N. Hirokawa, *EMBO J*, 34, 1270, (2015).
- [38] S. Rosenfeld, B. Rener, J. Correia, M. Mayo and H. Cheung, *Journal of Biological Chemistry*, 271, 9473, (1996).
- [39] T. Nakata, S. Niwa, Y. Okada, F. Perez and N. Hirokawa, *J Cell Biol*, 194, 245, (2011).
- [40] S. Klumpp and R. Lipowsky, *EPL*, 66, 90, (2004).
- [41] V. Popkov and I. Peschel, *Physical Review E*, 64, 026126, (2001).
- [42] T. Reichenbach, E. Frey and T. Franosch, *New J. Phys.* 9 159, (2007).

Self-organized lane-formation in bidirectional transport of molecular motors
SUPPLEMENTAL MATERIAL

Robin Jose and Ludger Santen

Department of Theoretical Physics & Center for Biophysics,
Saarland University, 66123 Saarbrücken, Germany

(Dated: February 28, 2020)

Mean-field analysis: In the continuum limit for a single, unidirectional exclusion process with particle exchange to a reservoir, the mean-field approach is given by [29]

$$\frac{\partial \rho(x, t)}{\partial t} = \frac{\partial J(x, t)}{\partial x} + \omega_a(1 - \rho(x, t)) - \omega_d \rho(x, t). \quad (\text{S1})$$

Here, we consider a system with periodic boundary conditions and translational invariant initial conditions, such that $\frac{\partial J}{\partial x} = 0$ and $\frac{\partial \rho}{\partial t} = 0$ holds in the stationary state. In absence of a floor-field, the effective density of particles bound to the filament is given by Langmuir kinetics [11, 29]. Hence, we obtain the following estimates for the stationary density and flux:

$$J_{\text{ud}} = \rho_{\text{eff}}(1 - \rho_{\text{eff}}) \quad \rho_{\text{eff}} = \rho \frac{\omega_a^0}{\omega_a^0 + \omega_d}. \quad (\text{S2})$$

Next, we consider in a system consisting of two filaments (top and bottom) and a mutual reservoir (unbound) of infinite capacity. Please note that we consider a single particle reservoir in the mean-field approach instead of two weakly coupled reservoirs in the full model, each of which being coupled to one of the two filaments. This simplification is valid because the weak coupling of the two particle-reservoirs of the full model suppresses the coupling of the density-fluctuations between the two filaments. Density-fluctuations, however, are not described by the mean-field approach.

Whereas the detachment rates are constant, the attachment rate is a function of particle densities and describes the impact of the floor-field in the full model. Eq. 2 in the main text describes that the attachment depends on the floor-field f_i on the particular site i on which the particle wants to attach. Due to the translational invariance of the model we consider consistently an average floor-field f . We estimate the average floor-field by the normalized difference of densities ρ^+ and ρ^- on the given filament, i.e. $f^t = (\rho_i^+ - \rho_i^-)/\rho^+$ for a plus-particle on the top filament. The attachment rates for plus- and minus-particles on the top filament $\omega_a^{t,\pm} = \omega_a^{t,\pm}(\rho_i^+, \rho_i^-)$ are then given by

$$\omega_a^{t,+} = \omega_a^0 \mu^{(\rho_i^+ - \rho_i^-)/\rho^+} \quad (\text{S3})$$

$$\omega_a^{t,-} = \omega_a^0 \mu^{(\rho_i^- - \rho_i^+)/\rho^-}. \quad (\text{S4})$$

The equations given above hold for attachment to the top-filament. An analogous set of equations describes the attachment to the bottom-filament.

As a result we arrive at the following mean-field equations for the two-filament system with particle reservoir and the previously defined attachment rates $\omega_a^{t,\pm}, \omega_a^{b,\pm}$, which depend on the difference of plus and minus motor density:

$$\frac{\partial \rho_t^+}{\partial t} = \omega_a^{t,+} \rho_u^+ - \omega_d \rho_t^+ \quad (\text{S5})$$

$$\frac{\partial \rho_u^+}{\partial t} = \omega_d (\rho_t^+ + \rho_b^+) - (\omega_a^{t,+} + \omega_a^{b,+}) \rho_u^+ \quad (\text{S6})$$

$$\frac{\partial \rho_b^+}{\partial t} = \omega_a^{b,+} \rho_u^+ - \omega_d \rho_b^+, \quad (\text{S7})$$

where ρ_u^+ denotes the density of the plus-particles in the particle reservoir. We get an analogous set of particles for minus particles. Furthermore, particle conservation leads to the relation $\rho^+ = \rho_t^+ + \rho_b^+ + \rho_u^+$ for plus-particles and $\rho^- = \rho_t^- + \rho_b^- + \rho_u^-$ for minus-particles. For simplicity, we consider $\rho^+ = \rho^-$.

We define $\Delta = (\rho_t^+ - \rho_t^-)/\rho^+$ which we use as an estimate of the average floor-field f (compare to Fig. 2). We also make use of the symmetry between plus- and minus-particles, i.e. we choose $\rho_t^+ = \rho_b^-$, $\rho_b^+ = \rho_t^-$ and $\rho_u^+ = \rho_u^-$ and drop the \pm index. Using these assumptions and definitions we get:

$$\frac{\partial \rho_t}{\partial t} = \omega_a^0 \mu^\Delta \rho_u - \omega_d \rho_t \quad (\text{S8})$$

$$\frac{\partial \rho_u}{\partial t} = \omega_d (\rho_t + \rho_b) - (\omega_a^0 \mu^\Delta + \omega_a^0 \mu^{-\Delta}) \rho_u \quad (\text{S9})$$

$$\frac{\partial \rho_b}{\partial t} = \omega_a^0 \mu^{-\Delta} \rho_u - \omega_d \rho_b. \quad (\text{S10})$$

From Eq. S8 to Eq. S10, we find the following equation for Δ :

$$\frac{1}{\omega_d} \frac{\partial \Delta}{\partial t} = \frac{\omega_a^0}{\omega_d} \frac{\rho_u}{\rho} (\mu^\Delta - \mu^{-\Delta}) - \Delta. \quad (\text{S11})$$

Making use of normalization and Eq. S9, we can determine an equation for Δ in the stationary state

$$\Delta = \frac{(\mu^\Delta - \mu^{-\Delta})}{\frac{1}{\omega_d} (\mu^\Delta + \mu^{-\Delta}) + \frac{\omega_d}{\omega_a^0}}. \quad (\text{S12})$$

Eq. S12 is numerically solvable and shows a pitchfork bifurcation at $\mu = \mu_{\text{crit}}(\omega_a^0, \omega_d)$ from a stable equilibrium point at $\Delta_0 = 0$ to the unstable equilibrium point $\Delta_0 = 0$

and two stable points at Δ_{\pm} . Note that this asymmetrical solution can be found for $|\Delta| > 1$ in some cases. By definition, the difference of physical densities cannot be larger than 1, so a solution $|\Delta| > 1$ will correspond to a total separation of particles at the border of the definition of Δ .

As a next step, we explicitly calculate the densities in each state by using the asymmetric solutions for Δ

$$\rho_t = \frac{\rho \Delta_{\pm} \mu^{\Delta_{\pm}}}{(\mu^{\Delta_{\pm}} - \mu^{-\Delta_{\pm}})} \quad (\text{S13})$$

$$\rho_u = \frac{\omega_d}{\omega_a^0} \frac{\rho \Delta_{\pm}}{(\mu^{\Delta_{\pm}} - \mu^{-\Delta_{\pm}})} \quad (\text{S14})$$

$$\rho_b = \frac{\rho \Delta_{\pm} \mu^{-\Delta_{\pm}}}{(\mu^{\Delta_{\pm}} - \mu^{-\Delta_{\pm}})}. \quad (\text{S15})$$

Using these results, we can calculate the flux for plus-particles on the top lane

$$J_{\text{MF}} = J_t^+ = \rho_t^+ (1 - (\rho_t^+ + \rho_t^-)) \quad (\text{S16})$$

and analogously for the bottom lane as well as for minus-particles.

List of parameters: In our simulations, we used the reference set of parameters shown in table I. Different choices of parameters are mentioned in the text.

Kymographs: In order to initialize our simulations, particles are randomly distributed in the unbound state on both filaments. In the top row of Fig. S1, we show a kymograph corresponding to a typical time-evolution of the system over one hour real time. Shown are bound particles of filament 1 and 2 in a long time interval in order to observe the system transitioning between the two following states. After an initial symmetrical state with clustering, particles distribute asymmetrically between the two filaments. The result is a clear majority of plus-minus particles on filament 1 (2). We then call the filament with a plus (minus) majority plus-lane (minus-lane). Also the floor-field clearly breaks symmetry in the same way. This lane-formation was not observed for neutral affinity modification (not shown).

In the bottom row of Fig. S1 we show parts of the kymographs in a higher time resolution. Intervals of 30 s are shown from the kymograph of filament 2. The left figure belongs to the early phase in which the system is in a symmetric state where immobile clusters drastically reduce the flux. The right figure shows the system in

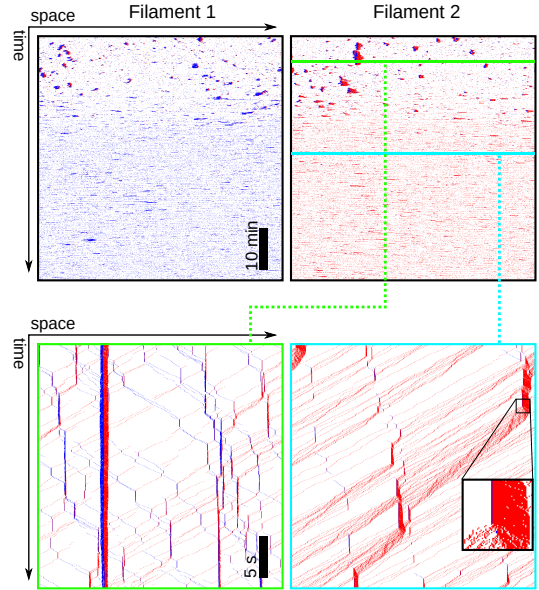


FIG. S1. Top: Kymographs in a two-lane system of length $L = 1000$, density $\rho = 0.08$ and modification $\mu = 6$. We studied the time-evolution of the system during the first hour (real time) after initialization in a random configuration and with a neutral floor-field. Bound plus-particles are blue, minus-particles red and empty space or unbound particles white. The scale bar shows a time interval of 10 minutes. The green and cyan line mark 30 s intervals which are shown in the bottom row. Bottom: 30 second intervals in a higher resolution show examples of the symmetric state (left) and the asymmetric state (right). The inset shows that typically only a single plus-particle blocks the runs of minus-particles temporally. The scale bar shows an interval of 5 seconds.

the asymmetric state where only a few plus-particles are present on the minus-lane. Minus-particles perform in coordinated runs, only temporarily blocked by plus-particles, which results in a more efficient transport state.

Length dependency: Beside the flux and symmetry dependencies on the density ρ and the affinity modification feedback μ , we study the influence of the system length. In Fig. S2(a) and (b) we plot J and Δf for a fixed density $\rho = 0.05$ under variation of L . On the one hand, lane-formation needs a minimum length so that enough particles are involved in the system i.e. the sharper transition in Fig. 3 in the main text for $L = 1000$ than $L = 300$ is consistent with the not reached maximum value for $L = 300$ in Fig. S2 (a) and (b). On the other hand, stable lanes were not able to form within our simulation of 3 hours simulated time for $L \geq 4000$, represented by the large error bars in this regime. For large systems it takes very long to reach the stationary state from random initial conditions so we check whether asymmetric initial

TABLE I. Reference set of parameters. The rates ω_s , ω_a , ω_d and ω_r are extracted from [12].

ρ	0.05	L	1000
ω_s	60 s^{-1}	N_p	13
ω_a^0	5 s^{-1}	ω_r	0.005 s^{-1}
ω_d	1 s^{-1}	ω_c	0.1 s^{-1}

conditions are stable and lane-formation persists in the stationary state. We add filled symbols for simulations started in asymmetric conditions to the open symbols for the reference start in symmetric conditions. Here, the system remains in the asymmetric state when high affinity modification was implied but produced traffic jams and lost asymmetry without the modification. Thus, we expect the system to self organize even for larger system sizes in the stationary state.

Number of sub-states: We now check our model calibration in Fig. S2 (c) and (d) by comparing two different numbers of sub-states $N_p = 13$ (empty symbols) and $N_p = 1$ (filled symbols). The number influences floor-field resistance against single particle induced changes for sub-states and leads to a majority effect. We compare the model to a version with only a single (sub-)state per site. This means, that each particle stepping to a given neutral site sets its affinity, i.e. $f_i = s_i$. This complete modification of the local floor-field by a single particle is not in agreement with experimental results which report a curvature of MTs at low kinesin concentrations corresponding to a partial excitation of the protofilaments [19, 25]. In our model the average of $N_p = 13$ sub-states takes this collective effect into account and determines the local preference from an average of all local-substates f_i . A lattice with only one sub-state shows similar but quantitatively smaller flux enhancement. In case of $\mu = 4$, there is no improvement compared to the neutral system. If $\mu = 6$, enhancement is visible but only for densities up to $\rho = 0.03$ before the flux breaks down. This behavior is also reflected in the floor-field in panel (d). Here, the asymmetry exhibition is shifted towards lower densities and is in case of $\mu = 4$ not as strong as for $N_p = 13$. For such small densities, the flux is close to J_{ud} so that the enhancement in the flux is hardly noticeable.

Number of filaments: An increasing of the number of lanes does not further improve the flux as it can be seen in panel (e) where filled symbols belong to a system of $N_L = 8$ lanes, being in good agreement with the two track version (open symbols).

Coupling rate ω_c : We also investigated the influence of the coupling rate ω_c which determines the amount of interaction between filaments. The actual value of the coupling rate has not been established in experiments. In all simulations we use the value $\omega_c = 0.1 \omega_d$ as given in table I. In Fig. S2 (f), the system supports lane-formation and enhanced flux for weakly coupled lanes. The flux breaks down if the coupling rate is of the order of attachment and detachment rate. This breakdown is related to traffic jams on both filaments, located at similar positions. The strong density correlation prevents traffic jams from resolution because motors cannot escape from crowded areas due to exclusion. Strongly coupled filaments cannot organize themselves into lanes anymore. It follows that tracks have to be weakly coupling for the mean-field assumption, which is consistent with studies

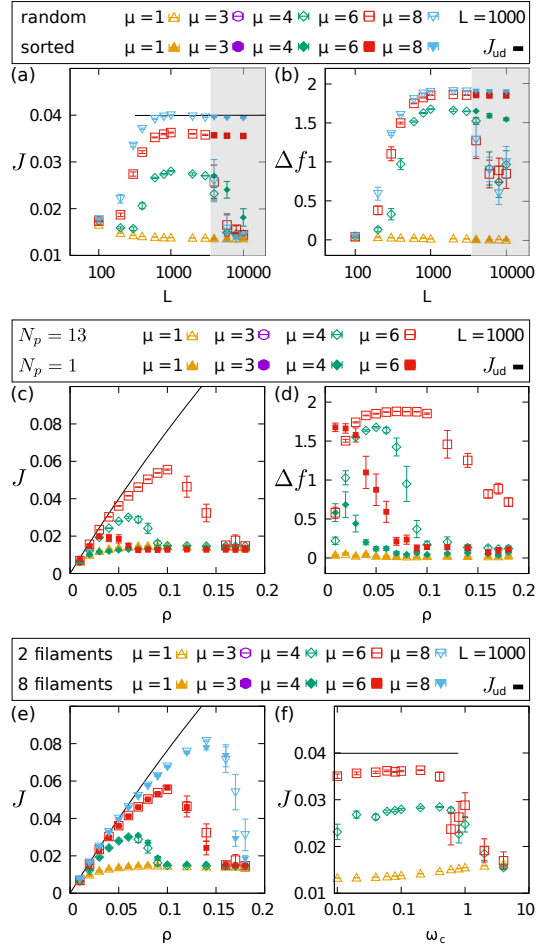


FIG. S2. Flux $\langle J \rangle$ (a) and asymmetry Δf (b) under variation of the system length L . Simulations did run for 3 hours simulated time, measurements started after 2 hours. Simulations which were initialized in random configurations are marked as open symbols, simulation data from asymmetric initial conditions are represented by filled symbols. The black line shows J_{ud} and the shaded area marks the length regime of large error bars and the second set of simulations started in sorted initial conditions. Model comparison in the fundamental diagram (c) and the floor-field asymmetry (d) between different numbers of sub-states. The reference system with 13 sub-states is given by open symbols, a lattice of only one sub-state by filled symbols. (e) Fundamental diagram for the reference system of 2 filaments (open symbols) compared to a system of 8 filaments (filled). (f) Variation of the filament coupling rate ω_c for different μ influences the particle flux. The reference value used in the main text is given by $\omega_c = 0.1$.

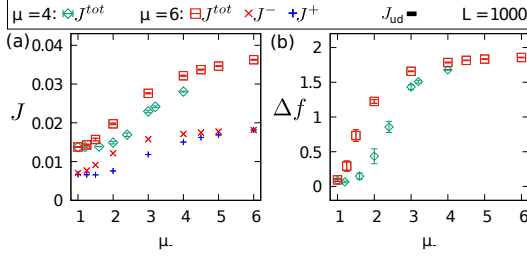


FIG. S3. Total particle flux J^{tot} (a) and floor-field asymmetry (b) in case of asymmetrical motor affinity modification factors μ_+ and μ_- . We fix $\mu_+ = \mu$ and vary μ_- in $[1, \mu]$. For $\mu = 6$, fluxes are shown for plus- and minus-particles separately.

about unidirectional transport on coupled tracks [42].

The idea of weak coupling is consistent with the biological findings that motor-cargo complexes have a very low diffusivity in the crowded cytosol of the axon *in vivo*. Hence, it makes a difference whether particles attach to a close MT or to a neighboring MT which is further away.

Asymmetric motor affinity modification: We investigate if symmetric affinity modification parameters are needed to generate symmetry-breaking in our system. For that, we distinguish μ for plus-particles μ_+ and minus particles μ_- . For a given $\mu_+ = \mu$, we decrease affinity of minus particles down to a neutral setting $\mu_- = 1$ and show fluxes and the floor-field asymmetry in Fig. S3.

We can see that no symmetry between plus and minus particle affinity modification is needed for having

an enhanced flux and asymmetric floor-fields. However, without a slightly modified affinity of minus-particles, we cannot see any enhancement of the flux no matter if binding of plus-particles is modified or not. This result is consistent with mean-field analysis for $\mu_+ = \mu$ and $\mu_- = 1$. Eq. S8 to Eq. S10 simplify for minus-particles, i.e.

$$\frac{\partial \rho_t^-}{\partial t} = \omega_a^0 \rho_u^- - \omega_d \rho_t^- \quad (S17)$$

$$\frac{\partial \rho_u^-}{\partial t} = \omega_d (\rho_t^- + \rho_b^-) - 2\omega_a^0 \rho_u^- \quad (S18)$$

$$\frac{\partial \rho_b^-}{\partial t} = \omega_a^0 \rho_u^- - \omega_d \rho_b^- \quad (S19)$$

These equation system has only a symmetrical solution. Using this result in the equations for plus-particles leads exclusively to symmetrical solutions for plus-particles, too. Hence, no lane-formation is found in a mean-field model if the attachment modification applies only to one of the two particle species.

In Fig. S3 (a), the plus and minus flux J^\pm is not identical for all μ_- . By having only a low affinity modification for minus-particles, it is the plus-particles which cannot produce flux more than in the neutral case. On the filaments, the plus density is concentrated to one filament but minus-particles are located on both. Hence, minus-particles on the minus-lane are rather free to move but most plus-particles are blocked by the minus-particles on the plus-lane. By increasing the minus affinity modification, this gradually changes until the fluxes of the two particle species are balanced.

Acknowledgments

Finally, I would like to thank the people who supported me during this research.

First of all, I want to give thanks to my supervisors Ludger Santen and Reza Shaebani for their support and guidance during the full time of the work. In many insightful discussions, I learned a lot about the research field but also on how to operate in the scientific environment. I appreciate the freedom I had and the opportunity to travel to conferences and to present our work. In particular, I am thankful for the support in finalizing all the articles and the thesis.

Furthermore, I would like to thank Chikashi Arita for the support and cooperation during the work on non-Markovian exclusion processes.

I want to thank the organizers and contributors of the Collaborative Research Center SFB 1027 and its integrated research training group for providing such an inspiring research environment.

Special thanks go to my co-workers Gina Monzon, Neda Safaridehkohne, Daniel Bahr and Erik Maikranz for many fruitful discussions, proofreading and, in particular, for the very good and friendly working atmosphere.

Finally, I thank my partner Sandra Hofmann and my family for all the support on my way.

